ADVANCEMENTS IN POINT-OF-CARE DIAGNOSTIC ASSAYS FOR NON-INVASIVE SAMPLES IN RESOURCE CONSTRAINED SETTINGS

By

Emily Camille Kight

Dissertation

Submitted to the Faculty of the

Graduate School of Vanderbilt University

in partial fulfillment of the requirements

for the degree of

DOCTOR OF PHILOSOPHY

in

Biomedical Engineering

May 12, 2023

Nashville, Tennessee

Approved:

Frederick Haselton, Ph.D.
Michael King, Ph.D.
Todd Giorgio, Ph.D.
David Wright, Ph.D.
Maria Hadjifrangiskou, Ph.D.

TABLE OF CONTENTS

ACKNOWLEDGEMENTS

First, I would like to thank Dr. Tanaka, Dr. Russell, Dr. Fu and the MARC cohort for supporting me as an undergraduate student and helping me make the transition to graduate school. I would like to thank my committee members, Dr. King, Dr. Hadjifrangiskou, Dr. Haselton, Dr. Wright, and Dr. Giorgio, for your wisdom and advice. I would like to thank Dr. Bowden for working with me on several projects and taking a chance on me. I would like to thank Dr. Iftak Hussain for his guidance and help on bringing multiple projects to fruition with me. I would like to thank my many lab members for their support and help over the years. I would like to thank Rosana Alfaro for her great work on our microneedle project. I would like to thank Dr. Stephanie Pearlman for her help and support over the year. I would like to thank Jaya Bhojwani for her support and helping me survive. Finally, I must thank my partner Mike and my family, for believing in me, and helping me on this journey. The support from all these individuals is the reason I am here today writing my Thesis Dissertation.

LIST OF TABLES

LIST OF FIGURES

LIST OF ABBREVIATIONS

AKI: Acute kidney injury

ANOVA: Analysis of variance

bp: base-pair

CDC: Center for Disease Control

cf-DNA: cell-free DNA

CKD: Chronic kidney disease

CKDnt: Chronic kidney disease of nontraditional origin

COVID-19: Coronavirus disease 2019

DNA: Deoxyribonucleic acid

dsDNA: Double-stranded DNA

ELISA: enzyme-linked immunosorbent assay

EDTA: ethylenediaminetetracetic acid

FRET: Förster (or fluorescence) resonance energy transfer.

HE4: Human epididymis protein four

HIV: Human immunodeficiency virus

LD: Lyme disease

LED: Light emitting diode

LMICs: Low and middle-income countries

MN: Microneedle

NAT: Nucleic acid test.

OC: Ovarian cancer

OCR: Ovarian Cancer Recurrence

PBS: Phosphate-buffered saline

PCR: Polymerase chain reaction

POC: Point-of-care

RNA: Ribonucleic acid

RPM: Revolutions per minute

ssDNA: Single-stranded DNA

TB: Tuberculosis

WHO: World Health Organization

w/v: weight per volume

CHAPTER 1: INTRODUCTION

The need for low-cost diagnostics

Diagnostic development is an important part of equitable healthcare. The improvement of global health depends on access to appropriate diagnostics for all citizens of all countries. Unfortunately, many current diagnostics simply do not meet the needs of low- and middle-income countries (LMICs)[2]. For several neglected or underserved diseases, diagnostic development has stalled, or the current options are not affordable or accessible for the patients and caregivers that need them[3]. Many reported clinic challenges include cost, low staff capacitates, irregular supply, transportation delays, inconsistent funding by governments, or limited technical aspects such as poor accuracy, and a long time to answer. Moreover, there is often little incentive for commercial diagnostic companies to spend their resources on developing diagnostic tools that communities in developing countries cannot adopt and support in their healthcare market. Additionally, LMICs often suffer from regulatory barriers and policies that are difficult to navigate for diagnostic developers[4]. As a result, many communities that suffer from underfunded healthcare infrastructure lack access to the diagnostic tools they need which leads to a higher mortality than the same disease in high-income countries. Therefore, new diagnostic technologies are urgently needed to reduce the burden of disease in developing countries.

Since many populations in LMICs do not have access to healthcare facilitates with good infrastructure and high level of staff training, development of assays at the point-of-care (POC) may help lower costs and barriers to access without sacrificing accuracy. However, this is largely dependent on the molecular biomarker of interest. A molecular biological marker or molecular biomarker is a disease-associated molecular change in the body that is measurable accurately[5]. The National Institutes of Health Biomarkers Definitions Working Group defined a biomarker as "a characteristic that is objectively measured and evaluated as an indicator of normal biological processes, pathogenic processes, or pharmacologic responses to a therapeutic intervention"[6]. Biomarkers can range widely from blood pressure

to complex laboratory blood tests to detect a specific gene mutation. Molecular biomarkers may include proteins, nucleic acids, hormones, response to toxins, antibodies, pathogens, glucose, or other analytes found in tissues or other fluid samples that indicate physiological or pathological state. Molecular biomarkers can be used for disease screening, diagnosis, characterization, monitoring, predicting response, and pharmacodynamic studies[7]. As biomarkers show various levels in healthy populations, elevated levels beyond a healthy baseline are often used to define an increased risk for disease or disease progression. An ideal biomarker would exhibit low variability in expression, low signal to noise ratio, be a stable product not susceptible to damage from handling or storage and be readily accessible for analysis. Additionally, a good biomarker would show a dramatically changed level in response to a successful therapy or change in disease condition. The best assays with biomarkers are devices that are specific, sensitive, reproducible, and reliable. To assess public health, identifying trends in disease levels in populations are required for global health monitoring and epidemic identification. Advances in low-cost biomarker collection allow for insight into public health issues and the effectiveness of health programs. New tools that use suitable molecular biomarkers in early diagnosis of diseases may enable development of cost-effective health interventions and reduce mortality.

The World Health Organization (WHO) has developed a set of characteristics that make a diagnostic test suitable in LMICs, which is abbreviated using the acronym ASSURED (**Table 1.1**). Additionally, other considerations include devices that can be operate reliably at ambient temperatures, or without electricity, running water or a sterile environment[8]. Diagnostics that rely on expensive or complicated equipment requiring routine maintenance each year are also less likely to be useful in LMICs. There is also a goal to increase the speed of testing so that patients do not leave before the results are presented. The minimum sensitivity for a diagnostic is 85-95% and a specificity of 76-97%[8]. Another particular concern is the issue of obtaining a specific sample type or sample volume needed for testing. For instance, the current HIV viral load tests currently requires a 1 mL of blood draw from venipuncture for detection which greatly limits this test in places without the staff and equipment[8].

Affordable by those at risk of infection.
Sensitive (few false-negative results).
Specific (few false-positive results).
User-friendly (simple to perform by persons with little training).
Rapid treatment at the first visit and robust use without the need for special storage.
Equipment-free (no large electricity-dependent instruments needed to perform the test other than small batteries for handheld portable devices).
Delivered to those who need it

Table 1.1 WHO parameters for the ideal diagnostic assay in LMICs.

Limitations of blood and serum

Reliable diagnosis is critical for early treatment and surveillance of disease. Currently, many WHO-recommended diagnostic assays are unreliable in resource limited settings partly because they often involve invasive sampling of infectious blood, sputum, or tissue. Although serum and plasma fluid have been traditional samples for biomarker collection and routine analysis at clinics, blood samples suffer from several limitations. Firstly, blood is collected in a limited sample volume which further restricts the amount of repeat testing from a single sample. Although blood can provide information on the presence or absence of substances, some substances are not stable in blood or blood may contain interfering substances that effect the accuracy of testing. Additionally, collecting blood is often a painful process for the patient and can contain infectious material that can cause harm to phlebotomists if not properly handled. Depending upon the analyte of interest or test, blood may be the least optimal sample type.

Blood collection routinely relies on a trained phlebotomist, a needle to pierce the skin, and a syringe to collect the sample. Needlestick injury (NSI) is a common healthcare hazard and is estimated to account for 80% of percutaneous injuries [9]. As humans are living longer with chronic health conditions, healthcare and support has increasingly moved towards the home environment. Due to this, NSI and transmission of

blood borne pathogens (BBP) through NSI have greatly increased [10,11]. These injuries are occurring outside of clinical settings by community nurses, home aides, family helpers or patients themselves. Compounding this issue is the lack of a safe disposal procedure for sharps waste in the home setting. The increased cost associated with a sharps container, returning to a designated facility for disposal, and transport of the sharps container results in a lack of compliance for proper sharps waste management [12]. This leads to needle discard into municipal wastes where waste employees are at greater risk of NSI and BBP transmission. Finally, in lower income countries where waste scavenging occurs, recycling medical waste, such as infectious sharps, results in increased risk for disease in the community [13].

Minimally invasive sample types

Samples which do not require a trained technician to acquire and are painless for the patient, are more likely to be collected. Minimally invasive biomarkers collection has been recognized as a promising method for patient health monitoring. Indeed, the market for non-invasive samples such as urine, stool, nasal swab, and saliva-based tests have grown considerably over the past few decades. Strategies to expand disease detection using minimally invasive samples are ongoing. Additionally, urine and skin ISF are considered non-infectious samples and would pose little hazard for caregivers to collect. Since the composition of urine and skin ISF are less complex than stool and saliva, I have focused my research efforts on these sample types in development of diagnostic tools.

Urine as a sample source.

Urine is an advantageous biofluid and a rich source of biomarkers. Unlike blood, urine is a non-invasive sample that can be easily collected without pain or hazard from needles, the need for special equipment or a trained phlebotomist. Moreover, urine allows large volume collection up to several times per day and can even be collected at home. Urine provides a snapshot of systemic biomarker levels without the risks posed by blood collection (i.e., disease transmission). Urinalysis, the physical and/or chemical analysis of urine, can be performed quickly to detect renal disease, pregnancy, urinary tract disease, liver

disease, diabetes mellitus, and general hydration [14] and recently, been used to assist in the diagnosis of prostate cancer [15].

The human body is 60% water and relies on the urinary system to remove waste products and excess water from the body. The urinary system filters blood with about 2 to 3 million specialized capillaries known as the glomeruli. Since the glomeruli filter blood based mostly on particle size, larger particulates like blood cells, platelets, antibodies, and albumin are usually excluded. Common solutes, such as ions, amino acids, vitamins, and wastes, are filtered to create a filtrate composition. As a biological waste material, urine typically contains metabolic breakdown products from a wide range of foods, drinks, drugs, environmental contaminants, endogenous waste metabolites and bacterial by-products. Chemical compounds commonly found in urine usually contain high concentrations of urea (from amino acid metabolism), inorganic salts (chloride, sodium, and potassium), creatinine, ammonia, organic acids, and pigmented products of hemoglobin breakdown, including urobilin, which gives urine its characteristic color. Characteristics of the urine change, depending on influences such as water intake, exercise, environmental temperature, and nutrient intake. Some of the characteristics such as color and odor are rough descriptors of the state of hydration. For example, during strenuous exercise, urine will be more concentrated and therefore appear darker and emit an odor. Additionally, many distinct types of food can influence the color or smell of urine such as beets, berries, and fava beans. Thus, urine is often used as a simple method to characterize a person's activity level, hydration level, and diet[16].

Urinalysis has been widely used to obtain clues to renal disease, diabetes, and urinary tract infections. A normal kidney generates 1-2 L of urine per day, with around 500 mL/day are required to rid the body of waste. Thus, volumes lower than this strongly suggest serious kidney conditions such as kidney disease. Volumes that exceed 2.5 L per day suggest diabetes mellitus or diabetes insipidus with the excess of glucose also appearing in the urine. The presence of ketones in the urine also suggest that the body is using fat as an energy source instead of glucose. Diabetic patients exhibit a lack of insulin or insulin resistance so their bodies do not take up insulin, and their cells must rely on fats for energy production instead. Ketones are the byproducts of fat metabolism so the presence in urine suggest either diabetes or

diet changes. Ketones appear in a patient's urine before they are seen in the blood[17]. As cells are not normally excreted in the urine, the presence of leukocytes often indicates a possible urinary tract infection (UTI)[18]. Additionally, leukocyte esterase which is released by leukocytes is often used as an indirect measurement of a UTI. Although nitrates are found in healthy urine, gram-negative bacteria metabolize nitrate to nitrite. Therefore, nitrite is another indirect measure of a potential UTI.

Other common urine analytes detected include small proteins, metabolites, small molecules, nucleic acids, pathogens, and exosomes. In the kidney, the glomerular capillary wall is only permeable to elements with a molecular weight of less than 15,000-60,000 Daltons[19]. After filtration, low-molecular weight proteins are reabsorbed by the proximal tubule cells. Normal urinary proteins include albumin, serum globulins, and other nephron secreted proteins. Proteinuria is defined as urinary protein excretion of more than 150 mg per day (10 to 20 mg per dL) and is associated with renal diseases. Hematuria, the presence of red blood cells, and proteinuria can both be indicators for conditions such as Fabry's disease, nail-patella syndrome, and several others [20]. Therefore, the quantification of proteins in urine is critical for diagnostic purposes.

Methods for analysis of urine

Analyzing proteins in urine is commonly done by electrophoresis, chromatography, mass spectrometry, immunoassay, fluorescence, infrared spectroscopy (IR), fluorescence spectroscopy, and Raman spectroscopy. Liquid chromatography and mass spectrometry are methods that are too expensive for routine clinic workflows and mostly reside in research institutions. Immunoassays are more widely used by clinics, laboratories and in some cases, patients themselves. IR and Raman spectroscopy are exciting new tools for urine diagnostics owing to the rapidness and low-cost per sample, but the high cost of the initial equipment acquisition and training, prevents clinic and home testing. Urine has significant potential for point-of-care testing (POCT) or home health monitoring and diagnosis. However, most urinalysis diagnostic platforms still require the use of sophisticated laboratory apparatus and skilled personnel, which precludes home testing or low resource testing environments. Consequently, urine based POC platforms

have aroused great interest in recent years. Easy-to-use urine platforms hold the potential to empower patients to monitor their own health status more frequently in the convenience of their home to enable earliest disease detection. Many recent advances in POC urinalysis tests have expanded upon qualitative or semi-qualitative dipsticks and lateral flow assays as well as newer microfluidic platforms.

DNA detection in urine is an emerging area. Nucleic acids have been recognized as a critical part of biological research and diagnostic technologies. Nucleic acids include deoxyribonucleic acid (DNA) and ribonucleic acid (RNA) are biopolymers consisting of four nucleotides that storage and expression of genomic information. DNA transcribes RNA in a process called transcription where after RNA is used for protein synthesis. Therefore, DNA is responsible for all proteins and enzymes for life to exist on earth. For much of history, nucleic acids were not considered important enough to drive evolution due to their small size and simple composition compared to proteins. In 1869 Friedrich Miescher was the first to isolate nucleic acids (which he referred to as nuclein) from hospital wound bandages. Miescher himself did not believe his discovery contained the "genetic code molecule", and it took until the discovery of the double helix model in 1953 to overcome this bias.

Watson-Crick base pair principle dictates that a purine adenine always pairs with pyrimidine thymine and pyrimidine cytosine always pairs with the purine guanine to form double-stranded DNA. This rigid base pairing principle has resulted in variety of technologies and fields based around DNA such as diagnostics which can detect a variety of diseases, criminal evidence in the field of forensics, genetically engineered agricultural crops, and historical evidence for human migration fossil analysis. Diagnostic technologies using DNA or RNA, or nucleic acid tests (NATs) include polymerase chain reaction (PCR), rolling circle amplification, and loop-mediated isothermal amplification.

In 1948 Mandel and Metais first described circulating cell-free DNA (cf-DNA) in plasma and blood[21]. Decades later, various groups have investigated cf-DNA. Tremendous growth in new technologies and improvements for sequencing DNA has resulted in more affordable cost of DNA sequencing at $1,500 or less in 2015[22]. As a result, cf-DNA in liquid biopsy samples is an emerging area of research. Several studies have investigated detecting cf-DNA in urine for a variety of applications such as detecting male

fetal cf-DNA in maternal urine[23] or male cf-DNA in the urine of female kidney female patients who received a kidney transplant from a male[24]. In 2000 that Botezatu injected mice with male human and detected the human DNA in the mice urine[25]. This suggested that once cf-DNA was circulating in serum, it would ultimately cross the kidney barrier where it could be detected in urine samples. Currently, urine cf-DNA has been regarded as an important biomarker spanning a variety of field from diagnostics[26,27,28] to prenatal genetic screening[29], organ transplant monitoring[24], and cancer mutation detection[30,31].

Skin ISF as a sample source.

Skin is the largest organ in the human body and provides a multitude of diagnostic clues for diagnosis. Interstitial fluid (ISF) is a type of body fluid that surrounds cells of tissues and organs in the body. The Starling hypothesis proposes that fluid filtered through the arterial end of a vessel and reabsorbed at the venous end results in convective transport of molecules in the interstitium[32]. ISF viscosity changes in response to temperature, temperature, and chemical species. Skin is highly assessable and consists of 70% ISF by volume[33]. ISF are rich sample sources that contain localized source of biomarkers which might provide more clinical value than measuring biomarkers circulating at the systemic level. Although varying in protein content, ISF composition correlates with plasma and serum. In one study, ISF was compared to both serum and plasma samples from the three healthy human subjects[34]. Proteomic analysis showed that all three sample types had high proteome overlap. These results indicate that ISF could replace serum and plasma in a variety of applications. Other analytes found in ISF include glucose, cholesterol, cortisol, lactate, lipids, sodium potassium chloride, and other metabolites. ISF is also non-coagulable allowing for monitoring over a longer period of time allowing for continuous sample collection[35]. However, ISF diagnostics are limited mainly by the accessibility to the sample. Although highly abundant throughout the human body, ISF remains difficult to collect and have resulted in high cost and invasive strategies.

Methods for analysis of ISF

To sample skin, a biopsy is often used but it is painful for the patient or requires anesthetic. In either case, a trained nurse or doctor must collect the biopsy. Swabbing or scraping of the skin are also methods used to collect skin samples but have limited applications for testing. For example, the analyte of interest must be in high abundance to be detectable by a swab or scrape. Biopsy, swabbing, and scrapping would also require additional laboratory processing steps to extract the analyte of interest which may result in a loss of starting material. Biopsy is invasive and are plagued by contamination of intracellular fluid contamination during processing steps of the tissue. Newer methods for skin sampling are needed for contamination-free ISF extraction.

Skin microdialysis allows continuous sampling of the ISF but its invasive. A small probe or catheter with a semipermeable porous membrane is inserted into the dermis layer of skin and fluid is pumped through the probe until equilibrium is reached allowing the end collection of the dialysate (**Figure 1.1**). Another method, Dermal open-flow microperfusion (dOFM) is similar to skin microdialysis (intradermal insertion) but relies on a peristaltic pump[36] (**Figure 1.1**). A less invasive method, reverse iontophoretic extraction uses low electrical current across the negatively charged dermis to move ions to the end of the electrode for collection (**Figure 1.1**). Finally, the suction blister technique relies on application of a suction force vacuum on the skin surface to extract ISF. As a fluid filled blister forms from the suction, a syringe or needle can be used to raw out the ISF[37]. The main drawback to these methods is the reliance on complicated equipment and expertise to operate that preclude them from being adopted in resource constrained settings or the home. Additionally, all these methods may permanently damage the skin, risk infection, and lead to discomfort for the patient.

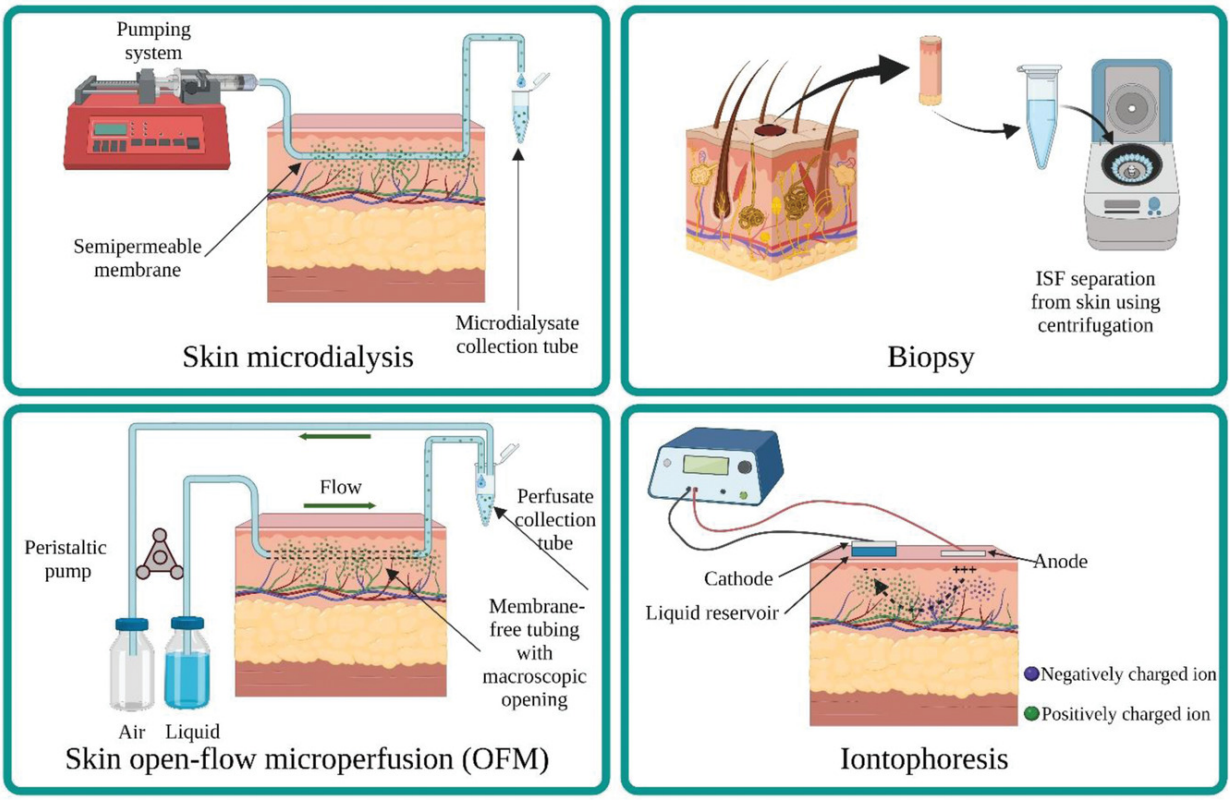

Figure 1.1. Different dermal ISF extraction methods include microdialysis, open-flow microperfusion, biopsy, and iontophoresis. Figure from cited reference[37].

Microneedles (MN) have become exciting tools for ISF extraction. Owing to their tunable penetration depth and variety of material fabrication methods and geometry options, multiple studies have collected ISF biomarkers, such as DNA, proteins, and pathogens, using MNs. MN offer ease of use and non-invasiveness over other methods previously mentioned. MN can be designed to be hollow, porous, swellable, solid, or dissolvable. Various sensing mechanisms of ISF are available with MNs. The surface of MNs can be functionalized with biorecognition elements including antibodies, antigens, nucleic acids, and peptides. MN have been used for long term monitoring purposes such as glucose monitoring and therapeutic agents. MN lengths from ~300-1500 µm can penetrate the skin and extract ISF.

To sense ISF solid MN can use integrated electrode made from conductive materials such as gold, platinum, or silver. Porous or hollow MNs can extract ISF due to capillary forces. By manipulating the

pressure gradient, ISF can travel to the micropores of the MN. Swellable MNs are typically made with crosslinking techniques such as photo initiators exposure to UV light. Zheng at al was able to further increase ISF extraction to 7.9 µl in a few minutes by using a osmosis driven hydrogel patch consisting of 100 arrays[38]. Laszlo et al used super welling hydrogel MNs to extract 15 µl of ISF from excised pig skin over the course of an hour[39]. However, swellable, hollow, porous MN usually feature less mechanical strength compared to solid MNs. Dissolvable MNs are usually made from biocompatible and biodegradable polymers and allow for manipulation for application. By fine tuning important features of MNs, a variety of global health needs can be met with microneedle designs.

Roadblocks for detection biomarkers in non-invasive samples.

Project 1: Current urinalysis dipsticks are not amenable for all users.

Urine dipsticks are often used as a simple point-of-care screening test in areas where other laboratory analyses are not available. Urinalysis dipsticks are affordable, semi-quantitative diagnostic tools that rely on colorimetric changes to indicate approximate physiological levels. Each dipstick can perform a wide variety of assays including testing for pH, osmolality, hemoglobin/myoglobin, hematuria, leukocyte esterase, glucose, proteinuria, nitrite, ketone, and bilirubin[40]. The principle of dipstick urinalysis relies on the occurrence of a timed reaction through which a color change on the dipstick pad can be compared to a chart to determine analyte concentration [41]. Given their affordability and ease of use, dipsticks are one of the most common tools for urinalysis in healthcare.

In 2011, results from a longitudinal study of 1.2 million adolescents and young adults, who underwent urinary screening examinations and 21 years of follow-up suggests that perhaps widespread dipstick testing for hematuria would help detect the development of end-stage renal disease over time[42]. However, a 2014 systemic review of guidelines for the use of urine dipsticks for screening in nine countries found little agreement in guidance among 67 different organizations[43]. Though urine dipsticks may offer greater health monitoring applications, the lack of standardization for processing the urine sample and analysis limits their impact. Additionally, many clinicians are unaware of the exact principles and limitations of dipstick urinalysis [44].

Traditionally, dipstick urinalysis relies on a trained nurse or medical technician to manually insert the dipstick completely into a cup of urine sample, wipe or blot off excess urine, and compare the color pads to chart colors at specific times[45]. While the dip-wipe method is the gold standard for dipstick analysis, its reliance on human visual assessment limits the quantitative information that can be obtained. Moreover, the two manual steps of dipstick urinalysis – the dip-wipe step and colorimetric result comparison – require accurate technique, which limits the possibility of reliable testing in home settings by patients directly.

Cross-contamination of the sample pads due to wiping or inability to remove excess liquid can cause inaccurate color changes (**Figure 1.2**).

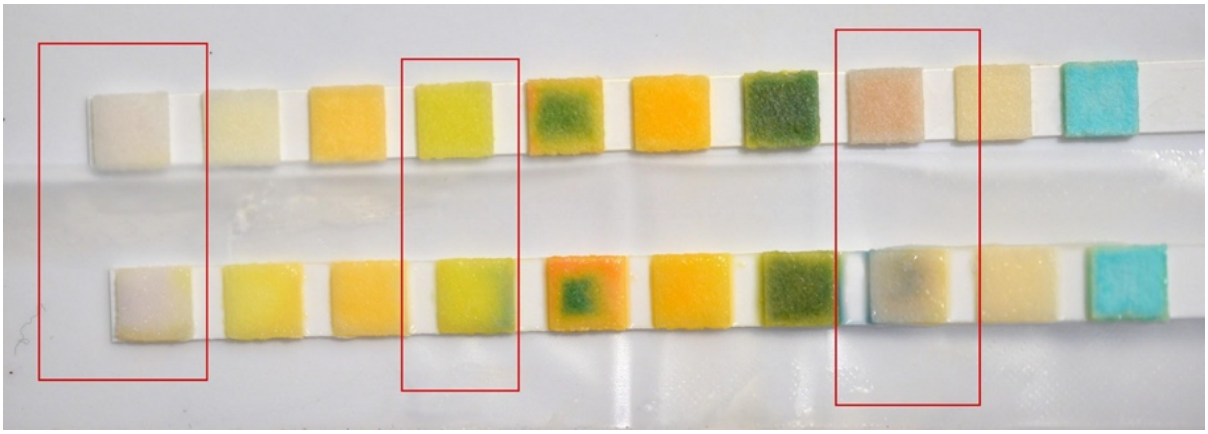

Figure 1.2. Dipstick cross-contamination from improper dip-wipe method. Red lined boxes indicate areas of cross-contamination on the bottom test strip compared to the top test strip.

Inconsistent volumes resulting from the lack of volume control during dipping or wiping can result in improper measurement of analyte concentrations (**Figure 1.3**). Importantly, the time between dipping the urine (i.e., the start of the assay) and comparison to a chart is critical for accurate analysis of the results and is a potential source of human error. The difficulty in manual colorimetric comparison is that many pads must be read at the same time, while some pads are read at different times. Even perfectly timed color comparisons still depend on the visual acuity of the human reader, who may suffer from color blindness or perceive different colors in different lighting environments. These challenges underscore why clinicians can only rely on dipstick urinalysis performed by trained personnel with an automated dipstick reader. However, an automated urinalysis system could address all the concerns by eliminating the need for manual dip-wipe steps and enabling simultaneous color comparisons with calibrated color references. This, in turn, would reduce user error, allowing for possible adoption in home settings or low resource settings.

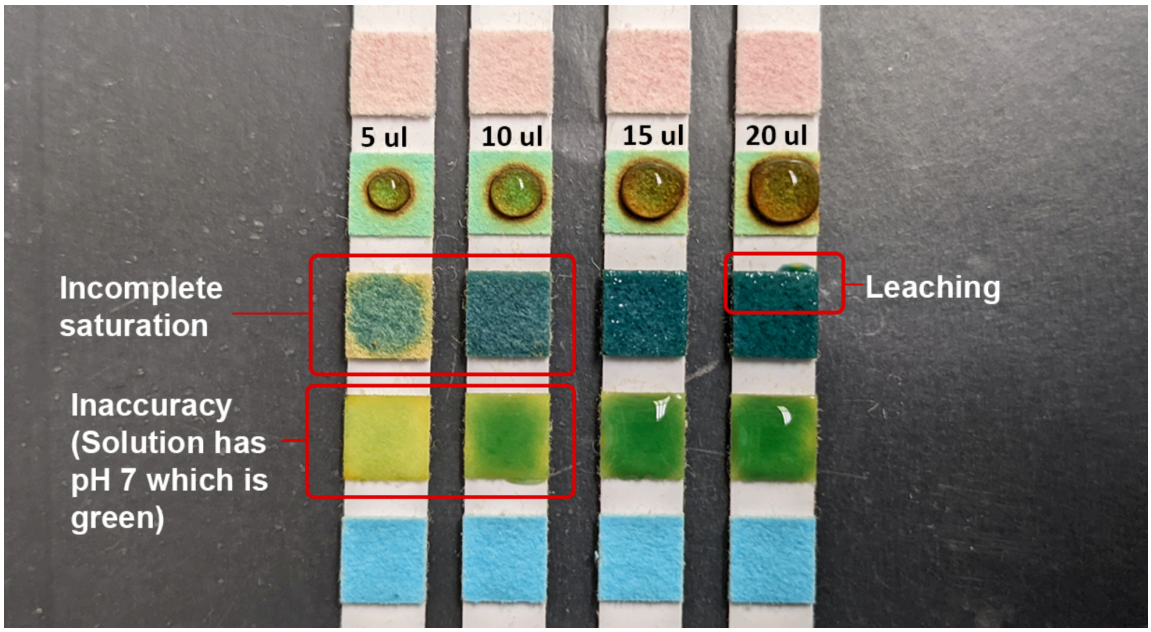

Figure 1.3. Various volumes tested on a dipstick urinalysis test.

Since visual acuity of observers is highly variable, electronic analyzers of dipstick tests have become common in the U.S. in the last 20 years. Such automatic analyzers have been employed to read the results of dipstick urine tests with the same accuracy as or exceeding visual analysis[46]. Many clinics and doctor offices use such machines to rapidly analyze and print traditional dipstick results. Various studies have demonstrated that discrepancies occur when visual reading of test strips with color blocks is compared against the reflectance meter measurement[47,48]. Most urinalysis machines minimize visual inspection errors and ensure consistency in results. They are easy to use and more efficient than manual inspection but still require the user to perform the dip-wipe method correctly. Additionally, each automatic analyzer only works with one brand of dipstick. Hence, these machines have limited applications to be operated by untrained persons such as at-home users; moreover, they can be expensive. After dipsticks are submerged into urine and then inserted into an analyzer, the test strip may possibly deposit bacteria inside the automatic analyzers. After robust clinical use, automatic analyzers usually require cleaning and routine maintenance for reliable operation. Finally, automatic analyzers rely on a power source which limits their use in resource constrained environments.

The need for affordable urinalysis for global health

Agricultural workers are at risk of continuous heat exposure during the day. Climate change is predicted to lead to increasing heat waves that threaten the health and safety of agricultural workers. In the United States, exposure to heat waves is the most common cause of mortality (even among tornados, earthquakes hurricanes)[49,50]. Heat waves are usually referred to as temperatures of >40° C for sustained period of time or any time temperature exceed 45°C[51]. Heat stress occurs when the human body cannot cool itself. Chronic exposure to the sunlight and heat during agricultural work puts worker's health in jeopardy. Intense sunlight, high moisture, high temperatures and strenuous work can result in heat stress. Recent studies have shown that heat stress during work is associated with an increased rate of kidney disease. Heatstroke (also known as hyperthermia) can lead to acute kidney injury or heat induced inflammatory injury to the kidney. Additionally, studies have shown chronic heat and dehydration can lead to chronic kidney disease, kidney stone formation and urinary tract infections from emergency department admissions[52]. Due to a global rise in temperature, more resources are needed to monitor the health of agricultural workers.

Heat exhaustion is the most common illness from heat related events. The signs include increased thirst, profuse sweating, weakness, paleness, dizziness, fainting, nausea, vomiting or headache. Agricultural worker fatality is 20 times higher than US civilian worker heat-related deaths[53]. Heatstroke is also common among agricultural workers in addition to military personal and athletes[54]. Heatstroke can also lead to cases of acute kidney injury. A heat wave in Chicago in 1995 resulted in more than 600 deaths and over 50% of heatstroke patients exhibited acute kidney injury[55]. The kidney plays a significant role in protecting the body from the effects of heat stress. However, this also means the kidney is vulnerable to heat related injuries. These effects can be temporary, permanent, or even result in death. As climate change continues, standardized screening systems for high-risk workers are needed in low resource areas.

Chronic kidney disease of non-traditional origin in LMICs

Nicaragua, El Salvador, Costa Rica, and Guatemala have had an epidemic of Chronic kidney disease (without relation to diabetes) since the 1970's[56]. Tens of thousands of workers die from chronic kidney

disease of nontraditional origin (CKDnt), particularly in sugar cane cutters[57]. By the 1990's, clinicians reported end-stage kidney disease in a disproportionally large number of sugar cane works[58]. The mechanism of how manual labor in hot environments leads to CKDnt is not fully elucidated but researchers suggest that repeated incidents of acute kidney injury mediate this association[59]. In a 2015 study with 189 sugarcane cutters (**Figure 1.4**), researchers reported a substantial heavy load on the kidney from dehydration[60]. Measurements, including dipstick urinalysis, were analyzed before and after work-shifts to reveal a very hot environment for the agricultural work can lead to high tubular reabsorption and reduced glomerular filtration[60]. In 2021, researchers used dipstick urinalysis to examine renal function for 65 female rice farmers in the Nan Province, Thailand[61]. Results of their work indicated that urinalysis dipsticks was a useful was to assess worker health and that female rice workers in this area should receive early renal screening to address any kidney function abnormalities[61]. Dipstick urinalysis could be affordable tools to identify agricultural workers at risk for CKDnt and therefore, allow for mitigation strategies before permanent damage occurs. Power-free automated platforms that can be used routinely in low resource environments to quickly monitor kidney function could offer a POC of method to protect vulnerable workers.

Figure 1.4. Sugarcane cutting (in Nicaragua; Photos Ed Kashi). Figure from cited reference[60].

Coronavirus disease 2019 and kidney damage

Coronavirus disease 2019 (COVID-19) resulted in a world-wide pandemic with high mortality. Primarily manifesting upper respiratory and pulmonary diseases, COVID-19 can also affect other organs in the body[62] and result in proteinuria[63] and acute kidney injury (AKI)[64]. Although it is unknown how the virus damages the kidney, the virus particles with distinctive spikes were observed by electron microscopy in patient samples of tubular epithelia cells as well as podocyte cells[65]. In 2022 study of a large cohort of hospital patients with COVID-19, researchers used dipstick urinalysis to show proteinuria and hematuria is associated with higher risk for developing AKI[66]. These results provided more evidence to validate an earlier 2021 study which also found an association with dipstick hematuria and proteinuria association with AKI in hospitalized patients with COVID-19[67]. Together, both studies suggest dipstick urinalysis is a useful tool to triage COVD-19 patients who are highest risk of developing AKI. As global COVID-19 pandemic

continues to impact the health of humans, affordable dipstick urinalysis remains an important tool in the context of global health.

Summary of roadblocks for project 1 `

1.) Cross-contamination of sample pads from improper dip-wipe technique results in error prone results.

2.) Inconsistent volume control can result in improper measurement of analyte concentrations.

3.) In the clinic, automated based dipstick platforms are designed for only one brand of dipstick.

4.) Automated urinalysis devices rely on power and maintenance to operate.

Project 2: Quantitative normalization of urine OC biomarker changes in a low-cost device could enable at home monitoring OC recurrence.

In 2020, ovarian cancer ranked as the third most common gynecological cancer worldwide[68]. Up to 90% of all ovarian cancer cases are comprised of ovarian carcinoma. OC is the most common cause of gynecologic cancer death in women, largely due to late diagnosis. Early identification of OC represents an unmet clinical need since no diagnostic tools have achieved FDA clearance for early detection. Certain factors increase the risk for ovarian cancer such as increasing age, family history of OC, and breast cancer gene (BRCA) mutations. Incidence of OC has increased significantly among young women. Reasons for this range from increasing incidence of obesity, estrogen exposure, and nulliparity[69]. Since 5-year survival rates dramatically decrease with the progression of disease, efforts to improve early detection, and the rapid identification of recurrence, have become a priority. Even after surgery and chemotherapy, approximately 70% of OC patients experience disease relapse within 2 years of the initial treatment.

The common tools for ovarian cancer assessment include pelvic exams, transvaginal ultrasound, magnetic resonance imaging, computed tomography, positron emission tomographic scanning, laboratory tumor markers, and histology of excised tissue from a biopsy. The majority of future OC patients will usually first present with an adnexal mass (i.e., masses of the ovary, fallopian tube, or surrounding tissues), which are commonly encountered by obstetrician-gynecologists and may be benign or malignant lesions with malignancy rates around 0-1%[70,71,72]. There is no FDA approved diagnostic tool to differentiate adnexal masses. In conjunction with transvaginal ultrasounds and family history, serum marker levels, such as cancer antigen 125 (CA-125), are often used to help separate masses into either a benign or a malignant category. However, elevated levels of CA-125 in serum are often due to other nonmalignant health issues (i.e. endometriosis, lupus, inflammatory bowel disease)[73] . The CA-125 test is a poor screening test because it lacks the specificity to rule out ovarian cancer, and a false-positive test may lead to unnecessary invasive surgeries[74]. CA-125 is also elevated in other cancers such as endometrial, pancreatic, lung, breast, colorectal, and other gastrointestinal cancers[75]. CA-125 serum level is elevated in only 50% of patients with

stage I Epithelial OC[76]. Therefore, serum marker testing is only used to evaluate risk of OC with other clinical factors (i.e., age, family history, menopausal status). The value of CA-125 in serum for OC surveillance is uncertain as a randomized trial concluded that early administration of chemotherapy based on increasing CA-125 levels had no effect on survival [77,78]. Although CA-125 serum testing is often used for women with an adnexal mass, because of the low sensitivity (50-62% for early stage epithelial ovarian cancer) as well as a low specificity especially among premenopausal women, CA-125 is not recommended as a screening test in asymptomatic women[77]. Since ovarian cancer presents subtly and physicians lack sensitive diagnostic tools, most diagnoses occur in later stages in which treatment options are often limited as well as costly.

Human epididymis protein 4 (HE4) is another OC biomarker that has garnered widespread attention. HE4 is a low molecular weight glycoprotein and is highly expressed by ovarian carcinomas[79]. HE4 in serum is overexpressed in ovarian carcinomas and is detected with high sensitivity and specificity[80]. HE4 has been found to have better sensitivity and specificity than CA-125 for the evaluation of adnexal masses[81]. Compared to CA-125, HE4 is less frequently overexpressed in some benign ovarian diseases[82,83,84], such as endometriosis, and HE4 correlates better with PET/CT results than CA-125[85]. Additionally, HE4 levels increased up to 5-8 months sooner than CA-125 in relapsed patients[86]. Recent studies have shown that HE4 in serum offers more forecasting power for OC recurrence than CA-125, a biomarker of many cancers[87].

There has been greater efforts to identify other biomarkers in multivariate index assays (MIA) to further increase clinical utility for OC[88]. Although CA-125 is not useful on its own as a diagnostic, it has been successful used monitor response to treatment[89]. In 1990, Jacobs et al developed the risk of malignancy index (RMI), which combines ultrasound findings, status of menopause and CA-125 level to triage women who present with adnexal mass[90]. RMI has been used to categorize women into high or low risk groups. Additionally, the FDA has approved two algorithms used to assess OC risk for women who present with a pelvic mass: the Risk of Malignancy Algorithm (ROMA) and OVA1/ Overa[74]. The ROMA and OVA1 are meant to be primarily used to triage patients during pre-surgical assessment to determine if a gynecologic

oncologist should be referred to for surgery. ROMA outputs a numerical score based on menopausal status, concentrations of CA-125 and HE4[91]. The ROMA score for patients is based on following equations depending on menopausal stage:

The ROMA score for the postmenopausal women is based on the following equation 1:

$$PI(\text{Predictive index}) = -8.09 + 1.04*LN(HE4)+0.732*LN(CA125) \quad (1)$$

The ROMA score for the premenopausal women is based on the following equation 2:

$$PI(\text{Predictive index}) = -12.0 + 2.38*LN(HE4)+0.0626*LN(CA125) \quad (2)$$

$$ROMA = \exp(PI)/ [1+\exp(PI)]*10 \quad (3)$$

Although the algorithm is not used as a diagnostic on its own, rather is used with both clinical and radiological assessment. The current OC algorithms requires a woman to take off work and rely on a phlebotomist to draw blood for analysis with bulky equipment. Studies have found that OC patients may withdraw from recurrence screenings due to anxiety, distress, and depression[92]. Understanding the psychological factors intersecting with repeated invasive and painful serum collection procedures has been well studied[93]. Factors such as the "time consuming steps" related to screening (i.e. making an appointment to have blood work done, traveling to location) as well as the "constant reminder of risk" associated with getting lab work done, seeing other patients in different stages of cancer diagnosis, and waiting for results contributed to patient screening withdrawal[94]. Additionally, the lack of frequency of testing and waiting on test results were a highlighted concern of OC patients[94].

Prophylactic ovary removal, also called prophylactic oophorectomy (PO), is usually recommended for women who have completed childbearing and face high risk of ovarian cancer. Studies suggest that women often take several years before deciding to have a risk reduction surgery like PO after receiving a gene test result [95,96] and so monitoring changes could help patients make informed choices about surgery

timing. Additionally, a small qualitative study with 14 women who had PO showed some premenopausal women felt that they had received insufficient and conflicting information regarding the effects of surgical menopause and the link between HRT and breast cancer[97]. Another other qualitative study of women who had undergone PO and women who had opted for screening reported that both groups would have liked more information to inform their decision[96]. Hallowell et all found evidence in a similar study that shows many women do not have sufficient information to make informed decisions regarding PO[98,99]. Therefore, there is a clear need to provide women with sufficient information on their options at the point of care. Patients scheduling their urine collection in the privacy their home with a painless test could increase patient participation in recurrence monitoring without the above-mentioned psychological factors associated with current screening practices and unnecessary harm from premature surgeries.

Moreover, management strategy of OC in remission still has little consensus among physicians despite having an abundance of patient data at hand[100]. As many academic papers have demonstrated various devices or methods that can differentiate healthy and OC urine[101], these devices have not been translatable in a clinical setting. Due to variation of OC (stage, grade, or subtype), biomarker cut off values are not very helpful at the individual patient level. Ideally, comparing patient disease levels prior to treatment presents a physician with a more specific comparison value for monitoring recurrence. Thus, a strategy that relies on patient specific levels may hold promise for the best recurrence monitoring strategy. Therefore, there is an urgent need to develop a recurrence monitoring strategy capable of overcoming the challenge of frequent interval testing that provides comparisons of patient specific levels of urinary biomarkers integrated into one device.

In 2009, FDA approved using serum HE4 levels to monitor ovarian cancer recurrence (OCR) risk, but this method also requires travel to clinic, phlebotomy, and it is expensive[102, 103]. Due to the ease of collection of urine, HE4 in urine has emerged as a promising target in ovarian cancer recurrence monitoring at home. Urine HE4 has been found to be a biomarker for ovarian neoplasms with improved sensitivity in early disease compared to HE4 in serum[104]; additionally, HE4 is detectable in urine earlier than in serum [105].

Unlike serum HE4, urine HE4 fluctuates with volume, and so urine HE4 requires normalization. Creatinine (CRE) is commonly used as an internal standard to normalize the ratio of urinary biomarkers[106] and HE4 in particular[107,108]. The ratio of HE4/CRE in urine has been found to be a better predictor of early and late-stage ovarian cancer than urine HE4 alone[24]. Hellstrom et al reported higher concentrations of HE4/CRE ratios in ovarian cancer patient urine ranging from -0.5 to 2.5 for log10 values of HE4/CRE[104]. HE4/CRE can range from 2 in healthy patient samples to nearly 45 (although most are less) in late stage ovarian cancer[104]. Importantly, Liao et al. reported that urine HE4 may also be more useful than serum HE4 in differentiating low malignant potential cysts from early ovarian cancer[109].

The concentration of urine analytes is affected by diet, water intake, sweating, and other factors. Concentration of biomarkers significantly varies depending on the amount of urine excreted at a certain time. As a result, a single urine sample may not provide accurate physiological information. Therefore, the 24-h volume test measures the amount of urine produced in a 24-hour day and is accepted a good representation of illness. However, 24-hour collection cumbersome for patients, often resulting in improper or incomplete collection. Since this requires around the clock collection of each urination and refrigerated storage to inhibit bacteria activity, it is not often used in routine analysis of urine. Instructions for collecting a 24-hour urine sample vary by the laboratory with some instructions discarding the patient's first voided morning urine[110]. Moreover, 24-h collection exhibits collection errors from 12-35%[111,112]. A more common option in practice is the creatinine to protein ratio in the sample as it correlates well to the 24-h volume test[113,106].

Variations in urinary analyte concentrations from changing water content in urine have been eliminated using urinary excretion rate (UER) calculations, urinary creatinine concentrations, specific gravity, and osmolality[114]. The most widely used method is creatinine adjustment that involves dividing the analyte concentration (micrograms analyte per liter urine) by the creatinine concentration (grams creatinine per liter urine). Creatinine is the terminal metabolite of muscular creatine. Its daily excretion is proportional to the muscle mass, so that the daily amount of creatinine excreted by a specific person is nearly constant[115]. Therefore, the influence of the urine volume can be compensated by expressing the concentration of the

urinary component of interest as the amount of analyte per amount of creatinine. This method of normalization is widely applied for rapid POC diagnosis, where the collection of 24 h urine is not an option[107]. However, these creatinine normalization methods have yet to be used with the cancer biomarker HE4 in a low-cost assay.

The need for low-cost assays for cancer in global health

Cancer has emerged as a global health priority due to the high global mortality. Studies from high-income countries have shown that early-detection programs are not just cost effective, but also reduce cancer mortality[116]. Adoption of these programs in lower-and middle-income countries (LMICs) has been limited. Cardiovascular disease, cancer, diabetes, and chronic respiratory diseases account for 63% of global deaths from non-communicable diseases. Additionally, 80% of those deaths are located in LMICs[117]. Of the leading cancer deaths, up to two-thirds of these occur in LMICs[118]. Due to population growth and aging populations as well as adoption of unhealthy behaviors (i.e. smoking and obesity), the burden of cancer is rising in LMICs[119]. The unprecedented rise of cancer in LMICs is not being with met with adequate investment in healthcare infrastructure. For women living in LMICs, a global health disparity has emerged in cancer care[120]. Up to 75% of women in high income countries have had a type of cervical screening during the last 5 years compared to just 5% of women in LMICs[121]. Cervical cancer provides a successful model for other cancers to follow in terms of reduction of mortality in LMICs and lowering of barriers to self-sample testing.

Cervical cancer screening

Globally, cervical cancer is the third most common cancer in women. Since the 1950's, cervical cancer incidence and mortality has declined by more than 70% in the United States which is largely due to the widespread use of Papanicolaou's test (also known as the "pap-test")[122]. It is estimated that 85% if cervical cancer deaths occur in LMICs[123]. Although this cytological based screening test has led to a substantial reduction, conventional cytology is not practical in developing countries due to the cost[124]. Alternatively,

manual inspection of the cervix and detecting DNA for human papillomavirus (HPV) is cheaper. Recently, WHO recommended self-sampling has emerged as a suitable approach as a screening method for early detection for women aged >30 years[125]. Additionally, community health works offering self-collection HPV test kits improved coverage and reduced barriers to testing in Argentina[126]. Since self-sampling has shown success in one type of gynecological cancer, further work could determine if similar tactics such as community test kit delivery and self-sampling could be adopted by other cancers to reduce mortality and achieve more equitable health outcomes in LMICs.

Barriers to cancer monitoring due to the COVID-19 pandemic

As COVID-19 results in unprecedented disruption to healthcare systems worldwide, physical distancing became critical to limit disease transmission. Many cancer patients were forced to postpone surgeries, treatments, procedures, and diagnostic testing[127]. For bladder oncology patients, the COVID-19 pandemic resulted in 67% less oncological procedures[128]. For monitoring recurrence of cancers, the threat of COVID-19 infection remains of concern. Implementing telehealth could be used for doctors and patients to discuss concerning symptoms without resulting in a risk of a pandemic disease transmission. Additionally, self-testing tools would enable physicians with a way to observe patient testing of devices to ensure proper technique. This would allow physicians to trust in the results and increase the accuracy of the results. Additionally, one gynecology cancer patient survey found that patients did not prefer telehealth appointments over in-person because they of the lack of exams or diagnostic monitoring services[129]. Self-testing tools for monitoring would alleviate this concern from patients and most telehealth services could be implemented. Another study also suggested that substituting in-person visits that include symptom reports as well as routine surveillance protocol (tumor marking test or imaging) is an appropriate method for detecting ovarian cancer recurrence while also limiting risks to health[130]. Therefore, more self-sampling tools would offer not just a more convenient recurrence monitoring strategy but also easily integrate into established protocols for surveillance.

Tools for self-sampling: Lateral flow assays

Lateral flow assays (LFAs) appeared in the 1970s and remain a cornerstone of modern medicine used to detect a wide range of protein biomarkers. One of the most common LFAs detects pregnancy hormone in urine. Introduced in the late 1970's[131], the LFA pregnancy test changed women's healthcare by allowing detection in the privacy of a woman's home. In a span of 25 years, home-based pregnancy tests became the norm[132]. Due to their low-cost, high specificity and ease of use, LFA industry continues to grow each year[133]. Due to COVID-19 pandemic, a surge of LFAs were used to detect the disease.

LFAs typically utilize labeled antibodies to capture and detect a biomolecule. In LFAs, fluids are transported via capillary action along a nitrocellulose strip that is preloaded with reagents. The chemistry and physical shape of the fibers helps control wetting rate. After 10-20 minutes, the end-user visually inspects the test for the presence of a "signal" at the test line. This line is a result of the aggregation of detection nanoparticles at the location of analyte-specific capture reagents. Thus, the end of the test results in a qualitative and/or semi- quantitative readout achieved by analyzing a colored band by eye or by a commercial reader or cell phone.

LFAs are attractive tools for point-of-care (POC) testing because they are inexpensive, portable, and rapid. They require minimal training and have a user-friendly workflow; the patient collects a sample, adds the sample to the test, and finally, adds a couple of drops of a running buffer. Single-use foil packages often include a test cartridge, a sample collection and transfer device, and a dropper bottle of running buffer to facilitate the workflow. The lateral flow assay is typically performed by observing the color changes in the test line by naked eyes. However, this qualitative (yes/no) detection method is not very suitable for changing levels of biomarker in urine. Moreover, there is not an easy way to account for volume fluctuation in urine which may impact biomarker measurement in home settings.

Summary of roadblocks for project 2

1.) There is not a user-based test to quantitatively measure HE4 in urine.

2.) HE4 requires normalization using a quantitative creatinine paper tests which are not commercially available.

3.) Both analytes must be measured quantitatively to accurately reflect long term changes in HE4.

Project 3: Screening tool for tick bites could prevent misdiagnosis and onset of LD.

The Biology and Current Impact of Lyme Disease

Tick-borne diseases represent major public and animal health issues worldwide. Lyme borreliosis disease is a multisystemic infectious disease first discovered in 1975[134]. In the late 1970's, an epidemic of arthritis occurred in adults and children in Lyme, Connecticut. Although physicians suspected a viral outbreak, knowledge and treatment were stalled until Dr. William Burgdorfer discovered the spiral-shaped bacterium in 1981[135]. Further research found that the etiologic agent, *Borrelia burgdorferi*, was transmitted to humans by the bite of infected species of *Ixodes* ticks resulting in Lyme disease (LD)[136]. LD is the most common vector-borne illness in both North America and Europe, with an estimated incidence of ~300,000 cases per year in America alone[137,138,139]. According to the Centers for Disease Control and Prevention (CDC), the number of reported cases of tickborne disease has more than doubled over the past 13 years (**Figure 1.5**)[140].

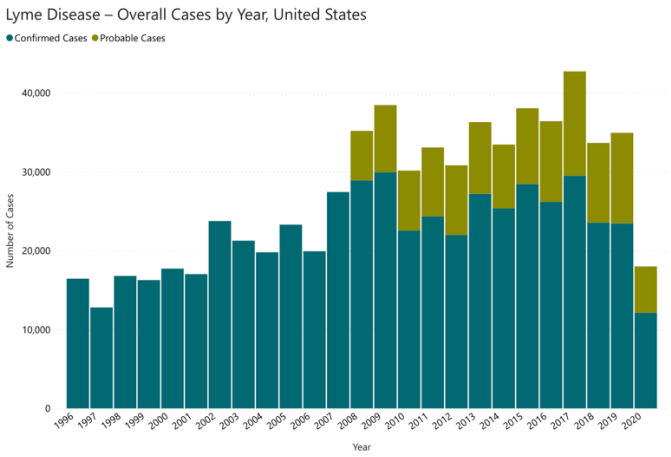

Figure 1.5. LD cases by year confirmed by CDC. Figure from cited reference[140].

Although clinical features of LD are diverse, infection typically begins with erythema migrans (EM), an expanding skin lesion at the site of the tick bite. If left untreated, spirochetes may disseminate from the site leading to neurologic, cardiac, and/or rheumatologic manifestations[141]. Death from Lyme disease is rare but late detection of Lyme disease can result in further complications including arthritis,

carditis, and permanent neurological disorders[142]. Therefore, timely identification and quick treatment (within 72 hours) are required for better health outcomes. Children 5 to 15 years old as well as adults older than 50 years have the highest infection rates[143]. Although many cases are effectively treated with antibiotics, 10 to 20% of patients report lingering symptoms after receiving appropriate therapy[144].

The majority of human infections are caused by three genospecies: *B afzelii* , *B garinii* , and *B burgdorferi* sensu stricto[145]. Among these, only *B. burgdorferi* causes Lyme disease in North America but in Europe up to five species (*Borrelia afzelii, Borrelia garinii, Borrelia burgdorferi, Borrelia spielmanii*, and *Borrelia bavariensis*) can cause the disease[146]. Although these species are found widely in temperate regions of the Northern hemisphere, the number and geographic distribution of cases has been increasing steadily. Geographic distributions, and ecological critical factors determine risk of human infection. The emergence of this disease is in part a direct result of the reforestation of the northeastern United States and the rise in deer populations from lack of predation[147]. Recent studies suggest LD will expand as climate change as the highly efficient reservoir hosts' territory, such as white-footed mouse, expend north as a result of milder winters[148]. As a result of temperature increases in northern or southern latitudes or at higher elevations, the vector species as well as reservoir hosts will likely spread their habitats[149].

Pathogen Life Cycle

Ixodes scapularis is the vector for *Borrelia burgdorferi* in the northeastern United States. Ticks act as both transmitters and reservoirs for pathogens. The bacteria can be transmitted at any stage of the life cycle of the bacterium as well as transmitted from the ovaries of one generation to the next[150]. The life cycle of Lyme disease is shown in **Figure 1.6**. When the tick larva first hatch, they may be uninfected if there was no transovarial transmission. After feeding on an infected host, *B. burgdorferi* may be acquired. Once the larva molt to the nymphal stage, the tick can transmit *B. burgdorferi* to the next animal during a blood meal. The highest risk of Lyme borreliosis transmission occurs by nymphs owing to their small size and their abundance in the environment[138]. The species of the next animal host varies considerably from deer, birds, and mice. When a tick bites a host, spirochaetes are inserted into the bite wound along with the

tick saliva. Infection may proceed if the tick has been attached for 48 hours or longer[151]. Infection rarely occurs during the first 24 hours of feeding.

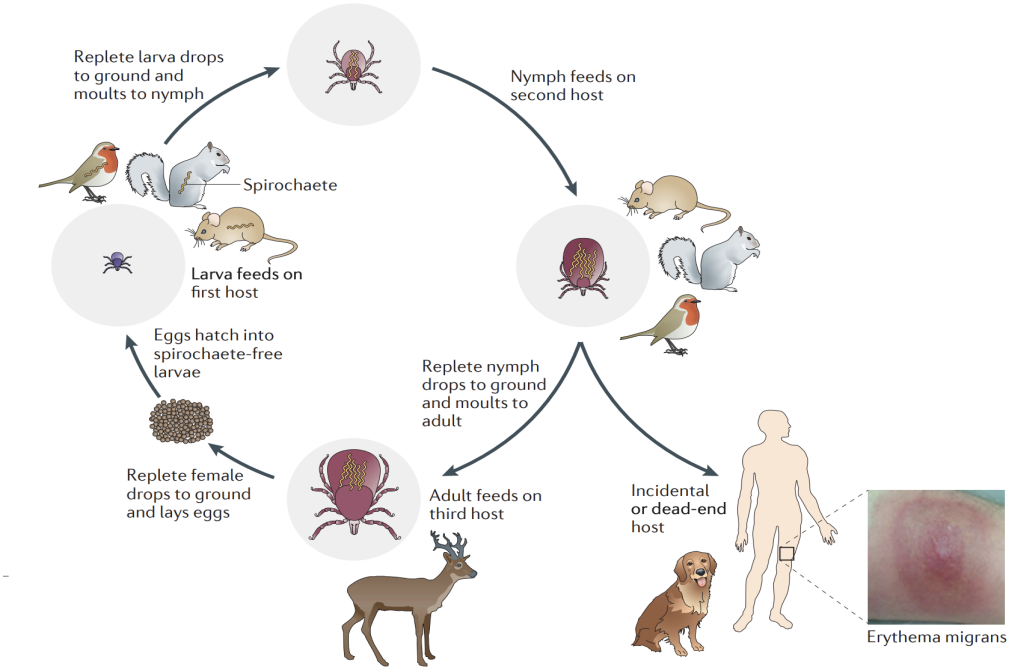

Figure 1.6. The enzootic cycle of *Borrelia burgdorferi.* Figure from cited reference[138].

Progression of Disease and Symptoms

Clinically, Lyme disease has three stages. The localized stage occurs 7-10 days after the initial infected bite. 80% of infected patients will exhibit a red ring-shaped lesion on the skin with a red outer border and partially clear center known as “erythema migrans" (**Figure 1.6**). For many cases, these lesions are accompanied by flu-like symptoms (fatigue, headache, fever, chills). The second stage, referred to as early disseminated disease, may occur weeks or even months after the first stage and include bacteria disseminating into the blood stream or the lymphatic system[152]. The second stage may consist of symptoms such as fever, fatigue, myalgia, neurological abnormalities, heart inflammation (carditis), and bouts of arthritis in larger joints such as knees and elbows[134]. Some research suggests that Lyme arthritis could be a form of autoimmune response to the major histocompatibility molecules on the cells in the joints. As the *B. burgdorferi* genome does not encode any known toxins, inflammation producing the tissue damage inside

the joint is likely mediated by the host immune response to the spirochetal proteins[153]. The third and last stage, referred to as late disseminated LD, may occur years later, and may include intermittent arthritis, peripheral neuropathy, and encephalitis. It is often characterized by the development neuron demyelination which often resembles Alzheimer's disease and multiple sclerosis.

Features of *B. Burgdorferi*

A notable feature of *B. burgdorferi* is that it does not require iron nor is it able to synthesize its own amino acids, nucleotides, and fatty acids[138]. Consequently, *B. burgdorferi* contains limited metabolic and biosynthetic abilities, and is considered dependent on the tick and mammalian host for essential nutrients[154]. One of the most interesting aspects of *B. burgdorferi* is that it contains a one megabase-sized linear chromosome, as well as many linear and circular plasmids[155,156,157,158]. The most complex genomes of all known bacteria are the members of the genus *Borrelia* and the cell envelope of *B. burgdorferi* are distinctly different from all other prototypical proteobacteria[138]. Although they are considered gram negative bacteria one of the most striking differences between *B. burgdorferi* and proteobacteria is the cell envelope[159]. The outer cell membrane architecture contains phosphatidylcholine, phosphatidylglycerol and glycolipids cholesteryl-6-*O*-acyl-β-D-galactopyranoside and cholesteryl-β-D-galactopyranoside[138]. Consequently, motility of *B. burgdorferi* is another defining feature. The flagella are located entirely inside the periplasmic space as opposed to being located on the outside[160]. This allows *B. burgdorferi* to move by posteriorly propagating planar waves using periplasmic flagellar filaments composed mostly from FlaB protein and FlaA protein[161]. The mobility of spirochetes allows dissemination within and between hosts to cross and invade complex tissues. Moriarty et al revealed the bacteria could move in tissue at speeds 4 μm per second[162] which is faster than phagocytes. Studies with wild type cells vs mutant cells (lacking periplasmic flagella) showed significant differences in establishing infection[163]. Sultan et al provided evidence that a FlaB mutant was nonmotile and mutant cells were unable to establish infection in mice via injection or by tick bite[161]. Wild type spirochetes can outmaneuver the host's immune cells which allows persistence of

infection and limited clearance of disease. Therefore, the motility of the bacteria is critical for survival inside ticks as well as mammalian host infection.

The Skin Interface

Skin is the sole interface in vector-borne diseases, such as malaria, trypanosomiasis, leishmaniasis, and dengue fever[164]. Initially, a tick uses the hypostome (calcified harpoon shaped structure on the mouth) to attach and anchor to the host's skin so it can remain in place during feeding. For successful feeding, ticks must remain attached to their host for several days without initiating a wound healing response at the bite site[165]. During the bite event, the saliva is secreted into the host's skin where the lytic activity helps to form a "feeding pit" (**Figure 1.7**). The saliva secretions also form a cement cone to help anchor the tick in place during feeding. Upon entry into the host, the first obstacle *B. burgdorferi* must evade is the host innate immune system. Inflammation is a primary part of the host's innate immune response. As a result of inflammation, vascular permeability is increased to allow an influx of immune cells to migrate the site of tissue damage. Anti-inflammatory and anti-itch mediators in their saliva allow the tick to remain feeding undetected upon the host until repletion[166]. Studies have shown that the tick saliva has a suppressive effect on specific pro-inflammatory mediator expression[167].

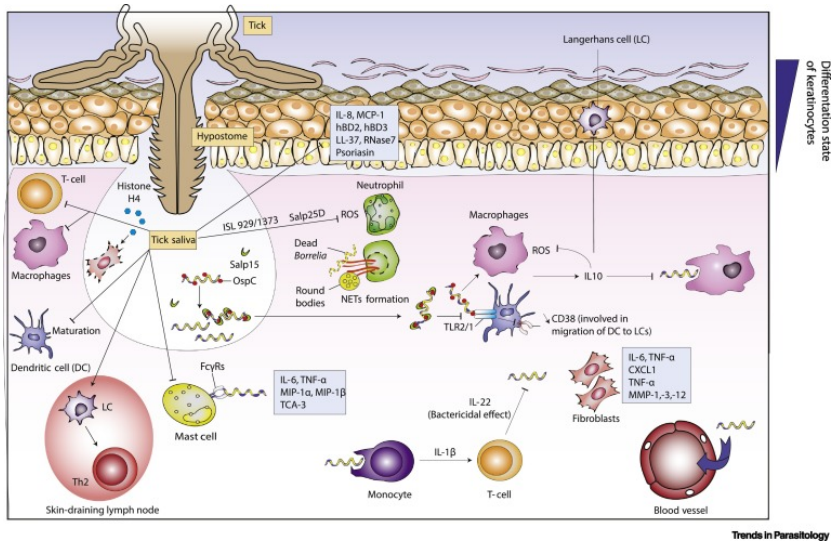

Figure 1.7. Inflammatory response on the host's skin during a tick bite. Figure from cited source[164].

Without the tick saliva, the host's cells may induce an inflammatory response against the bacteria. The mammalian host may detect *B. burgdorferi* through pattern recognition receptors on dendritic cells and sentinel macrophages inside the dermis tissue. Thus, tick saliva increases the virulence and survival of *B. burgdorferi* by blocking the inflammatory response[166]. For humans that are often exposed to tick bites, immune responses are characterized by increased inflammatory reactivity and often do not lead to the development of Lyme disease[168]. Burke et al provided evidence that suggest that prior tick bites from uninfected ticks actually help protect humans from LD by possibly helping to develop a cutaneous hypersensitivity that results in increased swelling and itchiness at the tick bite site[168].

Once more, skin is also important as it is the site of replication and persistence of *B*. *burgdorferi.* As a tick larva feeds on blood meal, replication of spirochaete is triggered and continues throughout the molting. During a tick bite, *B. burgdorferi* does not migrate away from the feeding site until several days after the tick has detached from the host[169]. In a study by Shih et al, researchers could culture spirochetes from the bite site of mice within a week after ticks were detached[169]. Thus, this may indicate that once the spirochetes are delivered into the skin, the spirochetes will multiply locally for several days before migrating to more distant areas in the body. Giving the various elements in the tick saliva that favor the spirochetes' survival, there is no rush to leave the protective environment during the establishment of infection. As neutrophils are normally the first cell to arrive to the infection, it is confounding that biopsies of EM skin lesions only showed a few neutrophils[170,171]. If neutrophils are present, they can trap the bacterium in neutrophil extracellular traps (NETs). It is believed that the traps kill the bacterium, but some bacteria might be able to survive by forming round bodies (which occurs during antibiotic treatment or during tick starvation periods)[172].

Ixodid ticks usually feed for several days until repletion. For starved hard ticks, little is understood on exactly how the bacteria can survive. The bacteria are neither dormant nor replicating during these periods of tick starvation[138]. Since the bacteria require some level of carbon for glycolysis, it is thought that a unique feature of ticks may help sustain the bacteria. To endure harsh winters, ticks produce glycerol as

a natural antifreeze. So, it is believed that the bacteria can use their non-specific transporters to intake the glycerol for sustenance[173].

If the tick can stay attached for up to 2 days, *B. burgdorferi* spreads to more tissues[166]. To expand through tissues, *B. burgdorferi* penetrates and degrades the matrix between cells to infiltrate capillary beds. As the spirochaete lacks surface proteases, it will instead harness the host's proteases (i.e., plasminogen or urokinase)[174,175]. Once the *B. burgdorferi* invades the capillaries, it may travel through the bloodstream. With diverse receptors, it can leave circulation and adhere to host tissues. To avoid detection of antibodies, *B. burgdorferi* displays antigenic variation[176,177]. In fact, for every change of host, there is an accompanied major antigenic change[138]. Consequently, *B. burgdorferi* can persist for years in a patient despite an active immune response.

Challenge of Identifying LD vectors

The identification of tick species and the determination of associated pathogens are essential to evaluate epidemiology and risks of human and animal diseases. Most cases of LD can be successfully treated if prophylaxis medicine is administered to the patient within 72 hours after a tick bite. Once a feeding tick it removed from a human, this presents as early window for treatment. However, proper identification of tick vectors vs nonvectors species remains a key challenge[178]. Not all ticks carry Lyme disease. Currently, 869 species or subspecies of ticks had been recorded to date[179]. Current approaches for tick identification include the use of morphology of taxonomic keys or gene sequencing in a laboratory[180]. Morphological identification is often difficult as it requires entomological expertise, and it is also challenging to identify a damaged tick, an engorged tick, or a tick at an immature stage of the life cycle. Morphological identifications require use of a dichotomous identification keys which may exist as a book format or software. One advantage of morphological method is it is inexpensive, reagent free, and can be quick at POC. However, the ID keys may not correspond with the specific species. Furthermore, dissection of key organs and analysis under a microscope is the only accurate method for identification of some tick species. Such a workflow is not conducive to large sample processing that a clinic may need to implement. Matrix-

assisted laser desorption/ionization time-of-flight mass spectrometry (MALDITOF MS) has been used as an accurate tool for the rapid identification of tick vectors and bacteria that requires no previous expertise in tick identification but suffers from high cost[180]. Additionally, tick collection usually takes place far from analytical laboratories and thus, requires proper storage of samples for the accuracy of mass spectrometry results.

Current laboratory-based methods to identify the species of ticks is labor intensive and takes time. As such, the current method cannot meet the short three-day window of time needed for treatment. Promptly identifying blacklegged ticks (carriers of LD) within the crucial window of time via computer vision technology is a promising solution to aid in this challenge. As many rural patients may not be able to travel to a clinic, most may have access to cell phones and be able to take advantage of telehealth programs instead.

Recently, a Canadian public platform for image-based identification and population monitoring of ticks was launched as an app[181]. Canadian citizens can submit tick photos to the app so that tick movements can be mapped across geographical areas. Such efforts highlight the growing expansion of ticks, as well as the time-sensitive identification needed for prompt administering of prophylaxis within a crucial window of time. In a study by Akbarian et al, photos taken by users of the eTick app were submitted to an entomologist for review and compared to a computer vision algorithm developed by researchers[182].The researchers developed computer vision algorithm to build a classifier that can automatically detect the correct tick species from thousands of images to identify vector ticks in real-time. The best classification model was able to identify black legged ticks with a 92% accuracy using LSR combined with AT. This work shows potential for automating identification to aid in clinical decision making. If the LD vector is identified accurately, treatment can be administered quickly. However, many patients will not have the tick available for inspection and so other methods are needed to improve the burden of LD.

Current diagnostic & future technologies

Conventional diagnosis of LB is often based solely on the presence of an erythema migrans lesion. Erythema migrans (EM) develops in only 70%–80% of patients[183]. EM begins as a red papule that expands into a round lesion median diameter 18 cm to 14 cm[184]. In the absence of EM, the signs and symptoms of Lyme disease are too nonspecific to be clinically useful for diagnosis. Additionally, misdiagnosis may occur due to the high degree of variability of skin lesions and the variation of interpretation. Additionally, African American patients often do not recognize early disease, resulting in increased rates of late manifestations[185].

As the skin is the inoculation site as well as displaying the first clinical manifestations, there are several laboratory methods developed to detect *B. burgdorferi* from human skin biopsies. The first method is in vitro culture of intact living bacteria and the second method is PCR to detect bacteria DNA[186]. Though the culture method provides confirmation of active infection, the bacteria itself is scarcely found in tissues. Compounding this, the bacteria grow very slowly for up to 12 weeks only in very specific growing conditions. Cultures as direct detection are too time consuming and not practical for routine use.

Quantitation using real-time qPCR can be performed from skin biopsies[186,187]. Since PCR provides high sensitivity, speed, and the ability to include original skin biopsy, early detection of Lyme disease may be possible. In addition, real time PCR allows the quantification of bacteria in many infected samples, such as animal tissues, ticks, human skin, and CSF[188]. PCR testing identified more positive samples than culture (77.7% PCR positive versus 55.1% culture positive)[186]. In another study, researchers found the higher amount of bacteria in the skin biopsy was associated with higher risk of constitutional symptoms accompanying EM and a higher risk of relapse post-treatment[189].

The US FDA has cleared a few serological diagnostics tests. The 2-tiered testing paradigm for serodiagnosis starts with an enzyme immunoassay (EIA), followed by Western immunoblotting to increase specificity[190]. For patients with late stage LD, this two-tiered testing features high diagnostic specificity (95%–100%) with high sensitivity (>90%)[191] but only 40% sensitivity for early-stage (meaning that it misses more than half of the cases). The serologic test feature both technical and biological shortcomings. Western blots cannot differentiate active infection from past exposure from a single serum sample.

Additionally, antibodies may persist for years after successful treatment. Therefore, antibody detection is not able to differentiate from past infection from a newly acquired infection even over multiple blood draws. Since development of host-antibody response takes several weeks, early diagnosis remains problematic and therefore, serologic tests are insensitive during the first several weeks of infection. The biggest problem being the time delay for the host to make detectable antibodies by current testing methods. It is often up to 3 weeks from initial infection for the B-cell production of pathogen-specific antibodies in sufficient quantities to be detectable[190]. The development of sensitive tests capable of directly detecting the organism in body fluids has proven challenging due mainly to the low microbe copies. Therefore, enhancement or enrichment methods will also be needed for better diagnostics.

Finally, the lack of standardization in the commercially available kits result in high variability. Once more, the results often take weeks. Therefore, the CDC recommends antibiotic prescription for cases with symptoms even if the first test is negative. However, over prescription practices drive antimicrobial resistance so high performing diagnostic methods are highly desirable.

Summary of roadblocks for project 3:

1.) Bacteria are present in low numbers in blood.

2.) Host antibody response to bacteria take weeks to develop and PCR requires direct capture of bacteria.

3.) Bacteria are localized in the skin, but extraction is difficult.

Project 4: Urine-based TB detection would improve diagnosis for vulnerable populations.

Globally, there are an estimated 10 million cases of tuberculosis (TB) each year, resulting in 1.6 million deaths[192]. Although numbers of deaths from TB are much lower in high-income countries, TB remains a significant problem in LMICs. TB is the leading cause of death from a single infectious agent worldwide. TB is mainly caused by *M.tuberculosis*, an acid fast bacillus which is usually transmitted through respiratory routes[193]. While infection primarily occurs in the lungs, other organs such as bones, joints, central nervous system can become infected[194]. Drug-resistant TB is another concern with half a million new multidrug-resistant TB emerging [195]. It is predicted that multidrug resistant mutation TB will increase 20% a year[196]. Additionally, it is estimated that up to one quarter of the world's population may be infected with latent TB[197]. Compounding this, TB control efforts are limited by a high loss of pre-treatment follow-up[198].

Screening for TB

Since latent TB is often asymptomatic, screening is often used to identify these individuals and are often used for identifying those who need more follow up testing to confirm or rule out a TB infection. For screening purposes, populations can fall into two distinct categories: high-risk vs low risk. High-risk individuals are typically those with immunosuppressive treatments or those with weakened immune systems or those who have been exposed to someone with active TB. There are two options for screening that are approved for TB screening. One is the tuberculin skin test and the other is the interferon-gamma release assays (IGRAs)[199]. IGRAs are considered more specific than the skin test[200]. Both screening tests are indirect since they do not directly measure the bacteria. Additionally, the frequency of screening test is another consideration for TB control. Typically, those who are categorized as low risk may only need to be screened once. Those who live with someone who has been diagnosed with TB or healthcare workers who take care of patients with TB are considered high-risk. High-risk individuals benefit from more frequent

screening or annual screening. Unfortunately, the screening test cannot differentiate between old TB infections and new TB infections.

Diagnostics

TB diagnostics utilized in developing countries, where TB is most prevalent, depend on smear microscopy[201] which routinely misses half of all cases[202]. Other diagnostic modalities such as chest radiographic findings and culture studies are also used, but both methods are often unavailable in low-resource settings[203]. TB is curable with treatment, but an estimated 30% of TB cases remain undiagnosed or unreported, in part due to limited performance in current diagnostics[204]. A lack of access to rapid and sensitive TB diagnostics delays or prevents appropriate treatment, contributing to increased mortality, TB transmission, and development of drug resistance[198]. Recently, the COVID-19 pandemic has posed new barriers to diagnosis which has resulted in a drop in TB detection and reporting worldwide (**Figure 1.9**)[205].

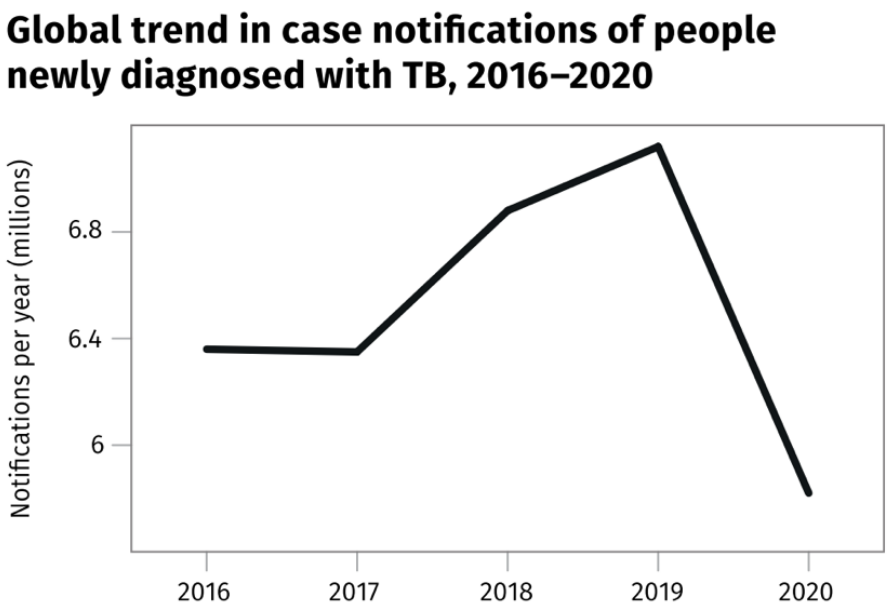

Figure 1.8. The effect of the COVID-19 pandemic led to a drop in new TB infection detections and reporting worldwide. Figure from cited reference[41].

TB detection remains a significant diagnostic challenge. Sputum smear is still a common laboratory test in the developing countries due to being inexpensive and relatively easy to perform but it exhibits a poor

clinical sensitivity of ~50% and requires a laboratory with staining reagents and skill. Additionally, after staining the samples, they still require manual examination which can take considerable amount of time for techniques who are pressed to examine an array of other samples[206]. Current diagnostic methods are most often based on detection of biomarkers in a sputum sample but HIV-infected individuals and children are often not able to provide sputum samples[207]. Even if sputum can be produced, HIV-associated tuberculosis may also contain relatively low mycobacterial concentrations in pulmonary secretions[208]. Also, sputum samples are not useful for cases of extrapulmonary TB which typically requires collection of a sample from the site of infection[209]. Additionally, peripheral blood is not a useful sample in the Gene Xpert PCR assay for TB diagnosis, and so other clinical samples are urgently needed[210]. Since urine poses low infection risk to healthcare workers during sample collection and is easily obtained from children and HIV adults, urine has been suggested as an alternative patient sample for diagnosis.

Urine as sample for TB diagnostics

A urine lateral flow test for TB is available based on the TB surface biomarker Lipoarabinomannan (LAM), but it exhibits a low sensitivity of 50%-70% depending on CD4 count[211]. TB bacteria DNA is also present in patient urine. It is thought that as TB bacteria die the DNA is released form the cell, where it can circulate, and some may cross the trans renal barrier where it can be detected in urine with various methods. PCR-based approaches, which potentially are much more sensitive and specific, have been proposed for detecting nucleic acid biomarkers in urine but remain controversial[212]. A particular challenge for TB DNA biomarker testing in urine is DNA degradation into fragments by Deoxyribonucleases (DNases) which are enzymes that degrade DNA and DNA cell-free fragments continuously[213,214,215]. To protect the stability of urine, storage of urine requires refrigeration or freezing to inhibit bacterial growth. Additionally, it has also been shown that numerous freeze/thaw cycles affect the composition of urine[216]. Overall, the use of preservatives, cold temperature ranging from −80°C to 4°C, and limited thaw cycles can extend the shelf life of urine as well prevent the overgrowth of microorganisms and activity of DNases.

DNA-based testing of urine is a rapidly evolving area for low resource diagnostic testing. Urine is a desirable patient sample matrix, but remaining challenges limit the use of PCR-based methods to detect nucleic acid biomarkers in urine. Two of the biggest challenges are the low concentration and small size of DNA fragments. A recent next-generation sequencing report characterizing TB DNA in urine[217] suggests that many more short fragments are present than previously thought. Some reports suggest significant numbers of fragments in the range of 29 to 45 bp in length are present[217,218,219,29] which is too short to be detected by traditional PCR assays. The other challenge is the low concentration of these small number of TB-specific fragments that can be used to detect active TB infection (median approximately 10 copies/mL)[220]. Notably, Oreskovic et al characterized urine cf-DNA using next-generation sequencing, revealing that TB-derived cf-DNA is significantly more degraded than human-derived cf-DNA[221].

In 2008, Cannas et al. discovered trans renal TB DNA fragments could be detected in the urine of patients with TB[220]. Their results showed that the TB specific sequences presented in 79% of the patients studied (n = 43). Additionally, the authors compared the PCR results with primers producing short and large amplicons with positive patient samples (n =7) and found shorter amplicons detected and the products were not produced for longer amplicons. Most PCR tests for TB target IS*6110* and amplify targets from 123-566 bp in length[222]. While it is possible to reduce the amplicon length to as short as 38 bp by redesigning the primers this resulted in sensitivity of only 64%[223]. Typically, primer sets are designed to maximize sensitivity and specificity, so redesigns based on amplicon length may reduce these properties. While shortening the amplicon should increase the statistical likelihood of encountering the full-length target in urine, it would have to be balanced with the tradeoff of a sub-optimal primer pair. Critically, another key experimental design by Cannas et al was the PCR analysis between the supernatant and pellet after centrifugation of the urine sample. The supernatant yielded detection in 7 of 8 samples while the pellet only detected 2 of the 8 positive patient samples[220]. Other studies have also verified the use of supernatant over pellet DNA for cf-DNA analysis[224,223]. Due to the variation in urine collection, treatment, storage and PCR amplicon size, multiple studies have generated various test sensitivities from 7-100%[222]. The majority of urine cf-DNA fragments are expected to be < 100 bps with TB cf-DNA being substantially shorter than

human genomic cf-DNA[221]. Despite the improvements in short cf-DNA fragment recovery, current methods are unable to reliably confirm the shortest cf-DNA fragments in urine.

Current research has shown that fragment recovery begins to decrease below 40 bp[219], and due to the nature of sequence read mapping algorithms, it is not possible to reliably map the origin or sequence reads below a specified seed length such as 19 bp[225]. Short DNA fragment in urine are thought to be present in concentrations between 1-200 ng/mL[219]. Prior work by Oreskovic and Lutz et al, showed success with a sequence specific hybridization method that recovered nearly 100% (95% CI: 82.6–117.6%) of target-specific DNA from 10 mL urine, independent of fragment length (25–150 bp), and featured a limit of detection of 0.5 copies of double-stranded DNA (0.5 copies/mL)[226]. A 2017 study found a minimum concentration of 3 copies/ml was measured on PCR but these fragments were longer at 75 bp-target[224]. Another paper by Oreskovic et al used dual biotinylated probes to capture complementary fragment sequence[227], which suggests that probes that are unique enough (little cross reactivity) would allow for multiple fragments to be captured on a bead. This in turn would provide a greater distribution of fragment targets for increased detection.

Summary of roadblocks for project 4:

1.) Full length IS*6110* TB DNA is not found in urine and small DNA TB fragments present are found in low concentrations.
2.) Fragments in urine are too short for extraction by available methods.
3.) Most TB cf-DNA fragments are too short for amplification by traditional PCR methods.

Thesis Goals and Overview

Throughout this dissertation, I work to overcome each of the previously described obstacles to the use of biomarker detection from non-invasive sample sources. In Chapter 2, I develop a platform to reliably transfer the correct volume of urine to dipstick pads coupled with a cell phone for automated dipstick interpretation that can meet ASSURED criteria. An easily assembled and operated device for robust urine dipstick operation without preprocessing devices, auxiliary instrumentation or control systems is still highly desired. To accomplish this, two innovations are proposed to overcome the roadblocks. To control the volume of liquid dispensed to the dipstick pad and ensure individual deposition, we propose to use the SlipChip design to dispense optimal volumes of sample onto each individual dipstick pads. To overcome roadblock 3, our proposed method can be easily modified to use with other brands of dipsticks by changing the dimensions and spacing of the through-holes. The volume applied to the dipstick can also be modified by changing the thickness of the acrylic used to fabricate the slide (with commensurate changes in the thickness of the ledges of the base plate) or the size of the through-holes. The current device combines a 3D-printed base plate and laser-cut top plate to form a plate sleeve. Both fabrication methods are affordable, and the material choices can be modified. Excluding the phone and dipstick, the acrylic used in the current device costs approximately $0.85, and material used in the 3D-printed base plate costs around $1.50 per device. Although the base plate we used is 3D-printed from acrylonitrile butadiene styrene (ABS), other polymers that form a hard and rigid surface are also suitable. For example, a version of the device can be made using a plate sleeve completely fabricated from acrylic.

In Chapter 3, I fund and develop a paper-based method to normalize a cancer biomarker in a LFA test strip. A screening test for ovarian cancer recurrence that is simple enough to perform at home would offer a convenient and less harmful sampling procedure, especially for repeated testing over an extended time. I also develop this device to meet the WHO's ASSURED criteria. In this work, we test the performance of the test using clinically relevant ratios of ovarian cancer recurrence. Surrogate patient samples were created based on previously published work by Liao et al., who measured patient HE4 urine values in pM and creatinine values in mg/dL as a ratio[105]. The range of 2 - 47 ratios are selected to ensure

that the paper-based test was operating in the range of ratio values associated with recurrence testing in urine[105]. Because both creatinine and HE4 can be present in high amounts, Liao et al diluted clinical samples by 1:40 prior to testing [105]. Therefore, I assume the same level of dilution for our test method and CRE values from 0-40 mg/day[228] were selected for testing as they are in the ranges of diluted urine samples as described by others[104,105]. I demonstrate an improved method to detect changes in urine HE4/CRE accurately at-home. In addition, due to its low-cost, this method can also be employed in low-resource settings where clinical visits are even more difficult. In the future, the methods demonstrated here could be evaluated with patient samples to further validate the clinical performance of the device.

In Chapter 4, I develop a dissolvable microneedle device that can capture inactivated *borrelia burgdorferi* in pig skin and be dissolved for PCR detection of the pathogen. A non-invasive sampling of skin ISF that could be performed at home or in resource limited areas would allow for surveillance of tick-borne pathogens. Although this work relies on PCR detection, the self-sampling method does meet many of the requirements for an ASSURED diagnostic. The MN could be applied at home or in a LMIC where it could be shipped to a centralized testing facility with test results delivered electronically for $25 (tick testing centers charge $50 but this service requires isolating the DNA from the tick leading to increased time and cost[229]). Reports indicate that up to thousands of bacteria are found in the skin biopsy of LD patients' EM. Therefore, I sought to detect that amount with our MN. We sample different amounts of bacteria using agar gel and porcine ear skin which is a close model to human skin. We use optical coherence tomography to verify penetration in both gels and pig ear skin. We characterize the swelling and mechanical strength of the MN. We demonstrate a low-cost and sensitive method to detect the causative agent of LD with average recovery of 80%. Future work will optimize the MN and validate the MN method with human who recently report a tick bite or who exhibit an EM.

In Appendix 4, I describe promising results using magnetic bead-based approach to capture TB cf-DNA fragments in urine and RT-PCR to reconstruct the fragment along the template to a length that can be amplified by a subsequent PCR reaction. Although this method also relies on PCR for detection, the sample source is affordable compared to blood, it's non-invasive and can be easily self-collected. Assuming

fragment capture is successful, the RNA will recognize the target nucleic acids – and only the target nucleic acids – and bind to them. The amplification step is facilitated by RT-PCR. In this aim, we refer to this method as Amplicon Reconstruction PCR (AR-PCR). This method overcomes challenge 4 by creating full length PCR target sequences if partial sequences of the TB target are present in a sample. To achieve this, we use a cDNA kit to reconstruct the fragment along the RNA strand on the magnetic bead. For a molecular diagnostic to be useful, it must be sensitive as well as specific. A major benefit of the strategies outlined here is the specificity—only fragments that contain portions of the IS*6110* amplicon will be captured, concentrated, and subsequently amplified by PCR.

CHAPTER 2: LOW-COST, VOLUME-CONTROLLED DIPSTICK URINALYSIS FOR HOME-TESTING

Adapted from: Kight, E., Hussain, I., Bowden, A. K. Low-Cost, Volume-Controlled Dipstick Urinalysis for Home-Testing. *J. Vis. Exp.* (171), e61406, doi:10.3791/61406 (2021).[230]

Abstract

Dipstick urinalysis provides quick and affordable estimations of multiple physiological conditions but requires good technique and training to use accurately. Manual performance of dipstick urinalysis relies on good human color vision, proper lighting control, and error-prone, time-sensitive comparisons to chart colors. By automating the key steps in the dipstick urinalysis test, potential sources of error can be eliminated, allowing self-testing at home. We describe the steps necessary to create a customizable device to perform automated urinalysis testing in any environment. The device is cheap to manufacture and simple to assemble. We describe the key steps involved in customizing it for the dipstick of choice and for customizing a mobile phone app to analyze the results. We demonstrate its use to perform urinalysis and discuss the critical measurements and fabrication steps necessary to ensure robust operation. We then compare the proposed method to the dip-and-wipe method, the gold standard technique for dipstick urinalysis.

2.1 Introduction

Urine is a non-invasive source of multiple metabolic indicators of disease or health. Urinalysis, the physical and/or chemical analysis of urine, can be performed quickly to detect renal disease, urinary tract disease, liver disease, diabetes mellitus, and general hydration[231]. Urinalysis dipsticks are affordable, semi-quantitative diagnostic tools that rely on colorimetric changes to indicate approximate physiological levels. Each dipstick can perform a wide variety of assays including testing for pH, osmolality,

hemoglobin/myoglobin, hematuria, leukocyte esterase, glucose, proteinuria, nitrite, ketone, and bilirubin[41]. The principle of dipstick urinalysis relies on the occurrence of a timed reaction through which a color change on the dipstick pad can be compared to a chart to determine analyte concentration[232]. Given their affordability and ease of use, dipsticks are one of the most common tools for urinalysis in healthcare. Traditionally, dipstick urinalysis relies on a trained nurse or medical technician to manually insert the dipstick into a cup of urine sample, wipe off excess urine, and compare the color pads to chart colors at specific times. While the dip- and-wipe method is the gold standard for dipstick analysis, its reliance on human visual assessment limits the quantitative information that can be obtained. Moreover, the two manual steps of dipstick urinalysis – the dip-wipe step and colorimetric result comparison – require accurate technique, which limits the possibility of reliable testing in home settings by patients directly. Cross-contamination of the sample pads due to wiping can cause inaccurate color changes. Additionally, inconsistent volumes resulting from the lack of volume control during wiping can result in improper measurement of analyte concentrations. Importantly, the time between dipping the urine (i.e., the start of the assay) and comparison to a chart is critical for accurate analysis of the results and is a huge potential source of human error. The difficulty in manual colorimetric comparison is that many pads must be read at the same time, while some pads are read at different times. Even perfectly timed color comparisons still depend on the visual acuity of the human reader, who may suffer from color blindness or perceive different colors in different lighting environments[233]. These challenges underscore why clinicians can only rely on dipstick urinalysis performed by trained personnel. However, an automated urinalysis system could address all the aforementioned concerns by eliminating the need for manual dip-wipe steps, incorporating timing controls, and enabling simultaneous color comparisons with calibrated color references. This, in turn, would reduce user error, allowing for possible adoption in home settings. In the last 20 years, automatic analyzers have been employed to read the results of dipstick urine tests with the same accuracy as or exceeding visual analysis[46]. Many clinics and doctor offices use such machines to rapidly analyze and print traditional dipstick results. Most urinalysis machines minimize visual inspection errors and ensure consistency in results[234]. They are easy to use and more efficient than manual inspection but still require the user to perform

the dip-wipe method correctly. Hence, these machines have limited ability to be operated by untrained persons such as at-home users; moreover, they are extremely expensive. Recently, cell phones have emerged as a resourceful tool for various biological colorimetric measurements[235,236,237,238] including for urinalysis[239,240,241]. Given their remote sensing capabilities and high imaging resolution, cell phones have become effective healthcare analytical devices[242,243]. Indeed, the FDA has cleared several smartphone-based home urine tests[244,245,246]. Some of the new smartphone-based commercial products incorporate established urinalysis dipsticks, while others feature proprietary colorimetric pads. All such products feature proprietary methods to calibrate for different lighting conditions across different phone types. Still, a problem with these solutions is that the user must manually take a picture at the right time in addition to carrying out a proper manual dip-wipe method (i.e., without cross contamination). Notably, none of these tests control the volume deposited onto the dipsticks, which we have found can affect the color change[247] and interpreted physiological result. The present gaps and costs in the workflows of these devices suggest an additional need to enable a human-free, volume-controlled urine deposition procedure and hands-free dipstick photography. We describe a protocol for volume-controlled, automated dipstick urinalysis without the need for a manual dip-wipe step. The key to the automated process is a device19 whose underlying principle is based on the SlipChip[248] and that transfers liquid between different layers using surface chemistry effects. In brief, the hydrophobic coating on the transfer slide and surrounding plate sleeve force the liquid to move effortlessly through the device and to release onto the dipstick pad once the slide is in its final position, at which point the bottom hydrophobic barrier is replaced with air. Additionally, the coordinated light-blocking box standardizes the lighting conditions, camera angle of view, and the distance for camera focus to ensure accurate and repeatable results that are not influenced by ambient lighting conditions. An accompanying software app automates the capture of images and colorimetric analysis. Following description of the protocol, we provide representative results of the urinalysis test under different conditions. Comparisons with the standard dip-wipe method demonstrate reliability of the proposed method.

2.2 Protocol

1. Fabricate and assemble the urinalysis device

1.1. Fabricate the base plate (**Figure 2.1A**).

1.1.1 Use a computer-aided design (CAD) software to draw a rectangular area with dimensions 2.1641 in x 0.0547 in x 6.3828 in (W x H x L) using the polyline tool.

1.1.2 Measure the test area (rectangular area encompassing the distance between the first and last pad and the width of the pads) on the dipstick.

NOTE: This information is needed to draw the through-holes that hold the dipstick in place and separate the liquid in between the pads (to prevent cross-contamination).

1.1.3 Add through-holes that mimic the size and position of each test pad in the test area.

1.1.4 Draw two raised side ledges that measure 2.1641 in x 0.6797 in (W x L).

1.1.5 Draw a stop (0.1172 in by 0.2109 in (W x L)) using the polyline tool to facilitate alignment between the base plate and the slide. The stop should be perpendicular to the ledges and physically stops the slide from moving passed the urine dipstick pads.

1.1.6 Select the lines for the stop and ledge to make one region using the “region” command. Use the “extrude” command to raise the region up to a height of 0.0703 in. Repeat this step on the other side of the device.

1.1.7 Create a notch (0.1719 in by 0.3500 in (W x L)) on both ledges to facilitate alignment with the box. Position it 0.466 in from the bottom edge of the ledge. Use the “region” command to create one region of the rectangle and make the extrusion to the height of 0.1103 in.

1.1.8 Use the “solid subtract” command, select device, press “enter”, select the notch region and press “enter”. Repeat on the other side of the device.

NOTE: The shape will be removed from the device.

1.1.9 Print the base plate on a 3D printer and sand the top face area between the ledges with sandpaper to roughen the surface.

NOTE: Sanding is important so that the hydrophobic coating can adhere to the base plate securely.

1.1.10 Tape the ledges with adhesive tape (to avoid spraying the ledges) and spray the base plate with a hydrophobic spray. Apply several (4-8) coats of the basecoat to the base plate. Hold the can approximately 8-12 in away from the base plate when spraying. The device should have a milky white appearance upon drying.

CAUTION: Follow manufacturer instructions for appropriate location and PPE for spraying

1.1.11 Wait 30 minutes before applying the topcoat several times (6-8). Allow the base plate to dry for 12 hours before use. Remove the tape from the ledges.

1.2. Fabricate the top plate (Figure 2.1B)

1.2.1. Draw a rectangular area to measure 2.05 in x 5.470 in (W x L) in a CAD software using the polyline tool.

1.2.2. Add a rectangular through-hole (the "viewing through-hole") slightly larger than the size of the test area of your dipstick (e.g., 0.230 in x 3.147 in (W x L)). Place it 0.921 in from the top, 1.165 in from the left, and 1.165 in from the right edges of the top plate.

1.2.3. Draw a second through-hole (the "Inlet-hole") sized 0.075 in x 3.146 in (W x L). Place it 0.236 in from the bottom edge, 1.737 in from the top edge, and 1.162 in from the left and right edges of the top plate.

1.2.4. Cut the top plate from a piece of clear acrylic with a laser cutter. Wipe off any remaining dust or debris.

1.3. Fabricate the inlet cover (Figure 2.1B)

1.3.1 Draw a rectangular area with dimensions 0.247 in x 3.3378 in (W x L) in a CAD software using the polyline tool. Add two circular through-holes with a diameter of 0.127 in approximately 0.073 in from the two edges of the inlet cover, one on either side.

1.3.2 Cut the inlet cover from a piece of clear acrylic with a laser cutter.

1.4. Fabricate the slide (Figure 2.1C)

1.4.1. Draw a rectangular area in CAD software that measures measure 2.771 in x 0.0625 in x 5.000 in (W x H x L) using the polyline tool.

1.4.2. Add through-holes that match the position of each test pad in the test area. Draw the first 0.105 in square through-hole to overlap with the placement of the first test pad: 1.096 in from the left and right edges of the slide, 0.960 in from the top edge, and 1.681 in from the bottom edge. Add more through-holes as needed (usually 10 total) for the selected dipstick brand of choice. Space each next through-hole by measuring the distance between test pads on the dipstick.

NOTE: The size of the through-holes is important in order to deposit the correct volume of liquid onto the dipstick pad. For our brand of dipstick, we created holes which deposit 15 µl onto each dipstick pad.

1.4.3. Cut the slide from a piece of clear acrylic using a laser cutter. Wipe off any remaining dust or debris.

1.4.4. Spray the front of the slide with a hydrophobic spray. Apply several coats (6-8) of basecoat to the slide. Hold the can approximately 8 -12 in away from the slide when spraying.

1.4.5. Wait 30 minutes before applying the topcoat several times (8-12). Allow the slide to dry for 12 hours before use.

1.4.6. Download a QR code from an online QR code generator and print your desired code on paper with sticky adhesive backing. Place the QR code 0.17 in from the right of the first through-hole along the same row as all the through-holes.

NOTE: As long as the QR code is adjacent to the through-holes, accurate placement is not important.

1.4.7. Use clear scotch tape to cover the QR code and secure it to the slide.

1.5. Assemble the inlet and plate sleeve (Figure 2.1D)

1.5.1. Fabricate the inlet by using acrylic cement to glue the inlet cover onto the top plate where the inlet-hole is located. Wait 24-48 hours to securely bond the pieces.

1.5.2. Spray the back of the top plate with a hydrophobic spray once the inlet cover is securely bonded to the top plate. Place the top plate upside down. Apply the first basecoat several times (4-8).

1.5.3. Hold the spray 8-12 inches away from the top plate and wait 30 minutes for it to dry. Apply the topcoat several times (6-8). Allow the top plate to dry for 12 hours before use.

1.5.4. Assemble the plate sleeve (combined top plate and base plate) by gluing the completed top plate to the ledges of the base plate with acrylic cement. The two pieces are easy to align by visual inspection, as the bottom edge of the top plate will align with that of the base plate. Apply a clamp to the base plate ledges to secure it during drying and wait 24-48 hours before use, as per the manufacturer's instructions.

1.6. Create the chart sticker

1.6.1. Download the color chart for your brand of dipstick from the manufacturer's website.

1.6.2. Open the downloaded file in a graphics editor software.

1.6.3. Open the digital file for the top plate template previously used for the laser cutter (Step 1.2 of this protocol) in a graphics editor software.

1.6.4. Create the color boxes for the chart sticker by matching color boxes from the manufacturer color chart. Select the first block of color on the manufacturer's chart with the dropper tool in the graphics editor software and then use the box shape tool to make a box shape in the same color on the top plate template, in the same row where the dipstick pad will be located. Repeat this for each color block corresponding to each pad row.

1.6.5. Delete the layers associated with the top plate template.

1.6.6. Print the chart sticker as a vinyl sticker with an online sticker print service. Place the chart sticker onto the plate sleeve and align it with each through-hole.

1.7. Fabricate the box (Figure 2.1E)

1.7.1. Draw the two long-sided box pieces (parts “a” and “b”) in the CAD software as rectangles with dimensions of 4.92 in x 6.63 in (W x L). Add a cut-out to part “a” centered on the bottom edge measuring 0.2 in x 6.11 in (W x L).

1.7.2. Draw the two narrow-sided box pieces (parts “d” and “e”) in the CAD software as rectangles with dimensions measuring 1.805 in x 6.63 in (W x L).

1.7.3. Draw the box top (part “c”) as a rectangle with dimensions 1.805 in x 6.63 (W x L). Draw the “imaging through-hole” on the top: 0.74 in x 0.910 in (W x L), positioned 3.17 in from the bottom, 2.53 in from the top, 0.65 in from the right edge, and 0.42 in from the left edge.

NOTE: The exact position of the imaging through-hole should be selected on the basis of the cell phones that will be used for the analysis.

1.7.4. Draw each box piece to feature a pattern of interlocking edges that will allow all the box sides to snap together on each edge as described in Figure 1D. To make an interlock edge pattern, alternate an extrusion/intrusion pattern on the long edge with 0.135 in by 1.17 in (W x L) protrusions. Draw two extrusions on each long edge for every side of the box. Use the same extrusion/intrusion pattern for the short edge, but with intrusions measuring 0.135 in by 0.460 in (W x L).

1.7.5. Cut the five pieces with a laser cutter or print them with a 3D printer.

NOTE: A laser-cut component using acrylic pieces will be cheap to manufacture and can be flattened for easy shipping. Use black acrylic as it is helpful to absorb scattered light during testing.

1.7.6. Add black color construction paper to the box interior to prevent scatter from the flash during image analysis if the box material has a gloss finish.

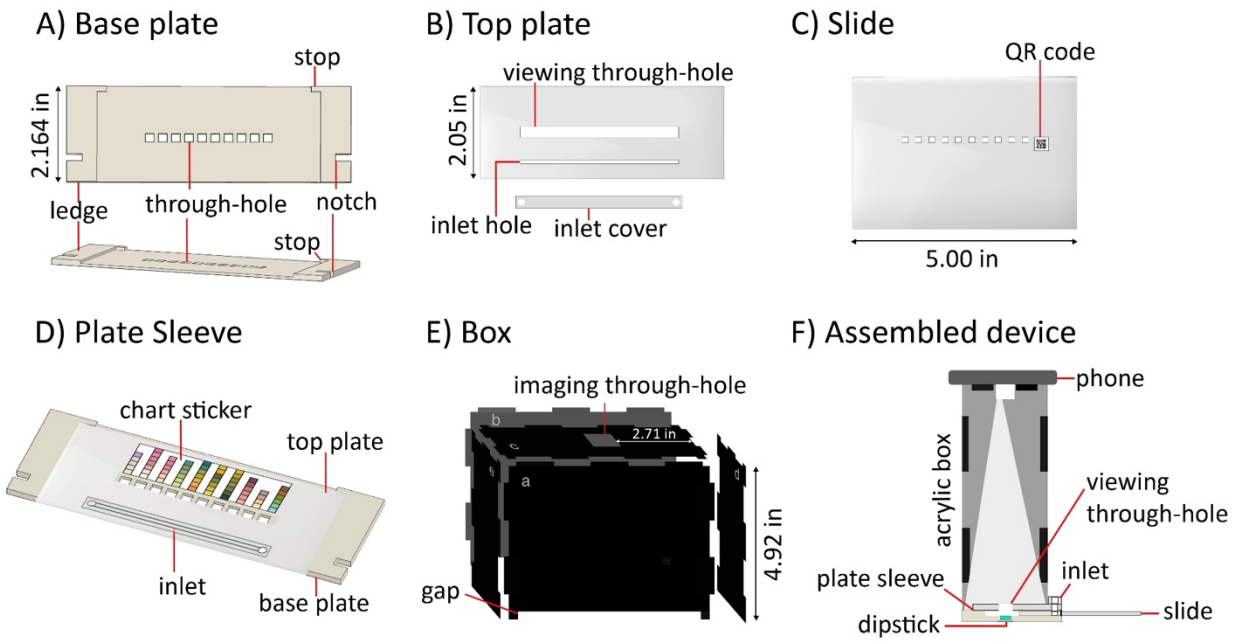

Figure 2.1. Schematic drawings of device components. A) Base plate. B) Top plate and inlet cover, which are glued together in Step 1.5.1. C) Slide and associated QR code used for timing control. D) Plate sleeve, formed by gluing the top plate to the ledges of the base plate in Step 1.5.4. The chart sticker next to the viewing through-hole enables color analysis. E) Box. F) Assembled device. During use, a mobile phone is placed on the top of the box such that its lens and flashlight are positioned above the imaging through-hole.

2. Prepare the test

2.1. Download the UrineTest mobile application from GitHub (https://github.com/Iftak/UrineTestApp).

2.2. Install the app onto a mobile phone.

NOTE: This step only has to be done once for all future uses of a given phone. You may need to enable developer status on the phone to do this.

2.3. Insert the dipstick into the through-holes underneath the plate sleeve.

2.4. Place the plate sleeve inside the box so that its notch is aligned with the box gap.

2.5. Place the slide inside the plate sleeve so that the through-holes align with the inlet.

2.6. Place the phone on the top of the box with the back-camera lens facing the viewing through-hole

to enable imaging. Ensure the camera visibility is not occluded by checking for the image on the phone screen prior to testing. The app will enable the flashlight on the phone automatically.

2.7. Launch the UrineTest application in the phone. (**Figure 2.2A**)

2.8. Change the analyte names and reading timings to match those for the dipstick of interest (based on the manufacturer's specifications) via the pop-up window on the screen. (**Figure 2.2C**)

NOTE: The necessary readout time for each dipstick pad will depend on the brand of the dipstick used.

2.9. Align the phone so that the dipstick coincides with the boundaries of the black rectangular overlay on screen. (**Figure 2.2F**)

2.10. Click the "Start" button on the app window to begin the test.

2.11. **NOTE:** This will open the phone camera to read the QR code once in view.

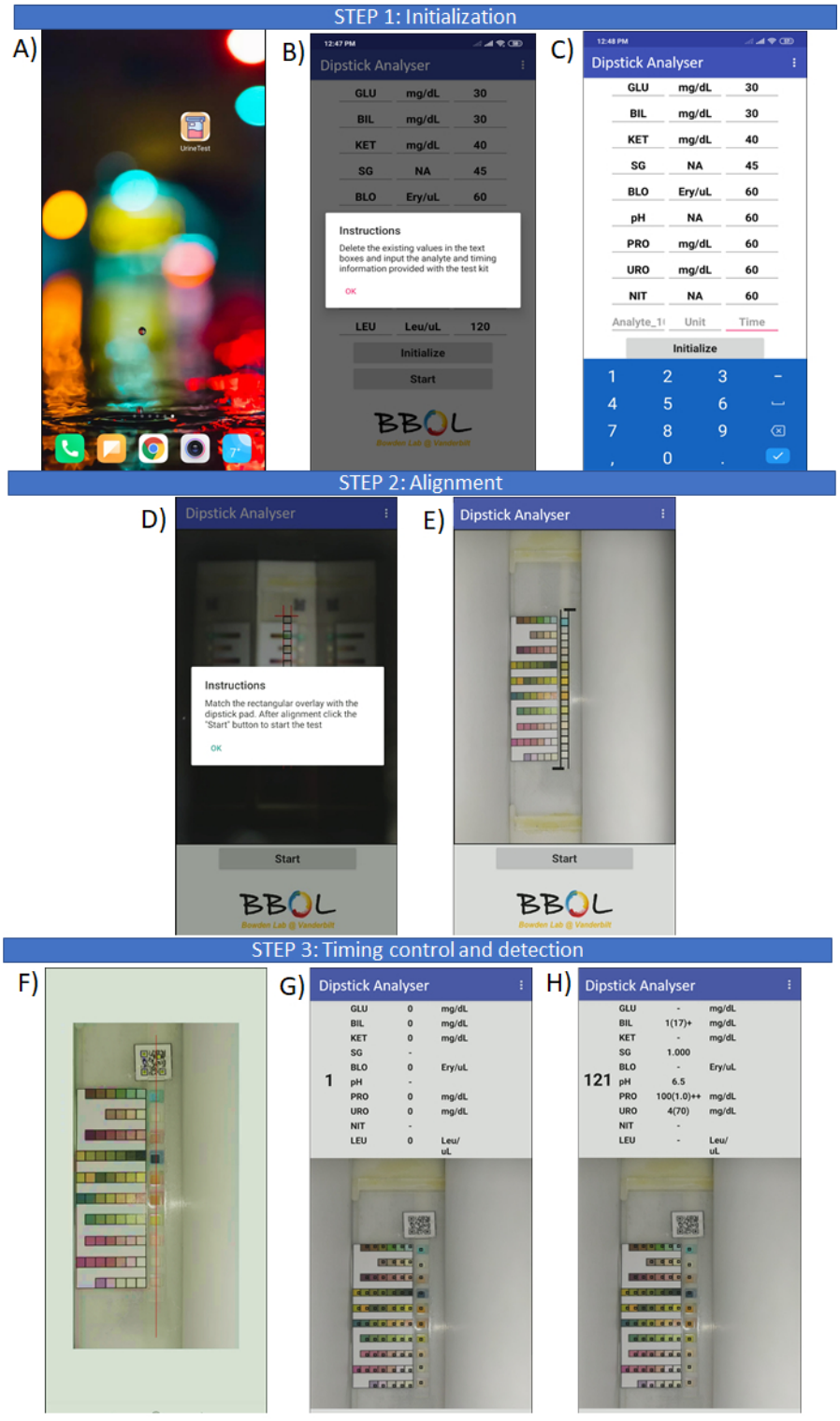

Figure 2.2. The process of the colorimetric analysis using the app. A) The icon on the phone screen "Urine test" is selected to launch the application. B) A pop-up window informs the user to modify the readout times. C) The user manually enters the analyte name and readout

times. D) A pop-up window to inform the user for phone alignment. E) Representative image of a properly aligned dipstick before testing. F) Screenshot after the slide is inserted and the QR code appears to initiate data acquisition. G) The screen one second after starting the test. The black square overlays show the user the exact location from where the app is collecting pixel information. H) The results of the completed dipstick test. Test results with dashes are considered normal for the chosen dipstick.

3. Conduct the test

3.1. Deposit urine into the inlet hole with a disposable polyethylene transfer pipet containing approximately 0.5 ml of urine. (**Figure 2.3**)

3.2. **NOTE:** The exact amount of liquid is not important, but it should be at least 0.5 mL to ensure that all the through-holes receive sufficient urine. Upon adding the liquid, you should be able to observe that it moves across inlet and is deposited in each through-hole of the slide.

3.3. Initiate the test by pushing the slide into the plate sleeve until it is stopped by the base plate stop. **NOTE**: Urine should make contact with dipstick pad when the QR code is in the field of view of the cell phone. (**Figure 2.2G**) After reading the QR code, the application will open a window to analyze the color changes and show the results automatically within the same window. (**Figure 2.2I**)

3.4. Discard the urine appropriately and clean the plate sleeve and slide with 10% bleach solution and rinse again with de-ionized water. Allow it to dry before additional use.

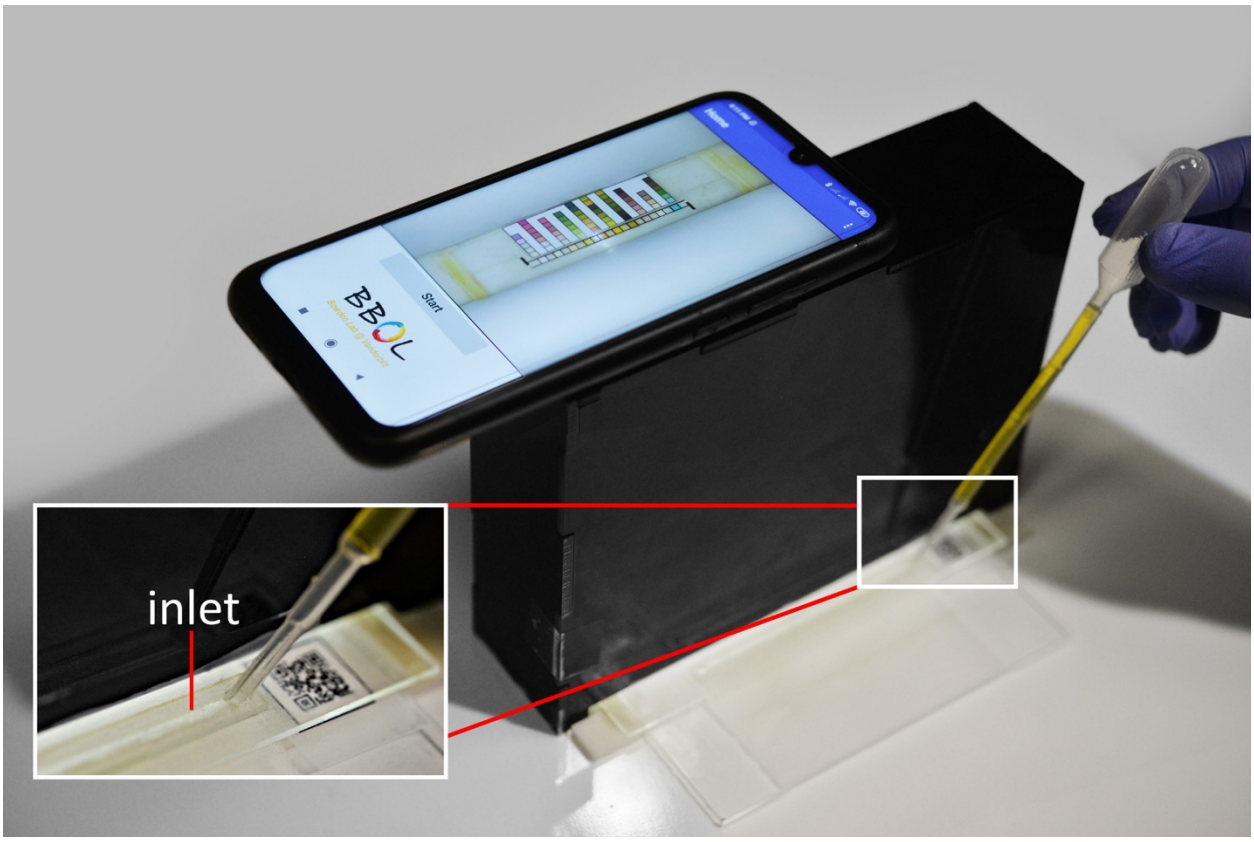

Figure 2.3. Photograph of the assembled device in action at the start of a urinalysis test

2.3 Representative Results

Figure 2.4 demonstrates how the urine is transferred to the dipstick during a urinalysis test. During a typical test, the transfer of urine is not observable because the box occludes the view. Once the sample is deposited in the inlet using a pipette (Step 3.1), it will fill the holes on the slide (**Figure 2.4A**). **Figure 2.4B** and **Figure 2.4C**, respectively, show the progressive movement of the urine across the plate sleeve and after the slide makes contact with the stop. Note that contact of the urine with the dipstick leads to a colorimetric reaction and color change on the dipstick pads.

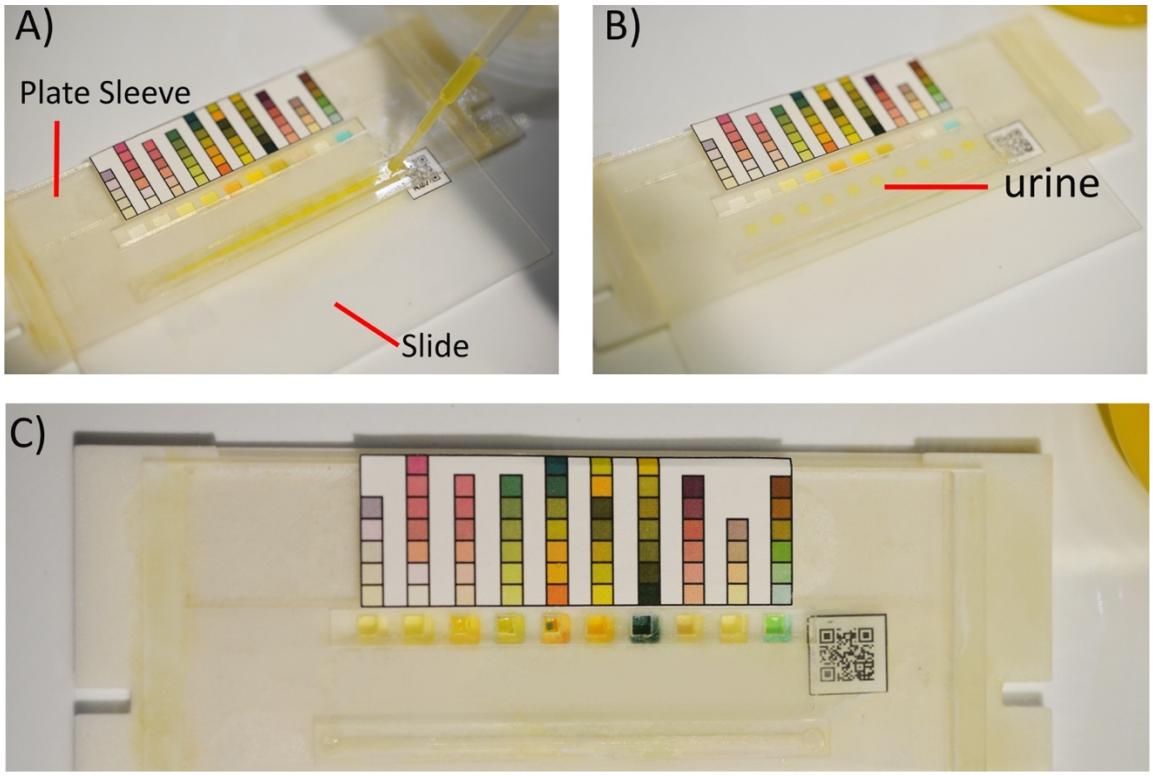

Figure 2.4. Internal process of liquid deposition onto the dipstick test from start to finish. A) Inserting the slide into the plate sleeve and aligning the slide through-holes with the inlet will allow the transfer pipette to deliver the urine into each through-hole of the slide. B) Slipping the slide through the interior of the hydrophobic coated plate sleeve enables liquid transport. C) When the slide reaches the stop in the baseplate, urine is delivered to the test pads, resulting in colorimetric changes.

Figure 2.5 demonstrates a potential problem that can arise if the surfaces for transferring the urine (i.e., base pate, top plate and slide) are not sufficiently coated with hydrophobic spray. An illustration of a well and poorly coated slide is shown in **Figure 2.5A**. If poorly coated, one may observe streaks (shown by white arrows in **Figure 2.5B**) during the sliding step that decrease the accuracy of the volume transferred. In addition, one may observe failure of the slide to transfer the urine to the dipstick (**Figure 2.5C**), and urine may remain in the through-holes even when the slide is removed from the device. These steps highlight the importance of obtaining good spray coverage (Steps 1.1.8, 1.4.4, 1.5.3, and 1.5.4). If there are concerns about the spray coverage or if you observe these performance errors, it is best to remake the base

plate, top plate, and slide.

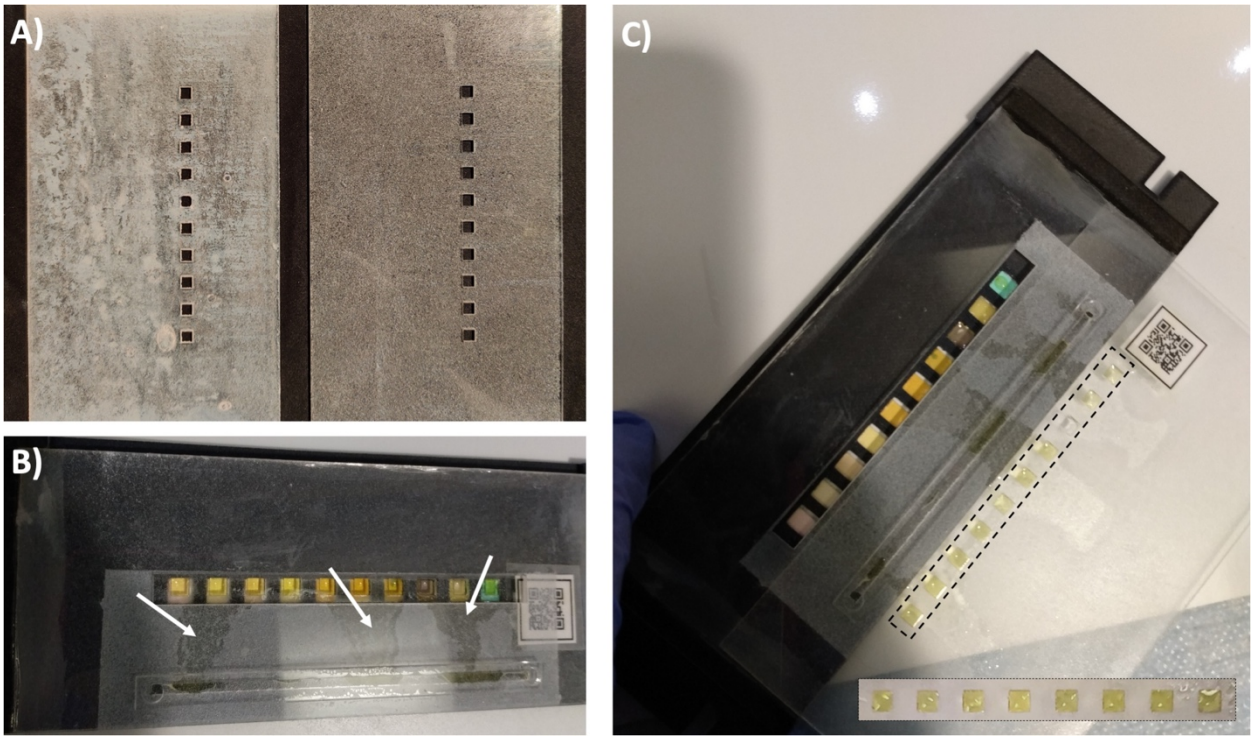

Figure 2.5. Potential problems associated with insufficient hydrophobicity. A) A slide with and without sufficient coating. B) Insufficiently coated slide shows leaking during the sliding step. C) An insufficiently coated slide does not transfer onto the dipstick pads even after being pulled back out of the device: the liquid remains in the slide through-holes, as seen in the inset on the bottom right.

A urinalysis test was performed with a high-quality smartphone: phone 1 (image resolution: 8000-pixels x 6000- pixels). Representative results are shown in **Figure 2.6**. We conducted tests with de-ionized water and commercial urine (both standard composition and with high glucose). The color pads on the dipstick change in time in response to the colorimetric reaction of the urine with the analytes in the dipstick. The error bars in **Figure 2.6** represents the standard deviation yielded for three consecutive measurements of each sample recorded by the two smartphones. **Figure 2.6A** plots the response for the glucose pad over time for the different test conditions. For the brand of dipstick used, the recommended readout time for the glucose measurement is 30 seconds. As expected, the color of the dipstick does not change over this interval for water, the final value for the standard urine matches with the "normal" urinary glucose threshold level

(160-180 mg/dL), and the final value for the “high glucose” condition is elevated above the normal value. Importantly, note that the correct value is not attained until 30 seconds, which illustrates the importance of setting the timing readout interval correctly in Step 2.8. The same experiment was performed with another smartphone having a lower image resolution: phone 2 (image resolution: 3264- pixels x 2448-pixels). Due to the difference in camera resolution, a significant difference from the previous results is observed in the image color and quality while capturing images of the dipstick panel, as shown in **Figure 2.6B**. The differences in flashlight specifications also contribute to the differences in image quality. From **Figure 2.6**, it can be seen that both phones yield similar trends in the change of color over time, though the actual colors detected are different. The color matching algorithm used by the smartphone application for the urinalysis test yields the same results for the analyte concentrations, despite differences in the physical appearance of the colors of the dipstick pads. The consistency of the results is due to the use of the chart sticker as a reference chart for the analysis. Since both the chart sticker and the dipstick are captured under the same lighting conditions and image quality, the smartphone application evaluates the (R,G,B) components and the color difference of both the reference square and dipstick pad in a similar fashion for both smartphones. These results confirm that the protocol described in this manuscript is independent of the smartphone model, as long as both the reference color chart and the dipstick are imaged under the same environment.

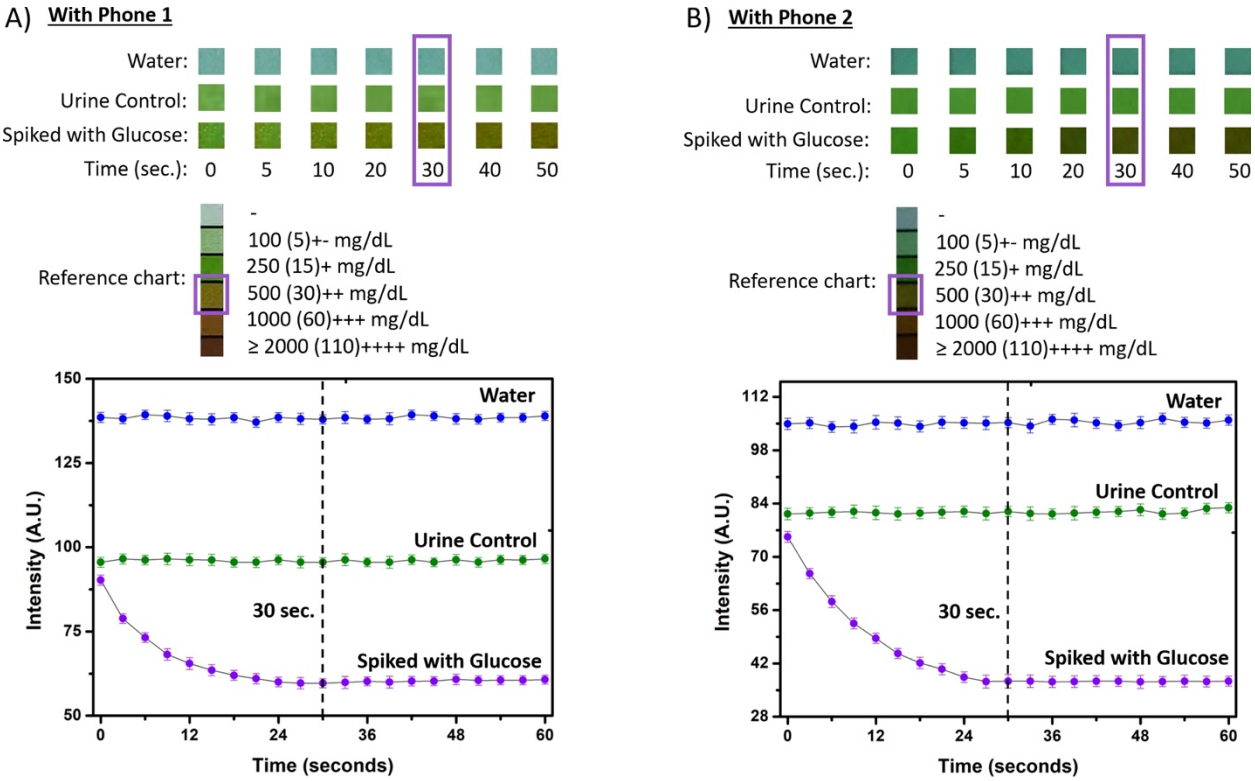

Figure 2.6. Urinalysis result for the glucose pad with two different smartphones for three types of samples. A) Response characteristics of the glucose pad over time for the different test conditions recorded with a high-camera-resolution camera phone (phone1). B) Response characteristics of the glucose pad over time for the different test conditions recorded with a low-resolution camera phone (phone 2). The readout at 30 seconds corresponds with the desired timing for the manufacturer.

We have previously evaluated the accuracy of the automated urinalysis device by comparing with traditional dip-and-wipe methods using a commercial urine standard[247]. Table 1 compares the results obtained with the two tests. The accuracy of the system depends on the volume transferred to each dipstick pad. The most accurate results were obtained when the automated urinalysis device was designed to transfer 15 µL of urine; therefore, it is crucial that the device transfer the required urine volume accurately and consistently to the dipstick pads. Representative results to validate the consistency of the device by transferring 15 µL volume of urine samples over seven different trials are shown in **Figure 2.7**. The overall standard deviation was found to be below 0.5 µL, which is within 4% range of the target value. The results confirm that the device can accurately and consistently transfer microliters of urine to perform the test.

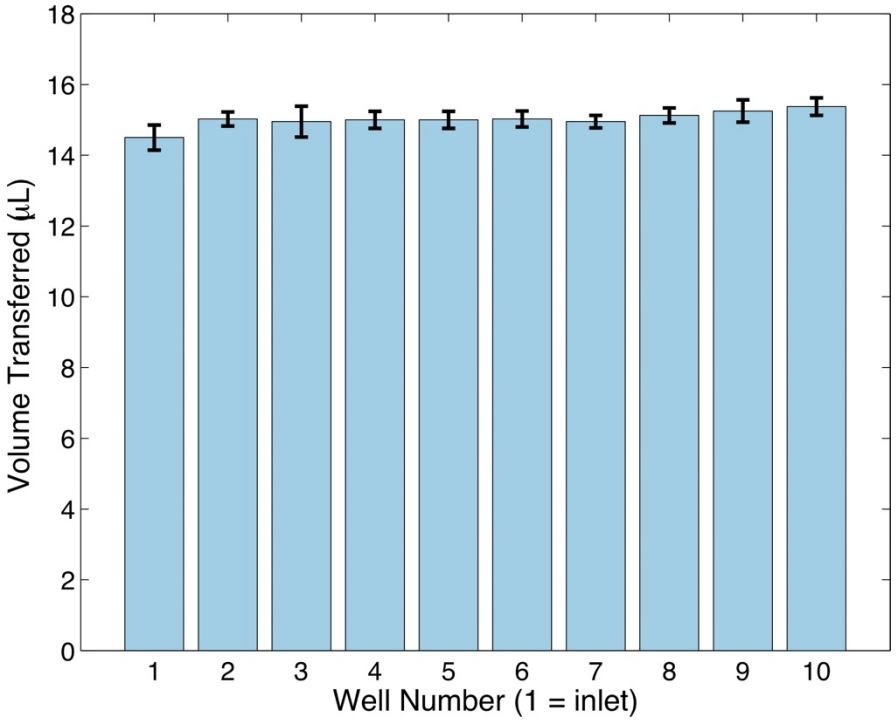

Figure 2.7. Well number vs average volume transferred. Each well corresponds to a through-hole for a given test pad; the first well is closest to the inlet. This figure has been modified from Smith, et al[1]. and reproduced with permission from the Royal Society of Chemistry.

	Analyte									Differences from dip-and-wipe
	LEU	NIT	URO	PRO	pH	BLO	SG	KET	GLU	
Dip-and-wipe	4 ± 0	2 ± 0	4 ± 0.53	2 ± 0.53	4 ± 0	5 ± 0	3 ± 0.53	4 ± 0.49	3 ± 0.58	n/a
5 µL	3*± 0	2 ± 0	3* ± 0	3* ± 0.49	3* ± 0	3* ± 0	2* ± 0.53	4 ± 0.38	1* ± 0	7
10 µL	3* ± 0.38	2 ± 0	4 ± 0	2 ± 0	3* ± 0.38	4* ± 0	1* ± 0.49	4 ± 0.49	2 ± 0.58	5
15 µL	4 ± 0	2 ± 0	4 ± 0.49	2 ± 0	4 ± 0.38	5 ± 0	2* ± 0.38	4 ± 0.49	3 ± 0.49	1
20 µL	4 ± 0	2 ± 0	4 ± 0.82	2 ± 0.53	4 ± 0.53	5 ± 0	2* ± 0.49	4 ± 0.49	3 ± 0	1

Table 2.1. Median values and standard deviations for analytes using various deposited volumes. The symbol ‡ indicates median values that differ from the median obtained with the dip-and-wipe method, the industry standard. The total number of analyte pads whose medians differ from the dip-and-wipe method are reported in the far right column. Note results are cumulative for all dipsticks used. LEU: leukocytes, NIT: nitrite, URO: urobilinogen, PRO: protein, BLO: blood, SG: specific gravity, KET: ketones, GLU: glucose. This table has been modified from Smith, et al.[1] and reproduced with permission from the Royal Society of Chemistry.

2.4 Discussion

Traditional dipstick urinalysis is affordable and convenient but requires manual attention to detail to yield accurate results. Manual dipstick urinalysis is subject to variable lighting conditions, individual color perception differences and cross-contamination. Many clinics and hospitals already have instruments to automate urine dipstick analysis, but the instruments are usually bulky, expensive, and still rely on proper performance of the dip-wipe method. Additionally, these instruments require yearly calibration and maintenance for accurate results.

The protocol automates and controls several important steps involved with dipstick urinalysis (e.g., distribution of liquid to the test pads, the timing of the start, control over the lighting and quantitative comparison with the reference standard), which is necessary to obtain reliable results. To this end, critical steps in the protocol relate to the design of the device include steps 1.4.3, 1.1.4, 1.4.7 and 1.1.5, which

match the size of the through-holes to the desired volume, ensure proper placement of the stops to align the through-holes with the dipstick, ensure proper placement of the QR code used as the timing indicator and ensure that the test is not influenced by ambient light, respectively. In addition, the transfer of urine through the slide and subsequent deposition onto the dipstick are highly dependent on the surface characteristics of the materials being used. Hence, if non-hydrophobic surfaces are used for the base plate, the top plate and the slide, it is important to apply an adequate amount of hydrophobic spray. It is especially critical to ensure that the inner surfaces of the through-holes of the slide have been sprayed so that the liquid will drop to the dipstick pad after slipping.

The protocol can be easily modified to use with other brands of dipsticks by changing the dimensions and spacing of the through-holes. The volume applied to the dipstick can also be modified by changing the thickness of the acrylic used to fabricate the slide (with commensurate changes in the thickness of the ledges of the base plate) or the size of the through-holes. The accompanying software app allows the user to modify the names and readout timings to align with those for the brand of dipstick used.

The current device combines a 3D-printed base plate and laser-cut top plate to form a plate sleeve. Both fabrication methods are affordable, and the material choices can be modified. Excluding the phone and dipstick, the acrylic used in the current device costs approximately $0.85, and material used in the 3D-printed base plate costs around $1.50 per device. Although the base plate we used is 3D-printed from acrylonitrile butadiene styrene (ABS), other polymers that form a hard and rigid surface are also suitable. For example, a version of the device can be made using a plate sleeve completely fabricated from acrylic[1]. Elastomeric materials such as polydimethylsilioxane (PDMS) are not desirable because their lower rigidity is less compatible with sliding a glass surface to enable the slipping action that is critical to the volume-control design.

One important limitation of the current protocol is that the hydrophobic coating applied to the slide and plate sleeve may peel with frequent use, limiting the stability of the device over time. After 3-4 test runs, the hydrophobic coatings often peel and alter the volume transferred, potentially reducing the accuracy in results. Future method modifications can include the use of more durable hydrophobic coating or

materials that are naturally hydrophobic. Additionally, the acrylic bonding may weaken during repeated testing as well. The low cost of the device, however, allows multiple prints to be made and reglued together as needed. Thus, the slide may be considered as a reusable part.

Another limitation is the inability to saturate the glucose pad with urine due to the hydrophobic nature of the pad. As such, it only partially absorbs liquid with the automated device. We did not find that this reduced the accuracy of the result, but it does require careful execution of Step 2.9 to ensure the camera viewing area captures data from the middle, not the edges of the glucose test pad. Future work may address this issue by incorporating a different brand of dipstick that does not feature hydrophobicity on any dipstick reagent pads on the test.

2.5 Conclusion

By controlling the major steps contributing to user error, this method allows for increased accuracy in results performed by non-trained individuals and is suitable for home testing. Unlike other urinalysis apps available[235,236,237] the system is modifiable to any brand of dipstick test. The device is reusable and requires no power to use outside of power consumed by the smartphone. In the future, we envision that the protocol could be amenable to patient self-testing. By ensuring the accuracy in dipstick test results, patients may monitor their own urine more frequently without the barriers associated with standard clinical urinalysis practice.

CHAPTER 3: RECURRENCE MONITORING FOR OVARIAN CANCER USING A CELL PHONE-INTEGRATED PAPER DEVICE TO MEASURE THE OVARIAN CANCER BIOMARKER HE4/CRE RATIO IN URINE

Adapted from: Kight, E.C., Hussain, I., Bowden, A.K. *et al.* Recurrence monitoring for ovarian cancer using a cell phone-integrated paper device to measure the ovarian cancer biomarker HE4/CRE ratio in urine. *Sci Rep* **11**, 21945 (2021). https://doi.org/10.1038/s41598-021-01544-4.[249]

Abstract

Ovarian cancer has a poor cure rate and rates of relapse are high. Current recurrence detection is limited by non-specific methods such as blood testing and ultrasound. Based on reports that human epididymis four (HE4) / creatinine (CRE) ratios found in urine are elevated in ovarian cancers, we have developed a paper-based device that combines lateral flow technology and cell phone analysis to quantitatively measure HE4/CRE. Surrogate samples were used to test the performance over clinically expected HE4/CRE ratios. For HE4/CRE ratios of 2 to 47, the percent error was found to be 16.0% on average whether measured by a flatbed scanner or cell phone. There was not a significant difference between the results from the cell phone or scanner. Based on published studies, error in this method was less than the difference required to detect recurrence. This promising new tool, with further development, could be used at home or in low-resource settings to provide timely detection of ovarian cancer recurrence.

3.1 Introduction

Despite treatment, up to 70% of patients with ovarian cancer (OC) will develop recurrence of disease [250], and patients faced with a high relapse rate are concerned about recurrence. Even though OC patients undergo long-term surveillance to improve recurrence detection, current diagnostic methods, such as pelvic examination, transvaginal ultrasonography, and blood tests such as cancer antigen 125 (CA-125),

are invasive and require a clinic visit. Factors such as making an appointment to have blood work done, traveling to the location, a lack of confidence in their symptoms (cramping, bloating, frequent urination), being too busy, not wanting to bother a doctor and the lack of frequency of testing were highlighted concerns of OC patients [94, 251]. Currently, there is no at-home monitoring test for ovarian cancer recurrence that can address many of these factors. As many cancer patients eventually relapse, there is a great need to develop at-home detection methods to monitor molecular biomarker levels indicative of recurrence and reduce mortality [252].

Human epididymis protein 4 (HE4) is a glycoprotein that is highly expressed by ovarian carcinomas[79]. HE4 in serum is overexpressed in ovarian carcinomas and is detected with high sensitivity and specificity[80]. Recent studies have shown that HE4 in serum offers more forecasting power for OC recurrence than CA-125, a biomarker of many cancers[87]. In 2009, FDA approved using serum HE4 levels to monitor ovarian cancer recurrence (OCR) risk, but this method also requires travel to clinic, phlebotomy, and it is expensive[102, 103]. Due to the ease of collection of urine, HE4 in urine has emerged as a promising target in ovarian cancer recurrence monitoring at-home. Urine HE4 has been found to be a biomarker for ovarian neoplasms with improved sensitivity in early disease compared to HE4 in serum[104]; additionally, HE4 is detectable in urine earlier than in serum [105].

Unlike serum HE4, urine HE4 fluctuates with volume, and creatinine (CRE) is commonly used as an internal standard to normalize the ratio of urinary biomarkers[106] and HE4 in particular [107,108]. The ratio of HE4/CRE has been found to be a better predictor of early and late stage ovarian cancer than urine HE4 alone with highly predictive cut-off range of 3.5[105]. Hellstrom et al reported higher concentrations of HE4/CRE ratios in ovarian cancer patient urine ranging from -0.5 to 2.5 for log10 values of HE4/CRE[104]. HE4/CRE can range from 2 in healthy patient samples with to nearly 45 (although most are less) in late stage ovarian cancer[104]. Importantly, Liao et al. reported that urine HE4 may also be more useful than serum HE4 in differentiating low malignant potential cysts from early ovarian cancer[109].

Due to their ease of use, low cost, and robust manufacturing, paper-based tests, such as lateral flow assays (LFAs), are attractive tests for both at-home testing and low-resource testing. Lateral flow assays

rely on a colorimetric reaction that can be read by the human eye as a simple yes/no result[253, 254]. In these yes/no applications, improving the limits of detection is the major challenge. However, both HE4 and creatinine are present in large quantities and are easily detectable in urine, so a lower threshold is not a concern. In addition to qualitative uses, LFAs have also been used for quantitative detection of various proteins or nucleic acids[255]. The challenge in a paper-based test for HE4/CRE is accurate quantification of HE4 and creatinine values in the clinically relevant ranges. For quantification of LFAs, an optical instrument is required for capturing and measurement of the output. Owing to their portability, low-cost, and widespread use, cell phones are well-studied instruments to quantitate LFAs for home-testing and low-resource setting testing[256, 257, 258].

In this report, we describe the development of an at-home paper-based device to measure both HE4 and creatinine in one device. Based on previous reports, we used surrogate samples containing HE4/CRE tested from 2 to 47 which are within the range of human samples reported by Hellstrom, with particular interest in the initial rising of values of HE4/CRE observed in recurrence. With further validation, this would require only the use of a single diluted urine sample to both test strips for analysis at the same time. The approach is based on standard LFA technology and incorporates a creatinine measurement in a low-cost assay format that can be imaged and quantified using a flatbed scanner as well as a cell phone app.

3.2 Methods

Ethics statement

No human or animal materials were used in this study.

Reagents

Monoclonal mouse anti-human epididymis protein 4 (HE4) was purchased from HyTest (Turku, Finland). The reporter reagent used in the LFA was BioReady150 nm gold nanoshells by nanoComposix Inc (San Diego, California). Ethyl-N;-(3-dimethylaminopropyl) carbodiimine hydrochloride (EDC) and Sulfo-NHS chemistry was used (sigma Cat# E1769-1G, Thermo, Prod# 24510) to covalently bind the antibody to the

nanoshell. Hydroxylamine (Sigma, cat# 467804) was used to quench remaining amine groups during the covalent conjugation protocol.

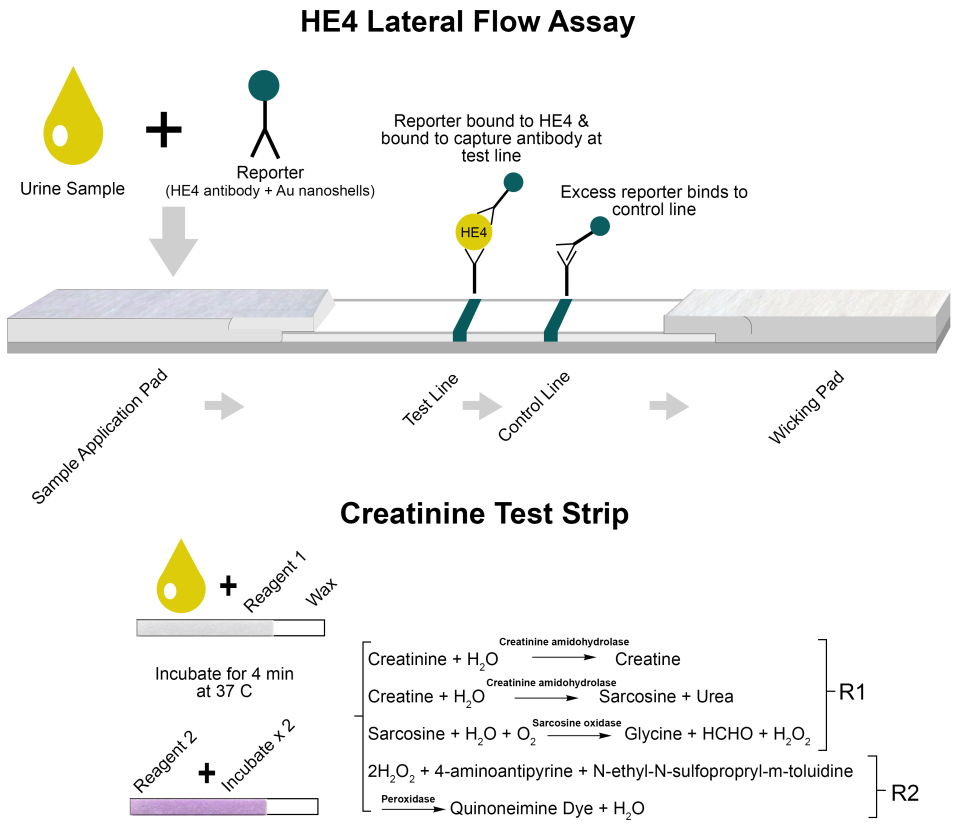

Figure 3.1. Schematic of the two paper test strips and components. For the HE4 test strip (top), the sandwich assay captures the biomarker in the middle at the test line. The control line is generated when excess reporter binds. For the creatinine test strip, a two-reagent system is used to generate a colorimetric reaction with creatinine from light to dark purple. The intensity of the purple color (bottom) indicates the amount of creatinine. The two strips are placed in a scanner or cassette for the cell phone to be analyzed.

HE4 antigen standards were provided by Fujirebio Diagnostics Inc. (Malvern, PA). For the enzymatic creatinine reaction, we purchased a Creatinine LiquiColor kit from Stanbio (Boerne, TX). The creatinine test paper used was Whatman no. 3, purchased from Cytiva (Marlborough, MA). The dipping soy wax was purchased from Hearts & Crafts (Brooklyn, NY). Parafilm tape was purchased from Hach

(Loveland, CO). Anhydrous creatinine was purchased from Thermo (Prod # C4225, lot# SLCF5841). All solutions were prepared with deionized water unless otherwise noted.

Lateral flow materials and design.

To create the lateral flow assay standards for HE4, we used lyophilized standards in the Fujirebio ELISA kit, which contained HE4 antigen in a phosphate buffered salt solution with bovine serum albumin, an inert yellow dye, and a non-azide antimicrobial preservative. To reconstitute, 1.0 mL of deionized water was added to each standard vial. The vial was vortexed and then allowed to stand at room temperature for 15 minutes. Prior to use, the vial contents were gently mixed by pipette. Standard dilutions were created from the standards for the simulated patient samples with creatinine solutions or deionized water. Vials were stored at 4° C before and after use as recommended by the manufacturer.

Both HE4 and creatinine were measured using paper-based methods (**Figure 3.1**). For HE4, we used standard LFA methods to spot reagents and assemble the test strips. An automatic antibody dispenser (IsoFlow from Imagene Technology Inc) was used to deposit HE4 sheep-derived polyclonal antibody (R&D Systems, Cat# AF6274) across the membrane as the capture antibody at the test line. To make the control line, the antibody dispenser deposited a goat anti-mouse antibody (Lampire, cat# 7455507, Lot# 17H40070) across the membrane. The mouse antibody was chosen for the control line so that the excess mouse antibody would bind to it. The striped membrane was dried for one hour in an oven at 37° C. Next, the striped membrane was placed onto an adhesive backing card. A sample pad was added to the right edge of the membrane and the wicking pad was added to the left edge, overlapping the membrane by 1 mm to allow for capillary action along the test strip. The assembled card was cut into individual test strips 3.9-mm wide by 70-mm long with an automated guillotine (Matrix 1201 Membrane cutter, Kinematic, Twain hart, CA). The strips were stored at room temperature in sealed pouches with desiccants until use.

Next, we optimized the selection of the reporter antibody and nitrocellulose membranes. To identify the best reporter, we screened three monoclonal HE4 reporter antibodies (R&D systems, LSBio, and Hytest). To test the binding and non-specific binding of each antibody we conducted a dot blot test. We spotted 1 µl spot of polyclonal antibody on the membranes and dried the membrane for 1 hour in an oven

at 37 ° C. We then mixed 1 µl of antigen with each of the reporters and spotted the solution onto the sample pad for the positive control test. For the negative control test, we spotted the reporter without antigen. Non-specific binding occurred when a colored spot was generated without antigen present. Unbound reporters were washed away by the addition of a running buffer to the sample pad. Since the Hytest antibody showed strong signal intensity in antigen binding in the positive control tests and the least non-specific binding in the negative control tests, it was chosen for further testing.

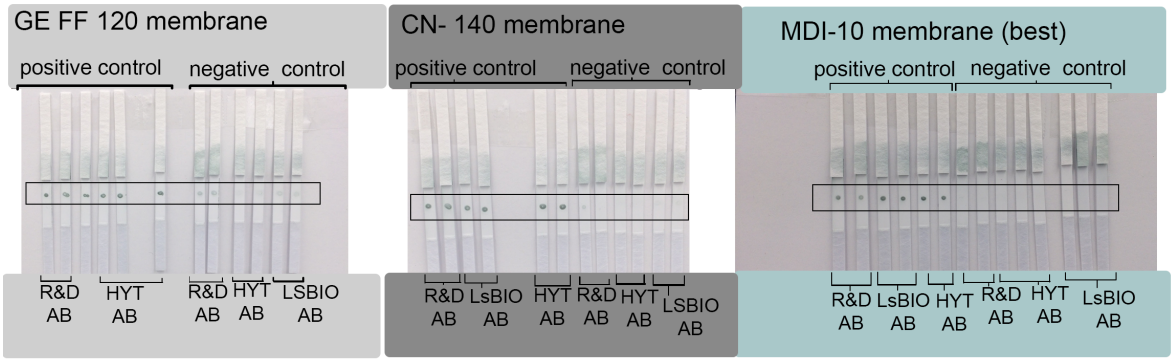

Figure 3.2. Dot blot test was conducted with three different antibody and three different membranes. For the three antibodies tested, the membrane MDI-10 showed the least non-specific binding for the negative control spots and strong signal for the positive spots.

We screened three different nitrocellulose membranes (**Figure 3.2**) and subsequently chose MDI CNPC (10 µm) membranes (MDI membrane technologies) since they exhibited the least non-specific binding in the dot blot test, and the antigen signal intensity was higher in the positive control tests. To run the LFA HE4 test, we used 20 µl of nanoshell+HE4 antibody incubated with 25 µl of sample for 10 minutes on a rotator prior to pipetting it onto the sample pad of the lateral flow test strip. After deposition onto the sample pad, the lateral flow test was left at room temperature before measurement on a flatbed scanner or cell phone.

Creatinine test design.

For the design and fabrication of the creatinine test, we used an enzymatic creatinine kit that comprises a two-reagent system that is typically found in automated analysis equipment [228]. Since chemicals can interfere with creatinine determination using the Jaffe reaction[259], we chose to use enzymatic reagents to measure creatinine. Enzymatic reaction has been chosen over the picrate reaction for the determination of creatinine in clinical labs as the results of enzymatic methods have been reported to match the gold standard method more closely, isotope-dilution-mass spectrometry (IDMS)[228,260,261]. In the first reaction mixture, reagent 1 (R1), the creatinine amidohydrolase, converts creatine to sarcosine, and the oxidation of sarcosine by sarcosine oxidase produces hydrogen peroxide. The hydrogen peroxide generated in R1 is then reacted with reagent 2 (R2) in the presence of peroxidase to react with Quinoneimine dye as shown in **Figure 3.1**. This reaction results in a light to dark purple dye in which the dark purple corresponds to high creatinine concentration in the sample.

Whatman no. 3 paper was used for its high absorbency, medium porosity and medium flow rate. To create the creatinine paper strips, Whatman no. 3 paper was cut with scissors into individual 2.5-mm long by 10-mm wide pieces. The test strip end was then briefly dipped in heated liquid soy wax. The wax end created a barrier for the chemical products generated during the chemical reaction[228] and allowed for tweezer handling of the test strips. As powdered creatinine dissolves readily in deionized water, we created a stock solution of creatinine at 80 mg/dL. Standard dilutions were made from the stock solution with deionized water into individual

Eppendorf tubes and refrigerated at 4° C until use. The creatinine enzymatic kit uses a 300 µl cuvette to measure absorbance and the manufacturer instructions suggest using 270 µl of R1 and 90 µl of R2. For our small paper-based tests, we reduced the volumes for the two creatinine enzymatic reagents (R1 and R2) but preserved the ratio as suggested by the manufacturer. This reduction in volume was necessary to prevent leaching out of the paper onto the cell phone housing or scanner bed during measurement. We pipetted 18 µl of R1 onto the test strip followed by 6 µl of sample. The test strip was then placed in a 37°

C oven for 4 min. Then the test strip was removed from the oven, and 6 µl of R2 was pipetted on the test strip. The test strip was then placed back into the 37° C oven for 4 min. The incubation in the oven was used to decrease the time to measurement: if left at room temperature, the result can be read in 30 minutes[262]. The test strip was finally removed from the oven and allowed to sit at room temperature before measurement on the flatbed scanner and cell phone. To prevent leaching out, a small 3 mm x 11 mm section of Parafilm tape (Hach, Loveland, CO) was added to the phone cassette well where the creatinine test is placed. The hydrophobicity of Parafilm tape ensures that the liquid remains inside the creatinine test strip during measurement.

Quantification of paper-based tests.

The quantitative LFA method involves measuring the amount of an analyte in a sample against a standard curve of known amounts of the analyte [263]. To measure the intensity of the reaction in both the LFA and creatinine tests, we used a CanoScan LIDE 300 scanner from Canon (Ōta, Tokyo, Japan) and a cell phone (Samsung galaxy s20).

In this report, we compare quantification using our cell phone app to a flatbed scanner as the "gold standard". Flatbed scanners have been used widely to quantitate LFAs and other colorimetric tests [264]. For the scanner measurement of HE4, the individual paper strips were placed face down. The auto scan button was pressed to create a PDF scan. The document was then opened in Adobe Photoshop to convert the PDF to JPEG. The JPEG was then opened in ImageJ. The test line in the image was measured with the "Measure tool". The output of the measured result was then copied and pasted into Excel for analysis.

In this study, determination of HE4 concentration was based on a sandwich assay format in a lateral flow method. Therefore, the timing of when the reaction is considered "complete" and ready to read on a scanner or cell phone app influences the intensity values. Per the manufacturer's instructions for the membrane of choice, MDI-10, the strip can be read at 15 minutes after sample application. Therefore, we analyzed the intensity associated with a concentration of 280 pM (the medium standard) over 5-minute

intervals from the earliest it could be read **(Figure 3.3).** We chose the 20-minute time mark because subsequent drying of the test reduced the intensity of the test value by about 12% as shown in **Figure 3.3**.

To determine the optimal time for reading the creatinine test strips, three concentrations of a standard curve were analyzed every two minutes until 14 minutes. The time point at 8-10 minutes was selected as the change from 8 -16 minutes is less than 2% change (**Figure 3.3).**

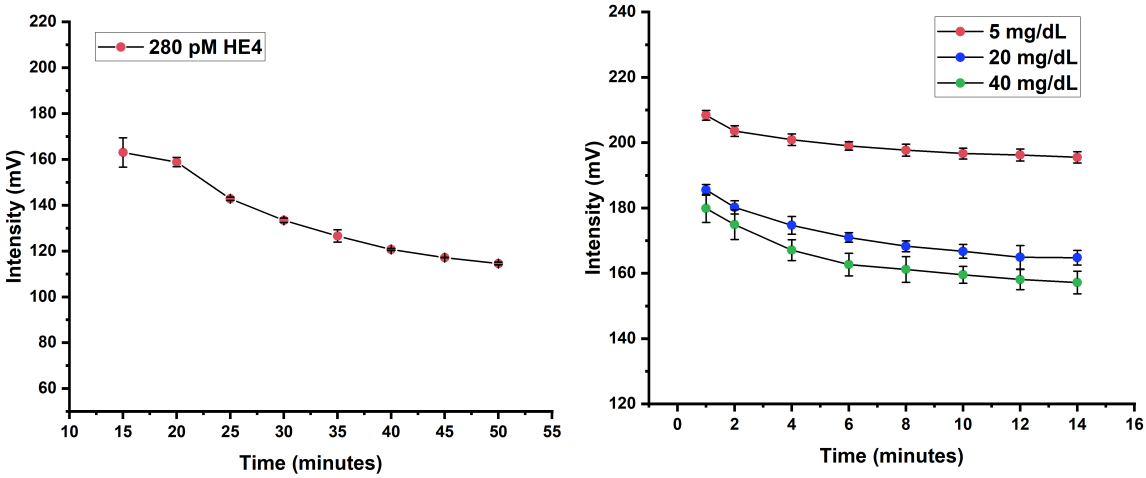

Figure 3.3. HE4 test line intensity as a function of the assay read time (Mean + s.d., n=2) (left panel). The color intensity as a function of assay read time for three creatinine concentrations of 5 mg/dL, 20 mg/dL, and 40 mg/dL (Mean + s.d, n=3) (right panel).

To make a standard curve for HE4, we serially diluted the 573 pM HE4 standard from the ELISA kit. We then compared the output of the value calculated from the standard curve to the known value **(Figure 3.4A)**. For the scanner measurement of Creatinine**,** an 80 mg/dL stock solution of creatinine was made and serially diluted to create a standard curve for creatinine. After incubation, the test strips were allowed to sit at room temperature for 8-10 minutes before being measured in the scanner. Creatinine concentrations up to 40 mg/dL were analyzed, and triplicate assays were performed for each concentration. The results demonstrated a second order polynomial fit range from 0 mg/dL to 40 mg/dL of creatinine (r^2=0.9893), as shown in **Figure 3.4B**.

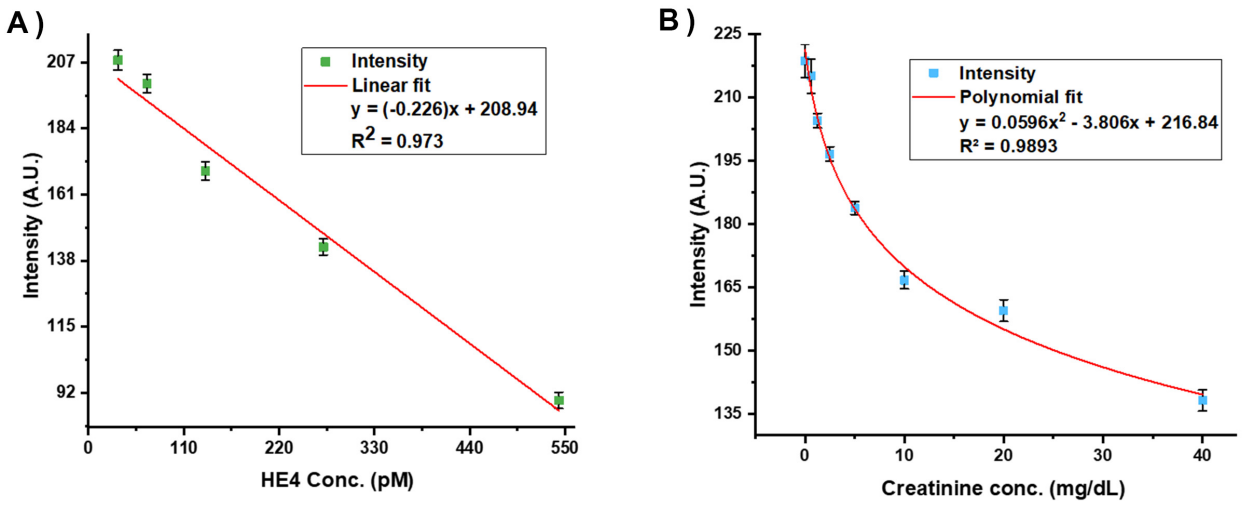

Figure 3.4 Calibration plots generated from the scanner. A) Standard curve for concentrations of HE4 (pM) (Mean + s.d, n=2). B) Standard curve for concentrations of creatinine (mg/dL) (Mean + s.d, n=3).

In addition to quantification with a flatbed scanner, we also developed a cell phone-based system for quantification of both HE4 and creatinine. **Figure 3.5A** shows a photograph of the developed device, which includes a 3D-printed black enclosure and a test strip holder. The black enclosure is used to mitigate the problem with varying external lighting conditions. The current system was implemented on an Android platform-based cell phone (Redmi Note 7 from Xiaomi, camera resolution 4000 pixels x 3000 pixels), but the same system can be used with other cell phones with a small adjustment in the design of the phone attachment. As shown in **Figure 3.5B**, an inexpensive plano-convex lens of focal length 75 mm was used to magnify the area of the test strips. The lens was attached to the phone attachment A, which is mechanically connected to the cell phone. Phone attachment B is connected to attachment A. The attachments are positioned perpendicular to the phone to eliminate the need to tilt the phone and to standardize the focal distance to reduce imaging inconsistencies. Both attachments are 3D-printed with black polylactic acid (PLA) material. The material of choice is not significant. Black was chosen to decrease the reflectance of light inside the test strip compartment. Once the test-strip holder is positioned inside of Phone attachment B, ambient light is blocked from entering the inside of the phone attachment B.

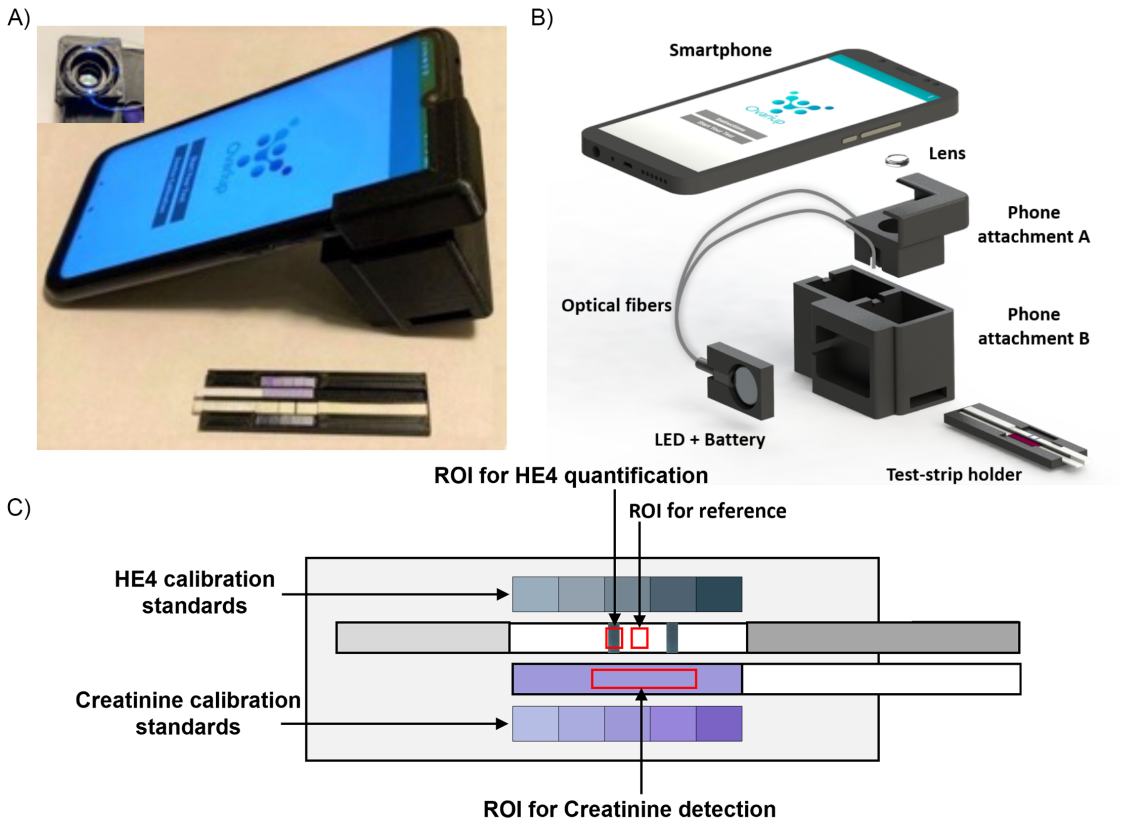

Figure 3.5. Overview of the smartphone quantification system. A) Image of the prototype components (lens, fiber optics, cell phone attachments and strip cassette). B) A CAD model providing an overview of the components used in developing the system. C) Schematic of the test-strip holder indicating the color detection scheme and the red boxes (arrows) indicate the region of interest (ROI) for HE4, for background reference, and a ROI for CRE.

Figure 3.5C shows the schematic of the test-strip holder. The test strips are inserted from the side and manually slid into the field of view. The test-strip holder contains the HE4 test, CRE test and calibration stickers to allow for simultaneously measurement of both tests and calibration stickers. We prepared calibration stickers indicating the color of both the HE4 and CRE standard solutions and attached them to the test-strip holder. The phone application captures both the test strips and the calibration stickers together in a single image frame to evaluates the intensity values. The intensity values from the calibration stickers are used to generate the respective calibration equations and the unknown HE4 and creatinine

concentrations are evaluated by interpolating corresponding intensities values in respective calibration equations. Our device evaluates the intensity of both tests and determines the corresponding concentration value by using the calibration sticker as a reference standard. The calibration standards are printed as a vinyl sticker to increase stability over time compared to typical inkjet printer paper. To facilitate on-board data processing, an Android application (app) was developed and installed on the cell phone. The detailed procedures for using this app are given in the supplementary information. To simulate an at-home user, both HE4 and creatinine were measured simultaneously on both the scanner and cell phone imaging modality (**Figure 3.5**).

It is possible to use a cell phone flashlight as a light source for colorimetric applications [265]. However, in the current application, it is not possible to use the flashlight to illuminate the test strips. This is attributed due to the use of the external lens to acquire an image with a large field of view to cover both the test strips and the calibration standards. Another problem in using the flashlight is that its position varies from phone to phone, therefore the illumination over the detection area will be different for different brands of cell phones [230]. Instead, here we achieve uniform illumination by using a novel optical fiber-based illumination scheme as shown in **Figure 3.6**. Light from a low-cost external battery-powered white LED (Finware LED, Amazon) is coupled to two plastic multimode optical fibers (980-μm core diameter, Edmund Optics), and the other ends of the optical fibers are connected to the phone attachment. The distances between the test strips and the optical fibers were optimized to achieve a uniform illumination area. The battery and the LED compartment are located on the outside of the attachment so that they are easily operable by the user and the battery. While the cell phone battery can be used to power an external LED [266] but we have observed that long term use of cell phone battery for powering external components heats up the phone and the output power of the LED is significantly reduced when the cell phone battery power is low (< 30%). Therefore, in the current application, we have used an external coin cell battery to power the LED, which can easily be replaced when needed.

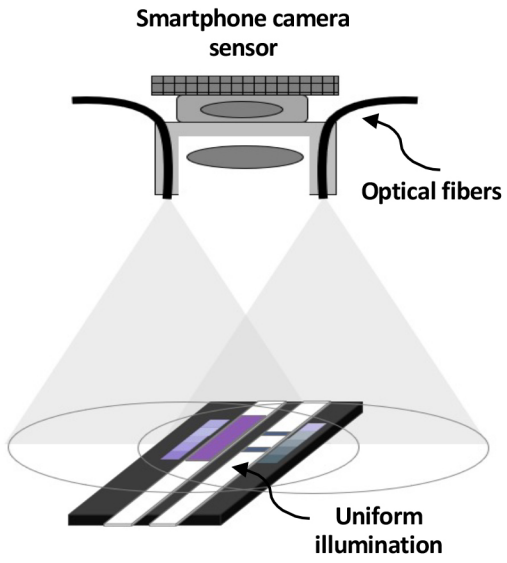

Figure 3.6. Details of the optical fiber-based illumination scheme used to provide uniform illumination over the field of view of the camera.

Figure 3.7 shows the calibration plots generated from the HE4 (pM) and CRE (mg/dL) standard solutions using the cell phone app. The analysis algorithm in the phone is simple, as the concentration can be determined by a linear relationship. In the case of HE4 we have selected the concentration range of 33.75 pM-543 pM, which indicates a co-efficient of determination (R^2) of 0.973 as shown by **Figure 3.7A**. This range was within the range of the ELISA kit. Similarly, for CRE, we evaluated a concentration range of 2.5 mg/dL-40 mg/dL, which shows a co-efficient of determination (R^2) of 0.97 as shown in **Figure 3.7B**. For the phone, a linear fit was chosen over a polynomial fit since the linear fit provided a high R^2 value and was computationally easier since there is only one answer given from the intensity calculation.

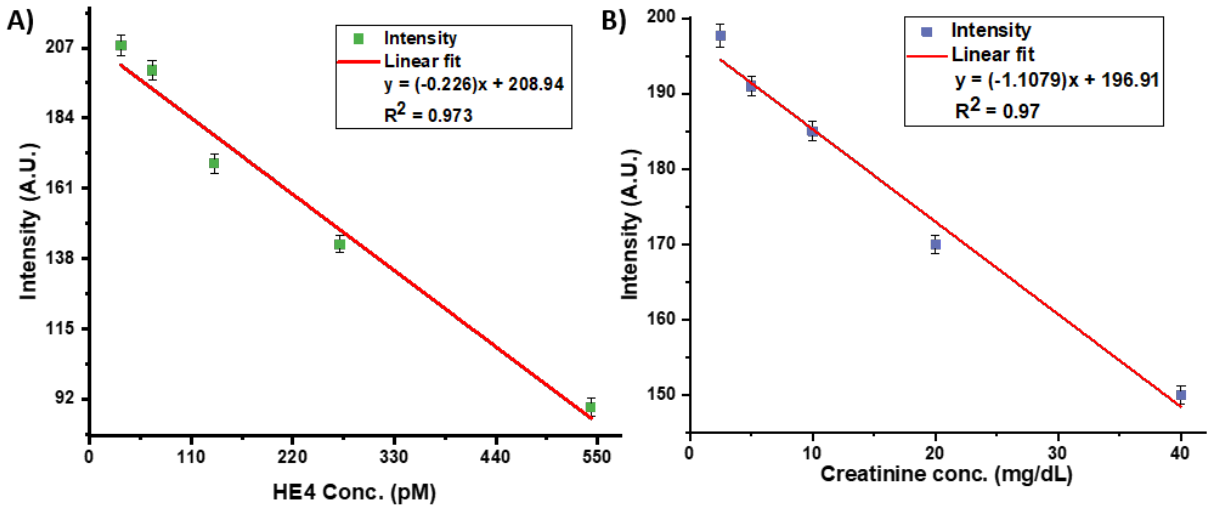

Figure 3.7. Calibration plots generated from the cell phone-based device. A) Standard curve for concentrations of HE4 (pM) (Mean + s.d, n=2). B) Standard curve for concentrations of creatinine (mg/dL) from cell phone (Mean + s.d, n=3).

Surrogate sample preparation

In this work, we tested the performance of our test using clinically relevant ratios of ovarian cancer recurrence. Surrogate patient samples were created based on previously published work by Liao et al., who measured patient HE4 urine values in pM and creatinine values in mg/dL as a ratio[105]. The range of 2 - 47 ratios was selected to ensure that the paper-based test was operating in the range of ratio values associated with recurrence testing in urine[105]. Because both creatinine and HE4 can be present in high amounts, Liao et al diluted clinical samples by 1:40 prior to testing [105]. Therefore, we assume the same level of dilution for our test method and CRE values from 0-40 mg/day[228] were selected for testing as they are in the ranges of diluted urine samples as described by others[104,105]. To create simulated patient samples, we made a 3 x 3 matrix of HE4/CRE solutions. For the three HE4 solutions, we included a high, medium, and low CRE version of each of the HE4 concentrations.

3.3 Results

Known Concentration	Scanner Concentration	% error	Cell phone Concentration	% error
4.4 mg/dL CRE	4.8 mg/dL CRE	9.9	4.2 mg/dL CRE	4.0
8.8 mg/dL CRE	8.2 mg/dL CRE	6.2	7.3 mg/dL CRE	16.4
17.5 mg/dL CRE	15.9 mg/dL CRE	8.9	17.9mg/dL CRE	5.8
35.0 mg/dL CRE	40.7 mg/dL CRE	14.1	37.9mg/dL CRE	8.3
70 pM HE4	66 pM HE4	4.8	61 pM HE4	12.2
94 pM HE4	109 pM HE4	16.6	102 pM HE4	9.2
140 pM HE4	162 pM HE4	16.2	149 pM HE4	7.1
280 pM HE4	287 pM HE4	2.5	288 pM HE4	3.1
415 pM HE4	437 pM HE4	5.4	425 pM HE4	2.6

Table 3.1. CRE (n=3) and HE4 (n=4) concentrations were calculated from the standard curve using the flatbed scanner and cell phone and compared to the actual known value. Percent error for all concentrations is reported.

In tests of the accuracy of this approach, we varied the concentration of HE4 or CRE individually shown in **Table 3.1**. Compared to the known sample concentration, our percent error was usually under 16% for both the scanner and cell phone. Scanner vs cell phone performance is compared to the known values of analyte in **Figure 3.8**. To determine the accuracy for one analyte individually, we varied only the HE4 parameter or only the creatinine parameter along the standard curve for each biomarker.

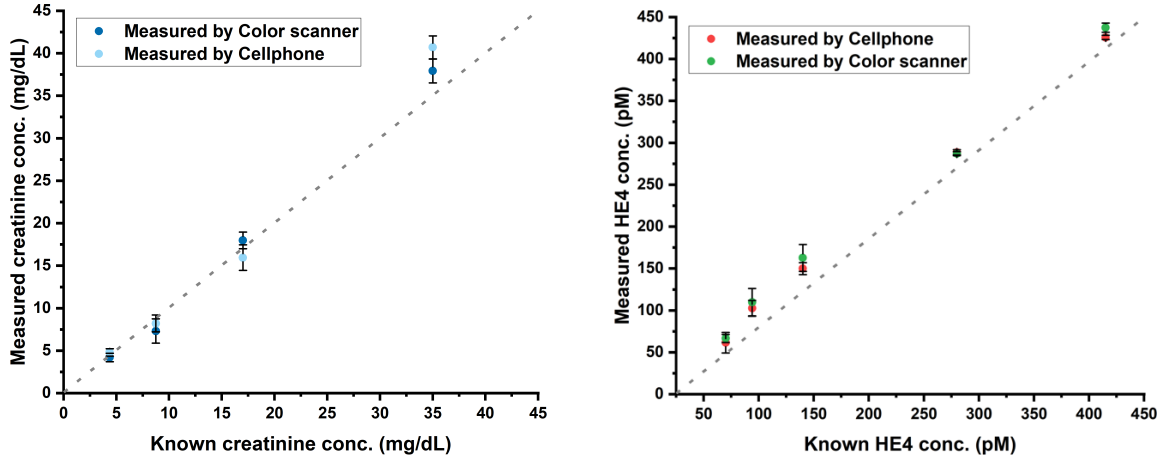

Figure 3.8. Comparison between flatbed scanner and cell phone measurement of HE4 concentrations (left) and of creatinine concentrations (right). Error bars the percent error

found for each concentration (Mean + s.d, n = 4). The dotted line indicates the line of identity.

We determined the limit of detection (LOD) of each test strip by analyzing a blank 5 times and calculated a 3 SD limit[267]. The LOD for HE4 is 15 pM and for creatinine test the LOD is 1.2 mg/dL. Average intensity of the blank for is 226.4856 ± 2.9178 for HE4 and 243.31 ± 2.99 for creatinine (**Figure 3.9**). A one-way ANOVA was done to compare the actual value, the scanner, and the cell phone for both HE4 and CRE values. For HE4, our calculated F value (0.0095) is smaller than our F critical value (3.8853) (P-value of 0.971). Similarly, for CRE, our calculated F value (0.0042) is smaller than our F critical value (4.2565) (P-value of 0.996). Therefore, the scanner, cell phone and known values are not significantly different for either HE4 or creatinine.

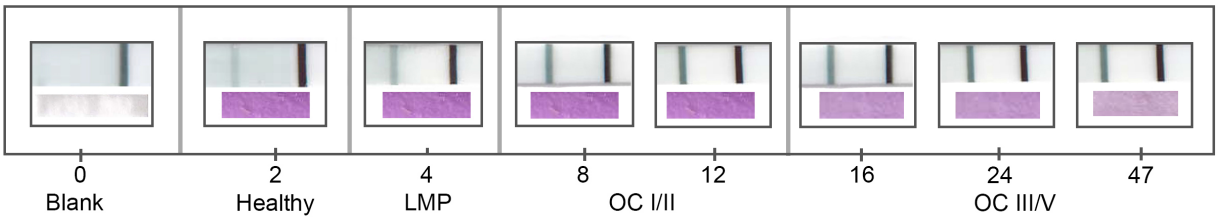

Figure 3.9. Simulated clinical patient ratios of urinary HE4/CRE. Each image shows a lateral flow strip and corresponding creatinine strip below. In the LFA strip, the left line is the test line and the right line is the control line. *LMP = low malignancy potential cyst. The labels below are the ratio of HE4/CRE and the corresponding stage of ovarian cancer stage given Liao et al (2015) and Hellstrom et al. (2010).

Known Ratio	Scanner Ratio	% error	Cell phone ratio	% error
2	2.2	9.77	2.1	3.74
4	4.4	11.06	3.6	8.74
8	7.1	10.72	7.7	5.02
11.9	13.2	11.33	11.5	2.67
16	17.4	9.04	16.2	1.08
23.7	23.7	10.33	23.6	0.28
47.4	49.6	4.50	50.9	7.40

Table 3.2. Surrogate patient samples created for three HE4 concentrations across three different creatinine concentrations. Scanner and cell phone values are reported for each biomarker. Percent error is reported for each concentration (n =5). Duplicate ratios are not shown.

Figure 3.9 shows flatbed scanner images covering the range of ratios from 2 to 47. Example cell phone images are contained in supplemental **Figure S3.1**. As this figure shows one can qualitatively see the ratio has changed by examining the HE4 test line and creatinine test strip color intensity. However, the images show you cannot get a quantitative answer by visual inspection. The quantitative analysis of images (**Figure 3.9)** is compared to the actual ratio of HE4/CRE and the measured ratios by the scanner and cell phone **(Figure 3.10)**. We performed a one-way ANOVA test on the matrix values. Our F value (0.0148) is smaller than our F critical value (3.4028) so there is no significant difference among the actual value, the scanner, and the cell phone (P-value of 0.985). The actual values for the known ratio, the scanner ratio and the cell phone with the associated errors are shown in **Table 3.2**. Our analysis showed that varying creatinine did not significantly alter the intensity of the HE4. Likewise, the level of HE4 did not interfere with the output of the creatinine result.

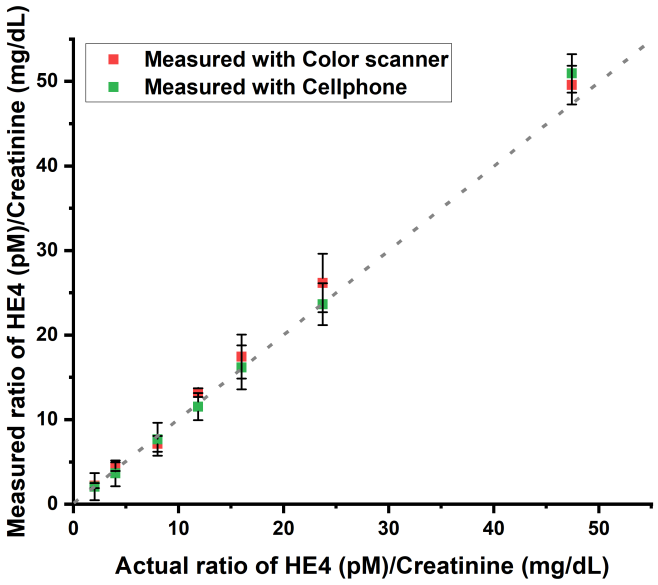

Figure 3.10. Comparison of mean values for HE4/CRE ratios for scanner and cellphone to actual values (Mean + s.d, n = 5). The dotted line indicates the line of identity.

3.4 Discussion

In this report, we found the method to measure HE4/CRE with a cell phone or scanner worked well over the clinical ranges expected for ovarian cancer recurrence [105]. The intended application for this device is aimed at repeated measurements within the same individual. Based on work by Liao et al, this ratio changes with stage of ovarian cancer. Our expectation is that when applied to a single individual, these ratios would mirror the expected increases found in group average values as reported by Liao. We found the percentage error for the surrogate testing was usually less than 27% for the scanner, with the average percent error being 10%. The worst percent error for the cell phone was better at 12% and was only 4.13% percent error on average for the cell phone. This assumption should be validated with clinical samples. Recurrence was defined by a doubling of the HE4 value in serum [87]. Since urine HE4/CRE correlates positively with serum HE4 [109, 104, 105], our method has much less error than the expected doubling in recurrence. Therefore, if a user sees a doubling in their HE4/CRE ratio, this is well outside the error range we observed and should be interpreted as a change in their risk of recurrence. These positive preliminarily results lay the groundwork for future longitudinal testing with real clinical samples.

Our results indicate that the cell phone app provides similar results to the flatbed scanner (**Figure 3.6 & Figure 3.8**. The particular brand of flatbed scanner was an ideal comparison to our cell phone app since both devices use LED illumination. Additionally, ImageJ was used to measure the intensity of the LFA and creatinine test. The custom phone app automatically analyzes the intensity of the test, which likely reduces human error compared with the manual measurement method in ImageJ. The cell phone app also produces results much faster compared to the scanner. The custom cell phone app allows a more streamlined and robust process for users as well as reduced cost and space over that required for a flatbed scanner without a significant difference in results. Additionally, the cell phone app analyzed two tests in a single image. This allows us to compare HE4 and CRE, but it could be done for any analyte in a sample. This streamlined process, affordability, and comparable accuracy to the scanner suggests our device shows promise as a valuable platform for home testing.

We chose our HE4/CRE test ranges based on published reports on the levels found in urine in early recurrence. Our values of HE4 concentration are inside the clinical urine ratio ranges published by Hellstrom et al. Since the HE4 concentrations in urine are much higher than the LoD of our assay, our method could be used with higher dilution factors. The normal creatinine range is around 20 – 275 mg/dL in women. We tested ranges to 4.4 to 35 mg/dL to be able to include the lower ranges of urine based on the need to dilute the urine sample. Hellstrom et al reported HE4 concentrations in urine of roughly 10-10,000 pM. We tested ranges of 28 – 543 pM based on the assumption of a 1:40 dilution. Since the intended use of the technology is for recurrence monitoring, where levels will be lower, we focused our testing where the initial rise would occur for greatest impact.

In contrast with other work by Wang et al [101], our device does not require the complicated infrastructure necessary to perform ELISA, making it more adoptable for home-testing. Wang et al. coupled a microchip ELISA with a cell phone mobile application that could detect the HE4 biomarker in urine from ovarian cancer patients. However, the authors did not normalize HE4 to creatinine. Also, an ELISA microplate and ELISA microchip both require numerous sample processing steps (i.e., three washing steps, several hour incubation steps, and manual mixing of the final solution), which increase cost and error. Limited lab infrastructure and skilled technicians are not widely available in low resource settings, which make ELISA and ELISA-based devices difficult to access. Our urine LFA is easily integrated with any cell phone with our customized app. The signal from the test line can be quantified by the custom designed urine LFA, making it possible to detect changes in HE4 level in urine by untrained users. Without the phone, our entire device is under $5.00 to create.

One application for this device is to facilitate biomarker tracking over time with patient-specific baseline HE4/CRE levels. Although many academic papers have demonstrated various devices or methods that can differentiate healthy and OC urine [101], these devices have not been translatable in a clinical setting [268]. Due to variation of OC (stage, grade or subtype), a single biomarker cut-off value may not very useful at the individual patient level [269]. However, measuring the amount of HE4 urine when first diagnosed with OC and again after debulking surgery and treatment may provide physicians with two critical biomarker

points to compare (disease level and no evidence of disease level). By serially monitoring HE4/CRE in urine and comparing patient-specific levels, users may be presented with new biomarker changes to guide further invasive testing.

This type of testing method would be useful in LMICs, which face a rapid rise in cancer incidence without increased infrastructure investments in healthcare [270]. Due to this constraint, methods that can detect biomarkers in human samples remotely without the need for training or expensive equipment will have greater adoptability. Low-cost and easy-to-use cancer management strategies would benefit less-developed regions as well as more developed countries. In 2013, the World Health Organization (WHO) endorsed self-sampling as an option for the initial screening for Human Papilloma virus (HPV) for low- to middle-income countries in an effort to reduce cervical cancer death [271]. Studies by Kamath et al showed that self-sampling for cervical cancer screening in low-resource environments was not just convenient, it was also able to reduce disparities in access to screening and reduce mortality [272].

Another application of this technology is to monitor early therapy responses. Serial measurements of HE4 in urine show that mean urine HE4 levels remained stable (7% decrease) in patients that proved to be platinum resistant, while they decreased 68% in those that proved to be platinum sensitive [105]. This indicates that urine HE4 levels may also be a useful tool for monitoring recurrence in patient with platinum resistance. Urine HE4 should be studied further to evaluate the predictability of chemotherapy response. One way to do this is by using the proposed method in this report. This remote testing method may indicate the need to switch to a more effective therapy in a timely manner when survival outcomes are higher.

Perhaps the most impactful use of this technology would be in early detection of ovarian cancer. Currently, there is no recommended screening test for ovarian cancer [273]. Since ovarian cancer presents subtly and physicians lack sensitive diagnostic tools, most diagnoses occur in later stages in which treatment options are often limited as well as costly. High-risk individuals (patients with a first-degree relative with ovarian cancer or carrier of a BRCA mutation), often undergo pelvic exams combined with Transvaginal Ultrasound (TVU) and blood test for changes in CA-125 levels even though these strategies have shown no proven benefit for reducing ovarian cancer mortality [274]. Interestingly, one study examined a “2-out-of-

3" decision rule that required 2 of 3 serum biomarker tests to be positive. Application of this rule identified 100% of the high-risk cases and showed a false-positive rate of 1.5% [275]. This suggests that multiple positive tests may help identify high risk patients for more follow-up testing at clinics. Longitudinal measurements of HE4 within a single patient with a genetic risk may be useful as an early detection tool for gynecological oncologist. In this use, if women who are at genetic risk would record their HE4 levels 3-4 times a year, a significant rise in HE4 could be used to suggest follow-up screening. Results may help guide decisions on the timing of more invasive procedures such as tissue biopsy or prophylactic ovary removal.

The proposed technology is a good match for lateral flow testing and the high abundance of analytes of interest in the urine. As both HE4 and creatinine are present in high amounts and much higher than the limit of detections in lateral flow tests and we expect the dilutions of urine may be necessary prior to application to test strip. A dilution step presents an additional step for a patient and is more error prone as a result. To offset this, a specific-sized pipette coupled with a pre-aliquoted deionized water vial can be combined easily to help offset errors in measurement. In fact, many pregnancy tests require users to use the included small pipette and deliver only 3-4 drops onto the sample pad. As many women are well accustomed to using such tests, this suggests adding a pre-aliquoted water vial to mix the pipetted urine into would not be an unreasonable step. A step-by-step guide with pictures or a "how to" video on the cell phone app would likely assist users in proper test procedure.

Most commercial LFAs include a spray-dried conjugate release pad in their test format. In our prototype, we did not use an air jet dispenser to spray our reporter onto a release pad. Instead, we combined our sample with the reporter in a single Eppendorf tube for 10 minutes and spotted onto the sample application pad. Future work may verify if the reporter performs in a spray-dried release pad. Additionally, the temperature needed for creatinine incubation presents another critical limitation in this method. Although making a small compartment with a heating element is feasible, we did not perform this additional step to make it suitable for home use. Without the two 4-minute incubation steps, the user must wait an additional 16 minutes for their result. Additionally, although the LED light in the cell phone cassette was affordable ($0.20 per light), the battery dies quickly if left on for more than 20 minutes. Automating the

light function with the camera function would help alleviate this issue. Therefore, an app that can inform the user of decreasing illumination from a dying LED battery would be a worthwhile effort.

3.5 Conclusions

The availability of a urine-based screening test for ovarian cancer recurrence that is simple enough to perform at home would offer a convenient and less harmful sampling procedure, especially for repeated testing over an extended time. We have demonstrated an improved method to detect changes in urine HE4/CRE accurately at-home. In addition, due to its low-cost, this method can also be employed in low-resource settings where clinical visits are even more difficult. In the future, the methods demonstrated here could be evaluated with patient samples to further validate the clinical performance of the device.

Chapter 4: DIRECT CAPTURE AND EARLY DETECTION OF LYME DISEASE SPIROCHETE IN SKIN WITH A MICRONEEDLE PATCH

Adapted from: Kight, E.; Alfaro, R.; Gadila, S.K.G.; Chang, S.; Evans, D.; Embers, M.; Haselton, F. Direct Capture and Early Detection of Lyme Disease Spirochete in Skin with a Microneedle Patch. Biosensors 2022, 12, 819. https://doi.org/10.3390/ bios12100819.[276]

Abstract

Borrelia burgdorferi sensu lato family of spirochetes causes Lyme disease (LD) in animals and humans. As geographic territory of ticks expands across the globe, surveillance measures are needed to measure transmission rates and provide early risk testing of suspected bites. The current standard testing of LD uses an indirect two-step serological assay that detects host immune reactivity. Early detection remains a challenge because the host antibody response develops several weeks after infection. A microneedle (MN) device was developed to sample interstitial fluid (ISF) and capture spirochetes directly from skin. After sampling, the MN patch is easily dissolved in water or TE buffer, and the presence of spirochete DNA is detected by PCR. Performance was tested by spiking porcine ear skin with inactivated Borrelia burgdorferi, which had an approximate recovery of 80% of spirochetes. With further development, this simple direct PCR method could be a transformative approach for early detection of the causative agent of Lyme disease and enable rapid treatment to patients when infection is early, and numbers of systemic spirochetes are low.

4.1 Introduction

Tick-borne diseases are major public and animal health issues worldwide. Ticks may transmit diseases such as babesiosis, anaplasmosis, ehrlichiosis, Lyme disease, Crimean Congo hemorrhagic fever, Powassan virus, and Rocky Mountain spotted fever to humans and animals [277]. According to the Centers for Disease Control and Prevention (CDC), the number of reported cases of all tick-borne disease has more than doubled over the past 13 years [140]. Of particular interest is Lyme disease (LD), the most common vector-borne illness

in both North America and Europe, with an estimated incidence of ~476,000 cases per year in America alone [278]. Lyme borreliosis disease is a multisystemic infectious disease caused by a spiral-shaped bacterium, *Borrelia burgdorferi*, also referred to as spirochetes, that is transmitted to humans by the bite of infected species of *Ixodes* ticks [137]. Recent studies suggest LD will expand due to climate change making the more northern areas more temperate [148, 149, 279].

LD infection typically begins with erythema migrans (EM), an expanding skin lesion at the site of the tick bite. If left untreated, spirochetes may disseminate from the bite site leading to cardiac, rheumatologic and /or neurologic manifestations [141, 142]. Conventional diagnosis of LD is often based solely on the presence of EM, however, it develops in only 70%–80% of patients [280]. In the absence of EM, the signs and symptoms of Lyme disease are not specific enough to be clinically useful for diagnosis [281]. Additionally, misdiagnosis may occur due to the high degree of variability of skin lesions and the variation of interpretation [282]. Additionally, patients with darker skin often do not recognize early disease, resulting in increased rates of late manifestations [185].

In regions where tick-borne infections are common, any tick bite may be of concern. One strategy to assess exposure of tick-borne disease is direct testing of a removed tick. Tick testing centers offer PCR testing of ticks, but these tests do not inform doctors if any tick-borne disease was transmitted to the patient's body. As ticks fall off their host, many patients do not have the tick that bit them, so they are unable to use these testing services. Additionally, testing ticks requires a series of DNA isolation steps prior to PCR testing. During these several DNA isolation steps, small amounts of bacteria may not be detectable given that many commercial DNA extraction kits lose 80-90% of the starting material [283].

Currently, the CDC approved diagnosis procedure is a two-tiered testing method based on spirochete host response using an enzyme-linked immunosorbent assay (ELISA) first, and if the results are positive, another specificity test by western blot is conducted. This two-tiered testing features high diagnostic specificity (95%–100%) with high sensitivity (80-90%) for late stages of Lyme disease [191, 284]. However, since development of host-antibody response takes several weeks, early diagnosis remains

problematic. The 2-tiered testing suffers from just 40% sensitivity for early-stage (meaning that it misses more than half of the cases). It also requires multiple tests and is technically laborious leading to high costs.

After being deposited into skin, *B. burgdorferi* multiplies locally before migrating through tissues [137]. There are two main laboratory methods available to detect *B. burgdorferi* in human body fluids: *in vitro* culture of intact living bacteria, and polymerase chain reaction (PCR) of a body fluid sample to detect bacterial DNA [285], [187]. Though the culture method provides confirmation of active infection, the bacteria grow very slowly for up to 12 weeks in culture before reaching diagnostic concentration [2]. Cultures as a detection method are too time consuming and not practical for routine use. PCR has been used to amplify and detect *B. burgdorferi* DNA in urine, blood, and cerebrospinal fluid (CSF) [286]. However, PCR is not routinely used for these sample types [281] because spirochetes are present in low copy number which results in reduced PCR performance with these sample types [285]. Skin biopsies have also been used for DNA extraction methods with quantitative PCR detection [186, 187] and was found to contain on average, 3,381 $\pm$ 544 spirochetes from a 2 mm skin sample [187]. In 2020, one study found that in 75.4% of patients who presented with EM, researchers could detect one or more *B. burgdorferi* genotypes in the skin using PCR [287]. However, obtaining a suitable skin biopsy may be painful as well as suffer from lower assay performance with PCR due to other inhibiting substances commonly used in tissue fixatives [288]. Additionally, a skin biopsy requires a trained nurse or doctor and the use of an anesthetic to numb the skin.

An inexpensive and simple means to collect the bacteria at the site where they are most concentrated may allow for early detection by PCR. Microneedles offer safe, affordable, and painless collection at the tick bite that may overcome the low numbers of spirochetes found in other sample types. The skin is the initial site of replication and persistence of *B. burgdorferi* [164]. During a tick blood-meal, *B. burgdorferi* does not migrate away from the feeding site until several days after the tick has detached from the host [169]. One study found detectable levels of bacteria remained in the skin for over a month in dogs [289]. This indicates that once the spirochetes are delivered into the skin, the spirochetes will multiply locally for several days and may still remain in the skin for longer periods of time. Therefore, it is likely that the bacteria load is concentrated in the skin and thus, easier to detect.

Since skin is easily accessed, sampling interstitial fluid (ISF) is an attractive alternative to blood but has received less diagnostic focus due to lack of methods for sampling [33]. Recently, studies have reported promising methods using MN to sample ISF [290, 291, 292]. Several types of MN have been designed to improve skin analyte sampling such as solid MN, hollow MN [293], porous MN [294], vacuum assisted MN [33], and hydrogel MNs [295, 296]. Many recent MN studies have used poly(vinyl alcohol) (PVA) since it is affordable, exhibits low toxicity, and is a highly biocompatible polymer [297, 298]. Another important property of PVA for sample collection is its swelling when immersed into a liquid sample driven by capillary force [299, 300] which can result in absorbing up to 30% of its weight in a few minutes [301] and up to 450% of its weight when crosslinked with polyvinylpyrrolidone [302]. Also PVA does not inhibit PCR [303, 304] which allows downstream detection by PCR feasible. Crosslinked PVA hydrogels can be easily prepared by dehydration at room temperature without the use of any other chemicals [305]. These properties suggest that microneedles made from PVA are a promising approach for non-invasive detection of bacteria in a skin lesion.

In this work, we hypothesize that a microneedle patch can be used to capture spirochetes in skin and, with subsequent direct PCR of the collected sample, detect the causative bacteria for LD. The feasibility of this approach is demonstrated with tick bite-appropriate PVA microneedle designs using in vitro and in vivo model systems.

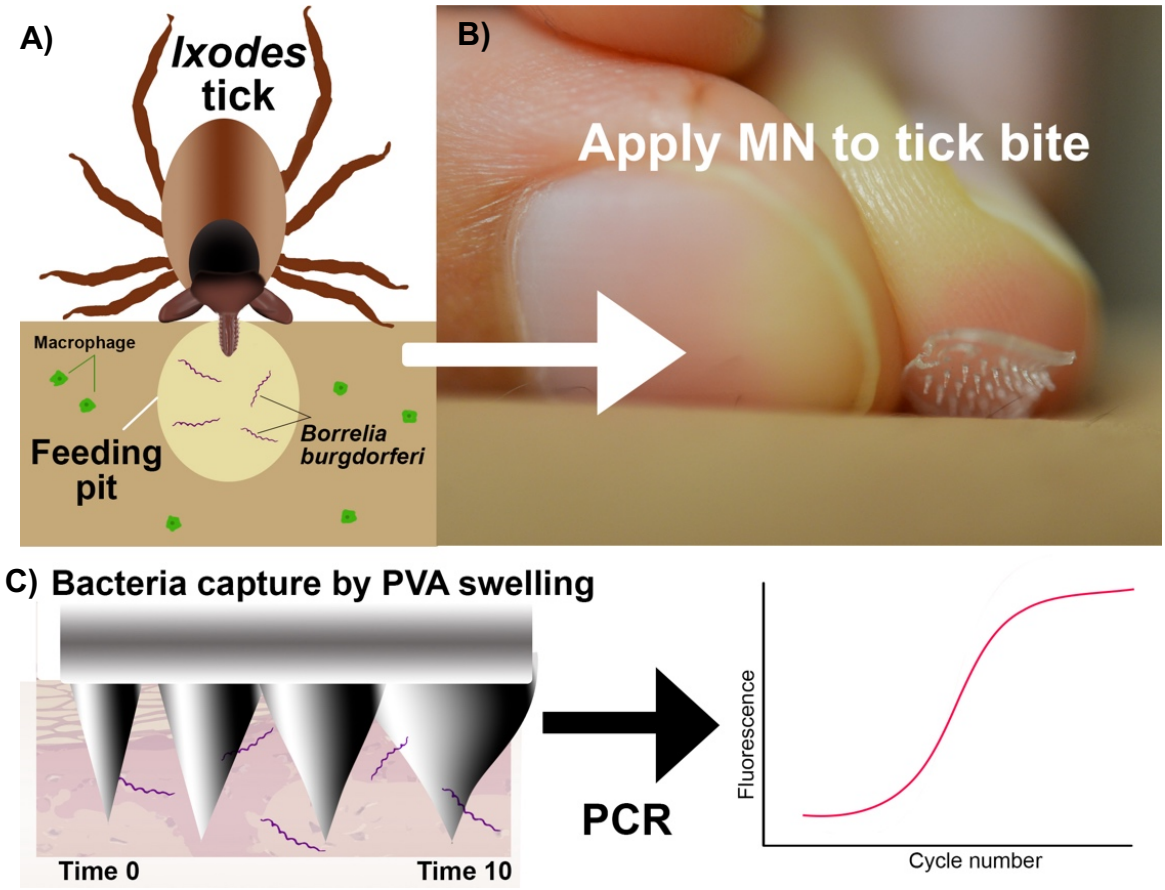

Figure 4.1. Overview of the bacteria detection method. (a) Graphic showing Ixodes tick feeding and inserting *B. burgdorferi* bacteria into skin. The tick saliva provides a feeding pit where bacteria are protected from immune cells. (b) A MN is placed onto the skin manually. (c) Illustration of MN capture of bacteria with swellable PVA and direct PCR detection.

4.2 Materials and Methods

Culture of a B. burgdorferi strain B31

Low passage *B. burgdorferi* wild-type strain B31 clone 5A19 was grown in BSK-II supplemented with 6% rabbit serum (Pel-Freez Biologicals, Rogers, AR, USA) at 34 °C in a trigas incubator (5% CO_2, 3% air, and the remainder N_2). In addition to 6% rabbit serum, this media contained antibiotics rifampicin, 45.4 µg/ml; phosphomycin, 194 µg/ml; and amphotericin B, 0.25 µg/ml. Spirochetes were grown to late logarithmic phase and then pelleted at 2000xg for 30 min before inactivation. At the end of the run, the rotor was left

to coast to minimize damage to the live spirochetes. The culture was washed twice using PBS and was inactivated by resuspension in 4% paraformaldehyde (PFA). Next, the tube was centrifuged at 2000 RPM for 15 minutes and resuspended in 1 x PBS with 0.01% sodium azide for storage at 4 °C until use. SEM of the bacteria are shown in **Figure S4.1**.

Design of Microneedles

The tick hypostome (mouth) has a range of sizes [306]. The length of the hypostome varies depending upon sex and stage (nymph vs adult) [307]. The adult female deer tick exhibits the largest hypostome which is ~500 μm long [308] and up to ~200 μm wide, while the males and nymphs have much smaller hypostomes [309]. Since the bacteria travel into a new host via tick saliva, the bacteria are likely deposited approximately close to the depth of the tick mouth. Researchers have used microscopy methods to image *Ixodes scapularis* feeding in the skin and observed a restructuring of the skin into a cone-shaped area surrounding the hypostome after 72 hours of feeding, which could be filled with ISF [310]. In the skin, ISF is located beneath the stratum corneum (SC) which is ~10-200 μm thick [292]. To include the full range of tick hypostome length sizes and penetrate to a depth beyond 200 μm, we designed microneedle patches to be 300 μm - 800 μm in height, and 250 to 350 μm in base diameter to increase stability. Specifically, the center-to-center spacing has been shown to be a crucial factor in the penetration performance into skin [311], with more densely packed microneedles leading to the "bed of nails" effect [312]. Therefore, we selected a spacing of 1000 μm for our MN patch since this spacing has been studied with our range of heights and diameters in pig skin penetration tests [311]. Four microneedle cast print designs with different heights were created using Solidworks 2018.

Table 4.1. Parameters of the 3D printed 5 x 5 microneedle cast prints used for molding.

MN patch ID	Needle length (µm)	Base (µm)	Distance between needles (µm)
Design A	1000	250	1000
Design B	1000	350	1000
Design C	1200	350	1000
Design D	1600	350	1000

Fabrication and Imaging of PVA Microneedles

Firstly, we developed a method to prepare PVA microneedle patches. Different types of PVA were tested ranging from 13-124 kDa molecular weight and 87-99% hydrolysis. Since a high viscosity solution cannot be pipetted with consistency for PCR, we tested the viscosity of the three molecular weight PVAs (**Table S1**). We pipetted 50 µl of the three different PVA's onto a weigh boat on a scale four times to examine the pipetting ability across the different molecular weight PVAs (**Table S2**). The PVA M_w 85-124 kDa exhibited higher standard deviation between the pipetting and lower mass when pipetted. Additionally, for PVA M_w 85-124 kDa all four drops showed bubbles and the pipette tip exhibited bubbles as well which indicates the solution is too viscous for accurate pipetting. Therefore, we did not choose higher molecular weight PVA for further testing. We pipetted both PVA M_w 30-50 kDa and PVA M_w 13-23 kDa into microneedles silicone casts as both solutions were easily pipetted. However, the lower molecular weight PVA did not form rigid uniform microneedles in the same duration (one week under vacuum) as the other PVA, so the low molecular weight was not chosen for further testing (data not shown).

The various types of PVA were cast and the PVA MNs that were solid and dry after a week were compared on a light microscope for needle shape and consistency. PVA with 30 – 50 kDa molecular weight

and 98-99%-degree hydrolysis (Sigma-Aldrich cat# 363138-25G) was selected for further development. Cone-shaped microneedles were created for casting with dimensions 1000-1600 µm height, base 250-350 µm, and spacing 1000 µm apart were created with a 3D printer (ProJet® 3510 HD plus) (**Table 1**). The method of fabrication PVA MN is shown in **Figure 2**. The 3D printed MNs were used to create a negative mold in silicone with a needle array of 5 x 5 cone shapes microneedles. PVA microneedles were then fabricated using the micromolding technique from a silicone mold (Mold Star™ 30 silicone rubber, Smooth-on). The 3D printed mold was cast in the silicone mold for 24 hours to produce a negative mold under vacuum pressure of 100 PSI. The 3D print was then removed from the silicone mold. To make a 10% (w/v) PVA solution, PVA was dissolved in 10 mL deionized (DI) water at 90 °C on a hot plate with stirring for 12-24 h. To cast the final MN patch, PVA solution was pipetted into the silicone mold and then placed inside a vacuum at 100 PSI for 5-6 days to allow the formation of solid PVA microneedles.

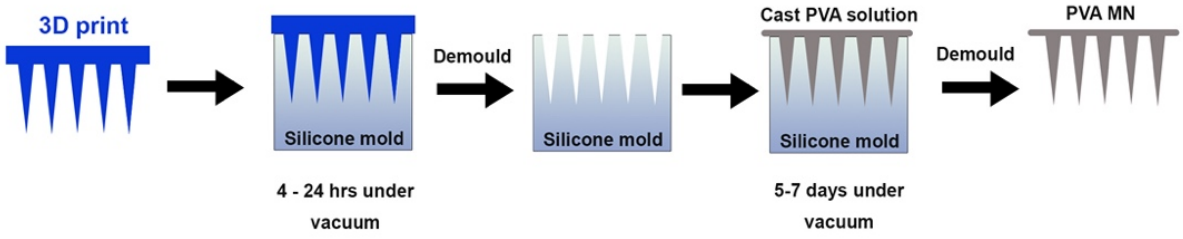

Figure 4.2. Fabrication method for PVA microneedle patches. A 3D print (blue) is used to cast the negative mold in silicone. In the final step, PVA (gray) is pipetted into the silicone mold and dried under vacuum for up to a week.

Penetration tests

Ideally, microneedles should penetrate the stratum corneum of the skin to allow extraction of ISF. Additionally, if the microneedles do not penetrate beyond 500 µm, this enables painless collection. To investigate the penetration performance, various lengths of microneedle arrays were created and tested with

the 3D print casts shown in **Table 1**. To verify that the microneedles can penetrate the depth required, we tested the penetration of the microneedles in skin substitutes such as Parafilm M® (PF) [313] and 2%(w/w) gels [314], [315]. PF is often used to quickly determine the depth of MN penetration since each layer is close to 100 microns [316]. We folded the PF into 8 layers, and we placed the MN on the top layer and pressed the MN with same force to press an elevator button. Next, we unfolded the PF sheets to examine the layers with holes on the microscope to visualize. If a hole was observed on the microscope, we considered the layer penetrated.

In addition, optical coherence tomography (OCT) was also used to visualize penetration studies of a 2% (w/w) gel since this mimics the properties of human skin [314], [317]. Gel samples were imaged before and during MN penetration under OCT imaging for cross-sectional and volumetric visualization. A Telesto series OCT imaging system (TEL220PSC2, Thorlabs. Inc) with an OCT-LK3 objective lens were used in the study. The system has a center wavelength of 1300nm, and a bandwidth of 170nm. The axial and lateral resolution of the system reported are 4.2µm (in water) and 13µm, respectively. Imaging data was acquired with 2D and 3D intensity mode at a A-scan rate of 48 kHz. From each sample, B-scans (4mm, 1024 A-scans) and volumetric scans (4mm x 2mm area, 1024 A-scans by 200 B-scans) were collected. Post-processing of acquired images were performed with ThorImageOCT (version 5.4.9, Thorlabs. Inc). The cross-sectional imaging capability of OCT allows evaluation of the penetration depth and structural integrity of the MNs in the sample. We assumed a refractive index of 1.33. In this study, one layer of PF was placed on top of the 2% (w/w) gel to mimic the skin outermost layer, the stratum corneum. Two gels, ~250-300 µm thick were stacked to mimic epidermis layers [296] and another sheet of PF was placed in between the two gel layers to enhance needle visualization. Microneedles were placed on top of gel and pressed with the same force as used to press an elevator button.

Mechanical tests

Compression tests are used to determine the modulus, elasticity, and malleability of a material. A compression test was conducted on three MNs patch to determine the behavior of a PVA MN under a load

using an Autograph AGS-J (Shimadzu, Kyoto, Japan). The patch was supported from below by a fixed, flat surface. A second flat surface, above and parallel to the supporting surface, was controlled to move in the direction of the lower surface, thereby compressing the material. The testing machine lowered the compression plate at a rate of 5 mm/min until the sample gave in. The following formulas were used to calculate the stress and strain of the PVA MN patch:

$$\sigma = F_n/A \quad (1)$$

Where σ is the normal stress in N/mm^2, F_n is the normal force in N given by the testing machine, and A is the average cross section for the needles in mm^2. This average cross section was calculated by taking the average of the base diameter (350 µm) and needle tip diameter (~10 µm). This average diameter was used to calculate the average cross section for a needle tip and multiplied to account for the 25 needles in the patch.

$$\varepsilon = \Delta L/L_\circ \quad (2)$$

Where ε is the strain (unitless), ΔL is the change in height of the MN patch in mm, and $L_\circ$ is the initial height of the microneedles (~600 µm).

Swell and Absorption Test

One method for capturing bacteria and bacterial DNA using PVA MN is to take advantage of the material's hydrophilic and water absorption properties. Therefore, PVA liquid absorption is a critical property that directly relates to capture performance. To qualitatively visualize liquid absorption performance, a 2% (w/w) gel was prepared. A small hole was made with the tip of a 25-gauge needle and 10 µl of green dye was injected into the hole. A sheet of PF was placed on top to ensure only the needle of the MN was extracting and not the underside of the MN patch. A MN was placed on top of the PF directly above the green dye spot as shown in supplemental **Figure S4.4**. The MN was applied for 10 minutes and then removed. A Kim wipe was used to blot excess of green dye off and the MN was examined for green color which indicated the MN absorbed the green dye.

To observe more detailed changes in the PVA MN swelling, scanning electron microscopy (SEM) was used to image a dry microneedle and a microneedle after 10 min with 10 µl of liquid. Each MN was sputter coated with gold and placed into the SEM Zeiss Merlin for imaging (Zeiss, Oberkochen, Germany).

In addition to these qualitative tests, a quantitative swell test was designed. To conduct a swell test, each individual MN patch was weighed while it was dry (m_o) three times and then placed face down (needle side facing down) onto a 40 µl droplet of water and manually flattened briefly so that the needles were submerged in the water. After 10 minutes, each MN was removed from the water droplet with tweezers, and carefully placed on tissue paper for 10 seconds to remove the extra water sticking to the sides of the patch so that only the water absorbed within the MNs was left. Then, each wet MN patch (m_t) was weighed three times. The percentage of swelling was determined by calculation from Equation 3.

$$\% \text{ Swelling} = \left(\frac{mt - mo}{mo} \right) x\ 100\% \quad (3)$$

Time and volume to dissolve MN for PCR testing

To enable direct PCR testing, it is critical to examine the volume and time needed to completely dissolve MN patches into a solution that can be pipetted accurately (a viscous solution is not pipetted accurately). The MN patches were inserted into 2% (w/w) gels for 10 minutes and then placed in a 1.5 ml Eppendorf tube. A volume of 15 - 100 µl of TE buffer was added to the tube. The tube was briefly vortexed and spun down before being placed in an incubator at 37°C for 15 - 30 min or onto a heat block at 115 °C for 10 minutes. Pictures were taken after initial placement into Eppendorf tube and checked every 10 min. We considered the microneedle to be dissolved when you could not visually see any of the microneedles in the tube and liquid was easily pipetted.

Preparation of pig ear skin and penetration of MN in porcine ear skin by OCT

Pig ears were obtained from Oak Hill Genetics from previously euthanized Yorkshire female pigs (32 kg). The samples were washed and soaked for 30 min prior to testing. Sterile surgical scissors were used to cut portions of the ear for testing.

OCT was used to image MN inserted into the skin of pig ears. OCT is a promising tool to image MN in tissue since OCT is nondestructive to tissues and tissue do not need pretreatment or chemicals for visualization [318]. In this test, we selected MN Design B (**Table 1**) due to penetration performance in prior tests. We tested the MN on a pig ear skin with hair and pig ear skin without hair to determine the effect of hair on the penetration performance. We assumed a refractive index of 1.33.

RNAse P Assay for extraction control

The RNAse P Assay detects the RNAse P gene which is often used as an endogenous control in sample specimens and is used to determine if a sample was adequate for testing DNA from clinical samples [319], [320]. For reverse transcription, samples were held at 55 °C for 10 minutes, followed by cycling from 94 °C for 10 seconds to 60 °C for 10 seconds for 50 cycles using a Rotor Gene Q thermal cycle (Qiagen, Germantown, MD). A forward primer of sequence 5'-GAT TTG GAC CTG CGA GCG -3', a reverse primer of sequence 5'-AAG CGG CGT TCT CCA CGA -3', and a probe sequence of 5'-Cy5-TTC CGA CCT-TAO-CAA GGC GCT GC-BHQ-3'. The Ct values from three experiments were compared in a one-way ANOVA test to assess sampling across the MN's used for bacteria extraction from pig ears.

Determination of bacteria recovery using qPCR

To determine the number of bacteria after reconstitution, qPCR was performed using the Luna® Universal Probe qPCR Master Mix (NEB #m3004) according to manufacturer's protocol. All primers, probes and targets were synthesized by Integrated DNA Technologies (Coralville, IA). FlaB is a structural component of flagellin in spirochetes, and is expressed during infection in both ticks and hosts [321], [322], [323]. The synthetic flaB target consisted of 5'- CTC AAG CGT CCT GGA CTT TAA GAG TTC ATG TTG GAG CAA ACC

AAG ATG AAG CTA TTG CTG TAA ATA TTT ATG CAG CTA ATG TTG CAA ATC TTT TCT CTG GTG AGG GAG CTC AAA CTG CTC AGG CTG CAC CGG TTC AAG AGG GTG TTC AAC AGG AAG GAG CTC AAC AGC CA -3'. We used IDT Primer Quest tool to generate 4 sets of primers specific to the synthetic flab target sequence. One set of primers was selected for further testing due to high reaction efficiency and single product melt analysis. A forward primer of sequence 5'-CAAGCGTCCTGGACTTTAAGA-3', a reverse primer of sequence 5'-AGCTCCCTCACCAGAGAAA-3', and a probe sequence of 5'-/56-FAM/TGTTGGAGC/ZEN/AAACCAAGATGAAGCT/3IABkFQ/-3' were used. For the initial PCR step the samples were held at 95 °C for 2 min. The samples were cycled from 95 °C for 15 s, to 60 °C for 30 s and 72 °C for 30 s for a total of 45 cycles in a Rotor Gene Q thermal cycle (Qiagen, Germantown, MD). In addition to a no template control, standards were made using 6 x 10^8 copies/reaction of flaB target were diluted 10-fold sequentially to 6 x 10^1 copies/reaction and 2 µl of each were added to each reaction for a total volume of 20 µl per tube. After the bacteria was reconstituted and diluted with water to achieve desired concentration. 2 µl of these tubes were used in the PCR reaction in triplicate to determine the number of bacteria in the tube.

MN Application to Pig Ear Skin and Capture Test

To mimic a feeding pit, we designed a single cone that was 300 µm long and 200 µm diameter at the base. We pressed the 3D printed cone into the pig skin. Then, we pipetted 5-10 µl of low passage *B. burgdorferi* wild-type strain B31 clone 5A19 containing a range of bacteria into the feeding pit area intradermally. The PVA MNs were pressed onto both the clean and infected pig ear samples for 10 minutes. Afterwards, they were each removed and placed into a 2 ml Eppendorf tube with 50 µl of TE buffer followed by briefly vortexing the tube and incubating the tubes at 115 °C for 10 minutes. We assume the bacteria are lysed during this heat step. A positive control tube was prepared by pipetting 10 µl of the spirochete strain into a different tube with 50 µl of TE buffer. PCR was performed in triplicate for these samples to calculate the amount captured by the MN patches. Capture recovery was determined by calculation from Equation

4, where Ce refers to the experimental concentration calculated from the standard calibration curves and Cs is the spiked concentration of bacteria pipetted into the pig skin.

$$\text{Capture Recovery \%} = (\text{Ce}/\text{Cs})x\ 100\% \quad (4)$$

4.3 Results

Microneedle Designs

We tested various types of PVA and found that the higher molecular weight PVA would often gel and not dissolve into water as easily as other lower molecular weight PVAs. The 31-50 kDa PVA was selected because it easily dissolved in water and the MNs showed sufficient hardness when demolded from the negative silicone mold. Less than 10% (w/v) PVA was not sturdy enough to form rigid needles. For this reason, 10% (w/v) PVA was selected for our methods for further development.

For bacterial capture, it is critical to consider the depth the bacteria will be placed by the tick hypostome. Although the tick hypostome varies in length across species and stages, for the *Ixodes scapularis* tick, the maximum length is close to 500 μm. By imaging a tick hypostome, **Figure 4.3A**, we verified the length and approximated that the penetration was likely not beyond 50%, which suggests the bacteria are likely deposited close to a depth of 250-300 μm during the tick feeding. Assuming the penetration would be close to 50% of the MN length, we selected four microneedle designs to test (**Table 4.1**). Each microneedle design was placed on the side and imaged with a light microscope. The images were imported into ImageJ. Individual PVA microneedles were measured. The average length and standard deviation of the needles was reported for each design (**Figure 4.3B**).

3D printed microneedles were shorter (**Figure S4.2**) relative to the computer-aided design (CAD) file used to create them (**Table 4.1**). A loss of ~ 30% decrease in 3D microneedle height was found compared to the design, but the width maintained close approximation to the CAD file. This is a very similar 3D printing phenomena reported in other microneedle papers [324]. One explanation for this reduction in height but not width is due to the scattering of UV light during the exposure of larger portions of 3D prints compared to smaller size parts. The less material, the less light scatter to initiate photopolymerization to

cure the material. Similarly, other authors found that with more light intensity, the more initiation of the photopolymerization. They also found an increase in size of structure increased with light intensity [325].

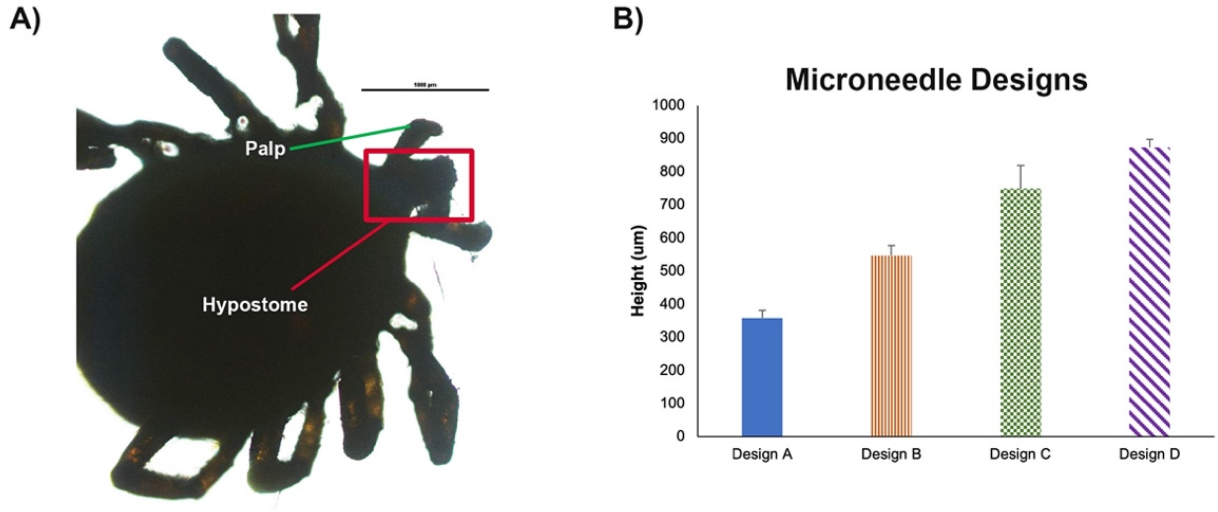

Figure 4.3. MN Design. A) Light microscope image of a tick hypostome around 500 µm. Scale bar 1000 µm. B) Measured height for each PVA MN design from Table 1 with four needles per patch (n = 3) ± SD.

Penetration Test

The penetration of a MN to a specific depth is an important characteristic. The PF test results indicate that the shortest microneedle design (400 µm in length) is not able to penetrate to 300 µm. Additionally, the longest microneedle (850 µm in length on average) exhibited bending between PF layers and did not penetrate efficiently to the third layer. Designs B and C showed efficient penetration to the third layer of PF (**Figure 4.4A**).

With MN designs from **Figure 4.3B**, we inserted the MN into a gel and visualized penetration with OCT imaging. Results show Design A and D did not penetrate the gel efficiently (**Figure 4.4B**). The red false coloring (Adobe Photoshop) shows the empty space between the microneedle and the top layer of PF. Both Designs A and D show empty space and thus, reduced penetration while Designs B and C show much less empty space. Therefore, the results indicate the ideal length for 10% PVA microneedles appears to be

between 500-750 µm in length. A OCT 2D cross-sectional (B-scan) of 2% (w/w) gel was imaged during application of a MN and after removal of a MN showing holes left behind in the gel (**Figure S4.5**).

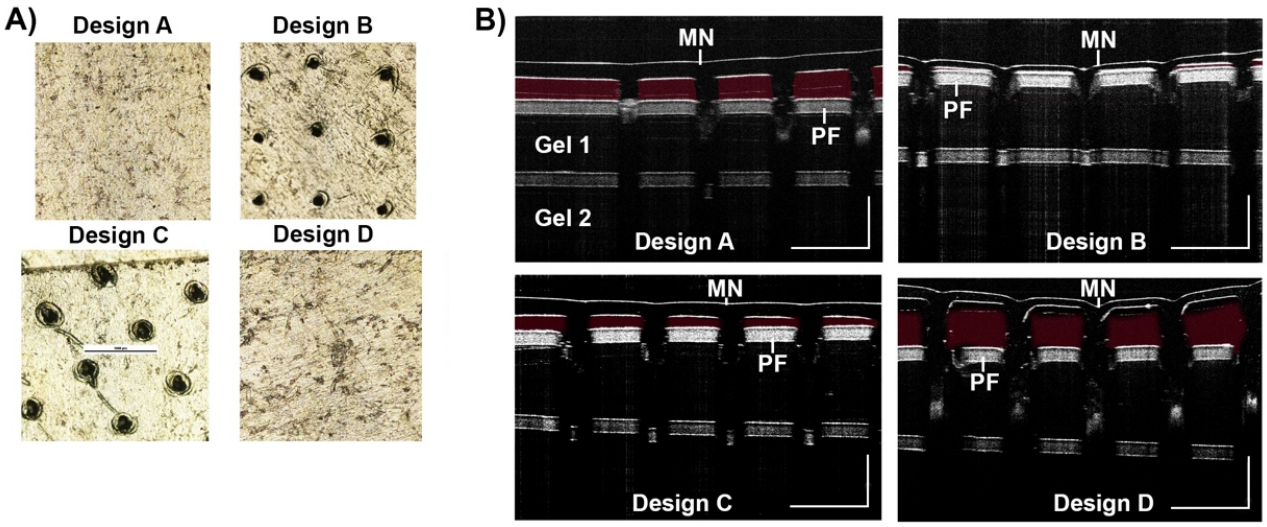

Figure 4.4. Penetration test for MN designs. A) PF penetration to the 3rd layer was imaged on a light microscope for the four designs. B) OCT 2D cross-sectional (B-scan) images were taken of each MN design after insertion into a 2% (w/w) gel with a one sheet of PF on top of the gel, a sheet of PF below gel 1, and another 2% (w/w) gel below the second sheet of PF (gel 2). Scale bar 1000 µm.

Mechanical Tests

Young's modulus was calculated to be approximately 0.0014 MPa. The yield strength for the patch is 0.00030 N/mm^2. The deformation force was found to be 4.2 N. This is in the range of what others have found with similar PVA microneedles [326].

Light microscope images taken before and after weights were placed on MN patches. The MN could withstand up to 255 g of weight added before slight bending was observed. However, when 80K g was placed on the MN patch, the 90-degree bending was observed (**Figure S4.3**).

Swell and Absorption Tests

Light microscope images taken before and after insertion of Design B MN into a gel (**Figure 4.5A**). In **Figure 4.5A**, the left side shows a smaller microneedle compared to a more swollen microneedle. Additionally, a dry microneedle was imaged on SEM **Figure 4.5B** (left) compared to a SEM image of microneedle after 10 µl of liquid was added to the center and allowed to sit for 10 min (right). Beyond 10 min, the MN did not change in mass so 10 minutes was set as the saturation time point.

Microscope images show green dye in the needle tips indicating the microneedle absorbed the green dye (**Figure 4.5C and 4.5D**). The top view of the microneedle shows the green color was absorbed into the individual microneedle only (**Figure 4.5E**).

Results of the swell test using 40 µl of water show on average, the weight of the design B MN patches increased by approximately 46% after being placed on a water droplet (n =4).

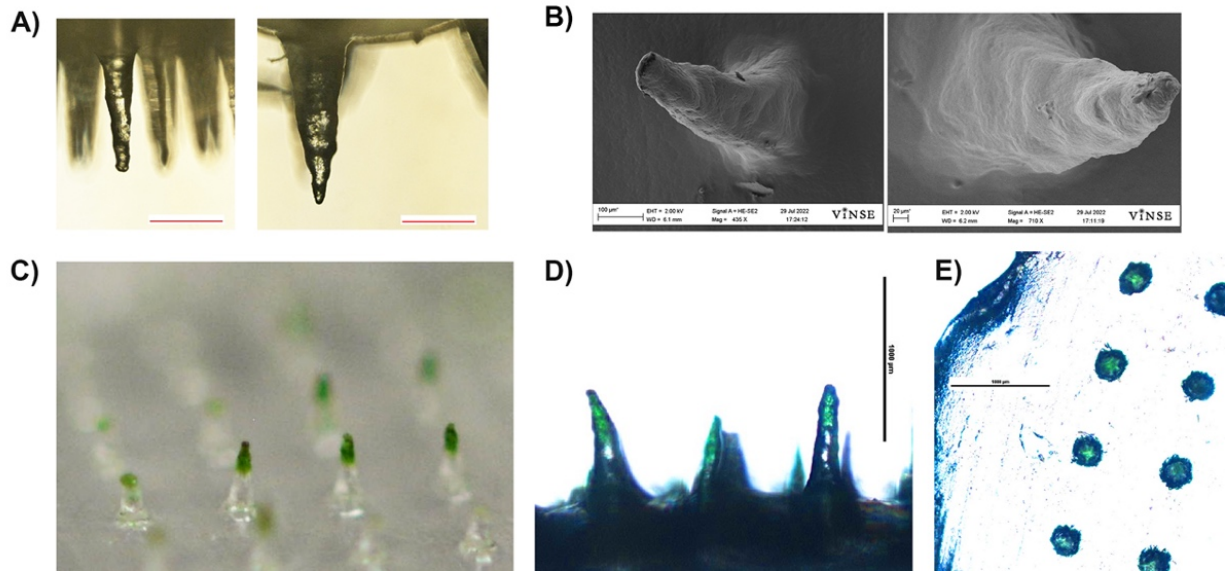

Figure 4.5. Representative images of the swell and dye absorption test. A) Light microscope images of a MN before insertion into a gel (left) and after insertion (right). Scale bar 200 µm. B) SEM images of a dry MN (left) and a MN insertion into liquid for 10 min (right). C) Photograph (Nikon D610) of the microneedle patch after insertion into a gel with green dye below PF layer. D) Light microscope image (4x) of microneedle after insertion into a gel with green dye below PF layer. Scale bar 1000 µm. E) Light

microscope image (4x) top view of the microneedle patch after insertion. Scale bar 1000 µm.

Volume needed to dissolve PVA MN

Four volumes were tested to dissolve a PVA MN (**Figure 4.6**). Testing showed the MN (mass ~ 11 mg) needed a volume 50 - 100 µl of TE buffer to fully dissolve. The 50 µl volume required incubation at 115 °C and vigorous vortexting. Although smaller volumes were tested, these solutions did not dissolve the MN after vortexing and 115 °C incubation (**Figure 4.6**). The results suggest dissolving the PVA MNs requires full submersion of the MN into the TE buffer.

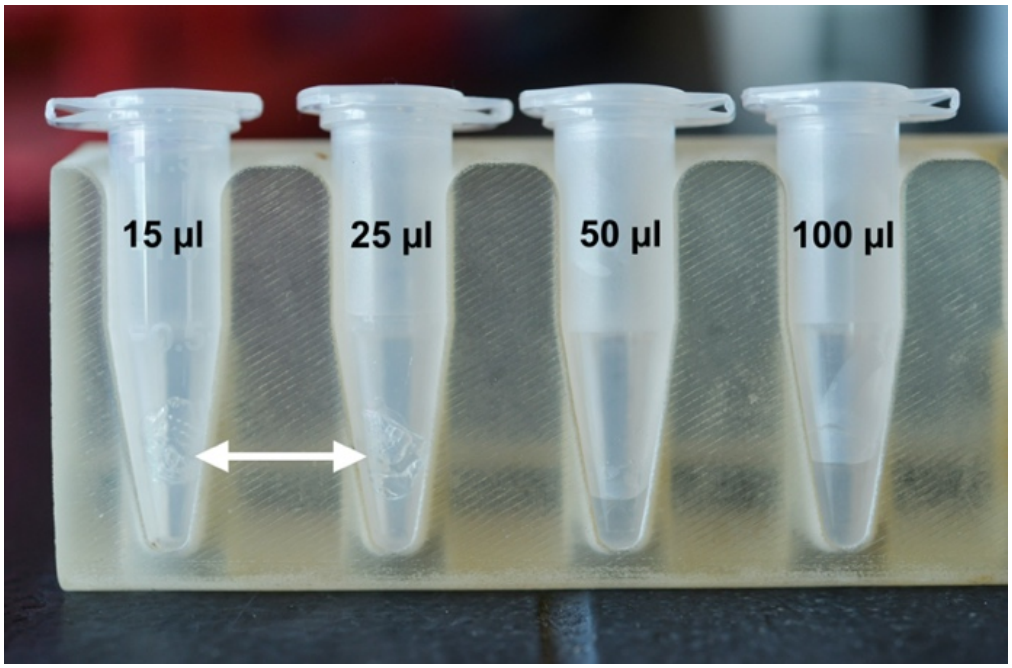

Figure 4.6. Representative images of microneedle inside tubes of TE buffer. A MN is placed into an Eppendorf tubes with 15, 25, 50, and 100 µl of TE buffer. (n =3). White arrows indicate an undissolved MN in the tube after 10 min of incubation at 115 °C.

Penetration of MN in porcine ear skin by OCT

OCT was used to confirm the penetration of MN into porcine ear skin. Results show the MN successfully penetrated the porcine ear skin. However, for pig ear skin samples with hair (**Figure 4.7A and Figure**

4.7B), there was a reduction in penetration as shown in **Figure 4.7D.** Red false coloring (Adobe Photoshop) was added to the space between the MN and the porcine skin to show the gap. In a pig skin sample with little to no hair (**Figure 4.7F and Figure 4.7G**), the penetration was more successful. Results show greater penetration occurred in samples with no hair (**Figure 4.7I and Figure 4.7H**) than in images of the samples with hair (**Figure 4.7C and Figure 4.7D**). This suggest that before application of a microneedle, hair should be removed to enhance penetration depth of the MN.

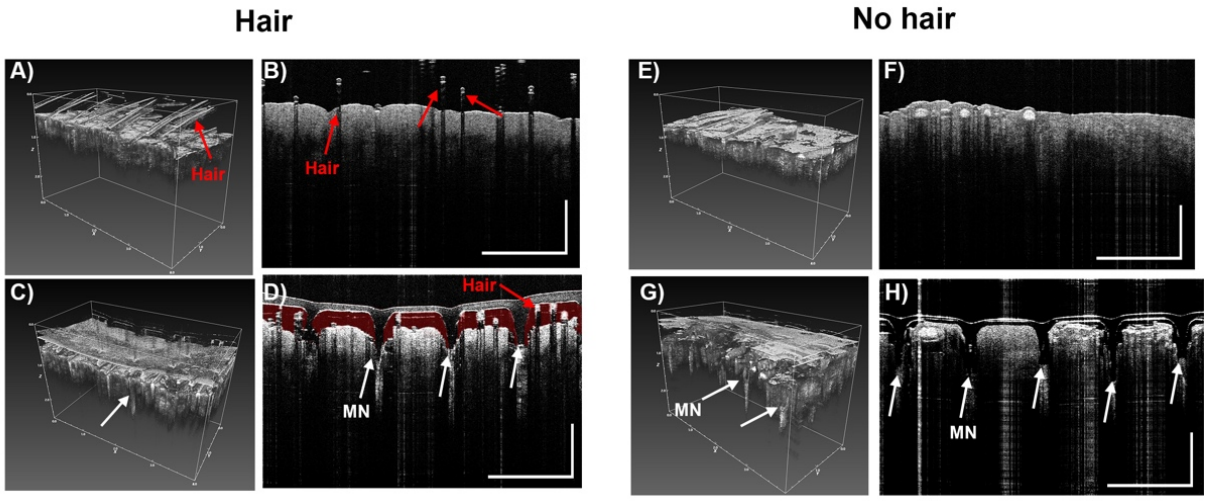

Figure 4.7. Representative OCT images from before and after penetrations of PVA MN array with microneedle height of 500 µm (Design B) into porcine ear skin. A) Without a MN there are no holes in the skin with hair in 3D OCT image, B) 2D cross-sectional (B-scan) image in skin sample with hair C) MN inserted into sample with hair in 3D OCT image, D) 2D cross-sectional (B-scan) image of MN inserted into skin sample with hair (red false coloring added to show gap between MN and skin). Scale bar 1000 µm. E) Porcine skin with no hair in 3D OCT image before MN application. F) 2D cross-sectional (B-scan) image in skin sample with no hair before MN application, G) MN inserted into sample with no hair in 3D OCT image, H) 2D cross-sectional (B-scan) image of MN inserted into skin sample with no hair. White arrows show the holes in the epidermis of the pig skin showing penetration (n = 3). Scale bar 1000 µm.

RNAse P Assay for sampling control

A one-way ANOVA was used to compare the MN collection of pig samples by using the RNAse P assay. There was no significant difference found between collection of the MNs applied to a porcine ear regardless of bacteria present in testing (F = 0.25, P value = 0.79). The average Ct value of the applied MNs were found to be 27 with a standard deviation of 2 cycles (**Figure 4.8**). As a negative control, a MN was not applied to pig ear skin but directly dissolved and tested against the three groups. The dissolved MN showed a significant difference in Ct value compared to the other three groups (F = 214 and P values < 0.001).

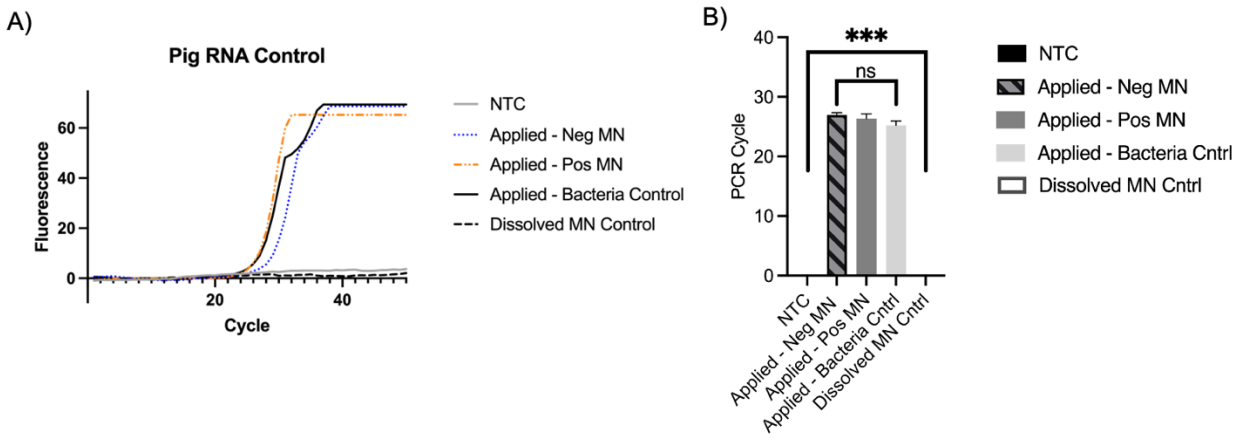

Figure 4.8. RNAse P Assay for extraction control results (n =4). Samples from **Figure 4.9** were re-run to test for the presence pig RNase P to ensure the MNs were applied long enough to the pig skin sample to collect RNA. A) RNAse P PCR results. B) Bar graph showing the comparison of the PCR amplification cycle.

All the MNs applied to the pig skin samples were positive as shown for both the positive MN and negative MN because each sample contained sufficient pig RNA sample. This test is for pig RNA detection in the MN so all MNs applied to the skin should be positive. In an assay that incorporates this control, if the MN sample is negative for RNAse P this indicates the MN did not collect sufficient sample to test and it is invalid.

MN Capture of inactivated B. burgdorferi

For capture testing, we measured the extraction recovery of two concentrations of inactivated *B. burgdorferi* spirochetes with our MN patch placed on pig ear skin. A PCR was performed in triplicate for these samples to calculate the amount captured by the MN patches. The standard curve shows intensity of fluorescence versus cycle number with the separation of curves in proportion to the logarithmic dilutions of target (*B. burgdorferi* gene flaB) (**Figure S4.6**).

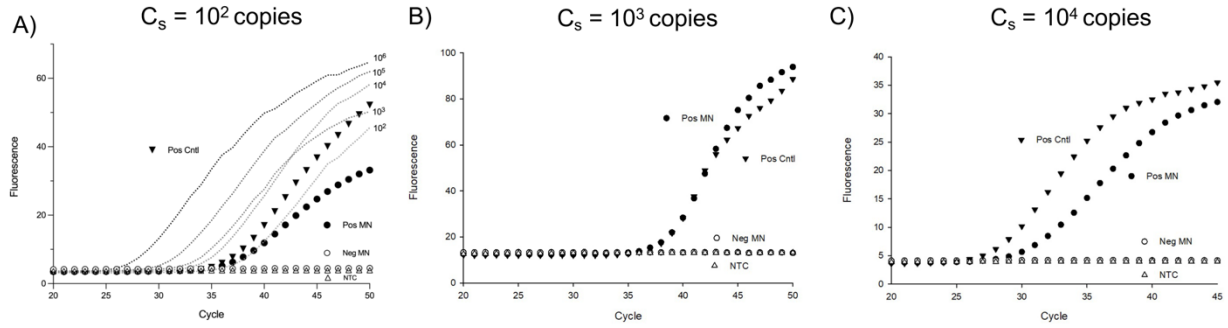

Figure 4.9. PCR results of MN patches applied to porcine ear skin. A) 10^2 bacteria were deposited to the depth of 300 µm and four MN were applied to the location for 10 minutes and subsequently dissolved in 50 µl of TE buffer for PCR (n = 4). B) 10^3 bacteria were deposited to the depth of 300 µm and four MN were applied to the location for 10 minutes and subsequently dissolved in 50 µl of TE buffer for PCR (n = 4). A positive control was made by pipetting 10^3 bacteria into 50 µl of TE buffer (n = 4). As a negative control, four microneedle patches were applied to porcine ear skin for 10 min and dissolved in 50 µl of TE buffer before PCR (n = 4). C) 10^4 bacteria were deposited to the depth of 300 µm and four MN were applied to the location for 10 minutes and subsequently dissolved in 50 µl of TE buffer for PCR (n = 4). A positive control was made by pipetting 10^4 bacteria into 50 µl of TE buffer (n = 4). As a negative control, four microneedle patches were applied to porcine ear skin for 10 min and dissolved in 50 µl of TE buffer before PCR (n = 4).

Performance of the MN patches to recover bacteria was obtained by comparing the concentration recovered by microneedle patches with the initial concentration of bacteria spiked into pig skin (positive control). Our results show an approximate 80% recovery of bacteria compared to the bacteria spiked. Variation was also

seen in the PCR experiments with the microneedle's recovery of bacteria (**Figure S4.7**). In other experiment, we found a large variation in the positive control tubes likely due to the bacteria clumping during the reconstitution and dilutions. For lower concentrations, variation was larger.

4.4 Discussion

In this report, PVA MN patches have been studied for their penetration performance, swelling characteristics and recovery of bacteria spiked into a pig ear. Our results showed the most successful MN was Design B, which was 500 μm in height (**Table 4.1, Figure 4.3B**). Design B showed successful penetration beyond 200 μm (**Figure 4.4** and **Figure 4.5**) which is the depth that bacteria would likely be found. Additionally, ISF fluid is also at depths > 200 μm so our MN show successful penetration into the area to collect LD biomarkers. Our results showed 46% swelling that can further be optimized with various other cross-linking reagent to enhance swelling [302]. After inserting into pig ear skin, the MN showed successful capture of inactivated B. burgdorferi (**Figure 4.9**). On average, our assay was able to capture approximately 80% of the bacteria spiked into porcine skin. Since the MN did not penetrate far enough to be painful (500 μm), the PVA MNs herein show promise as a detection tool that is easy to use and painless to apply.

We have developed a method to sample skin with a swellable MN that detect inactivated bacteria in a purification-free method. Conventional tissue biopsy or tick testing takes hours by comparison and results in the destruction of the bacteria as well as a loss of starting material after numerous processing steps. We show the extracted bacteria can be directly detected by PCR without further processing steps (**Figure 4.9**). We also show 10 minutes is sufficient time to recover the majority of bacteria present. Further studies should confirm the optimal time to capture bacteria at different depths in the skin.

Our results show 50-100 μl of TE buffer is required to successful dissolve the MN. Additionally, it is critical to vortex and incubate at 37 °C - 115°C for the MN to fully dissolve prior to PCR testing. Future work may investigate addition of smaller volumes of reagents that may disrupt the cross-linking of PVA and successfully dissolve the MN without diluting the sample. In this report, we did not test the stability of

the microneedles before dissolving, however, researchers showed 10% PVA MNs have been shown to be stable for up to a week after DNA extraction from plants [327]. This suggests that if PCR cannot be performed directly after extraction, non-dissolved MNs can be tested for up to a week after extraction. Given the ease of use and affordability, this bacteria extraction method could be further optimized to enable direct to lab processing for suspicious arthropod bites.

Human skin is the most suitable sample to evaluate microneedle performance, but the availability of human skin is limited by ethical, regulatory, and cost considerations [328]. Therefore, murine and porcine skin has been used as a substitute to human skin [329]. Porcine skin is considered a closer approximation to human skin since it is histologically and anatomically closer to human skin [330]. These similarities include the epidermal thickness, dermal-epidermal thickness ratio, hair follicle and blood vessel density and collagen and elastin content [328], [331]. Specifically, porcine ear skin is 10 μm thick so it is closer to human epidermis thickness and therefore is considered a closer model to human skin [332]. Our comparison across the MN used in bacteria extraction showed each group was applied to the porcine skin long enough to capture pig RNA and that the groups did not differ in their extraction of pig RNA (**Figure 4.8**). In future work, a pig RNA control could be used in a multiplexed PCR reaction to verify the MNs recovered adequate sample regardless of bacteria present.

Although LD may present with the characteristic EM, other pathogens could still be transmitted with *B. burgdorferi* in the tick bite. These co-infections of multiple tick-borne diseases results in diagnostic challenges. Ticks may acquire and transmit many pathogens such as parasites, bacteria and viruses [333]. In 2018, one study examined 16,080 ticks that were mostly removed from humans and found that 88% were co-infected [334]. A MN-based method combined with multiplex PCR would give more information to the patient and physician about the possibility of co-infection of multiple tick-borne diseases.

There are several areas to further improve bacterial capture of this method. Although PVA does swell, other reports have shown much greater degree swelling (up to 450%) by using cross-linking reagents [302]. A greater amount of swelling would likely capture more bacteria and result in higher recovery. One other limitation in our approach is the use of inactivated bacteria. To match patient skin testing, live bacteria

should be tested to better understand our assay performance and if additional steps for bacterial lysis are required prior to PCR. To increase live bacterial capture, one future approach is the use of a chemoattractant. Uptake of the spirochete in blood by an uninfected tick requires chemical signaling in the tick saliva to attract spirochete, which is the principle of xenodiagnoses (i.e., using a vector to acquire the pathogen for further testing)[335]. Recently, researchers have compared different motility assays to identify chemoattractants in tick saliva in order to improve diagnosis (via skin MN patch or subdermal injection/implant) [336, 337]. Tick saliva contains many molecules that are able to be used by infectious agents to promote transmission [338]. A microneedle patch doped with chemoattractants for the bacteria may draw the bacteria to the patch for capture and detection while also blocking an inflammatory response to the MN [336]. Without the tick saliva, the host's cells may induce an inflammatory response against the bacteria. Anti-inflammatory molecules in tick saliva prevent attraction of dendritic cells, mast cells, macrophages, and lymphocytes [167]. Thus, tick saliva increases the virulence and survival of B. burgdorferi by blocking the inflammatory response [166]. With the inclusion of chemoattractants and cross-linking agents to enhance swelling in a MN, the low levels of bacteria that remain problematic for traditional testing, may be overcome with such a technology.

The number of spirochetes in the skin can vary widely due to the stage of the tick attached and duration of attachment to host. We did not do a complete limit of detection in this report. We tested three concentrations of inactivated *B. burgdorferi* (**Figure 4.9**) based on what has been reported in skin biopsy reports [187], and one limitation in this report is that this concentration may not match the number from an initial tick bite. This needs further investigation and development. Our PCR was not reliable for detecting low amounts of the inactivated spirochetes. Attempts to test lower ranges were limited by variability of clumping of the fixed bacteria. This could be overcome in a few ways. By picking a different gene target that repeats multiple times in the spirochete genome, a lower limit of detection could be achieved possibly. Nested PCR has shown a lower limit of detection of just one spirochete from culture [323]. Another way is digital PCR (dPCR) which allows individual segmentation of into wells with either none or one target before amplification. In 2020, researchers developed a dPCR assay that was able to detect three genome

copies of *B. burgdorferi* [339]. By including an enrichment step to pre-amplify DNA prior to dPCR amplification, the authors overcame the low sensitivity in patient blood samples that are due to low numbers of bacteria [188].

4.5 Conclusions

This poly(vinyl alcohol) microneedle method enables rapid detection of tick-borne pathogens in skin models. We demonstrated the MN had sufficient stiffness to penetrate porcine ear skin and the MN could extract inactivated *Borrelia burgdorferi* for direct PCR detection. With further development, this technology could eventually achieve early detection of the causative agent of Lyme disease.

CHAPTER 5: IMPACT OF STUDIES AND FUTURE DESIGNS FOR FURTHER IMPLEMENTATION

My work presented in this dissertation endeavored to overcome specific challenges in multiple low resource diagnostics technologies that benefit underserved populations. Although diverse projects are shown, the work showed a common theme of demonstrating how more easily obtained sample types could be used in low resource settings specifically since many of these diseases are impacted by underfunded healthcare systems. From the development of a use power-free volume deposition device for urine dipstick pads, to a device to monitor HE4 levels in urine over time, to direct bacteria sampling from a tick bite with a low-cost MN for early LD disease detection, and finally detection of short DNA fragments in urine for TB detection in populations who cannot produce sputum. All these technological projects focus on underserved populations such as Mesoamerican CKDnt patients, OC patients who cannot pay for expensive blood tests, populations who are exposed to tick bites and lack diagnostic tools for direct sampling, and finally, populations who cannot produce sputum for TB testing such as infants, children, and HIV patients. The results of my work help to overcome some of the gaps in equitable healthcare and provide a contribution to the development of technology to reduce barriers to diagnostic testing. Overcoming challenges in self-sampling for non-invasive samples is critical to facilitate testing for public health technologies.

Impact, Limitations & Future Directions for Chapter 2

In chapter 2, I address the challenge of creating a power-free volume deposition method for dipstick urinalysis keeping ASSURED criteria in mind. This method is affordable with just using 3D printed and acrylic for fabrication. The device is also user friendly and can be rapidly performed by untrained users quickly. The device is also equipment free. With inclusion of appropriate dipsticks of other urine-based test formats, the device may also achieve high sensitivity and specificity. In the context of underserved diseases in LMICs, this tool could be used for CKDnt early detection. Deaths from chronic kidney disease of nontraditional origin (CKDnt) have reached to the tens of thousands per year in Mesoamerica[340]. CKDnt has been often reported in sugarcane and other similar high intensity agricultural work in heat stressed

environments. As increasing temperatures threaten to increase CKDnt burdened countries, widespread adoption of kidney screening with dipsticks could reduce mortality. Publication of this work in JoVE has added to the field by greatly reducing the possibility of user error and controlling several aspects dipstick operation for untrained users.

A major limitation in this approach is the peeling of the Neverwet coatings after frequent use. As the coating peeled, the liquid could leak and alter the volume deposited. Another problem was the acrylic glue used to adhere the top plate and base plate could weaken after several uses and require more acrylic glue to adhere again. An alternative our SlipChip dipstick platform without acrylic glue and without hydrophobic coating was also designed and tested (**Figure 5.1**). This design drastically reduces the time needed to fabricate the device as there were no waiting periods to allow the acrylic glue to dry (24-28 hours) or waiting periods for the hydrophobic coatings to dry (12-24 hours). The platform was all acrylic and easily assembled with screws. The device can be adequately cleaned as needed between sample testing without suffering from hydrophobic coat peeling or acrylic bonding weakening. To speed up drying, a can of compressed air can be used to remove any remaining droplets. As this platform is easily assembled, cleaned, re-useable, and power-free, this would allow for remote monitoring of kidney function in areas with barriers to resources are higher such as in LMICs.

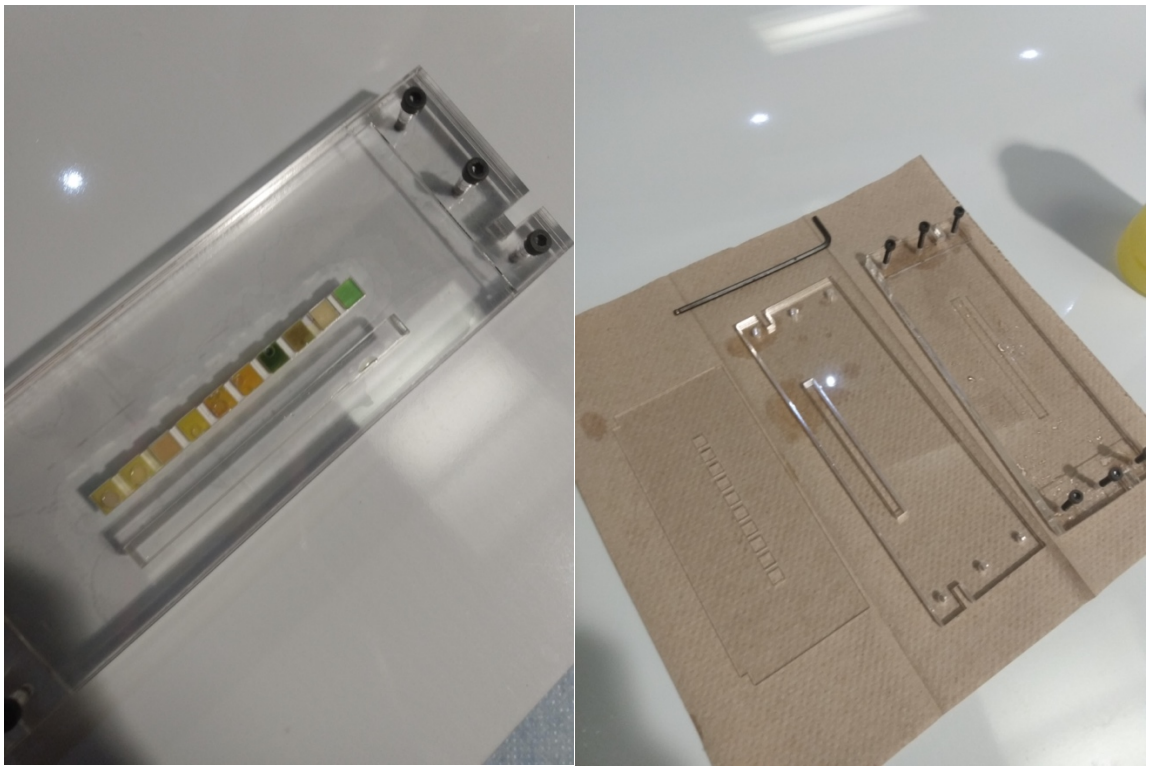

Figure 5.1. A spray-free and glue-free version of the SlipChip urinalysis platform made from acrylic.

One other limitation is the reliance on a smartphone. Another alternative feature would be inclusion of a blue tooth enabled color sensor to identify frequency of reflected light and report RGB values wirelessly to a user's phone app or a physician's data base. Both the chart sticker and the dipstick can be measured by a color sensor under the same lighting conditions. A smart phone application can receive the (R,G,B) components and calculate the color difference of both the reference chart and dipstick pad. This would allow for increased testing standardization since direct measurement by cell phones varies greatly by type of cell phone lens, image resolution, sensor, and lighting vary by manufacturer and model[230]. A urinalysis platform that includes a standardized dipstick image analysis would be more amenable to patient self-testing or remote monitoring by a physician.

Impact, Limitations & Future Directions for Chapter 3

In Chapter 3, an important advancement of monitoring a urine protein is a built-in control to allow for normalization of the biomarker since urine volume fluctuates throughout the day. I funded and

developed a quantitative lateral flow assay to detect the ovarian cancer biomarker HE4 in urine. This technology also adheres to the ASSURED criteria in several ways. The device is user-friendly, equipment free aside from cellphone, and affordable as the fabrication is all 3D printed and paper-based test components. I characterized the limit of detection and the accuracy of both the HE4 and creatinine. Both analytes are easily detectable in the method. Clinical testing with the device could be further studied with patient samples to identify sensitivity and specificity to fully meet the ASSURED parameters for low resource testing. Early detection of ovarian cancer and ovarian cancer recurrence would greatly reduce mortality. Since up to 70% patients will face a recurrence of disease, physicians continue to seek tools for monitoring ovarian cancer. I confirmed the device worked across the ratios associated with recurrence of ovarian cancer as well as testing with a positive patient sample for OC. Additionally, we also confirmed that test strips could be quantitated with a benchtop scanner as well as a cell phone. A direct comparison between the FDA approved blood test to measure HE4 for risk assessment and the developed technology in this chapter would provide an insight into the possibility of home-testing for users in developed countries as well as suitability in LMICs. Publication of this work in *Nature Scientific Reports* is the first of its kind to use conventional LFA technology coupled with creatinine measurement to normalize a cancer biomarker in urine.

One critical limitation is the reliance on a dilution step as this presents an additional step for a patient and is more error prone as a result. To offset this, a specific-sized pipette coupled with a pre-aliquoted deionized water vial can be combined easily to help offset errors in measurement. A step-by-step guide or QR to a “how to” video might reduce complication. It should also be noted, many COVID-19 at-home test also required users to mix their sample with a pre-aliquoted tube before applying it to the lateral flow. This suggest that an extra step to add a sample to a pre-aliquoted tube, is likely amenable to users, especially for users who have done it previously.

Another limitation to this work is that while most commercial LFAs include a spray-dried conjugate release pad in their test format but in our prototype, we did not use an air jet dispenser to spray our reporter onto a release pad. Instead, we combined our sample with the reporter in a single Eppendorf tube for 10

minutes and spotted onto the sample application pad. It is critical to verify if the reporter performs in a spray-dried release pad in future work. Additionally, another limitation to the current device is the temperature needed for creatinine incubation at 37 °C. Using a small heating element that is battery powered might be able to achieve this temperature affordably, but we did not achieve this. Finally, the battery powered light in the device would decrease when the battery was low. This could cause image analysis errors from decreasing illumination without the user knowing until after the test is completed. Therefore, automating the light function with the camera function could prevent this from occurring.

On-going efforts to explore the functions of extracellular HE4 protein will elucidate the role played in OC and OCR. Recently, Wang et al reported that HE4 ANXA2-MMP2 forms a triple protein complex that promotes the migrations of cancerous cell lines[341]. 2022 study by Yu et al indicates that antibody neutralization of HE4 suppresses ovarian cancer cells and improves cisplatin resistance therapeutic effects-based chemotherapy[342]. Therefore, a future application of our technology could quantitatively monitor the reducing levels of HE4 in urine to assess therapeutic efficacy and patient prognosis. Finally, studies have shown multiple biomarkers have shown to have higher diagnostic performance than a single biomarker alone. Some candidates to include in the device include matric metalloproteinases (MMPs), MicroRNAs, and other proteins such as glycosylated forms of osteopontin fragments. Therefore, by including other biomarkers in the developed device, the sensitivity and specificity could greatly be enhanced or be suitable as a screening tool in higher risk populations such as those with genetic predisposition coupled with concerning symptoms (i.e., cramping, frequent urination or bloating) or menopausal status.

Impact, Limitations & Future Directions for Chapter 4

In Chapter 4, I characterized the requirements for optimal microneedle penetration into skin for depths suitable to tick-borne disease detection. I measured a tick hypostome length with a microscope and consulted literature on the published depths in LD carrying ticks. I used 3D printing to print multiple sizes and spacing of microneedle patches to test the penetration to in parafilm, gels, and porcine ear skin. Additionally, I characterized the penetration of microneedles using optical coherence tomography. We tested various solutions of PVA and characterized the degree of swelling as well as mechanical performance

of the MN. Critically, I test the volume required to dissolve the microneedle to facilitate PCR testing. I tested the performance to capture inactivated *borrelia burgdorferi* by spiking known amounts into the pig ear skin and comparing it to the positive control with PCR. I ensured the microneedle patches were sampling equally regardless of pathogenic bacteria present by comparing PCR cycle amplification from a RNase P assay. Publication of this work in *Biosensors* was the first of its kind to use a low-cost, easy to use microneedle patch for direct capture of a tick-borne pathogen in the skin. Although it needs additional development to fully meet all of the ASSURED criteria, the microneedle patch is affordable, delivered to the patient, user friendly. LAMP (loop-mediated isothermal amplification) allows amplification of nucleic acids at one temperature as a visible colorimetric read out. Recent work has shown detection of vector borne diseases using LAMP[343]. The MN patch I developed could be paired with LAMP technology to fully meet the ASSURED requirements.

There are several areas to further improve bacterial capture of this method. Although we have shown PVA MNs swell up to 46% of weight, other reports have shown much greater degree swelling (up to 450%) by using cross-linking reagents [302]. A greater amount of swelling would likely capture more bacteria as well as result in higher recovery. Another limitation in our method is the use of inactivated bacteria. To validate the method could work in a patient sample, live bacteria should be used to with the microneedle. It remains unclear if additional steps for bacterial lysis are required prior to PCR in our approach. Another limitation was we did not complete a LOD of detection. Finally, our last limitation is the inability to combine the RNAseP assay and the bacteria detection in one multiplexed test. It would be ideal to run both PCR reactions on the same PCR machine simultaneously to validate the workflow.

Since many ticks are co-infected, we can modify our current MN technology to include a multiplexed PCR reaction capable of detecting both types of live bacteria in PCR. In one objective, we can determine the limit of detection of the PCR reaction for both bacteria. In another objective, we can modify the MN to improve extraction with cross-linking agents that enhance swelling. We could characterize the extraction efficiency of this system and compare to a biopsy skin approach to determine the overall clinical utility.

In another approach, we can take advantage of the fact that tick saliva contains many chemoattractants that attract *B*. *burgdorferi* [21]. We can characterize the release of the tick saliva from the MN using optical coherence tomography or fluorescence-based imaging. We can then determine the amount of tick saliva needed to attract bacteria and formulations of chemoattractant that attract the most wild-type strains of bacteria to the MN in 2% (w/w) gels. Recent work in 2022 has shown the topical steroid Clobetasol increases the abundance of *Borrelia burgdorferi* in the skin up to 70 times[344]. The authors postulated that the topical application of Clobetasol could increase the sensitivity of a direct diagnostic methods such as skin biopsy or culture. Therefore, we could either dope a MN patch with clobetasol or apply the topical steroid before application of the MN patch. Finally, we use our tick-saliva doped MN to capture multiple bacteria and arboviruses in either mice or primate models. We can determine the performance of the MN to detect multiple pathogens from a recent tick bite and from late-stage LD. After IRB approval, we will use our best performing MN design to apply to patients who present with an EM at clinics. After application, the MN patches will be tested for multiple tick pathogens. The results will be compared to the standard diagnostic testing results to determine sensitivity and specificity of the diagnostic.

Impact, Limitations, & Future Directions for Preliminary studies in for Detection of Tuberculosis Cell Free DNA in Urine

In Appendix section 4, I tackled the problem of capturing and reconstructing short TB cf-DNA fragments with a magnetic bead. I tested multiple coupling chemistries and beads with a DNA capture strand. I investigated various methods to prevent false positives such as boiling strategies to stabilize the capture strand DNA on the bead, uracil glycosylase degradation with capture DNA strand designed with uracil, uracil intolerant polymerases to inhibit amplification of uracil containing DNA templates, and finally, use of RNA capture strand on a magnetic bead. I tested the ability to detect a 15 bp and 22 bp fragment of the IS*6110* genome. I compared the incubation times of a fluorescent labeled 15 bp fragment with flow cytometry and found 30 minutes at room temperature is sufficient to hybridize a fragment to a capture strand. I compared the capture of various amounts of a 22 bp fragment and determined that the

method could detect 10^2 copies of the fragment. I also detail the work that remains to bring this project further into development below.

A limitation in this project is the lack of urine samples provided to simulate real testing conditions. It is unknown if the designs and methods could perform with actual urine samples. Another limitation in this project is the frequent contamination encountered throughout the various designs. Having the high copy number DNA boiled throughout the lab by multiple lab members as well as multiple people using the same sequence in the same PCR spaces possibly contributed to the contamination issues. A significant limitation is the lack of reagent control throughout this project. Although I successfully reconstituted IDT nucleotide tubes in chapter 4, I was forced to rely on someone else reconstituting TB tubes for unknown reasons. This reduced the knowledge of reagent handling and possible issues accounting for the performance of the various designs tested. I was limited in many ways on this project in terms of reagent design, and reagent handling. Another critical limitation is the reliance on a specific sequence of *IS*6110. It is possible that other sequences are present in a positive patient sample that will be missed because of the reliance on a small portion of *IS*6110. Future work may seek to include other portions of *IS*6110. I am confident my suggestion using RNA for the capture strand and make cDNA from the fragment will be useful.

Due to the presence of PCR inhibitors, PCR cannot be used directly on most clinical samples, including human urine, without pre-treatment[345]. For the extraction recovery of surrogate patient samples, we could quantify post-extracted samples using PCR with a standard curve. The, we could take the ratio of the amount of DNA recovered after extraction divided by the amount of DNA spiked into the surrogate sample to obtain the fraction of DNA recovered. A primary aim is to determine the diagnostic accuracy of our TB sequence-based assay in clinical urine specimens. In a clinical cohort study, urine from 40-80 participants in South Africa could be studied. In addition to calculating assay sensitivity and specificity, we can compare assay performance across subgroups (HIV status, CD4 count, and smear status) and analyze the detected cf-DNA concentrations for correlations with clinical data (CD4 count, days to culture positivity). The results of this study may show that our approach is promising for the diagnosis of TB from

urine with cf-DNA and contribute to the growing body of evidence for urine cf-DNA as a biomarker for TB.

After initial urine collection, urine is often kept in a freezer for periods ranging from a few days to several months before analysis. However, studies documenting the impacts of sample collection conditions and storage temperature on urine sample integrity remains an area of ongoing research. In a 2015 study analyzing the impact of urine collection conditions with mass spectrometry[346], authors found that the use of preservative prevents bacterial overgrowth, but does not avoid metabolite instability in solution, whereas storage at 4 °C inhibits bacterial overgrowth at least over a 72-h period and slows the chemical degradation process. To further investigate these matters, we can use our pooled urine aliquots from the IRB, and store samples at different temperatures (4°C, -20°C, -80°C) for different time periods (days, weeks, months) to compare the degree of stability. Another important issue is the stability of the samples following the freeze–thaw process. In one LC–MS-based metabonomic study[347], urine stability was analyzed up to nine freeze thaw cycles without any effect on the profile. Finally, for frozen urine samples, we can compare the number of freeze thaw cycles with the first to determine the number of cycles which impact sample integrity.

Ethylenediaminetetraacetic acid (EDTA) is a chelating agent for divalent ions (Ca^{+2}, Mg^{+2} and Mn^{+2}) which is required for DNase activity[348]. The relative DNase activity of urine samples can be determined using the DNaseAlert™ QC System (Thermo Fisher Scientific catalog # AM1970) according to manufacturer's instructions. As described by Bordelon et al, different concentrations of EDTA can be added to the healthy urine samples in order to determine the sufficient amount of EDTA needed to suppress DNase activity[349]. Urine sample fluorescence values can be compared to a DNase negative control to confirm the presence of DNase activity.

As successful TB treatment is highly impacted by identifying drug resistant mutations, methods to detect mutations are urgently needed. Detection Minor Groove Binder (MGB) oligonucleotides selectively bind to the minor groove of DNA and form stable conjugations and duplexes with ssDNA while permitting shorter probe for hybridization studies. MGB exhibit a higher melt temperature and therefore, an increased specificity, particularly when there is a bp mismatch. The MGB with fluorophores are considered more

specific than typical DNA probes for SNP detection and could be used to detect drug resistant mutations in patient samples.

APPENDIX

Appendix 1. Supplemental Data for Chapter 2

Name	Company	Catalog Number	Comments
Black Cast Acrylic Sheet 12" x 24" x 1/8"	McMaster Carr	8505K742	$14.27
Chart sticker	Stickeryou.com		$12.39
Clear Scratch- and UV-Resistant Cast Acrylic Sheet 12" x 24" x 1/16"	McMaster Carr	8560K172	$9.52
disposable polyethylene transfer pipet	Fischer Brand	13-711-9AM	lot# : 14311021
Fortus ABS-M30	Stratasys	345-42207	lot# : 108078
Githut: https://github.com/Iftak/ UrineTestApp			
Innovating Science - Replacement Fluids for Urinalysis Diagnostic Test Kit (IS3008)	Amazon		$49
Nonwhitening Cement for Acrylic Scigrip 4, 4 oz. Can	MCM	7517A1	$9.22
Rust-Oleum 274232 Repelling treatment base coat-9 oz and topcoat 9-oz , Frosted Clear	Amazon	Color: Frosted Clear	$6.99
Urinalysis Reagent Strips 10 Panel (100 Tests) MISSION BRAND	Medimpex United, Inc	MUI-MS10	$10.59

Table S1. The components, source, and cost.

Appendix 2. Supplemental Data for Chapter 3

Python Code for LFA test line imaging

```
# Import necessary libraries

import cv2

import numpy as np


# Read

img = cv2.imread("lateral_flow_assay.jpg")


# Convert to grayscale

gray = cv2.cvtColor(img, cv2.COLOR_BGR2GRAY)


# Use Otsu's thresholding method to segment the test line

thresh = cv2.threshold(gray, 0, 255, cv2.THRESH_BINARY + cv2.THRESH_OTSU)[1]


# Clean up the thresholded image

kernel = np.ones((3,3), np.uint8)

opening = cv2.morphologyEx(thresh, cv2.MORPH_OPEN, kernel, iterations=2)


# Find the contours

cnts = cv2.findContours(opening, cv2.RETR_EXTERNAL, cv2.CHAIN_APPROX_SIMPLE)

cnts = cnts[0] if len(cnts) == 2 else cnts[1]


# Loop over the contours and draw them on the original image

for c in cnts:

    x,y,w,h = cv2.boundingRect(c)
```

```
    cv2.rectangle(img, (x, y), (x + w, y + h), (36,255,12), 2)


# Show the image with the contours

cv2.imshow("LFA", img)

cv2.waitKey(0)
```

Matlab code to image analysis;

```
clc;
clear;
close all;
imtool close all;
workspace;

%%Read in image (must be in source folder)
I = imread('1000_strip2.jpg');
imshow(I)
%figure
%imhist(I)

RGB =mean(I);
R = mean(RGB(:, :, 1));
G = mean(RGB(:, :, 2));
B = mean(RGB(:, :, 3));

hsv_image = rgb2hsv(I); %conversion from RGB to HSV
h = hsv_image(:,:,1); %HSV layer separation
s = hsv_image(:,:,2);
v = hsv_image(:,:,3);

%%Plots separate histograms for hue, saturation, and value
figure(2)
 subplot(3,3,1), imshow(h), title('Hue Image');
 subplot(3,3,2), imshow(s), title('Saturation Image');
 subplot(3,3,3), imshow(v), title('Value Image');

 subplot(3,3,4), imhist(h);
 subplot(3,3,5), imhist(s);
 subplot(3,3,6), imhist(v);

 %Uses any nonzero Counts and Calculates Average
```

```
%Components of Histogram
[hueCounts, hueBinValues] = imhist(h);
[saturationCounts, saturationBinValues] = imhist(s);
[valueCounts, valueBinValues] = imhist(v);
% Plot all 3 histograms in one plot.
subplot(3, 3, 8);
 plot(hueBinValues, hueCounts, 'r', 'LineWidth', 2);
 hold on;
 plot(saturationBinValues, saturationCounts, 'g', 'LineWidth', 2);
 plot(valueBinValues, valueCounts, 'b', 'LineWidth', 2);
 % Make x-axis to just the max gray level on the bright end.
 xlim([0 1]);

 %Uses any nonzero Counts and Calculates Average
 [rowHCounts]=find(hueCounts);
 ValuesofHueCount=hueCounts(rowHCounts,1);
 ValuesofHueBin=hueBinValues(rowHCounts,1);
 AverageHue=mean(ValuesofHueBin)


 [rowSCounts]=find(saturationCounts);
 ValuesofSaturationCount=saturationCounts(rowSCounts,1);
 ValuesofSaturationBin=saturationBinValues(rowSCounts,1);
 AverageSaturation=mean(ValuesofSaturationBin)

 [rowVCounts]=find(valueCounts);
 ValuesofValueCount=valueCounts(rowVCounts,1);
 ValuesofValueBin=valueBinValues(rowVCounts,1);
 AverageValue=mean(ValuesofValueBin)
```

Example Output:

```
AverageHue =

   0.5430

AverageSaturation =

   0.3829

AverageValue =

   0.4967
```

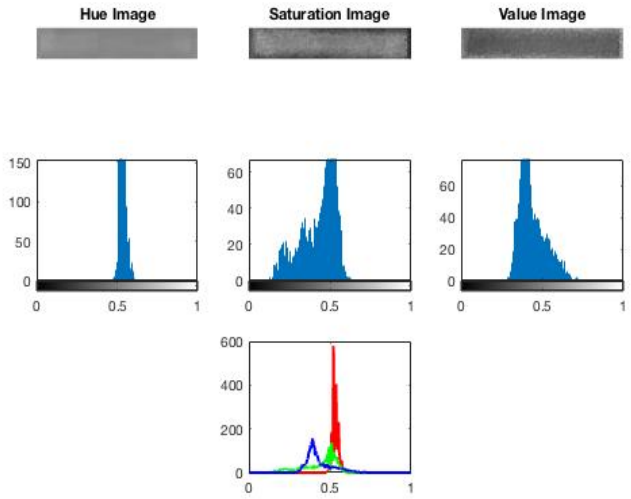

Output Negative Patient Sample

AverageHue =

0.5296

AverageSaturation =

0.2745

AverageValue =

0.5765

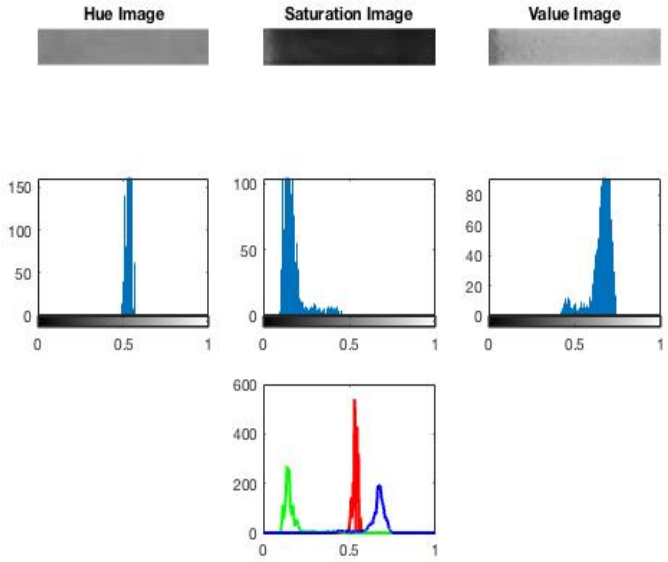
Hue Image
Saturation Image
Value Image
150
100
50
0
0
0.5
1
100
50
0
0
0.5
1
80
60
40
20
0
0
0.5
1
600
400
200
0
0
0.5
1

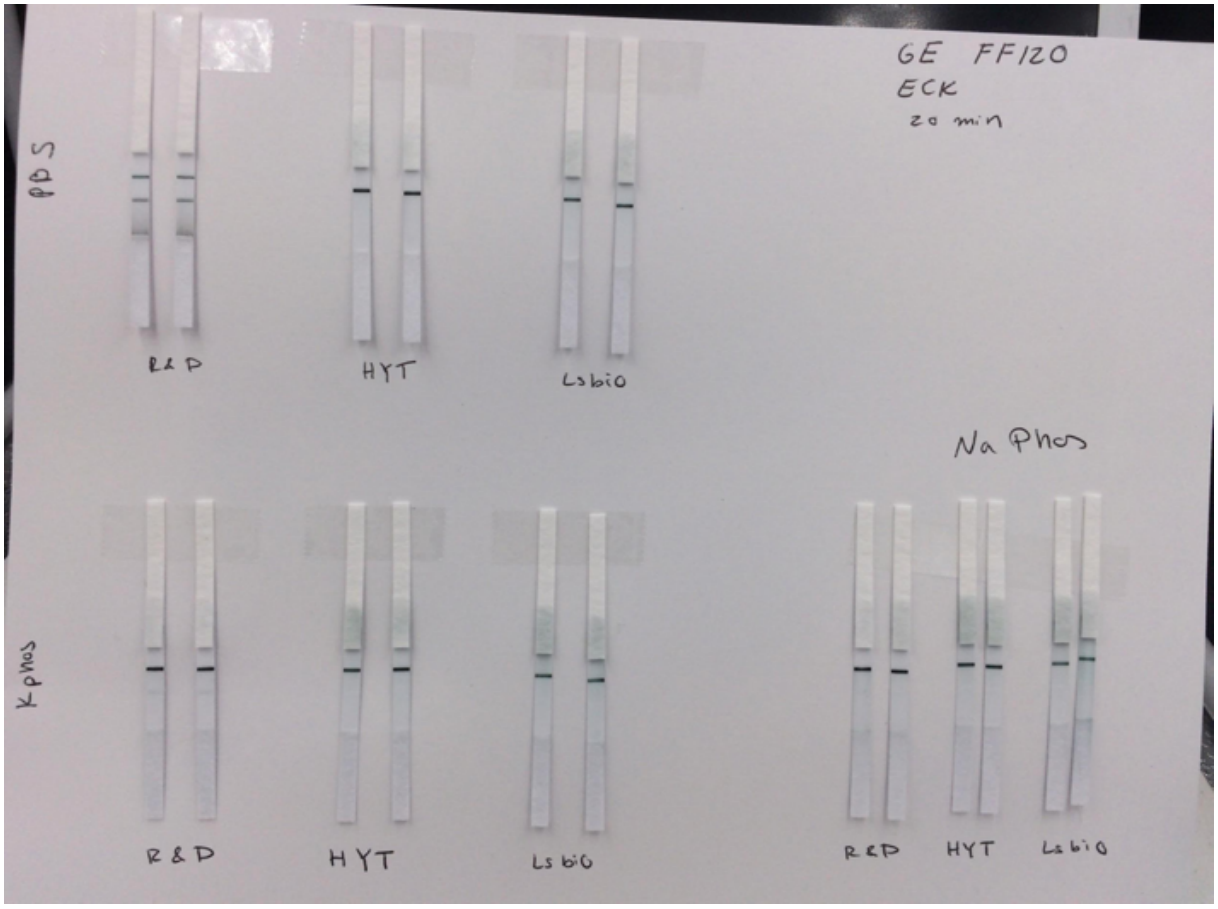

Figure S3.1. Photo of test strips of three types of mouse monoclonal antibody conjugated to a nanoparticle across three types of buffers (PBS, KPhos, NaPhos). Each membrane was striped with a Chicken Igy bottom line as a negative control. Each test was also striped with a positive control with goat anti-mouse at 1 mg/ml above the negative control line. Since all of our antibodies were mouse derived, they should only react at the positive control line (top). R&D antibody in PBS running buffer bound to the negative control line which means it's not a good candidate to test with as it would likely have lots of non-specific binding.

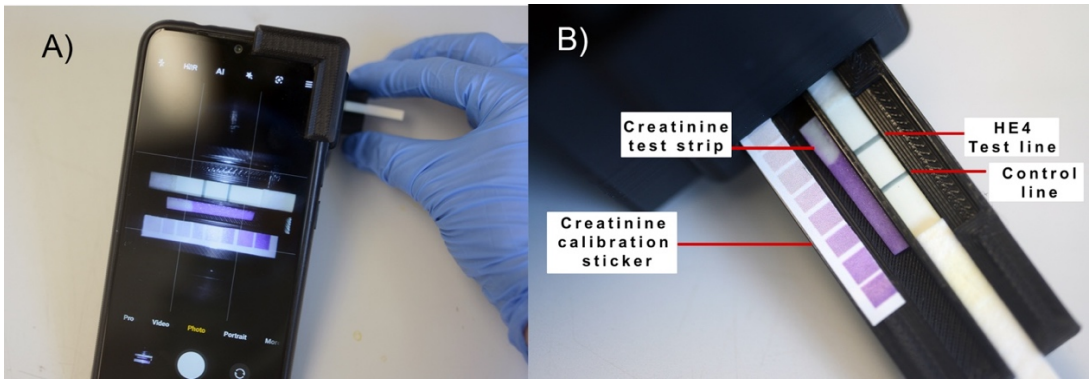

Figure S3.2. Photographs of the cellphone reader for the HE4/CRE test. A) Shows the camera screen with the two test strips in view with the calibration sticker. B) Shows the compartment with the test strips. Red line indicates the label.

The ELISA test validated that the sandwich assay with the polyclonal and the HE4 monoclonal antibodies worked outside of lateral flow test format.

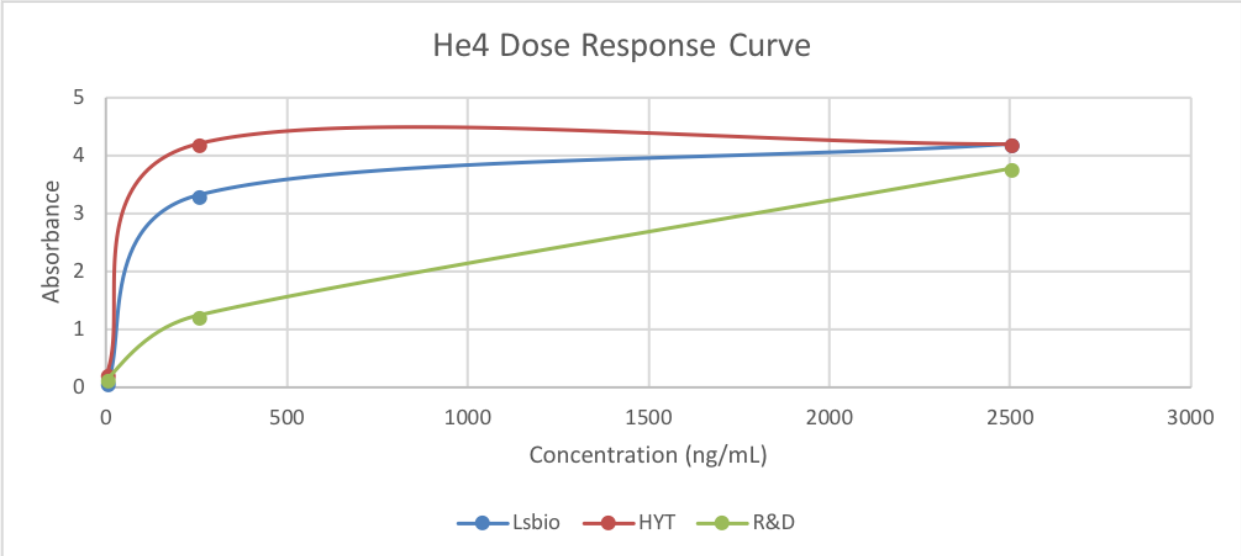

Figure S3.3. Graph showing the dose response curve from ELISA test for three different monoclonal antibodies displaying a signal (absorbance on y-axis) for three concentrations of He4 antigen (0 ng/mL, 250 ng/mL, and 2500 ng/mL).

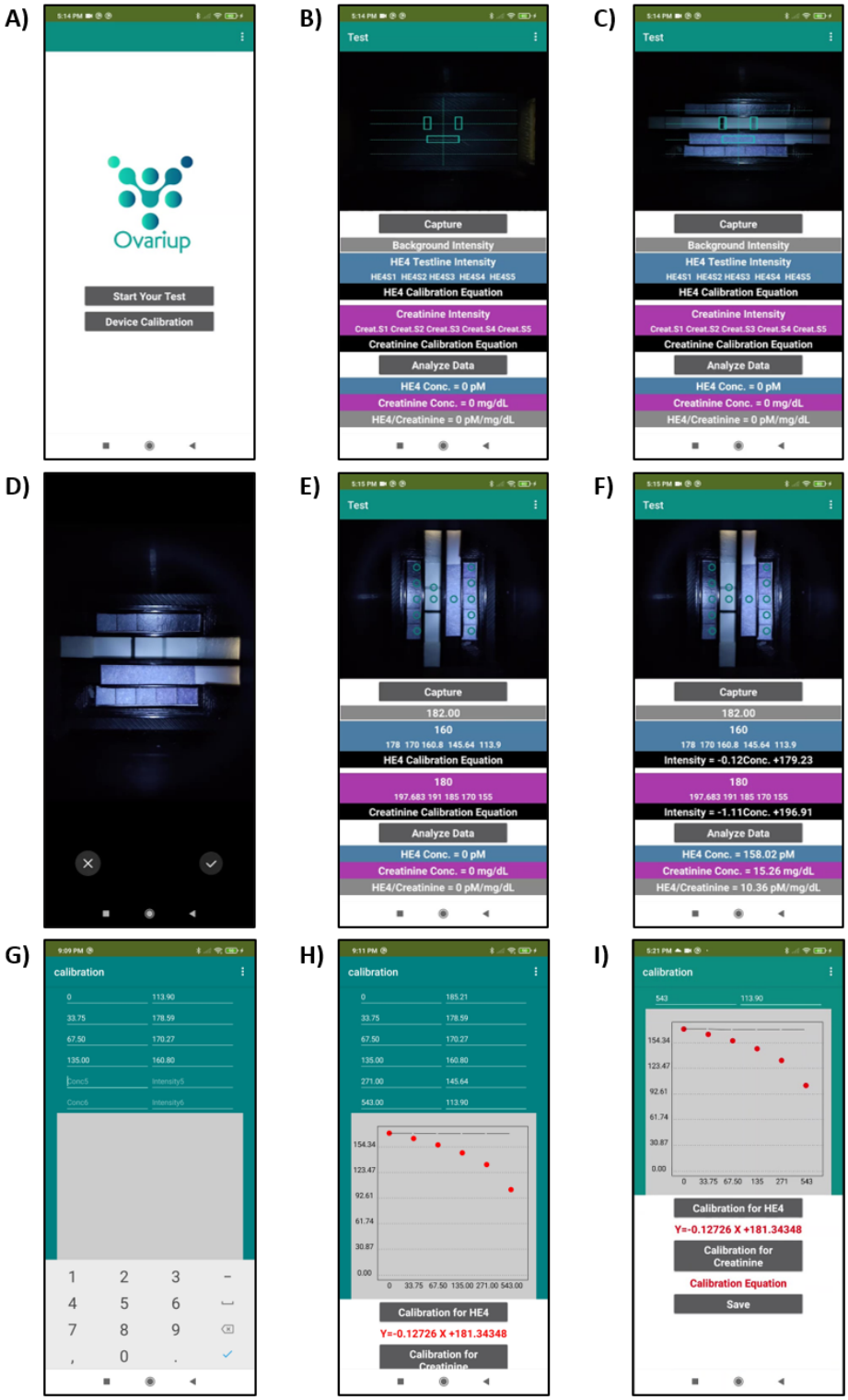

Figure S3.4. Workflow of the cell phone app.

Cell Phone app operation. The cell phone app was developed using MIT app inventor 2: a cloud based open-source platform [350]. This app is compatible with any cell phone with an operating system of greater than 2.3 (Gingerbread). The workflow of the app is shown in **Figure S3.4**. **Figure S3.4A** shows the main window of the app, it provides two buttons to the user "Start Your Test" and "Device Calibration". On clicking the "Start Your Test" button, it will open the test window which contains a live camera view with floating positioning markers as shown in **Figure S3.4B**. The user needs to position the test-strip holder in the device so that the HE4 test line and creatinine test-strip reaction areas are within the boundary of the rectangular markers on the cell phone screen as shown in **Figure S3.4C**. Now, on clicking the "Capture" buton, the app will pop-up the in-built phone camera and capture an image of the test strips as shown in **Figure S3.4D**. After capturing the image the app will process the image internally and calculate the grayscale intensity of the HE4 test line, the white area of the HE4 test for reference, creatinine test strip and the intensity of the calibrations stickers marked by the circles. As shown in **Figure S3.4E**, the app will change the place holders texts for the intensity values to the grayscale intensity respectively. On clicking the "Analyze Data" button, the application generates the calibration equation from the intensity values of HE4 and creatinine standards as shown in **Figure S3.4F** and determines the unknown concentration by fitting the intensity values of the biomarkers. Although, the app is self-content to calibration from the calibration stickers but there are situations where a device calibration in needed with freshly prepared standard solutions. To facilitate on-site calibration, the user need to click on the "Device Calibration" button on the home screen, which will open he calibration window as shown in **Figure S3.4G**. In this window, the user types the standard concentration values for HE4 and the corresponding intensity values into the respective boxes. After inserting the values, the user clicks the "Calibration for HE4" button, the app performs the least square fitting and generates the calibration equation as shown in **Figure S3.4H**. After that on clicking the "Save" button shown in **Figure S3.4I**, the calibration curve can be implemented to the app data processing algorithms. The same procedure can be used to calibrate the device with creatine standards. A copy of the code is available.

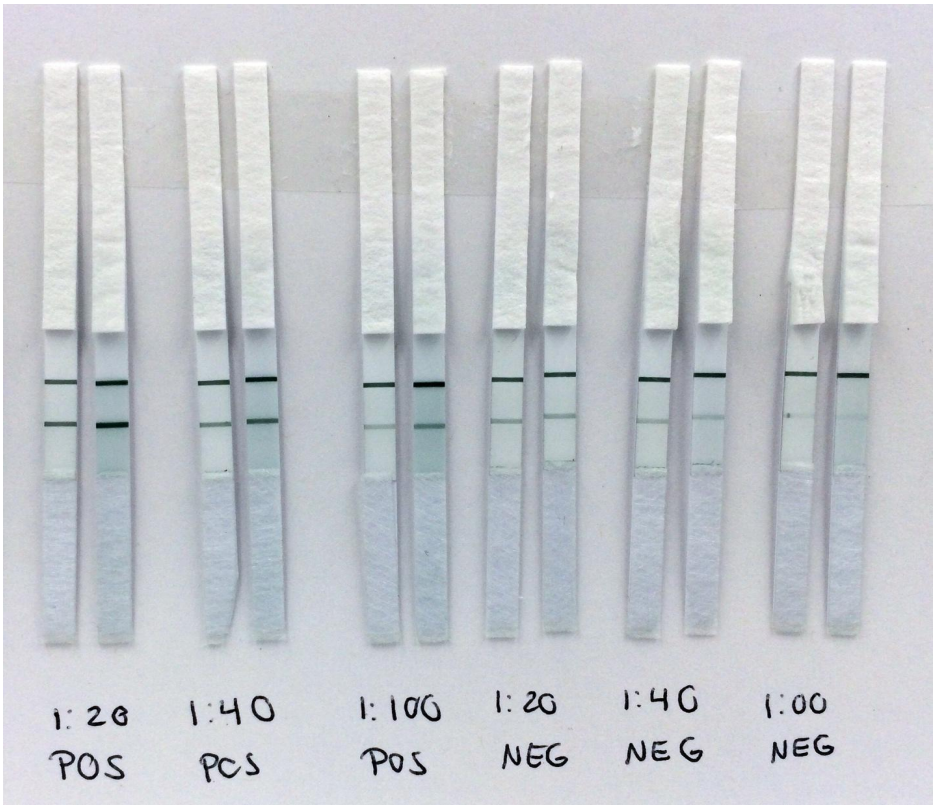

Figure S3.5. Patient urine sample test. Urine samples are diluted by a factor of 1:20, 1:40, and 1:100. (Left) Positive patient urine (Pos) shown in duplicate across three dilutions. (Right) Negative urine sample across the three dilutions in duplicate.

A picture was taken 15 minutes after pipetting the samples onto the LFA. Ovarian cancer patient positive urine test strips display a darker test line compared to negative patient urine sample for the three different dilutions. However, comparing this to the standards created from recombinant HE4 antigen in PBS buffer, we noticed the background is not as clean and so we need to quantify this background noise in the urine. The pH can affect conjugate stability so buffering up the urine during testing may be necessary going forward.

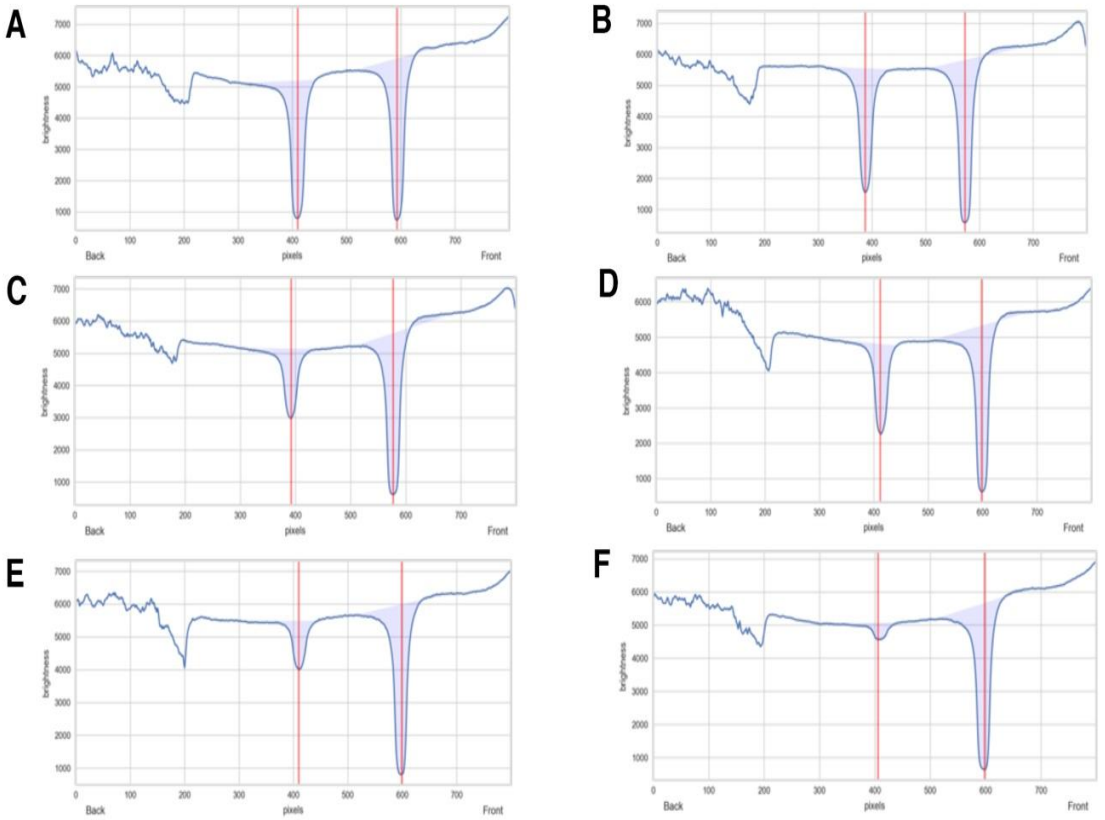

Figure S3.6. A-F absorbance graphs of the test strips from patient urine samples above. Panels A, B, C are dilutions from a patient positive urine sample for OC and panels D, E, F are dilutions from a negative urine sample. Left peak is the reading on the test line and the right peak is the control line test reading. A) Shows the line reading for the Ovarian patient positive urine sample diluted 1:20. B) Shows the line reading for the Ovarian patient positive urine sample diluted 1:40. C) Shows the line reading for the Ovarian patient positive urine sample diluted 1:100. D) Shows the line reading for the Ovarian patient negative urine sample diluted 1:20. E) Shows the line reading for the Ovarian patient negative urine sample diluted 1:40. F) Shows the line reading for the Ovarian patient negative urine sample diluted 1:100.

Dil. Factor	Sample	Absorbance	Abs	X value calculated	Multiplied by Dil.
1:20	POS	-4388.1	4388.1	1291.535	25830.70
1:40	POS	-3598.7	3598.7	1049.781	41991.24
1:100	POS	-2115.5	2115.5	595.550	59555.01
1:20	NEG	-2551.15	2551.1	728.968	14579.36
1:40	NEG	-1274.4	1274.4	337.962	13518.51
1:100	NEG	-787	787	188.696	18869.62

Table S3.3. Shows the patient positive and negative samples at three different dilutions with absorbances read by the Lumos reader. From the standard curve, the concentration can be calculated and then multiplied by the dilution factor. A dilution of 1:100 (highlighted in yellow) showed the biggest difference between a negative and positive patient urine sample shown in **Figure 3.5S**.

Dipstick test over three ranges of creatinine

Figure S3.7. A scanner image of three different concentrations of creatinine (high, medium, low) were pipetted onto a dipstick test pad (4th pad from left). The color of the dipstick did not change in proportion to the changing concentrations of creatinine. Therefore, enzymatic reaction for creatinine determine was used in our method.

Appendix 3. Supplemental Data for Chapter 4

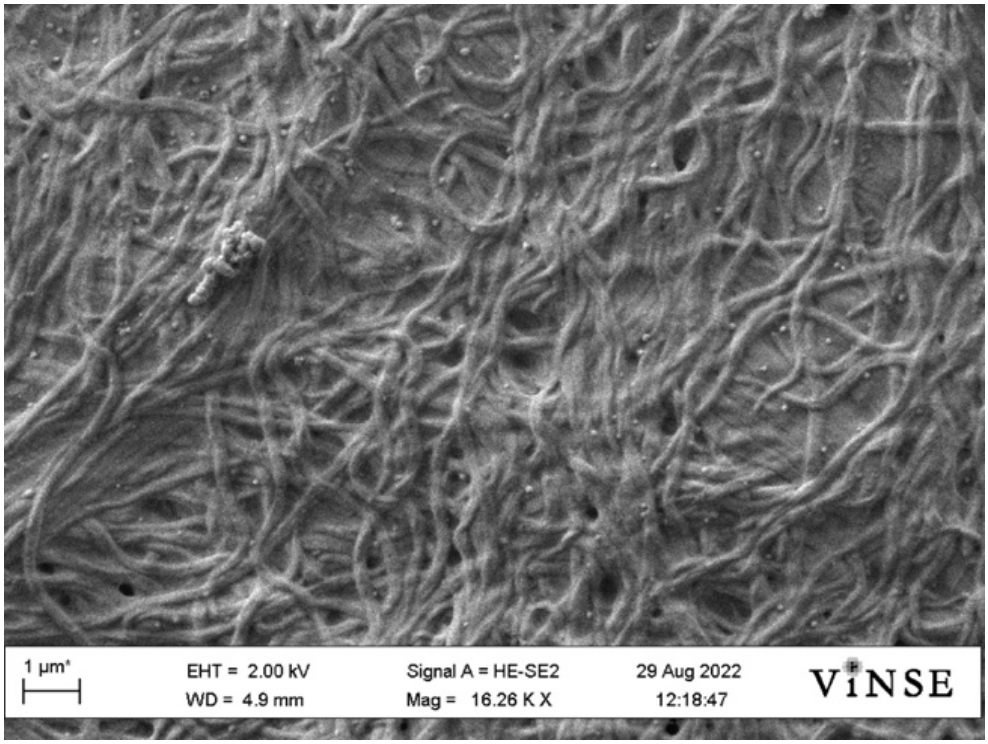

Figure S4.1. SEM of *B. Burgdorferi* on parafilm.

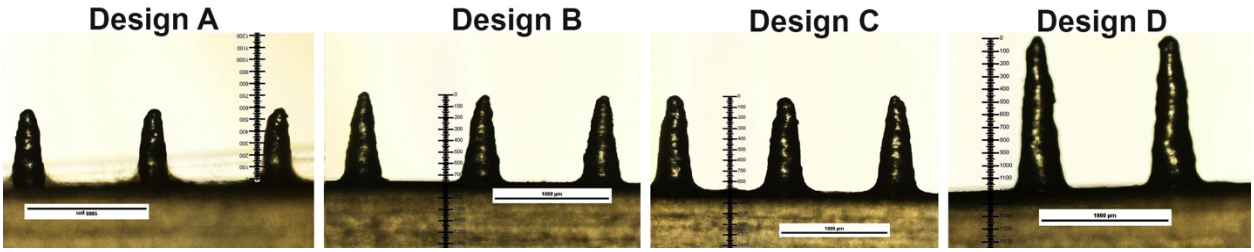

Figure S4.2. 3D printed MN designs shown in table 1 imaged on light microscope (2x).

Type of PVA	**Average Viscosity (cP)**
PVA M_w 13-23K	15.7 ± 2.5
PVA M_w 30-50K	**48.4 ± 6.1**
PVA M_w 85-124K	377.6 ± 2.8

Table S4.1. Average Viscosity measurements of different molecular weight PVA. The same solutions were measured three times each and average ± SD.

Type	13-23K (g)	31-50K (g)	85-124K (g)
average 50 µl droplet	0.0451 ± 0.002	0.0465 ± 0.005	0.0266 ± 0.007

Figure S4.3. Pipette test of different molecular weight PVA. 50 µl of each solution was pipetted onto a weigh boat three times. Average ± SD.

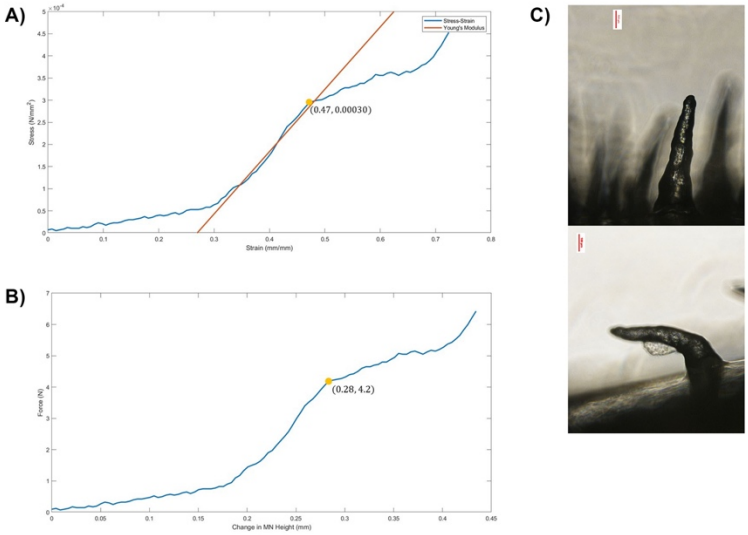

Figure S4.4. Representative compression test results. A) shows the stress-strain curve, B) shows the deformation force. C) shows light microscope pictures before and after 80K g force was applied to a MN (scale bar 100 µm).

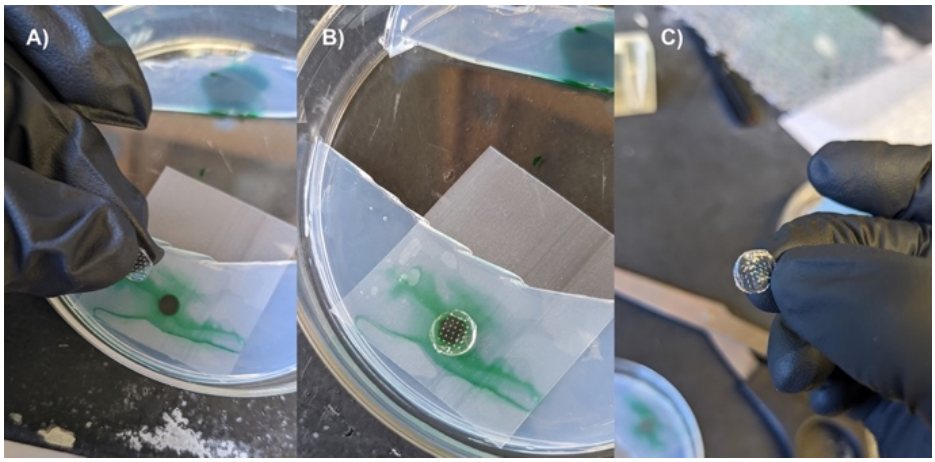

Figure S4.5. Qualitative absorption test. A) A sheet of PF is placed above a 2%(w/w) gel with 10 µl of green dye in a hole in the gel. B) A MN is applied to the PF and gel. C) A

MN is removed after 10 minutes and needles from the patch show the green dye is absorbed.

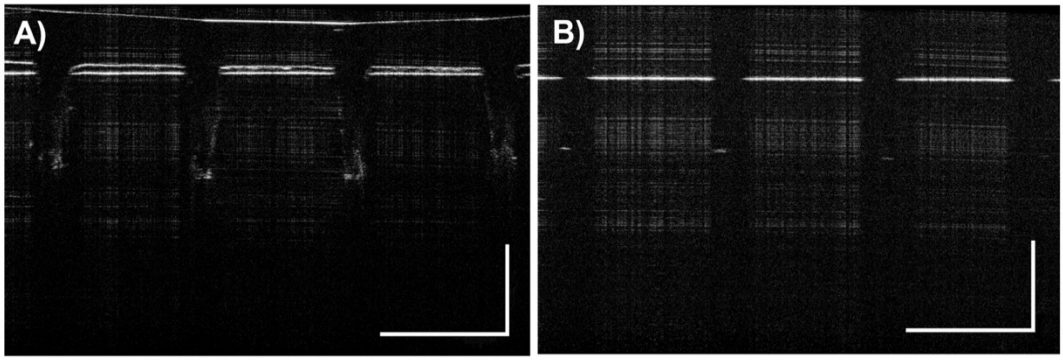

Figure S4.6. OCT 2D cross-sectional (B-scan) images visualization of holes in 2% (w/w) gel from MN. A) 2% (w/w) gel with a MN inserted on top. B) After MN removal, holes are in gel (space between horizontal white lines). Scale bar 1000 µm.

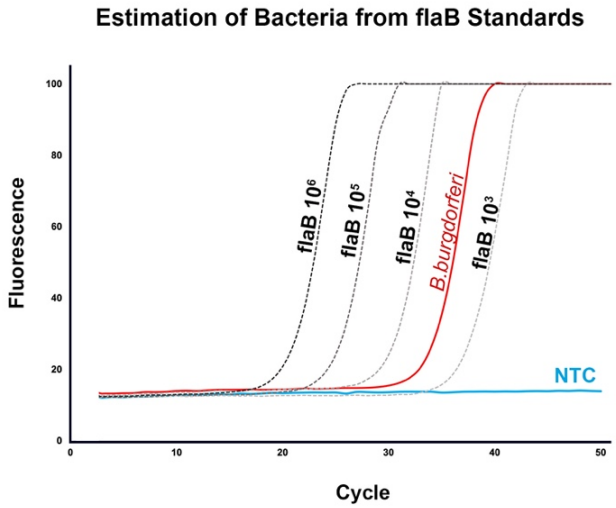

Figure S4.7. The estimation of B. burgdorferi (red) based on flaB standard curve (black).

To confirm the number of bacteria after a possible loss during reconstitution and possible degradation of bacteria in tubes, a tube of bacteria was tested in the PCR. The standard curve shows intensity of fluorescence versus cycle number with the separation of curves in proportion to the logarithmic dilutions of target (*B. burgdorferi* gene flaB). The limit of detection of PCR reagents was found to be 180 copies per reaction. The R^2 of the standard curve was found to be 0.998 (**Figure S4.7**).

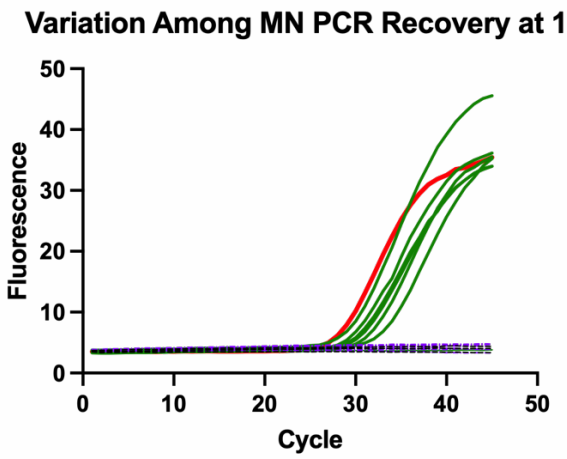

Figure S4.8. Single PCR experiment with 4 pig MN extractions spiked with 10^3 bacteria. Each PCR was run in duplicate. The positive patches are shown in green. The red line shows the spiked positive control. The dashed black lines are the NTC samples, and the dashed purple lines are the negative MN patches.

OLIGONUCLEOTIDE SEQUENCES

Table S4.2. List of oligonucleotide sequences used for PCR detection from flaB region.

Assay Set 1	**Sequence**	**Tm**	**GC %**	**Amplicon**
Forward Primer	ACAGCTGAAGAGCTTGGAATG	62.686	47.619	106
Probe	ACACACCAGCATCACTTTCAGGGT	68.143	50	
Reverse Primer	CTTGGTTTGCTCCAACATGAAC	62.441	45.455	
Assay Set 2				
Forward Primer	CAAGCGTCCTGGACTTTAAGA	62.038	47.619	108
Probe	TGTTGGAGCAAACCAAGATGAAGCT	67.061	44	
Reverse Primer	AGCTCCCTCACCAGAGAAA	62.376	52.632	
Assay Set 3				
Forward Primer	GTTGGAGCAAACCAAGATGAAG	61.972	45.455	127
Probe	CCTGAGCAGTTTGAGCTCCCTCAC	68.051	58.333	
Reverse Primer	CTTCCTGTTGAACACCCTCTT	62.079	47.619	
Assay Set 4				
Forward Primer	TGCAGCTAATGTTGCAAATCTT	61.93	36.364	97
Probe	CCTGAGCAGTTTGAGCTCCCTCAC	68.051	58.333	
Reverse Primer	CTGTTGAGCTCCTTCCTGTT	61.806	50	

Appendix 4: PRELIMINARY STUDIES FOR DETECTION OF TUBERCULOSIS CELL FREE DNA IN URINE

Abstract

Currently, many of the World Health Organization (WHO)-endorsed tuberculosis (TB) diagnostic assays are unreliable in resource limited settings partly because they often involve invasive sampling of infectious blood, sputum, or tissue. Urine is an appealing patient sample due to its noninvasiveness, ample volume, ease of collection, and low biohazard. Increasing evidence suggests that although DNA biomarkers of infectious agents, such as TB, are found in urine, it is very difficult to detect because of 1) the low concentration of DNA in urine and 2) the short (<25 bp) DNA fragments cannot be efficiently amplified and detected in nucleic acid amplification reactions. We are developing a new extraction and amplicon reconstruction approach, based on using magnetic beads to concentrate small DNA fragments of known TB genomic repeat, IS*6110*, and extending the length of these fragments to incorporate primer sites for PCR amplification and detection.

A4.1 Introduction

Tuberculosis (TB) is one of the most lethal communicable diseases in the world. The global burden of TB disease is 10 million cases per year[192]. TB is caused by the bacillus *Mycobacterium tuberculosis* which is spread by aerosols in the air (e.g., coughing). Prior to coronavirus (COVID-19) pandemic, TB caused more mortalities than any other single infectious agent[351]. Although much progress has been made to better diagnose and treat TB disease, in 2020-2021deaths from TB have increased for the first time in almost a decade due to restricted access to TB services and TB diagnostic testing due to COVID-19 disruption[352]. There is a higher TB disease burden in lower and middle income countries (LMICs) driven by overcrowding, poverty and poor nutrition[353,354]. The COVID-19 pandemic exacerbated strained resources for patients in LMICs by the disruption of testing as many laboratories became dedicated to processing COVID-19 patient samples instead[355].

Often, children and HIV patients are not able to produce sputum for sputum smear microscopy testing (the gold standard for TB testing), and so there is a great need to develop diagnostics to detect TB non-invasively and affordably at the point-of-care. Urine has emerged as a promising sample since essentially unlimited in volume, non-infectious to handle, and painless to collect. Recently, cell free-DNA (cf-DNA) has emerged as a novel biomarker for TB in urine. Pulmonary TB cf-DNA likely travels from the point of cell death (in the lungs), where the DNA is shed from the cells and into the blood stream. A small fraction of this TB cf-DNA is excreted by the kidneys into urine (**Figure A4.1**). Once urine is collected, cf-DNA is readily degraded by DNases and requires cold storage or immediate processing. Studies also have shown centrifugation of the urine sample and testing of the soluble fraction resulted in higher yields of cf-DNA than what is found in urinary sediment[224,223].

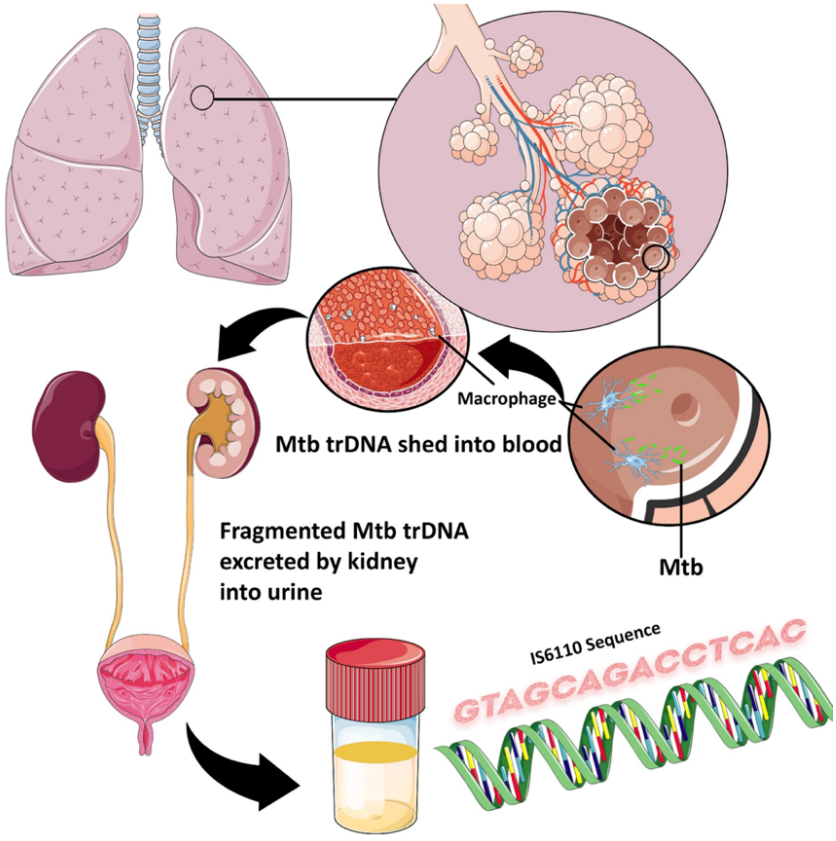

Figure A4.1. Physiologic processes that result in cell-free TB DNA in urine. *M. tuberculosis* genomic DNA is released from dead bacilli as a result of apoptosis or macrophage directed cell death. The released DNA fragments cross the vascular barrier into the bloodstream,

where they travel to the kidney. Very short fragments (<25 nucleotides) cross the kidney barrier and are then excreted into patient urine. Figure was partly generated using Servier Medical Art, provided by Servier, licensed under a Creative Commons Attribution 3.0 unported license.

Recovery of short fragment of DNA in samples is an active area of research. Many laboratories use commercially available silica-based extraction kit (based on centrifuge column or magnetic bead solid substrates) as they are easy to operate and reliably absorb DNA and RNA onto the silica surface under chaotropic conditions (also known as the "boom method"). Some examples of these commercial kits are Norgen Urine DNA Isolation Kits, QIAamp DNA Mini Kit, and Thermo Scientific MagMAX Total Nucleic Acid Isolation Kit. Since the interaction relies on hydrophobic interactions between the DNA phosphate backbones and silica, capture and recover of nucleic acids is significantly dependent on DNA length, with recovery dropping considerably below 50 bp as shown in **Figure A4.2**. Therefore, silica-based supports are unable to efficiently recover most short fragment DNA found in urine. These methods are both volume-dependent and become laborious when large dilute samples are processed. Additionally, **Figure A4.2** shows different sample and elution buffers can have a significant impact on the recovery of DNA despite containing the same concentration of DNA fragments. Recent work indicates most of the fragments in patient urine are much shorter than 50 bp. A next-generation sequencing report by Oreskovic et al. found most TB cf-DNA was highly fragmented compared to human DNA in urine with TB cf-DNA increasing in frequency below 25 bp[221].

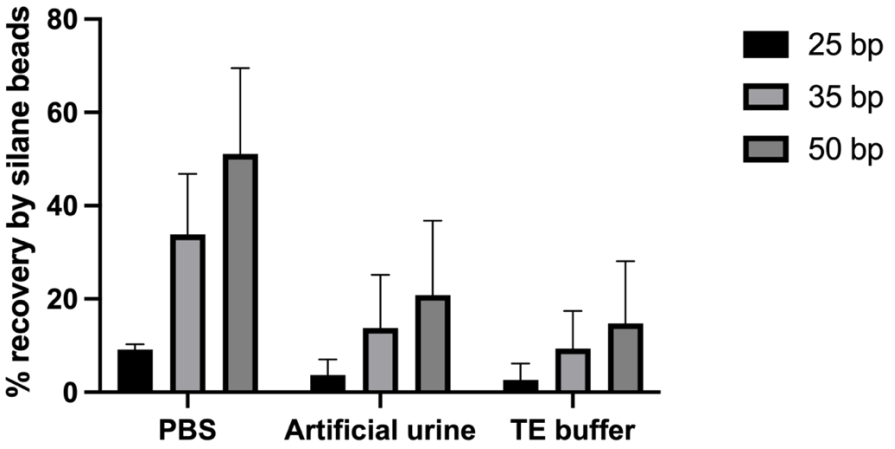

Figure A4.2. Size of DNA capture by silane magnetic beads in three different buffers (n=3). Error bars depict the mean of three trials, ± one standard deviation. Silica adsorption exhibits poor recovery of short DNA fragments across different buffers.

Since urine cf-DNA is highly fragmented, a diagnostic that is optimized to detect short cf-DNA is important. Another challenge for detection of TB cf-DNA is caused by the very dilute concentration, ranging from <1 to 200 ng/mL[219], so a volumetric concentration method is needed to effectively collect enough DNA for reliable detection. Other methods to silica/chaotropic-based extraction include other solid-phase extraction methods such as Q-Sepharose and Wizard resin/guanidinium thiocyanate. The Q-Sepharose method preconcentrates the DNA with an ammonium anion exchange resin used prior to desalting step with a spin column. Shekhtman et al used Q-Sepharose method to detect 25 bp male fetal cf-DNA from maternal urine samples[356]. Cannas et al used Wizard Resin (Promega, Madison, WI, USA) to capture TB cf-DNA from 6 M guanidine isothiocyanate treated TB patient urine[220]. Using this method, researchers found they could detect a 67 bp DNA from 34 of the 43 TB patients analyzed using a semi-nested approach (two sets of primers and two successive PCR runs)[220]. Since the "boom method" (chaotropic condition resulting in DNA absorption to the bead) is not able to capture short DNA, magnetic beads or other solid substrates may be functionalized with binding groups such as streptavidin or carboxylic acids to enable functionalization with sequence specific capture probes as shown in **Figure A4.3**. This is known as hybridization capture and is often used for sequencing libraries. Additionally, hybridization

capture has been shown to be successful in capturing short 25 bp fragmented by Oreskovic et al who authored numerous reports on methods to extract TB cf-DNA using streptavidin functionalized magnetic beads and sequence-specific hybridization[219,227]. In 2019, Oreskovic et al compared the analytical performance of the various capture methods discussed above[219]. She found hybridization capture and Q-Sepharose method performed better than other the silica or column-based methods featuring recovery efficiencies of 60-90%[219].

The work in this chapter differs from published work by Oreskovic et al. in a key different way. We are hoping to reconstruct fragments that are not amplifiable whereas Oreskovic et al detected the fragments long enough for amplification. Because they can be easily functionalized and manipulated using a simple magnet, we chose to use similar magnetic beads as the solid-phase separation unit. To try and achieve maximum recovery, in this report we have tested multiple covalent and noncovalent coupling chemistries, capture strand sequence features, and spacers sequences in our capture probe design (**Figure A4.3**).

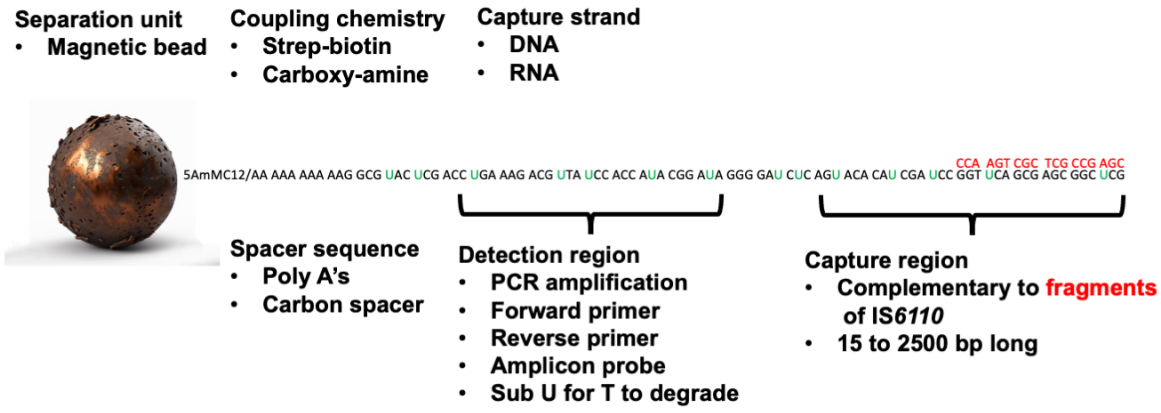

Figure. A4.3. Capture template design characteristics and modification options.

A4.2 Materials and Methods

Selection of genomic targets.

IS*6110* is a *Mycobacterium tuberculosis* insertion sequence (IS) that has been commonly used in TB molecular diagnosis. IS*6110* element is presence in multiple copies (up to 25 per genome)[357] at different locations in the genome[358] which may allow increased detection ability compared to single copy insertion elements. It also is only found in TB-causing strains of mycobacteria, providing an additional method of differentiating environmental mycobacteria from TB. We designed different capture strands, PCR primers and probes to target different size amplicon ranging from 105 bp within the IS*6110* region shown in **Figure A4.4**. For the creation of the most efficient and robust diagnostic assay, primer pairs must be evaluated according to cycle threshold and their tendency to form hetero- and homodimers. Primers found in previous literature[283,359] and newly designed primers were evaluated. New primer pairs were selected using the IDT PrimerQuest tool. Chosen primers and probes were characterized according to length, melting temperature, %GC, and likelihood to dimerize. A complete list of the sequences screened are provided in **Table 4.2**. The steps taken to screen the various primer pairs included PCR cycle comparison, melt curve comparison, and gel electrophoresis to confirm the size of products produce in the PCR reaction compared to the primer pairs. A limit of detection of the PCR reagents is shown in **Figure A4.14**.

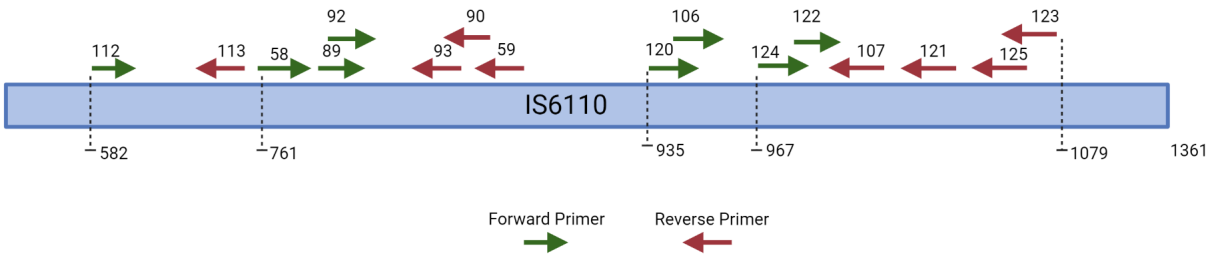

Figure A4.4. Primer map for IS*6110* sequences.

Oligonucleotides.

DNA and RNA sequences were purchased from Integrated DNA Technologies (Skokie, IL). A complete list of chosen sequences is provided in **Table A4.1**. All oligonucleotides were HPLC-purified and were suspended in TE buffer at a concentration of 100 μM. For long-term storage, these tubes were stored at -20 °C. Short term, aliquots were made with RNase free molecular grade water or TE buffer and stored at 4 °C.

Table A4.1. List of oligonucleotide sequences used for detection of TB cf-DNA from IS*6110* region (r=RNA).

Oligo	**Sequence**
IS6110 primer forward/ fragment	GAA GGC GTA CTC GAC CTG AAA G
IS6110 primer reverse	CGG TTG GAT GCC TGC CT
IS6110 RNA	5Biosg/ rArArA rArArA rArArA rA rCrGrG rUrUrG rGrArU rGrCrC rUrGrC rCrUrC rGrGrC rGrArG rCrCrG rCrUrC rGrCrU rGrArA rCrCrG rGrArU rCrGrA rUrGrU rGrUrA rCrUrG rArGrA rUrCrC rCrCrU rArUrC rCrGrU rArUrG rGrUrG rGrArU rArArC rGrUrC rUrUrU rCrArG rGrUrC rGrArG rUrArC rGrCrC rUrUrC
IS6110 105 bp DNA with deoxy uracil and amine	5AmMC12/AA AAA AAA AAG AAG GCG UAC UCG ACC UGA AAG ACG UTA UCC ACC AUA CGG AUA GGG GAU CUC AGU ACA CAU CGA UCC GGT UCA GCG AGC GGC UCG CCG AGG CAG GCA UCC AAC CG
IS6110 Probe PrimeTime® 5' 6-FAM™/ZEN™/3' IB®FQ	56-FAM/AG TAC ACA T/ZEN/C GAT CCG GTT CAG CG/3IABkFQ/

Table A4.1 All nucleotide sequences were selected based off the TB IS*6110* genome and were screened against other selections (**Table A4.2**).

Immobilization of capture DNA on carboxy functionalized PVA magnetic beads

Polyvinyl alcohol (PVA) magnetic beads (Perkin Elmer product# CMG-207) were briefly sonicated and vortex before being resuspended in the vial evenly. Next, the beads were pipetted into bead suspension tube. The bead suspension tube was placed on a magnetic rack for one minute and the supernatant was discarded. Next, 1 mL of activation buffer (0.1 M 2-(N-morpholino)ethanesulfonic acid buffer at pH 5.5). The bead suspension was then vortexed and placed back on the magnetic rack where the supernatant was removed again. These wash steps were repeated three times. Next, 37.5 mg of EDC and 2.5 mg NHS in 400 µl of activation buffer and added to the bead solution. Next, the tube was vortexed and incubated on a rotator for 40 minutes at room temperature. Next, the bead solution was washed twice with 1 mL of activated buffer and once with 1 mL coupling buffer. The tube was then placed on a magnetic rack for one minute and discard the supernatant. Then 600 µl of prepared DNA coupling buffer solution and mix. This tube was placed on a rotator for 2 hours at room temperature. Next, the beads were washes and separated magnetically. Then 1 mL of deactivation buffer (0.05 M Tris buffer containing 0.1% ethanol amine, pH 7.5) was added to the tube and the tube was placed on a rotator for 2 hours at room temperature. Next, we placed the tube on a magnetic rack and was twice with 1 mL coupling buffer and washed again with 1 mL of TE buffer. The beads were then stored at 4°C until use.

Immobilization of capture DNA on carboxy functionalized Pierce NHS activated *magnetic beads*

Pierce NHS-Activated Magnetic Beads (ThermoScientific Cat#88827) were vortex and sonnictaed briefly and brought to room temperature. We pipetted 300 µl of the bead solution into a 1.5 mL microcentrifuge tube. We placed the bead tube on a magnetic for 1 min and discarded the supernatant. We added 1 mL of ice-cold 1mM hydrochloric acid and vortex for 10-15 seconds. Next, we placed the tube back on the magnetic stand and discarded the supernatant once again. Then we pipetted 100 µl of the amine labeled

DNA into the bead tube. The bead tube was placed on a rotator for 2 hours at room temperature, with vortexing every 5 minutes for the first 30 minutes, and vortexing every 15 minutes until incubation was finished. Next, the beads were placed on a magnetic rack and the supernatant was discarded. We added 1 mL of 0.1M glycine, pH 2.0 to the bead tube and vortexed the tube for 15 seconds. Next, we placed the tube on the magnetic stand for 1 min and discarded the supernatant. This was repeated twice. Then we added 1 mL of 3M ethanolamine, pH 9.0 to the bead solution and vortexed for 30 seconds. Next, the tube was placed on a rotator for 2 hours at room temperature. Then the bead tube was placed on a magnetic rack and the supernatant was discarded. The bead tube was washed with purified water twice and 300 µl of TE buffer was added to the tube for final suspension. The tube was stored at 4°C until use.

Immobilization of capture DNA on streptavidin *functionalized magnetic beads*

Prior to coupling of DNA, we prepared binding and wash buffers (B&W) which are 10 mM Tris-HCl (pH 7.5) 1mM EDTA and 2 M NaCl. We vortexed the Dynabeads MyOne Streptavidin C1(ThermoFisher Cat# 65001) vial briefly to resuspend the beads. Next, 100 µl of the bead solution was pipetted into the tube. Next, 1 mL of B&W buffer was added to the tube and resuspended. Next, the bead tube was placed on the magnetic rack and the supernatant was discarded. Once, again 1 mL of B&W buffer was added to the tube, briefly vortexed, and placed on the magnetic rack where the supernatant was discarded. This was repeated a total of three times. Next, the biotinylated DNA capture strand was added to the beads and incubated at room temperature for 30 minutes on a rotator. Next, the tube was placed on a magnetic rack for at least 1 minute and the supernatant was discarded. The beads were washes for a total of five times with washing buffer and reconstituted in TE buffer. The tube was stored at 4°C until use.

Immobilization of capture RNA on streptavidin *functionalized magnetic beads*

Firstly, we prepared two buffers. Solution A was made from DEPC-treated 0.05 NaCl and solution B was made with DEPC-treated 0.1 M NaCl. We vortexed the Dynabeads MyOne Streptavidin C1 (ThermoFisher Cat#65001) bead vial briefly to resuspend the beads. Next, 100 µl of the bead solution was pipetted into the tube. Next, 1 mL of B&W buffer was added to the tube and resuspended. Next, the bead tube was placed on the magnetic rack and the supernatant was discarded. Once, again 1 mL of B&W buffer was added to the tube, briefly vortexed, and placed on the magnetic rack where the supernatant was discarded. This was repeated a total of three times. Next, we washed the bead solution with solution A twice and we washed the bead solution with solution B. The RNA capture strand was added to the beads and incubated at room temperature for 25 minutes on a rotator. Next, the tube was placed on a magnetic rack for at least 1 minute and the supernatant was discarded. The beads were washed with solution B three times. The solution was resuspended with 100 µl of DEPC treated water and was stored at 4°C until use.

Hybridization time

Typically, anneal temperature (Ta) is 5°C below the melt temperature of primers. Usually, the annealing step for primers occurs for 30 sec to 1 min at 45-60°C. Since the temperature for the fragment melt temperature was 58 °C, the hybridization temperature was calculated to be 52°C. However, the samples needed to be mixed with the capture DNA strands at room temperature, and we investigated three times to determine the best duration for complete capture hybridization. We tested 10 min, 30 min, and 60 min to determine the optimal time for hybridization and analyzed the green labeled fragment fluorescence with flow cytometry. Flow cytometric techniques provide a signal intensity for each fragment proportional to the amount in the sample. Forward and side scattering allows for the separation of single beads from other signals based on size. Cytometry data was analyzed with cytometry software.

Stabilization of ssDNA on magnetic beads with boiling method

Throughout these investigations, we found that it was not uncommon even after repeating washing for the capture DNA strand to fall off the magentic bead surface during short-term (overnight) or long-term storage (days to weeks). We observed this issue for both streptavidin and carboxyl functionalized magnetic beads. Therefore, we investigated the use of boiling washes as a method to remove poorly coupled capture DNA, which in theory should improve long-term stability of the capture beads. This was performed by using a kettle to pour boiling water on the beads after coupling to remove any poorly bound functional groups on the magnetic bead. PVA and Pierce™ NHS-activated magnetic beads were tested. To kettle treat the beads, the beads were pipetted in a glass beaker with a magnet taped to the outside of the beaker. Once the water reached a boil, the boiling water was poured onto the beads and the water was poured out. The beads were concentrated by the magnet so they could be pipetted and collected into another tube where the supernatant was tested by PCR. After confirming stability, we incubated the fragments at 1x 10^6 copies and 1x 10^{10} copies with each type of bead at room temperature for 30 minutes on a rotator. We than ran an extension step in the Qiagen RotorGene with a hold at 72°C for 10 minutes using EpiMark® Hot Start Taq polymerase kit (NEB cat# M0490S). Next, 2 ul of this solution pipetted into another PCR reaction with Luna® Universal Probe qPCR Master Mix (NEB cat# M3004S). PCR was used to test the presence of unbound DNA in the supernatant as well as to detect the reconstructed fragment.

Uracil template degradation

As most TB cf-DNA fragments are <100 bps, PCR detection remains difficult since typical PCR requires at least 40 bp for a set of primers to anneal to. Oreskovic et al used a 40 bp ssDNA capture strand from the IS*6110* segment of the TB genome to hybridize with fragments and used ultrashort primers for PCR detection. In our approach, we attempted to use a 105 bp capture ssDNA strand from a segment from the repeated IS*6110* region of the TB genome to provide a template for fragment extension along the DNA strand to facilitate PCR detection. However, after coupling the 105 bp ssDNA to the magnetic beads, it was found that the DNA coupled to the bead was not stable and could be shed from the bead with minimal

handling (**Figure A4.16**). This would lead to false positives if the capture strand was to proceed to the detection step. Therefore, a capture strand was developed containing deoxy uracil in place of thymine, which allows for template strand degradation using Uracil-DNA glycosylases (UDG) prior to end point PCR detection (**Figure A4.5**). UDGs are evolutionary, well-preserved DNA-repair enzymes. The biological function of UDG is to remove uracil from DNA, creating free uracil and alkali-sensitive apyrimidic sites in DNA[360]. UDG removes uracil incorporated into single- and double-stranded DNA by catalyzing hydrolysis in the N-glycosylic bond between uracil and deoxyribose sugar. UDG is often used to specifically degrade products that have already been through the PCR process to reduce amplicon contamination. UDG allows previous PCR amplifications, and nonspecific uracil-containing products to degrade, leaving native nucleic acid templates (which don't contain uracil) intended for amplification intact. We purchased UDG (NEB cat#M0280) and tested 1 µl of UDG and 7 µl of UDG it on 10^5 copies of dU template ssDNA following the manufacture's direction.

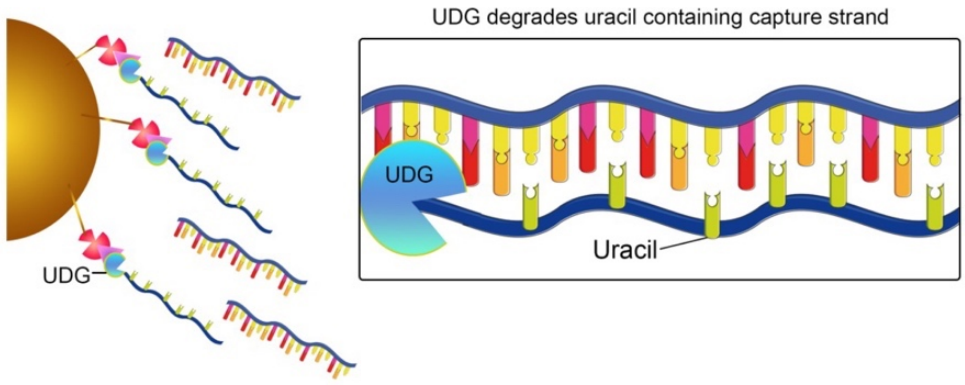

Figure A4.5. UDG degradation of capture DNA with uracil. The Figure was partly generated using Servier Medical Art, provided by Servier, licensed under a Creative Commons Attribution 3.0 unported license.

Uracil intolerant polymerases

We also investigated using an alternative to UDG degradation of the capture strand by performing PCR amplification using a polymerase that cannot amplify DNA templates containing uracil. A family of

B DNA polymerases from archaea, such as *Pyrococcus furiosus*, specifically recognize uracil in DNA templates and stall amplification[361]. Many of these extremophiles are isolated in thermal hot springs as shown in **Figure A4.6A,** making them compatible for use in PCR. Theses archaea polymerase can strongly bind to template with uracil and stall polymerization when contact occurs with an uracil base (shown in **Figure A4.6 B and C**)[362]. These types of polymerases are categorized as "uracil intolerant". This intrinsic ability to identify uracil arises from a binding pocket in the amino-terminal domain[363]. It is potentially possible that this polymerase mediated uracil stalling is one of the first steps in DNA replication correction mechanism. Therefore, using this polymerase to amplify only reconstructed fragment DNA (which does not contain uracil) would be useful. Vent polymerase first isolated from a submarine thermal hot springs in Italy, the native organism can grow at up to 98°C[364]. We purchased Vent® DNA Polymerase gene from *Thermococcus litoralis*[365] (NEB Cat# m0254S) and Vent (exo-) DNA polymerase which is engineered to lack the 3'→5' proofreading exonuclease activity that Vent DNA polymerases possesses (NEB Cat# m0257S). We followed the manufacturer protocol to test the polymerases by PCR with a 120 bp dU template and a non-dU template.

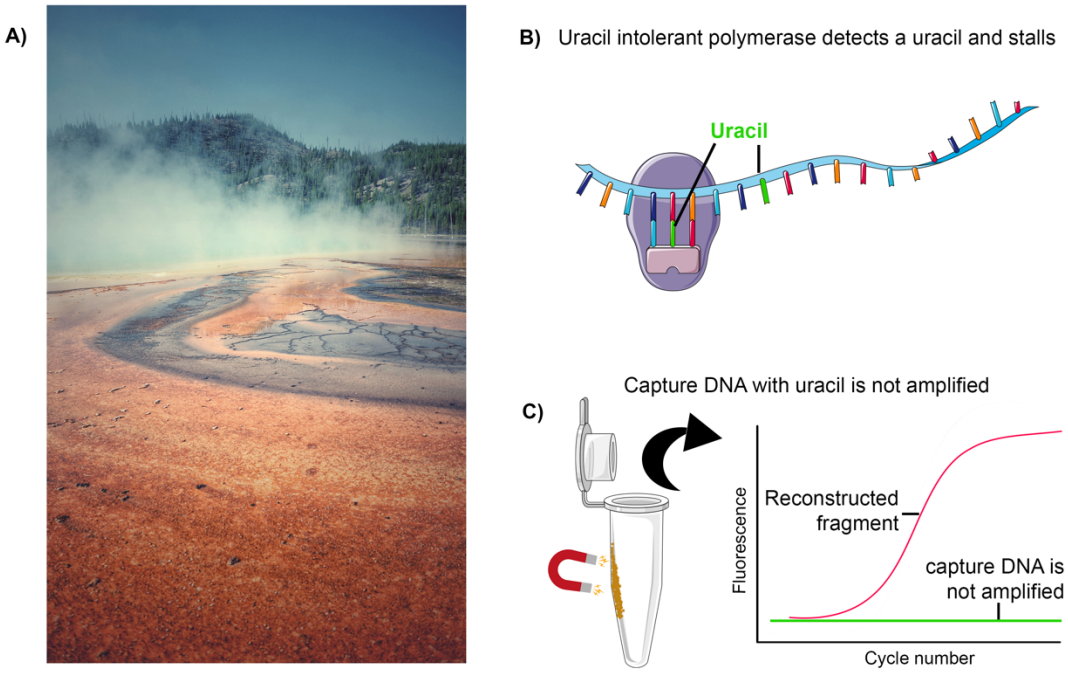

Figure A4.6. Uracil intolerant polymerases. A) Extremophile environment in Yellowstone national park. B) a uracil intolerant polymerases bind to a uracil (green) and stalls amplification. C) Final round PCR only amplifies non-uracil containing DNA such as the reconstructed fragment (red). The Figure was partly generated using Servier Medical Art, provided by Servier, licensed under a Creative Commons Attribution 3.0 unported license.

cDNA synthesis of TB fragment with reverse transcriptase

Another approach to prevent contamination of the downstream amplification reaction by the hybridization strand is using an RNA capture strand that does not amplify with DNA polymerases and instead use another enzyme to extend the fragment along the RNA strand. For example, Taq DNA polymerase possess RNA-dependent DNA polymerase activity, but this activity is low and only active during specific buffer conditions that are not present in PCR. *Bacillus stearothermophilus* (*Bst*) Pol cannot amplify RNA directly[366]. Reverse transcriptase is a special enzyme that uses RNA as a template to make complementary DNA often referred to as "cDNA". It is widely used in many molecular applications since the synthesized DNA can be amplified by PCR. Reverse transcription is catalyzed by retroviral DNA polymerases known as reverse transcriptase. Common retroviral DNA polymerases are murine leukemia virus or human immunodeficiency virus type 1 reverse transcriptase and can synthesize DNA from either DNA or RNA templates[367]. Although reverse transcriptase lack 3'→ 5' proofreading activity, transcription accuracy can be enhanced by performing the reaction at higher temperatures (e.g.,55°C compared to 37°C)[368]. Since RNA is not amplified by typical DNA polymerases, we designed our capture template with RNA and modified the 5' end with a biotin to couple to a streptavidin magnetic bead (Thermofisher MyOne C1 cat# 65001). The sequence is provided in **Table A4.2**. After fragment hybridization with RNA, the fragment is used as a primer during reverse transcription to extend the length of the fragment as shown in **Figure A4.7**. The longer length allows amplification by PCR. To perform cDNA synthesis from our RNA template, we purchased the LunaScript RT Master Mix Kit (Primer-free) (NEB cat#3025S). The kit features a thermostable reverse transcriptase at elevated temperatures, and we made 20 µl reaction tubes with spiked in 10^4 copies of a 22 bp TB fragment (GAA GGC GTA CTC GAC CTG AAA G) that would be located on

the 3' end of the RNA template strand. We placed the tube a Qiagen Rotorgene at 55°C for 10 min followed by 95°C hold at 1 minute to inactivate the RT. We also performed a no RT control and NTC. We then pipetted 2 µl of this tube into a Luna PCR kit (NEB #3004) for detection. Since RNA is not amplified by Taq or Luna DNA polymerases, any RNA that is shed off the bead, will not be amplified.

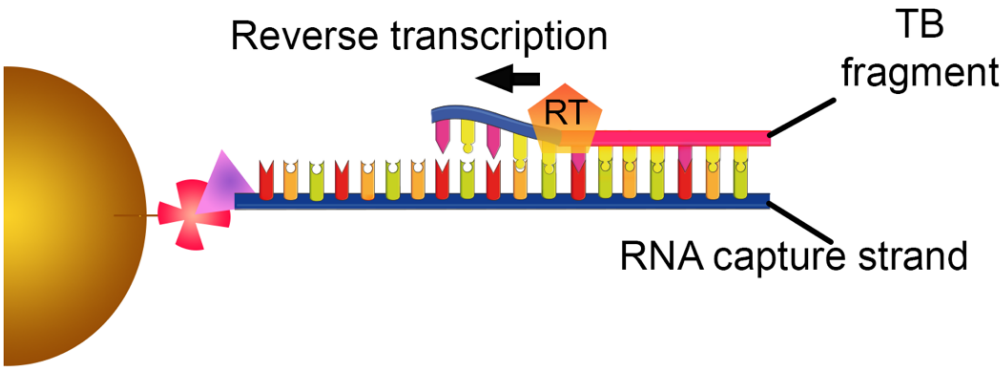

Figure A4.7. Overview graphic of reverse transcription process to make cDNA from the TB fragment and RNA capture template. The Figure was partly generated using Servier Medical Art, provided by Servier, licensed under a Creative Commons Attribution 3.0 unported license.

cDNA synthesis of TB fragment hybridized to capture RNA strand on magnetic bead

Since the fragment was detected in with our RT and PCR method, we added streptavidin magnetic beads (Dyna MyOne C1, ThermoFisher). 100 µl of beads were coupled to 1 x 10^{12} copies of our RNA capture template. 20 µl of this stock solution was pipetted into a tube (Protocol in appendix). Next, 5 µl of a TB DNA fragment (22 bp) that hybridized to the 3' end of the RNA was pipetted at 10^2 copies into the 20 µl tube of magnetic beads and incubate at room temperature for 30 minutes on a rotator. Then RT step with LunaScript RT Master Mix Kit (Primer-free) (NEB cat#3025S) was used. We performed a negative control (no fragment), no template control (NTC) and our hybridized 10^2 fragments with magnetic beads. 2 µl of each solution was pipetted into the 18 µl of the RT mixture. The tubes were placed into the Qiagen for 10 minutes at 55°C followed by a heat inactivation step at 95°C for 1 minute. Next, we made a PCR

reaction with Luna PCR 3004 kit at 18 µl per tube. We pipetted 2 µl from the RT step into the PCR reaction. We placed the tubes back into the Qiagen for 1 min hold at 95C followed by cycling for 45 times at 95°C for 15 second and 60°C for 30 sec, and 72°C for 20 sec.

A4.3 Results

Hybridization time

After incubation with a fluorescent labeled fragment for three time points, fluorescence was measured with flow cytometry. Results in **Figure A4.8** show that although the beads exhibited some autofluorescence, the 30 minutes time point provided almost the same fluorescence as the 60-minute time point, indicating that the bulk of fragment capture and hybridization occurred within 30 min. Both of those times exhibited the more fluorescence than the 10-minute incubation. Therefore, the 30-minute incubation was selected.

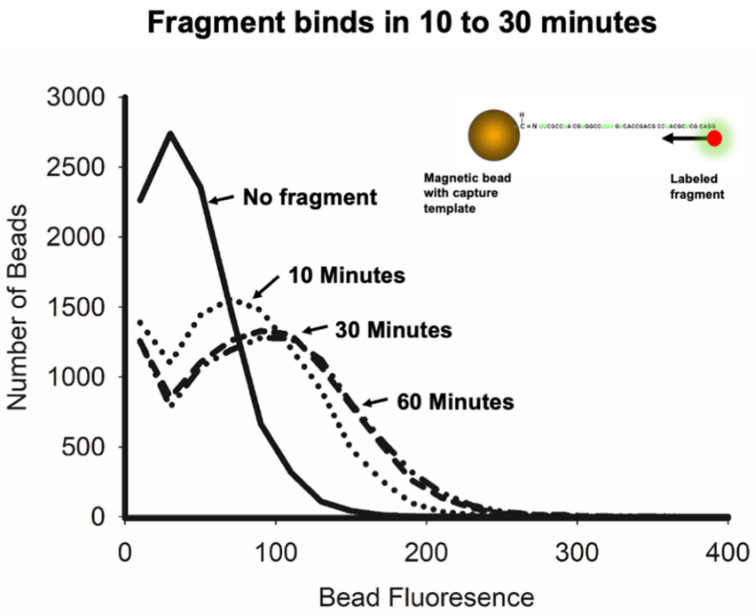

Figure A4.8. Fluorescent labeled TB DNA fragment hybridization time (n=3). A shift to the right indicates more hybridization, as it indicates an increase in fluorescence seen from DNA hybridization.

Stabilization of ssDNA on magnetic beads with boiling method

Results from the boiling method indicated that although the beads could be stabilized (no DNA is detected in the supernatant), the reduction in DNA capture on the bead negatively impacted the final PCR detection of the captured fragments. I compared the PCR performance with two concentrations 10^{10} vs 10^{6} copies of fragments on the PVA magnetic beads. Results showed the fragment detection was reduced greatly by the boiling treatment of the beads compared to the positive control (**Figure A4.9**).

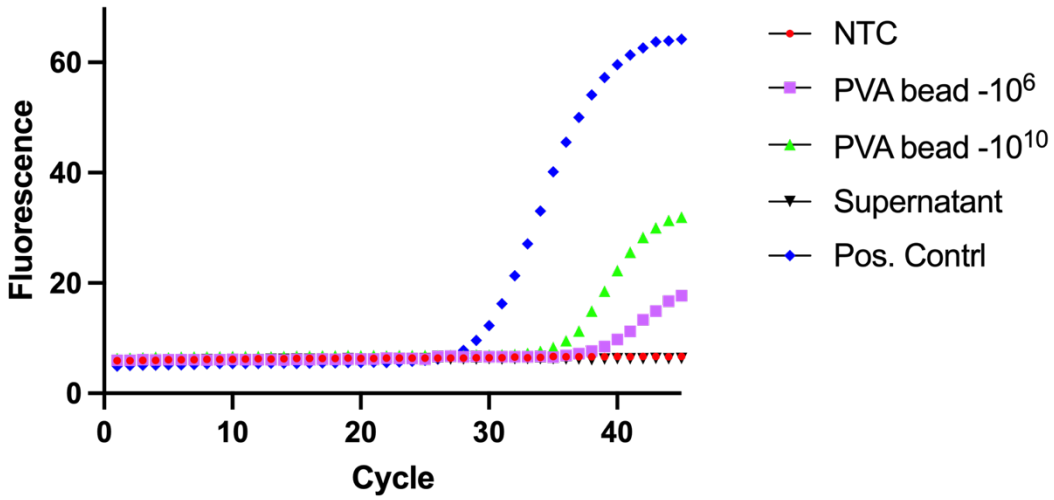

Figure A4.9. PCR detection of boiled treated PVA magnetic bead with two concentrations of IS*6110* fragment (n=2). Positive control are the beads before boil treatment and fragment capture.

Uracil template degradation

Our experiment indicates 1 µl of UDG enzyme was not able to degrade 10^{5} copies of dU template ssDNA and that although 7 µl could degrade more, this was cost prohibitive (**Figure A4.10**). However, the UDG enzyme provided mixed results and after multiple uses, the enzyme lost degradation activity. Additionally at higher concentrations, the UDG enzyme may have inhibited PCR instead of helping eliminate trace template strand that made it into the PCR reaction (**Figure A4.17**).

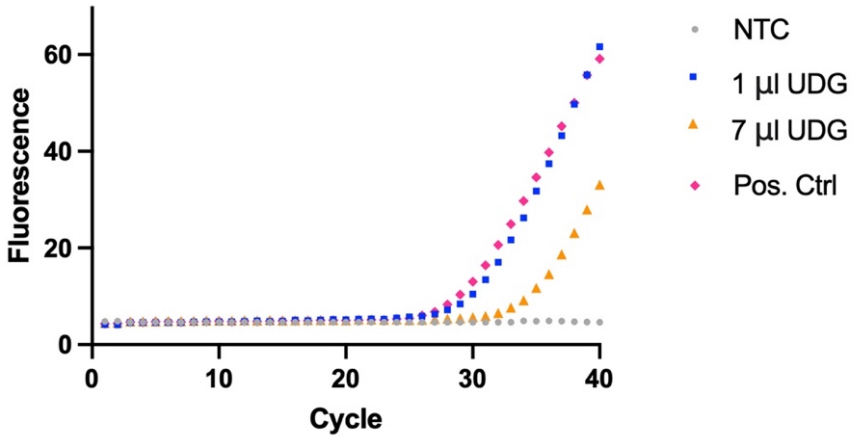

Figure A4.10. UDG degradation results. A) Shows UDG degrading the capture template DNA with deoxy uracil while the reconstructed fragment remains intact. B) Comparison of 1 µl and 7 µl of UDG incubated at 37°C for 30 minutes with dU template DNA compared to positive control (n =2).

Uracil intolerant polymerases

The results showed that both types of archaea-based polymerases could amplify a deoxy uracil DNA template. It was observed over several experiments that the template with deoxy uracil would amplify up to 10 cycles after a non-uracil DNA template (**Figure A4.11A**). This may suggest that the archaea polymerase is stalled more so by the deoxy uracil DNA templates but may contain other non-uracil intolerant polymerases in the kit that enable amplification of those templates. Additionally, I reduced the amount of Vent polymerases and the cycle delay between a non-uracil and uracil DNA template was significantly reduced (**Figure A4.11B**). In fact, both templates amplified at the same cycle. This suggests the archaea polymerases are not suitable for end point detection of reconstructed fragments since the capture strand would amplify without any fragments present.

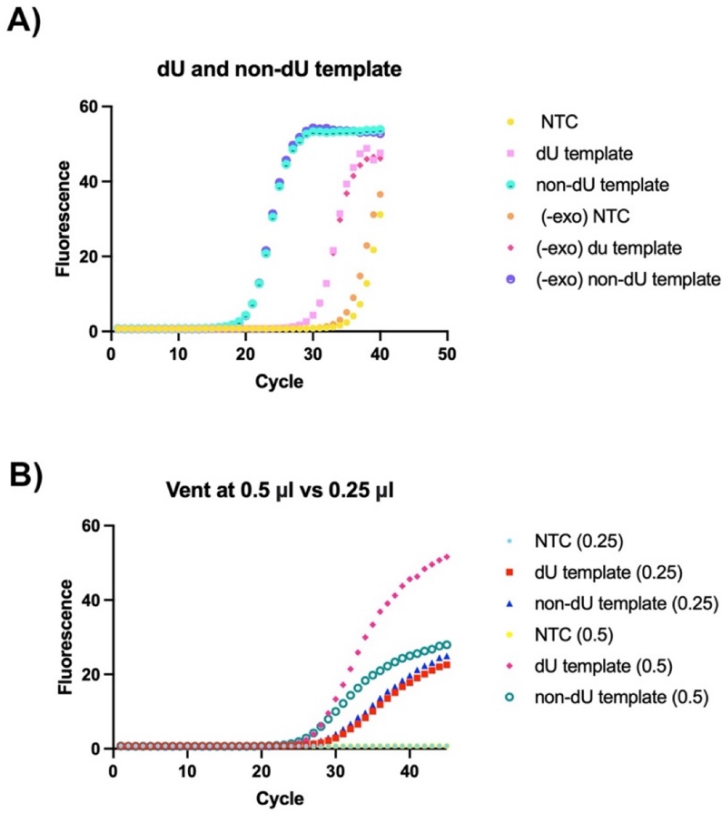

Figure A4.11 A) PCR comparison of Vent and Vent (-exo) PCR amplification of dU template and non-dU template. B) PCR results of a reduction in Vent polymerase with a dU template and non-dU template (n =2). Two concentrations of enzyme were used at 0.25 and 0.5 µl.

cDNA synthesis of TB fragment with reverse transcriptase

Our experiment indicates the cDNA synthesis of the 22 bp fragment was successful with our RNA capture template (**Figure A4.12**). I tested two concentrations of fragments, and both appear to be successfully reconstructed since both amplify in the subsequent PCR reaction. We assume there is no genomic contamination since the no rt control (no reverse transcriptase) did not amplify in the subsequent PCR reaction. As expected, the negative control (no fragment) also did not amplify.

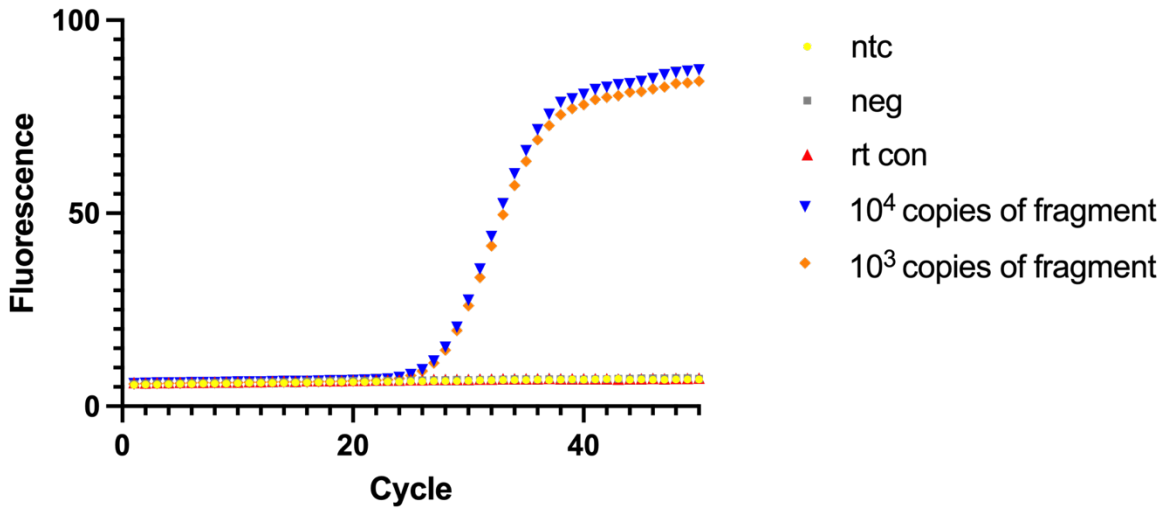

Figure A4.12. PCR Detection of 10^4 and 10^3 copies of TB DNA fragment after RT step (n =3).

cDNA synthesis of TB fragment hybridized to capture RNA strand on magnetic bead

After coupling 10^{12} copies of RNA capture strand to magnetic beads and incubating with a 5 µl of 10^2 copies of fragment, cDNA kit was used to extend the fragment along the RNA template. This was subsequently pipetted into a PCR reaction. Results in **Figure A4.13** indicate the fragment was extended and amplified in the PCR reaction.

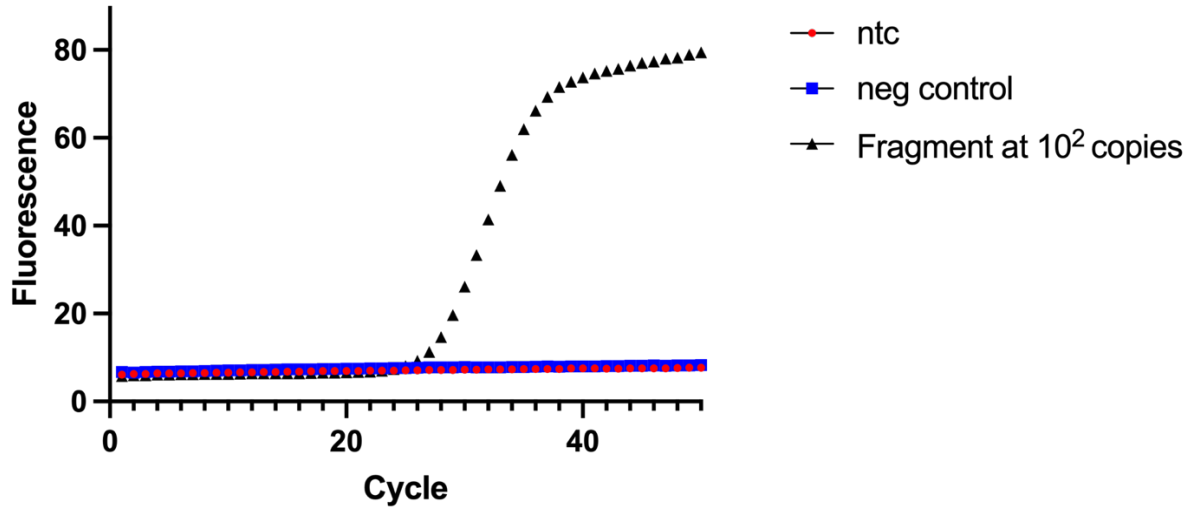

Figure A4.13 Detection of fragment at 10^2 copies (n=3).

A4.4 Discussion

The time for fragment hybridization is important parameter of this method, as optimizing the time for capture of short DNA fragments is critical to maximizing detectable material while also eliminating unnecessary protocol incubation time. Using flow cytometry, we were able to be able compare hybridization of DNA on the bead using fluorescence tag on the DNA fragment. The results in **Figure A4.8** show the 30 min and 60 min incubation showed nearly equal fluorescence which suggests that there is no gain in hybridization beyond the 30-minute time point. These results agree with Oreskovic et al who also incubated fragments with capture probes for 30 minutes and found no significant benefit in longer hybridization times[226]. Therefore, all other experiments performed a 30-minute incubation with fragments before further testing.

Since shedding of the DNA capture strand was observed across different types of beads and concentration, we used a boiling method to stabilize the DNA. After stabilization, we hybridized two concentrations of TB fragments. Unfortunately, the result showed the fragment was only faintly detected at 10^{10} copies (**Figure A4.9**) which is far beyond the physiological concentration likely seen in patient urine samples ($<10^3$ copies per ml). Only one replicate of the 10^6 copies of fragment was detected with the PVA magnetic beads. Therefore, boiling the beads is not a suitable pre-treatment prior to fragment hybridization. One possible reason is because the high heat of the water disrupts the coating of the magnetic bead which could impact the functional groups on the bead. A comparison between the beads is shown in **Figure A4.17**.

UDG are repair enzymes that are programmed to eliminate uracil in ssDNA by excision repair forming an abasic site. Although we followed the manufacturer's protocol for UDG, we found that the results were variable and inconsistent. Specifically, UDG was not able to reliably degrade higher concentrations of DNA. Additionally, we found that with higher amounts of UDG, the presence of the enzyme inhibited PCR. Taken together, these results suggest that UDG has limited performance to degrade uracil containing templates and should be used with caution. Our results suggest that 1 µl of UDG enzyme was not able to degrade 10^5 copies of dU capture strand despite the manufacturer's direction. We found 7 µl of UDG could degrade more, but this was costly (**Figure A4.10**). However, the UDG enzyme provided

mixed results with variable degradation results. Additionally at higher concentrations, the UDG enzyme may have inhibited PCR instead (**Figure A4.16**).

Archaea polymerase family B feature uracil recognition sites that stall amplification. Therefore, we tested various polymerases with template containing uracil and template without uracil. We found that the u-intolerant polymerases exhibited a cycle delay. The results indicated that both types of Vent polymerase were unable to completely stall amplification with dU templates compared to the non-dU template (**Figure 4.11A**). A reduction in the amount of polymerase in the PCR reaction did not stall amplification of dU templates at all (**Figure A4.11B**).

Since the capture strand on the magnetic bead is prone to shedding or amplification, false positives are the primary concern moving forward with this work and were a primary barrier to completion of this project. After testing multiple methods to address this, I found that use of an RNA capture strand with two concentrations of 22 bp fragment (10^3 VS 10^4) and proceeded to an cDNA RT step per the manufacturer's instructions was the most reliable method for preventing downstream contamination of the final detection reaction. PCR results indicated that the captured fragments could be detected even at a few hundred copies (**Figure A4.12**). Although it should be noted that physiological concentrations range widely from 1 to 3,000 copies/ml of target sequence in a patient urine sample. The results show the cycle is not drastically different between the two concentrations. Considering this, lower amounts of fragment can be used to characterize the limits of detection.

After coupling the RNA to the magnetic beads, we proceeded to hybridize the solution with 5 ul of 10^2 copies of 22 bp DNA fragment (**Table A4.1**). We proceeded to the cDNA RT step per the manufacturers' instructions and pipetted the tubes into a PCR reaction for detection. Our results in **Figure A4.13** indicate that the magnetic beads can create cDNA from even a low concentration of fragment and that the beads do not appear to inhibit PCR as the cycle in **Figure A4.11** is not significantly delated compared to the cycle in **Figure A4.13**. Future work should characterize and compare the limit of detection of this method with and without magnetic beads.

A4.5 Conclusion

Results from this work show the various methods, and possible solutions to detecting low concentrations of short fragment DNA for applications in dilute samples. Sequence specific hybridization of RNA with TB DNA improved the detection of the fragment without suffering from false positives. Future work with clinical samples could lead to expanding access for TB diagnostics for populations that cannot produce sputum and would benefit from urine testing such as infants and HIV populations.

OLIGONUCLEOTIDE SEQUENCES

Primer Name	Sequence	Maximum Delta G (kcal/mol)	Length	Tm	%GC	Self-dimer Highest Delta G Value (kcal/mol)	Number of base pairs	Second Highest Delta G (kcal/mol)	Number of base pairs
MEP058	CTCGTCCAGCGCCGCTT	-39.58	17	66.2	70.6	-9.89	4	-8.35	4
MEP059	ACGCCTACGCTCGCAGG	-38.36	17	65.6	70.6	-4.67	3	-3.61	2
MEP092	CACCTAACCGGCTGTGG	-35.02	17	61	64.7	-9.75	4	-3.3	3
MEP093	GGTGACAAAGGCCACGTA	-35.21	18	61	55.6	-9.28	4	-6.3	4
MEP106	ATC TGG ACC CGC CAA	-32.44	15	58.8	60	-5.02	3	-3.61	2
MEP107	CCT ATC CGT ATG GTG GAT AA	-36.48	20	57.4	45	-7.08	5	-3.61	2
MEP112	CCG CCA ACT ACG GTG TTT A	-38.2	19	61.3	52.6	-6.68	3	-3.61	2
MEP113	CAG GCC GAG TTT GGT CAT	-36.21	18	61.1	55.6	-9.28	4	-3.61	2
MEP120	CGA TCG AGC AAG CCA TCT	-36.47	18	60.9	55.6	-11.85	6	-6.76	4
MEP121	AAC CGG ATC GAT GTG TAC TG	-36.77	20	60.8	50	-9.75	4	-9.71	6
MEP122	CTG GAC CTG AAA GAC GTT ATC C	-40.12	22	61.5	50	-6.3	4	-4.64	3
MEP123	CGA CCG ACG GTT GGA TG	-36.12	17	61.2	64.7	-8.02	4	-3.61	2
MEP124	GAA GGC GTA CTC GAC CTG AAA G	-41.97	22	63.6	54.5	-6.76	4	-4.67	3
MEP125	CGG TTG GAT GCC TGC CT	-37.56	17	63.7	64.7	-3.61	2	-3.14	2

Table A4.2. Self-dimer characterization using the IDT oligo-analyzer tool under standardized conditions. A ΔG of less than -9 indicates a potential primer dimers formation (shown in red cells).

Primer 1	Primer 2	Amplicon Length	Difference in Tm	Hetero-Dimer Highest Delta G Value (kcal/mol)	Base Pairs
MEP058	MEP059	116	0.6	-8.35	4
MEP92	MEP093	77	0	-6.37	4
MEP106	MEP107	63	1.4	-5.02	3
MEP112	MEP113	110	0.2	-6.97	3
MEP120	MEP121	99	0.1	-8.24	5
MEP122	MEP123	103	0.3	-6.12	4
MEP124	MEP125	105	0.1	-7.81	4

Table A4.3. Hetero-dimer characterization using the IDT oligo analyzer tool.

Primer pair	Approx. Melting Temperatures (°C)
58/59	83
92/93	86
106/107	92

112/113	92
120/121	84
122/123	92
124/125	**85**

Figure A4.14. Melt temperature of the product generated by the sets of primer pairs listed in Table A4.1. The desired 100 bp was calculated to be ~80°C. Primer sets in the >90°C were suboptimal.

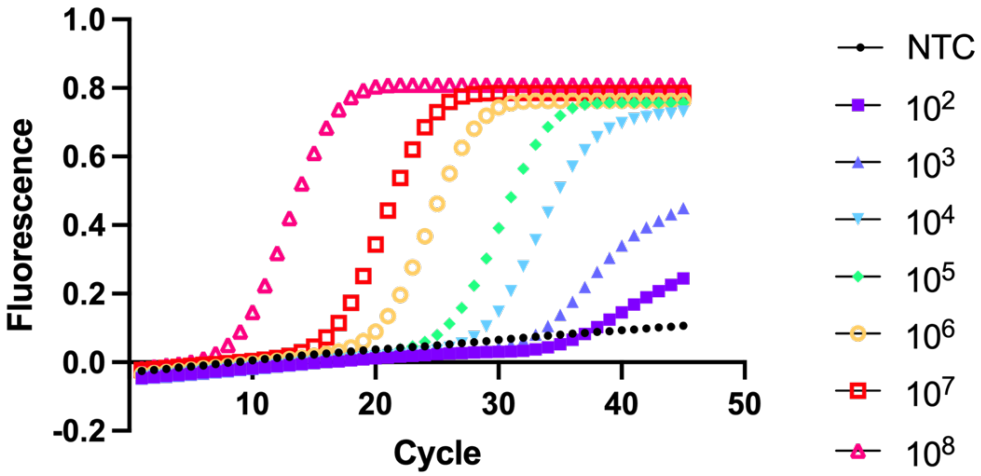

Figure A4.15. IS*6110* 105 bp with deoxy uracil and amine PCR limit of detection.

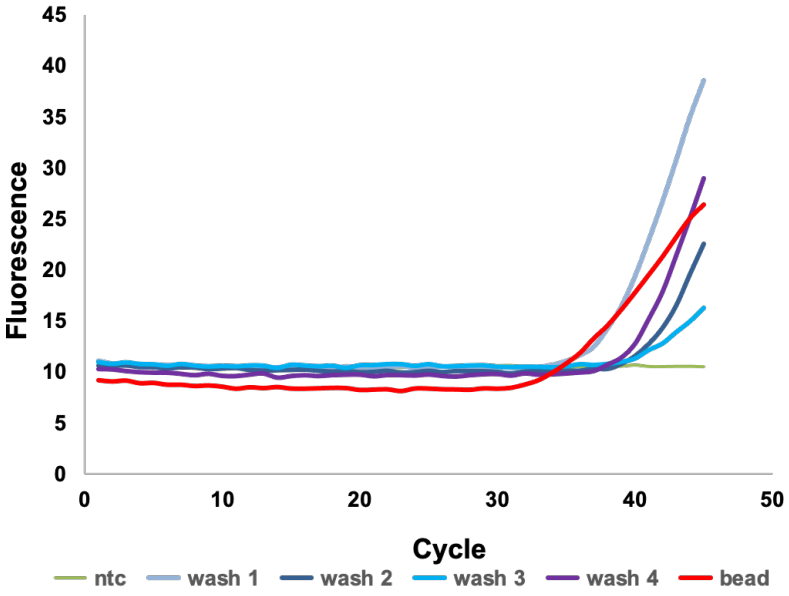

Figure A4.16. Washes of bead result in shed ssDNA (n =2).

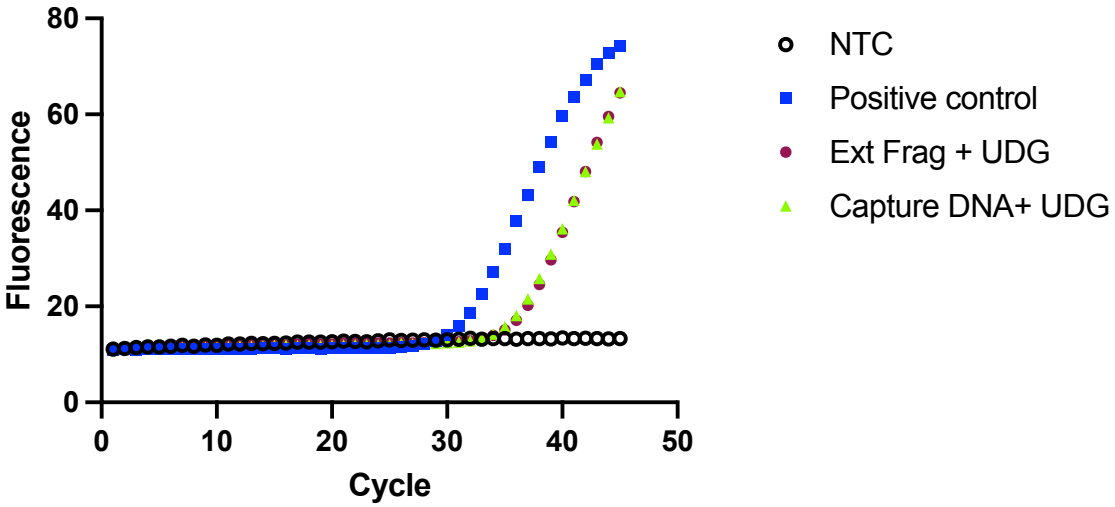

Figure A4.17. Inhibition of ribose uracil DNA strand with and without fragment (n =2).

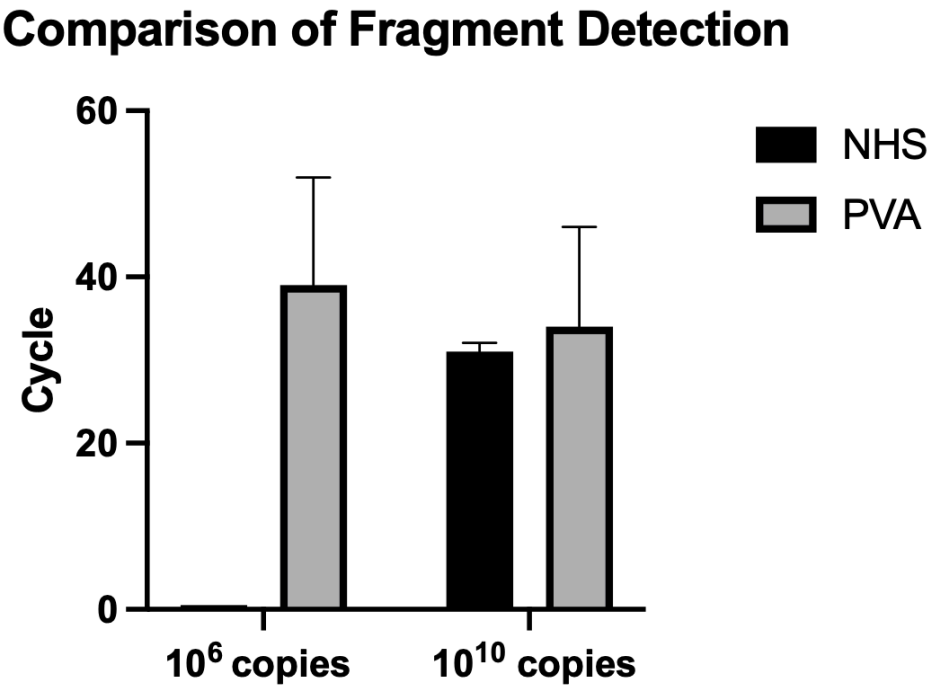

Figure A4.18. Comparison of 15bp fragment detection at 1 x 10^6 and 1 x 10^{10} concentration with PVA and NHS-activated magnetic beads.

Proposed Collection for cf-DNA analysis.

1) Prior to urine collection, prepare 15 mL Eppendorf DNA LoBind tubes with 500 µL 0.5 M EDTA and 100 µL 1M Tris-HCl pH 8 (Tube A).
2) Collect a clean-catch first morning urine sample in a clean, dry plastic dup. Collect at least 30-50 ml of urine.
3) Immediately after urine collection, add 10 mL of urine to each prepared 15 mL tube (Tube A). The final concentration of EDTA and Tris-HCl will be ~25 mM and ~10 mM, respectively. Mix by inversion.
4) Centrifuge the tubes at 850 x g for 10 min at 4 °C or at room temperature.
5) Carefully transfer 10 mL of the upper part of the urine supernatant from Tube A into two 5-mL tubes, leaving at least 2 mL of the supernatant above the cell pellet. NOTE: Pipetting the top portion of the supernatant reduces the risk of contamination by cells or cellular debris.
6) Discard the pellet and immediately freeze the supernatant at -80 °C until use.

REFERENCES

1. Smith, G. T. *et al.* Robust dipstick urinalysis using a low-cost, micro-volume slipping manifold and mobile phone platform. *Lab on a Chip* **16**, 2069–2078 (2016).

2. Girosi, F. *et al.* Developing and interpreting models to improve diagnostics in developing countries. *Nature* **444**, 3–8 (2006).

3. Engel, N. *et al.* Addressing the challenges of diagnostics demand and supply: Insights from an online global health discussion platform. *BMJ Global Health* **1**, 1–8 (2016).

4. Mugambi, M. L., Peter, T., Martins, S. F. & Giachetti, C. How to implement new diagnostic products in low-resource settings: an end-to-end framework. *BMJ global health* **3**, e000914 (2018).

5. Poste, G. Bring on the biomarkers. *Nature* **469**, 156–157 (2011).

6. Group, B. D. W. *et al.* Biomarkers and surrogate endpoints: preferred definitions and conceptual framework. *Clinical pharmacology & therapeutics* **69**, 89–95 (2001).

7. Aronson, J. K. & Ferner, R. E. Biomarkers—a general review. *Current protocols in pharmacology* **76**, 9–23 (2017).

8. Urdea, M. *et al.* Requirements for high impact diagnostics in the developing world. *Nature* **444**, 73–79 (2006).

9. Centers for Disease Control (CDC. 'Workbook for designing, implementing, and evaluating a sharps injury prevention program.' (2004).

10. Haiduven, Donna, and S. F. Sharps injuries in the home health care setting: risks for home health care workers. *Aaohn Journal* **52.3**, 102-108. (2004).

11. Gershon, R. R. M. *et al.* The prevalence and risk factors for percutaneous injuries in registered nurses in the home health care sector. *American Journal of Infection Control* **37**, 525–533 (2009).

12. McConville, A., Hegarty, C. & Davis, J. Mini-Review: Assessing the Potential Impact of Microneedle Technologies on Home Healthcare Applications. *Medicines* **5**, 50 (2018).

13. Coker, A. *et al.* Medical waste management in Ibadan, Nigeria: Obstacles and prospects. *Waste Management* **29**, 804–811 (2009).

14. Lei, R., Huo, R. & Mohan, C. Expert Review of Molecular Diagnostics Current and emerging trends in point-of-care urinalysis tests. *Expert Review of Molecular Diagnostics* **00**, 1–16 (2020).

15. Visser, W. C. H. Commercialized Blood-, Urinary- and Tissue-Based Biomarker Tests for Prostate Cancer Diagnosis and Prognosis. *Cancers* **12**, (2020).

16. Bottin, J. H., Lemetais, G., Poupin, M., Jimenez, L. & Perrier, E. T. Equivalence of afternoon spot and 24-h urinary hydration biomarkers in free-living healthy adults. *European Journal of Clinical Nutrition* **70**, 904–907 (2016).

17. Klasner, S. A. *et al.* Paper-based microfluidic devices for analysis of clinically relevant analytes present in urine and saliva. *Analytical and Bioanalytical Chemistry* **397**, 1821–1829 (2010).

18. Mambatta, A. K. *et al.* Reliability of dipstick assay in predicting urinary tract infection. *Journal of*

family medicine and primary care **4**, 265 (2015).

19. Jia, L. *et al.* An attempt to understand kidney's protein handling function by comparing plasma and urine proteomes. *PLoS ONE* **4**, (2009).

20. Simerville, J. A., Maxted, W. C. & Pahira, J. J. Urinalysis: A comprehensive review. *American Family Physician* **71**, 1153–1162 (2005).

21. Mandel, P. & Metais, P. Nuclear acids in human blood plasma. *Comptes rendus des seances de la Societe de biologie et de ses filiales* **142**, 241–243 (1948).

22. Wetterstrand, K. A. (NIH). The Cost of Sequencing a Human Genome. (2021). Available at: https://www.genome.gov/about-genomics/fact-sheets/Sequencing-Human-Genome-cost. (Accessed: 1st December 2023)

23. Lo, Y. M. D. *et al.* Presence of fetal DNA in maternal plasma and serum. *The lancet* **350**, 485–487 (1997).

24. Zhang, J. *et al.* Presence of donor-and recipient-derived DNA in cell-free urine samples of renal transplantation recipients: urinary DNA chimerism. *Clinical chemistry* **45**, 1741–1746 (1999).

25. Botezatu, I. *et al.* Genetic analysis of DNA excreted in urine: a new approach for detecting specific genomic DNA sequences from cells dying in an organism. *Clinical chemistry* **46**, 1078–1084 (2000).

26. Chakrabarti, A. K. *et al.* Detection of HIV-1 RNA/DNA and CD4 mRNA in feces and urine from chronic HIV-1 infected subjects with and without anti-retroviral therapy. *AIDS research and therapy* **6**, 1–11 (2009).

27. Weerakoon, K. G. & McManus, D. P. Cell-free DNA as a diagnostic tool for human parasitic infections. *Trends in parasitology* **32**, 378–391 (2016).

28. Fernández-Carballo, B. L., Broger, T., Wyss, R., Banaei, N. & Denkinger, C. M. Toward the development of a circulating free DNA-based in vitro diagnostic test for infectious diseases: a review of evidence for tuberculosis. *Journal of clinical microbiology* **57**, e01234-18 (2019).

29. Tsui, N. B. Y. *et al.* High resolution size analysis of fetal DNA in the urine of pregnant women by paired-end massively parallel sequencing. *PloS one* **7**, e48319 (2012).

30. Reckamp, K. L. *et al.* A highly sensitive and quantitative test platform for detection of NSCLC EGFR mutations in urine and plasma. *Journal of Thoracic Oncology* **11**, 1690–1700 (2016).

31. Fujii, T. *et al.* Mutation-Enrichment Next-Generation Sequencing for Quantitative Detection of KRAS Mutations in Urine Cell-Free DNA from Patients with Advanced CancersKRAS Mutations in Urine cfDNA. *Clinical Cancer Research* **23**, 3657–3666 (2017).

32. Chary, S. R. & Jain, R. K. Direct measurement of interstitial convection and diffusion of albumin in normal and neoplastic tissues by fluorescence photobleaching. *Proceedings of the National Academy of Sciences* **86**, 5385–5389 (1989).

33. Samant, P. P. *et al.* Sampling interstitial fluid from human skin using a microneedle patch. *Science translational medicine* **12**, eaaw0285 (2020).

34. Tran, B. Q. *et al.* Proteomic characterization of dermal interstitial fluid extracted using a novel microneedle-assisted technique. *Journal of proteome research* **17**, 479–485 (2018).

35. Steijlen, A. S. M., Jansen, K. M. B., Bastemeijer, J., French, P. J. & Bossche, A. Low-Cost

Wearable Fluidic Sweat Collection Patch for Continuous Analyte Monitoring and Offline Analysis. *Analytical chemistry* (2022).

36. Holmgaard, R. *et al.* Comparison of open-flow microperfusion and microdialysis methodologies when sampling topically applied fentanyl and benzoic acid in human dermis ex vivo. *Pharmaceutical research* **29**, 1808–1820 (2012).

37. Himawan, A. *et al.* Where Microneedle Meets Biomarkers: Futuristic Application for Diagnosing and Monitoring Localized External Organ Diseases. *Advanced Healthcare Materials* 2202066 (2022).

38. Zheng, M. *et al.* Osmosis-powered hydrogel microneedles for microliters of skin interstitial fluid extraction within minutes. *Advanced healthcare materials* **9**, 1901683 (2020).

39. Laszlo, E., De Crescenzo, G., Nieto-Argüello, A., Banquy, X. & Brambilla, D. Superswelling microneedle arrays for dermal interstitial fluid (prote) omics. *Advanced Functional Materials* **31**, 2106061 (2021).

40. Rahmat, R. F. *et al.* Automated color classification of urine dipstick image in urine examination. *Journal of Physics: Conference Series* **978**, (2018).

41. Kavuru, V. *et al.* Dipstick analysis of urine chemistry: benefits and limitations of dry chemistry-based assays. *Postgraduate Medicine* **5481**, (2019).

42. Brown, R. S. Has the Time Come to Include Asymptomatic Young Adults ? **02215**, 6–7 (2011).

43. Krogsbøll, L. T. Guidelines for screening with urinary dipsticks differ substantially - A systematic review. *Danish Medical Journal* **61**, 1–9 (2014).

44. Fogazzi, G. B., Verdesca, S. & Garigali, G. Urinalysis: Core Curriculum 2008. *American Journal of Kidney Diseases* **51**, 1052–1067 (2008).

45. Diagnostics, C. Urs 1-11(06-11-2013). 1–8

46. Van Delft, S. *et al.* Prospective, observational study comparing automated and visual point-of-care urinalysis in general practice. *BMJ Open* **6**, 1–7 (2016).

47. Rumley, A. Urine dipstick testing: comparison of results obtained by visual reading and with the Bayer CLINITEK 50. *Annals of clinical biochemistry* **37**, 220–221 (2000).

48. Peele Jr, J. D., Gadsden, R. H. & Crews, R. Semi-automated vs. visual reading of urinalysis dipsticks. *Clinical chemistry* **23**, 2242–2246 (1977).

49. Luber, G. & McGeehin, M. Climate change and extreme heat events. *American journal of preventive medicine* **35**, 429–435 (2008).

50. CDC, A. Z. Extreme heat: a prevention guide to promote your personal health and safety. in (CDC Atlanta, 2004).

51. Pai, D. S., NAIR, S. & Ramanathan, A. N. Long term climatology and trends of heat waves over India during the recent 50 years (1961-2010). *Mausam* **64**, 585–604 (2013).

52. Borg, M., Bi, P., Nitschke, M., Williams, S. & McDonald, S. The impact of daily temperature on renal disease incidence: an ecological study. *Environmental Health* **16**, 1–30 (2017).

53. Jackson, L. L. & Rosenberg, H. R. Preventing heat-related illness among agricultural workers. *Journal of agromedicine* **15**, 200–215 (2010).

54. Wästerlund, S. Managing heat in agricultural work: increasing worker safety and productivity by controlling heat exposure. *FAO: Roma, Italy* **53**, (2018).

55. Dematte, J. E. *et al.* Near-fatal heat stroke during the 1995 heat wave in Chicago. *Annals of internal medicine* **129**, 173–181 (1998).

56. Wesseling, C. *et al.* Mesoamerican nephropathy: geographical distribution and time trends of chronic kidney disease mortality between 1970 and 2012 in Costa Rica. *Occupational and Environmental Medicine* **72**, 714–721 (2015).

57. Ordunez, P. *et al.* Chronic kidney disease mortality trends in selected Central America countries, 1997–2013: clues to an epidemic of chronic interstitial nephritis of agricultural communities. *J Epidemiol Community Health* **72**, 280–286 (2018).

58. Johnson, R. J., Wesseling, C. & Newman, L. S. Chronic kidney disease of unknown cause in agricultural communities. *New England Journal of Medicine* **380**, 1843–1852 (2019).

59. Kupferman, J. *et al.* Acute kidney injury in sugarcane workers at risk for Mesoamerican nephropathy. *American Journal of Kidney Diseases* **72**, 475–482 (2018).

60. García-Trabanino, R. *et al.* Heat stress, dehydration, and kidney function in sugarcane cutters in El Salvador–a cross-shift study of workers at risk of Mesoamerican nephropathy. *Environmental research* **142**, 746–755 (2015).

61. Arphorn, S. *et al.* Working conditions and urinalysis dipstick testing among female rice farmers: A preliminary cross-sectional study. *International Journal of Environmental Research and Public Health* **18**, 8942 (2021).

62. Thakur, V. *et al.* Multi-organ involvement in COVID-19: beyond pulmonary manifestations. *Journal of clinical medicine* **10**, 446 (2021).

63. Mohamed, M. M. B. & Velez, J. C. Q. Proteinuria in COVID-19. *Clinical kidney journal* **14**, i40–i47 (2021).

64. McAdams, M., Ostrosky-Frid, M., Rajora, N. & Hedayati, S. Effect of COVID-19 on kidney disease incidence and management. *Kidney360* **2**, 141 (2021).

65. Su, H. *et al.* Renal histopathological analysis of 26 postmortem findings of patients with COVID-19 in China. *Kidney international* **98**, 219–227 (2020).

66. McAdams, M. C. *et al.* Using dipstick urinalysis to predict development of acute kidney injury in patients with COVID-19. *BMC nephrology* **23**, 1–10 (2022).

67. Patel, D. M. *et al.* Association of AKI-D with urinary findings and baseline eGFR in hospitalized COVID-19 patients. *Kidney360* **2**, 1215 (2021).

68. Sung, H. *et al.* Global cancer statistics 2020: GLOBOCAN estimates of incidence and mortality worldwide for 36 cancers in 185 countries. *CA: a cancer journal for clinicians* **71**, 209–249 (2021).

69. Salehi, F., Dunfield, L., Phillips, K. P., Krewski, D. & Vanderhyden, B. C. Risk factors for ovarian cancer: an overview with emphasis on hormonal factors. *Journal of Toxicology and Environmental Health, Part B* **11**, 301–321 (2008).

70. Alcázar, J. L., Castillo, G., Jurado, M. & García, G. L. Is expectant management of sonographically benign adnexal cysts an option in selected asymptomatic premenopausal women? *Human Reproduction* **20**, 3231–3234 (2005).

71. Ekerhovd, E., Wienerroith, H., Staudach, A. & Granberg, S. Preoperative assessment of unilocular adnexal cysts by transvaginal ultrasonography: A comparison between ultrasonographic morphologic imaging and histopathologic diagnosis. *American Journal of Obstetrics and Gynecology* **184**, 48–54 (2001).

72. Modesitt, S. C. *et al.* Risk of malignancy in unilocular ovarian cystic tumors less than 10 centimeters in diameter. *Obstetrics and Gynecology* **102**, 594–599 (2003).

73. Kumari, S. Serum Biomarker Based Algorithms in Diagnosis of Ovarian Cancer: A Review. *Indian Journal of Clinical Biochemistry* **33**, 382–386 (2018).

74. Su, Z., Graybill, W. S. & Zhu, Y. Detection and monitoring of ovarian cancer. *Clinica Chimica Acta* **415**, 341–345 (2013).

75. Carlson, K. J., Skates, S. J. & Singer, D. E. Screening for ovarian cancer. *Annals of internal medicine* **121**, 124–132 (1994).

76. Bast, R. C. *et al.* New tumor markers: CA125 and beyond. *International Journal of Gynecological Cancer* **15**, 274–281 (2005).

77. Sölétormos, G. *et al.* Clinical Use of Cancer Biomarkers in Epithelial Ovarian Cancer: Updated Guidelines from the European Group on Tumor Markers. *International Journal of Gynecological Cancer* **26**, 43–51 (2016).

78. Chitale, R. Monitoring Ovarian Cancer: CA125 Trial Stirs Controversy. *JNCI: Journal of the National Cancer Institute* **101**, 1233–1235 (2009).

79. Heliström, I. *et al.* The HE4 (WFDC2) protein is a biomarker for ovarian carcinoma. *Cancer Research* **63**, 3695–3700 (2003).

80. Simmons, A. R., Baggerly, K. & Bast, R. C. The emerging role of HE4 in the evaluation of epithelial Ovarian and endometrial carcinomas. *ONCOLOGY (United States)* **27**, 548–556 (2013).

81. Wu, L. *et al.* Diagnostic value of serum human epididymis protein 4 (HE4) in ovarian carcinoma: a systematic review and meta-analysis. *International Journal of Gynecologic Cancer* **22**, (2012).

82. Welsh, J. B. *et al.* Analysis of gene expression profiles in normal and neoplastic ovarian tissue samples identifies candidate molecular markers of epithelial ovarian cancer. *Proceedings of the National Academy of Sciences* **98**, 1176–1181 (2001).

83. Escudero, J. M. *et al.* Comparison of serum human epididymis protein 4 with cancer antigen 125 as a tumor marker in patients with malignant and nonmalignant diseases. *Clinical Chemistry* **57**, 1534–1544 (2011).

84. Zhang, Y., Qiao, C., Li, L., Zhao, X. & Li, Y. Serum HE4 is more suitable as a biomarker than CA125 in Chinese women with benign gynecologic disorders. *African health sciences* **14**, 913–918 (2014).

85. Hynninen, J. *et al.* Serum HE4 profile during primary chemotherapy of epithelial ovarian cancer. *International Journal of Gynecologic Cancer* **21**, (2011).

86. Piovano, E. *et al.* The role of HE4 in ovarian cancer follow-up: a review. *International Journal of Gynecologic Cancer* **24**, (2014).

87. Innao, P., Pothisuwan, M. & Pengsa, P. Does human epididymis protein 4 (HE4) have a role in prediction of recurrent epithelial ovarian cancer. *Asian Pacific Journal of Cancer Prevention* **17**, 4483–4486 (2016).

88. Longoria, T. C. *et al.* Clinical performance of a multivariate index assay for detecting early-stage ovarian cancer. *American journal of obstetrics and gynecology* **210**, 78-e1 (2014).

89. Lutz, A. M. *et al.* Early diagnosis of ovarian carcinoma: is a solution in sight? *Radiology* **259**, 329–345 (2011).

90. Jacobs, I. *et al.* A risk of malignancy index incorporating CA 125, ultrasound and menopausal status for the accurate preoperative diagnosis of ovarian cancer. *BJOG: An International Journal of Obstetrics & Gynaecology* **97**, 922–929 (1990).

91. Moore, R. G. *et al.* Comparison of a novel multiple marker assay vs the Risk of Malignancy Index for the prediction of epithelial ovarian cancer in patients with a pelvic mass. *American journal of obstetrics and gynecology* **203**, 228-e1 (2010).

92. Meraner, V. *et al.* Monitoring physical and psychosocial symptom trajectories in ovarian cancer patients receiving chemotherapy. *BMC cancer* **12**, 1–10 (2012).

93. Lifford, K. J. *et al.* Withdrawal from familial ovarian cancer screening for surgery: Findings from a psychological evaluation study (PsyFOCS). *Gynecologic Oncology* **124**, 158–163 (2012).

94. Lifford, K. J., Clements, A., Fraser, L., Lancastle, D. & Brain, K. Catalysts to withdrawal from familial ovarian cancer screening for surgery and reactions to discontinued screening: A qualitative study. *Familial Cancer* **12**, 19–26 (2013).

95. Manchanda, R. *et al.* Factors influencing uptake and timing of risk reducing salpingo-oophorectomy in women at risk of familial ovarian cancer: A competing risk time to event analysis. *BJOG: An International Journal of Obstetrics and Gynaecology* **119**, 527–536 (2012).

96. Brain, K., Gravell, C., France, E., Fiander, A. & Gray, J. An exploratory qualitative study of women's perceptions of risk management options for familial ovarian cancer: Implications for informed decision making. *Gynecologic Oncology* **92**, 905–913 (2004).

97. Tiller, K. *et al.* Psychological impact of prophylactic oophorectomy in women at increased risk of developing ovarian cancer: A prospective study. *Gynecologic Oncology* **86**, 212–219 (2002).

98. Hallowell, N. 'You don't want to lose your ovaries because you think "I might become a man"'. Women's perceptions of prophylactic surgery as a cancer risk management option. *Psycho-Oncology* **7**, 263–275 (1998).

99. Hallowell, N. A qualitative study of the information needs of high-risk women undergoing prophylactic oophorectomy. *Psycho-Oncology* **9**, 486–495 (2000).

100. Yandell, K. Little Consensus on Ovarian Cancer Monitoring. *Cancertodaymag.org* (2016). Available at: https://www.cancertodaymag.org/winter2016-2017/little-consensus-on-ovarian-cancer-monitoring/. (Accessed: 1st May 2020)

101. Wang, S. *et al.* Integration of cell phone imaging with microchip ELISA to detect ovarian cancer HE4 biomarker in urine at the point-of-care. *Lab on a Chip* **11**, 3411–3418 (2011).

102. RequestATest. HE4 Test in Price, Utah. Available at: https://requestatest.com/he4-test-price-utah-377-n-fairgrounds-rd-84501.

103. Moore, R. G. *et al.* A novel multiple marker bioassay utilizing HE4 and CA125 for the prediction of ovarian cancer in patients with a pelvic mass. *Gynecologic Oncology* **112**, 40–46 (2009).

104. Hellstrom, I. *et al.* Detection of the HE4 protein in urine as a biomarker for ovarian neoplasms. *Cancer Letters* **296**, 43–48 (2010).

105. Liao, J. B. *et al.* Detection of the HE4 protein in urine as a biomarker for ovarian neoplasms: Clinical correlates. *Gynecologic Oncology* **137**, 430–435 (2015).

106. Kamińska, J., Dymicka-Piekarska, V., Tomaszewska, J., Matowicka-Karna, J. & Koper-Lenkiewicz, O. M. Diagnostic utility of protein to creatinine ratio (P/C ratio) in spot urine sample within routine clinical practice. *Critical Reviews in Clinical Laboratory Sciences* **57**, 345–364 (2020).

107. Hiraoka, R. *et al.* Paper-Based Device for Naked Eye Urinary Albumin/Creatinine Ratio Evaluation. *ACS Sensors* **5**, 1110–1118 (2020).

108. Macuks, R., Baidekalna, I. & Donina, S. Urinary concentrations of human epididymis secretory protein 4 (He4) in the diagnosis of ovarian cancer: A case-control study. *Asian Pacific Journal of Cancer Prevention* **13**, 4695–4698 (2012).

109. Qu, W. *et al.* HE4-test of urine and body fluids for diagnosis of gynecologic cancer. *Expert Review of Molecular Diagnostics* **17**, 239–244 (2017).

110. Corder, C. J., Rathi, B. M., Sharif, S. & Leslie, S. W. 24-Hour Urine Collection. *StatPearls [Internet]* (2020).

111. Parag, K. B. & Seedat, K. The protein / creatinine index. *S Afr Med J* **69**, 42–43 (1986).

112. Newman, D. J., Pugia, M. J., Lott, J. A., Wallace, J. F. & Hiar, A. M. Urinary protein and albumin excretion corrected by creatinine and specific gravity. *Clinica Chimica Acta* **294**, 139–155 (2000).

113. Huang, Y. *et al.* Correlation of urine protein/creatinine ratios to 24-h urinary protein for quantitating proteinuria in children. *Pediatric Nephrology* **35**, 463–468 (2020).

114. Barr, D. B. *et al.* Urinary creatinine concentrations in the US population: implications for urinary biologic monitoring measurements. *Environmental health perspectives* **113**, 192–200 (2005).

115. Wyss, M. & Kaddurah-Daouk, R. Creatine and creatinine metabolism. *Physiological reviews* **80**, 1107–1213 (2000).

116. Beaglehole, R., Bonita, R. & Magnusson, R. Global cancer prevention: an important pathway to global health and development. *Public health* **125**, 821–831 (2011).

117. Abegunde, D. O., Mathers, C. D., Adam, T., Ortegon, M. & Strong, K. The burden and costs of chronic diseases in low-income and middle-income countries. *The Lancet* **370**, 1929–1938 (2007).

118. Jemal, A. *et al.* Global cancer statistics. *CA: a cancer journal for clinicians* **61**, 69–90 (2011).

119. Thun, M. J., DeLancey, J. O., Center, M. M., Jemal, A. & Ward, E. M. The global burden of cancer: priorities for prevention. *Carcinogenesis* **31**, 100–110 (2010).

120. Varughese, J. & Richman, S. Cancer care inequity for women in resource-poor countries. *Reviews in Obstetrics and Gynecology* **3**, 122 (2010).

121. Denny, L., Quinn, M. & Sankaranarayanan, R. Screening for cervical cancer in developing countries. *Vaccine* **24**, S71–S77 (2006).

122. Safaeian, M., Solomon, D. & Castle, P. E. Cervical cancer prevention—cervical screening: science in evolution. *Obstetrics and gynecology clinics of North America* **34**, 739–760 (2007).

123. Bedell, S. L., Goldstein, L. S., Goldstein, A. R. & Goldstein, A. T. Cervical cancer screening: past, present, and future. *Sexual medicine reviews* **8**, 28–37 (2020).

124. Goldie, S. J. *et al.* Cost-effectiveness of cervical-cancer screening in five developing countries. *New England Journal of Medicine* **353**, 2158–2168 (2005).

125. Nishimura, H., Yeh, P. T., Oguntade, H., Kennedy, C. E. & Narasimhan, M. HPV self-sampling for cervical cancer screening: a systematic review of values and preferences. *BMJ Global Health* **6**, e003743 (2021).

126. Arrossi, S. *et al.* Effect of self-collection of HPV DNA offered by community health workers at home visits on uptake of screening for cervical cancer (the EMA study): a population-based cluster-randomised trial. *The Lancet Global Health* **3**, e85–e94 (2015).

127. Tulchiner, G. *et al.* The "COVID-19 pandemic gap" and its influence on oncologic outcomes of bladder cancer. *Cancers* **13**, 1754 (2021).

128. Roscigno, M. *et al.* A snapshot from the department of urology in Bergamo evaluating the timeline of the SARS-CoV-2 outbreak: Which patients are we missing? *European urology focus* **6**, 1120–1123 (2020).

129. Quam, N. *et al.* Perception of telehealth during the COVID-19 pandemic among survivors of gynecologic cancer. *The Oncologist* **27**, 512–515 (2022).

130. Feinberg, J. *et al.* Ovarian cancer recurrence detection may not require in-person physical examination: an MSK team ovary study. *International Journal of Gynecologic Cancer* **32**, (2022).

131. Wide, L. Inventions leading to the development of the diagnostic test kit industry–from the modern pregnancy test to the sandwich assays. *Upsala journal of medical sciences* **110**, 193–216 (2005).

132. Leavitt, S. A. 'A private little revolution': The home pregnancy test in American culture. *Bulletin of the History of Medicine* **80**, 317–345 (2006).

133. Lee, J. H. *Based Medical Diagnostic Devices: As a Part of Bioanalysis-Advanced Materials, Methods, and Devices*. **10**, (Springer Nature, 2020).

134. Steere, A. C. *et al.* The spirochetal etiology of Lyme disease. *New England Journal of Medicine* **308**, 733–740 (1983).

135. Burgdorfer, W. *et al.* Lyme disease—a tick-borne spirochetosis? *Science* **216**, 1317–1319 (1982).

136. Steere, A. C. *et al.* An epidemic of oligoarticular arthritis in children and adults in three connecticut communities. *Arthritis & Rheumatism* **20**, 7–17 (1977).

137. Steere, A. C. *et al.* Lyme borreliosis. *Nature Reviews Disease Primers* **2**, (2016).

138. Radolf, J. D., Caimano, M. J., Stevenson, B. & Hu, L. T. Of ticks, mice and men: understanding the dual-host lifestyle of Lyme disease spirochaetes. *Nature reviews microbiology* **10**, 87–99 (2012).

139. Hinckley, A. F. *et al.* Lyme disease testing by large commercial laboratories in the United States. *Clinical Infectious Diseases* **59**, 676–681 (2014).

140. Prevention, C. for D. C. and. National center for emerging and zoonotic infectious diseases. *Internet address: http://www. cdc. gov/nczved/divisions/dfbmd/diseases/campylobacter/technical. ht ml. Accessed Jan* (2014).

141. Wormser, G. P. *et al.* The clinical assessment, treatment, and prevention of Lyme disease, human granulocytic anaplasmosis, and babesiosis: clinical practice guidelines by the Infectious Diseases

Society of America. *Clinical Infectious Diseases* **43**, 1089–1134 (2006).

142. Marques, A. Chronic Lyme disease: a review. *Infectious disease clinics of North America* **22**, 341–360 (2008).

143. Mead, P. S. Epidemiology of Lyme disease. *Infectious Disease Clinics* **29**, 187–210 (2015).

144. Rebman, A. W. & Aucott, J. N. Post-treatment Lyme disease as a model for persistent symptoms in Lyme disease. *Frontiers in medicine* 57 (2020).

145. Cerar, T. *et al.* Differences in genotype, clinical features, and inflammatory potential of Borrelia burgdorferi sensu stricto strains from Europe and the United States. *Emerging infectious diseases* **22**, 818 (2016).

146. Stanek, G., Wormser, G. P., Gray, J. & Strle, F. Lyme borreliosis. *The Lancet* **379**, 461–473 (2012).

147. Lemon, S. M. *et al.* Vector-borne diseases: understanding the environmental, human health, and ecological connections. Workshop summary. in *Vector-borne diseases: understanding the environmental, human health, and ecological connections. Workshop summary.* (National Academies Press, 2008).

148. Simon, J. A. *et al.* Climate change and habitat fragmentation drive the occurrence of B orrelia burgdorferi, the agent of Lyme disease, at the northeastern limit of its distribution. *Evolutionary Applications* **7**, 750–764 (2014).

149. Zell, R. Global climate change and the emergence/re-emergence of infectious diseases. *International Journal of Medical Microbiology Supplements* **293**, 16–26 (2004).

150. Parola, P. & Raoult, D. Ticks and tickborne bacterial diseases in humans: an emerging infectious threat. *Clinical infectious diseases* **32**, 897–928 (2001).

151. Sood, S. K. *et al.* Duration of tick attachment as a predictor of the risk of Lyme disease in an area in which Lyme disease is endemic. *Journal of Infectious Diseases* **175**, 996–999 (1997).

152. Hu, L. T. In the clinic. Lyme disease. *Annals of Internal Medicine* **157**, ITC2-2 (2012).

153. Lochhead, R. B., Strle, K., Arvikar, S. L., Weis, J. J. & Steere, A. C. Lyme arthritis: linking infection, inflammation and autoimmunity. *Nature Reviews Rheumatology* **17**, 449–461 (2021).

154. Kuhn, H. W. *et al.* BB0562 is a nutritional virulence determinant with lipase activity important for Borrelia burgdorferi infection and survival in fatty acid deficient environments. *PLoS pathogens* **17**, e1009869 (2021).

155. Baril, C., Richaud, C., Baranton, G. & Saint Girons, I. Linear chromosome of Borrelia burgdorferi. *Research in microbiology* **140**, 507–516 (1989).

156. Ferdows, M. S. & Barbour, A. G. Megabase-sized linear DNA in the bacterium Borrelia burgdorferi, the Lyme disease agent. *Proceedings of the National Academy of Sciences* **86**, 5969–5973 (1989).

157. Davidson, B. E., MacDougall, J. & Saint Girons, I. Physical map of the linear chromosome of the bacterium Borrelia burgdorferi 212, a causative agent of Lyme disease, and localization of rRNA genes. *Journal of bacteriology* **174**, 3766–3774 (1992).

158. Casjens, S. & Huang, W. M. Linear chromosomal physical and genetic map of Borrelia burgdorferi, the Lyme disease agent. *Molecular microbiology* **8**, 967–980 (1993).

159. Schröder, N. W. J. *et al.* Acylated cholesteryl galactoside as a novel immunogenic motif in Borrelia burgdorferi sensu stricto. *Journal of Biological Chemistry* **278**, 33645–33653 (2003).

160. Goldstein, S. F. *et al.* Borrelia: molecular biology, host interaction, and pathogenesis. *Samuels, DS* 167–187 (2010).

161. Sultan, S. Z. *et al.* Motility is crucial for the infectious life cycle of Borrelia burgdorferi. *Infection and immunity* **81**, 2012–2021 (2013).

162. Moriarty, T. J. *et al.* Real-time high resolution 3D imaging of the Lyme disease spirochete adhering to and escaping from the vasculature of a living host. *PLoS pathogens* **4**, e1000090 (2008).

163. Sultan, S. Z. *et al.* Motor rotation is essential for the formation of the periplasmic flagellar ribbon, cellular morphology, and Borrelia burgdorferi persistence within Ixodes scapularis tick and murine hosts. *Infection and immunity* **83**, 1765–1777 (2015).

164. Bernard, Q., Grillon, A., Lenormand, C., Ehret-Sabatier, L. & Boulanger, N. Skin interface, a key player for Borrelia multiplication and persistence in Lyme borreliosis. *Trends in parasitology* **36**, 304–314 (2020).

165. Titus, R. G. The immunomodulatory factors of bloodfeeding arthropod saliva. *Parasite immunology* **22**, 319–331 (2000).

166. Šimo, L., Kazimirova, M., Richardson, J. & Bonnet, S. I. The essential role of tick salivary glands and saliva in tick feeding and pathogen transmission. *Frontiers in cellular and infection microbiology* **7**, 281 (2017).

167. Scholl, D. C. *et al.* Immunomodulatory effects of tick saliva on dermal cells exposed to Borrelia burgdorferi, the agent of Lyme disease. *Parasites & vectors* **9**, 1–17 (2016).

168. Burke, G. *et al.* Hypersensitivity to ticks and Lyme disease risk. *Emerging infectious diseases* **11**, 36 (2005).

169. Shih, C.-M., Pollack, R. J., Telford III, S. R. & Spielman, A. Delayed dissemination of Lyme disease spirochetes from the site of deposition in the skin of mice. *Journal of Infectious Diseases* **166**, 827–831 (1992).

170. Salazar, J. C. *et al.* Coevolution of markers of innate and adaptive immunity in skin and peripheral blood of patients with erythema migrans. *The Journal of Immunology* **171**, 2660–2670 (2003).

171. Müllegger, R. R. *et al.* Differential expression of cytokine mRNA in skin specimens from patients with erythema migrans or acrodermatitis chronica atrophicans. *Journal of investigative dermatology* **115**, 1115–1123 (2000).

172. Menten-Dedoyart, C. *et al.* Neutrophil extracellular traps entrap and kill Borrelia burgdorferi sensu stricto spirochetes and are not affected by Ixodes ricinus tick saliva. *The Journal of Immunology* **189**, 5393–5401 (2012).

173. Pappas, C. J. *et al.* Borrelia burgdorferi requires glycerol for maximum fitness during the tick phase of the enzootic cycle. *PLoS pathogens* **7**, e1002102 (2011).

174. Coleman, J. L. *et al.* Plasminogen is required for efficient dissemination of B. burgdorferi in ticks and for enhancement of spirochetemia in mice. *Cell* **89**, 1111–1119 (1997).

175. Coleman, J. L., Benach, J. L. & Karzai, A. W. Endogenous and Borrowed Proteolytic Activity in the Borrelia. *Microbiology and Molecular Biology Reviews* **85**, e00217-20 (2021).

176. Zhang, J.-R., Hardham, J. M., Barbour, A. G. & Norris, S. J. Antigenic variation in Lyme disease borreliae by promiscuous recombination of VMP-like sequence cassettes. *Cell* **89**, 275–285 (1997).

177. Norris, S. J. Antigenic variation with a twist–the Borrelia story. *Molecular microbiology* **60**, 1319–1322 (2006).

178. Yssouf, A., Almeras, L., Raoult, D. & Parola, P. Emerging tools for identification of arthropod vectors. *Future Microbiology* **11**, 549–566 (2016).

179. Camicas, J. L., Hervy, J. P., Adam, F. & Morel, P. C. The ticks of the world (Acarida, Ixodida): nomenclature, described stages, hosts, distribution. *The ticks of the world (Acarida, Ixodida): nomenclature, described stages, hosts, distribution.* (1998).

180. Yssouf, A. *et al.* Matrix-assisted laser desorption ionization–time of flight mass spectrometry for rapid identification of tick vectors. *Journal of clinical microbiology* **51**, 522–528 (2013).

181. Koffi, J. *et al.* eTick: A Lyme disease surveillance and public health information tool. in *2016 International Congress of Entomology* (ESA, 2016).

182. Akbarian, S. *et al.* A computer vision approach to combat lyme disease. *arXiv preprint arXiv:2009.11931* (2020).

183. Glatz, M., Golestani, M., Kerl, H. & Müllegger, R. R. Clinical relevance of different IgG and IgM serum antibody responses to Borrelia burgdorferi after antibiotic therapy for erythema migrans: long-term follow-up study of 113 patients. *Archives of dermatology* **142**, 862–868 (2006).

184. Strle, F. *et al.* Comparison of erythema migrans caused by Borrelia burgdorferi and Borrelia garinii. *Vector-Borne and Zoonotic Diseases* **11**, 1253–1258 (2011).

185. Fix, A. D., Peña, C. A. & Strickland, G. T. Racial differences in reported Lyme disease incidence. *American journal of epidemiology* **152**, 756–759 (2000).

186. O'Rourke, M. *et al.* Quantitative detection of Borrelia burgdorferi sensu lato in erythema migrans skin lesions using internally controlled duplex real time PCR. *PLOS one* **8**, e63968 (2013).

187. Liveris, D. *et al.* Quantitative detection of Borrelia burgdorferi in 2-millimeter skin samples of erythema migrans lesions: correlation of results with clinical and laboratory findings. *Journal of clinical microbiology* **40**, 1249–1253 (2002).

188. Liveris, D. *et al.* Improving the yield of blood cultures from patients with early Lyme disease. *Journal of Clinical Microbiology* **49**, 2166–2168 (2011).

189. Stupica, D. *et al.* Correlation of culture positivity, PCR positivity, and burden of Borrelia burgdorferi sensu lato in skin samples of erythema migrans patients with clinical findings. *PLoS One* **10**, e0136600 (2015).

190. Branda, J. A. *et al.* Advances in serodiagnostic testing for Lyme disease are at hand. *Clinical Infectious Diseases* **66**, 1133–1139 (2018).

191. Nowakowski, J. *et al.* Laboratory diagnostic techniques for patients with early Lyme disease associated with erythema migrans: a comparison of different techniques. *Clinical infectious diseases* **33**, 2023–2027 (2001).

192. Laura, A. Global tuberculosis report 2018. *Geneva: World Health Organization* (2018).

193. Flynn, J. L. & Chan, J. Tuberculosis: latency and reactivation. *Infection and immunity* **69**, 4195–

4201 (2001).

194. Golden, M. P. & Vikram, H. R. Extrapulmonary tuberculosis: an overview. *American family physician* **72**, 1761–1768 (2005).

195. Rao, M. *et al.* Improving treatment outcomes for MDR-TB—novel host-directed therapies and personalised medicine of the future. *International Journal of Infectious Diseases* **80**, S62–S67 (2019).

196. Silva, S., Arinaminpathy, N., Atun, R., Goosby, E. & Reid, M. Economic impact of tuberculosis mortality in 120 countries and the cost of not achieving the Sustainable Development Goals tuberculosis targets: a full-income analysis. *The Lancet Global Health* **9**, e1372–e1379 (2021).

197. Cohen, A., Mathiasen, V. D., Schön, T. & Wejse, C. The global prevalence of latent tuberculosis: a systematic review and meta-analysis. *European Respiratory Journal* **54**, (2019).

198. MacPherson, P., Houben, R. M. G. J., Glynn, J. R., Corbett, E. L. & Kranzer, K. Pre-treatment loss to follow-up in tuberculosis patients in low-and lower-middle-income countries and high-burden countries: a systematic review and meta-analysis. *Bulletin of the World Health Organization* **92**, 126–138 (2013).

199. Hamada, Y. *et al.* Tests for tuberculosis infection: landscape analysis. *European Respiratory Journal* **58**, (2021).

200. Connell, T. G. *et al.* A three-way comparison of tuberculin skin testing, QuantiFERON-TB gold and T-SPOT. TB in children. *PloS one* **3**, e2624 (2008).

201. Caulfield, A. J. & Wengenack, N. L. Diagnosis of active tuberculosis disease: From microscopy to molecular techniques. *Journal of Clinical Tuberculosis and Other Mycobacterial Diseases* **4**, 33–43 (2016).

202. Small, P. M. & Pai, M. Tuberculosis diagnosis—time for a game change. *New England Journal of Medicine* **363**, 1070–1071 (2010).

203. Gupta-Wright, A. *et al.* Rapid urine-based screening for tuberculosis in HIV-positive patients admitted to hospital in Africa (STAMP): a pragmatic, multicentre, parallel-group, double-blind, randomised controlled trial. *The Lancet* **392**, 292–301 (2018).

204. Organization, W. H. Global tuberculosis report 2020: executive summary. (2020).

205. Organization, W. H. Global tuberculosis report 2021. Geneva: WHO; 2021. (2021).

206. Cambanis, A., Ramsay, A., Wirkom, V., Tata, E. & Cuevas, L. E. Investing time in microscopy: an opportunity to optimise smear-based case detection of tuberculosis. *The International Journal of Tuberculosis and Lung Disease* **11**, 40–45 (2007).

207. Denkinger, C. M. *et al.* Xpert MTB/RIF assay for the diagnosis of extrapulmonary tuberculosis: a systematic review and meta-analysis. *European Respiratory Journal* **44**, 435–446 (2014).

208. Elliott, A. M. *et al.* The impact of human immunodeficiency virus on presentation and diagnosis of tuberculosis in a cohort study in Zambia. *The Journal of tropical medicine and hygiene* **96**, 1–11 (1993).

209. Lee, J. Y. Diagnosis and treatment of extrapulmonary tuberculosis. *Tuberculosis and respiratory diseases* **78**, 47–55 (2015).

210. Abu, A. PERIPHERAL BLOOD SAMPLE MAY NOT THE SPECIMEN OF CHOICE FOR THE

DETECTION OF MYCOBACTERIUM TUBERCULOSIS (MTB) BY GENEXPERT PCR ASSAY. 0–5 (2020).

211. Peter, J. G. *et al.* Effect on mortality of point-of-care, urine-based lipoarabinomannan testing to guide tuberculosis treatment initiation in HIV-positive hospital inpatients: a pragmatic, parallel-group, multicountry, open-label, randomised controlled trial. *The Lancet* **387**, 1187–1197 (2016).

212. Bordelon, H. *et al.* Design and use of mouse control DNA for DNA biomarker extraction and PCR detection from urine: Application for transrenal Mycobacterium tuberculosis DNA detection. *Journal of Microbiological Methods* **136**, 65–70 (2017).

213. Umansky, S. R. & Tomei, L. D. Transrenal DNA testing: progress and perspectives. *Expert review of molecular diagnostics* **6**, 153–163 (2006).

214. Cheng, T. H. T. *et al.* Genomewide bisulfite sequencing reveals the origin and time-dependent fragmentation of urinary cfDNA. *Clinical biochemistry* **50**, 496–501 (2017).

215. Nadano, D., Yasuda, T. & Kishi, K. Measurement of deoxyribonuclease I activity in human tissues and body fluids by a single radial enzyme-diffusion method. *Clinical chemistry* **39**, 448–452 (1993).

216. Stevens, V. L., Hoover, E., Wang, Y. & Zanetti, K. A. Pre-analytical factors that affect metabolite stability in human urine, plasma, and serum: A review. *Metabolites* **9**, (2019).

217. Sinkov, V. V *et al.* Metagenomic analysis of mycobacterial transrenal DNA in patients with HIV and tuberculosis coinfection. *Infection, Genetics and Evolution* **77**, 104057 (2020).

218. Markus, H. *et al.* Sub-nucleosomal organization in urine cell-free DNA. *BioRxiv* 696633 (2019).

219. Oreskovic, A., Brault, N. D., Panpradist, N., Lai, J. J. & Lutz, B. R. Analytical Comparison of Methods for Extraction of Short Cell-Free DNA from Urine. *Journal of Molecular Diagnostics* **21**, 1067–1078 (2019).

220. Cannas, A. *et al.* Mycobacterium tuberculosis DNA detection in soluble fraction of urine from pulmonary tuberculosis patients. *The international journal of tuberculosis and lung disease* **12**, 146–151 (2008).

221. Oreskovic, A. *et al.* Unbiased sequencing of Mycobacterium tuberculosis urinary cell-free DNA reveals extremely short fragment lengths. *medRxiv* (2021).

222. Green, C. *et al.* Rapid diagnosis of tuberculosis through the detection of mycobacterial DNA in urine by nucleic acid amplification methods. *The Lancet infectious diseases* **9**, 505–511 (2009).

223. Patel, K. *et al.* Evaluation of a urine-based rapid molecular diagnostic test with potential to be used at point-of-care for pulmonary tuberculosis: Cape Town cohort. *The Journal of Molecular Diagnostics* **20**, 215–224 (2018).

224. Labugger, I. *et al.* Detection of transrenal DNA for the diagnosis of pulmonary tuberculosis and treatment monitoring. *Infection* **45**, 269–276 (2017).

225. Oreskovic, A. *et al.* Unbiased sequencing of. (2021).

226. Oreskovic, A. & Lutz, B. R. Ultrasensitive hybridization capture: Reliable detection of <1 copy/mL short cell-free DNA from large-volume urine samples. *PLoS ONE* **16**, 1–26 (2021).

227. Oreskovic, A. *et al.* Diagnosing pulmonary tuberculosis by using sequence-specific purification of urine cell-free dna. *Journal of Clinical Microbiology* **59**, (2021).

228. Talalak, K., Noiphung, J., Songjaroen, T., Chailapakul, O. & Laiwattanapaisal, W. A facile low-cost enzymatic paper-based assay for the determination of urine creatinine. *Talanta* **144**, 915–921 (2015).

229. Tick Ressearch Lab of Pennsylvania. Test My Tick. Available at: https://www.ticklab.org/test-my-tick#. (Accessed: 2nd August 2023)

230. Kight, E., Hussain, I. & Bowden, A. K. Low-Cost, Volume-Controlled Dipstick Urinalysis for Home-Testing. *JoVE* e61406 (2021). doi:doi:10.3791/61406

231. Lei, R., Huo, R. & Mohan, C. Current and emerging trends in point-of-care urinalysis tests. *Expert review of molecular diagnostics* **20**, 69–84 (2020).

232. Pugia, M. J. Technology behind diagnostic reagent strips. *Laboratory Medicine* **31**, 92–96 (2000).

233. Dungchai, W., Chailapakul, O. & Henry, C. S. Electrochemical detection for paper-based microfluidics. *Analytical chemistry* **81**, 5821–5826 (2009).

234. Urisys 1100 Analyzer. Available at: https://diagnostics.roche.com/us/en/products/instruments/urisys-1100.html.

235. Filippini, D. & Lundström, I. Measurement strategy and instrumental performance of a computer screen photo-assisted technique for the evaluation of a multi-parameter colorimetric test strip. *Analyst* **131**, 111–117 (2006).

236. Shen, L., Hagen, J. A. & Papautsky, I. Point-of-care colorimetric detection with a smartphone. *Lab on a Chip* **12**, 4240–4243 (2012).

237. Ra, M. *et al.* Smartphone-Based Point-of-Care Urinalysis under Variable Illumination. *IEEE Journal of Translational Engineering in Health and Medicine* **6**, (2018).

238. Yetisen, A. K., Martinez-Hurtado, J. L., Garcia-Melendrez, A., Da Cruz Vasconcellos, F. & Lowe, C. R. A smartphone algorithm with inter-phone repeatability for the analysis of colorimetric tests. *Sensors and Actuators, B: Chemical* **196**, 156–160 (2014).

239. Wang, S. *et al.* Integration of cell phone imaging with microchip ELISA to detect ovarian cancer HE4 biomarker in urine at the point-of-care. *Lab on a Chip* **11**, 3411–3418 (2011).

240. Zhang, D. & Liu, Q. Biosensors and bioelectronics on smartphone for portable biochemical detection. *Biosensors and Bioelectronics* **75**, 273–284 (2016).

241. Choi, K. *et al.* Smartphone-based urine reagent strip test in the emergency department. *Telemedicine and e-Health* **22**, 534–540 (2016).

242. Kwon, L., Long, K. D., Wan, Y., Yu, H. & Cunningham, B. T. Medical diagnostics with mobile devices: Comparison of intrinsic and extrinsic sensing. *Biotechnology Advances* **34**, 291–304 (2016).

243. Vashist, S., Schneider, E. & Luong, J. Commercial Smartphone-Based Devices and Smart Applications for Personalized Healthcare Monitoring and Management. *Diagnostics* **4**, 104–128 (2014).

244. Inui. Available at: https://www.inuihealth.com/inui/home.

245. Healthy.io. Available at: https://healthy.io/.

246. Scanwell. Available at: https://www.scanwellhealth.com/.

247. Smith, G. T. *et al.* Robust dipstick urinalysis using a low-cost, micro-volume slipping manifold and mobile phone platform. *Lab on a Chip* **16**, 2069–2078 (2016).

248. Du, W., Li, L., Nichols, K. P. & Ismagilov, R. F. SlipChip. *Lab on a Chip* **9**, 2286–2292 (2009).

249. Kight, E. C., Hussain, I., Bowden, A. K. & Haselton, F. R. Recurrence monitoring for ovarian cancer using a cell phone-integrated paper device to measure the ovarian cancer biomarker HE4/CRE ratio in urine. *Scientific Reports* **11**, 1–11 (2021).

250. Giampaolino, P. *et al.* Role of biomarkers for early detection of ovarian cancer recurrence. *Gland Surgery* **9**, 1102–1111 (2020).

251. Coleman, M. P. *et al.* Cancer survival in Australia, Canada, Denmark, Norway, Sweden, and the UK, 1995-2007 (the international cancer benchmarking partnership): An analysis of population-based cancer registry data. *The Lancet* **377**, 127–138 (2011).

252. Davidson, B. A. The breast is yet to come : current and future utility of circulating tumour DNA in breast cancer. *British Journal of Cancer* (2021). doi:10.1038/s41416-021-01422-w

253. Ricks, K. M., Adams, N. M., Scherr, T. F., Haselton, F. R. & Wright, D. W. Direct transfer of HRPII-magnetic bead complexes to malaria rapid diagnostic tests significantly improves test sensitivity. *Malaria Journal* **15**, 1–8 (2016).

254. Scherr, T. F., Gupta, S., Wright, D. W. & Haselton, F. R. Mobile phone imaging and cloud-based analysis for standardized malaria detection and reporting. *Scientific Reports* **6**, 1–9 (2016).

255. *Lateral Flow Immunoassay*. (Springer Science & Business Media, 2008).

256. Analytical Tools to Improve Optimization Procedures for Lateral Flow Assays. *Diagnostics* **7**, 29 (2017).

257. Dutta, S. Point of care sensing and biosensing using ambient light sensor of smartphone: Critical review. *TrAC - Trends in Analytical Chemistry* **110**, 393–400 (2019).

258. You, D. J., Park, T. S. & Yoon, J. Y. Cell-phone-based measurement of TSH using Mie scatter optimized lateral flow assays. *Biosensors and Bioelectronics* **40**, 180–185 (2013).

259. Brouwer, B. G. B. and H. J. The Accuracy of Creatinine Methods Based on the Jaffé Reaction: A Questionable Matter. *Eur. J. Clin. Chem. Clin. Biochem.* **32**, 909–913 (1994).

260. Debus, B. *et al.* Two low-cost digital camera-based platforms for quantitative creatinine analysis in urine. *Analytica Chimica Acta* **895**, 71–79 (2015).

261. Panteghini, M. Enzymatic assays for creatinine: Time for action. *Scandinavian Journal of Clinical and Laboratory Investigation* **68**, 84–88 (2008).

262. Fossati, P., Prencipe, L. & Berti, G. Enzymic creatinine assay: a new colorimetric method based on hydrogen peroxide measurement. *Clinical Chemistry* **29**, 1494–1496 (1983).

263. Foysal, K. H., Seo, S. E., Kim, M. J., Kwon, O. S. & Chong, J. W. Analyte quantity detection from lateral flow assay using a smartphone. *Sensors (Switzerland)* **19**, (2019).

264. Göröcs, Z. & Ozcan, A. Biomedical imaging and sensing using flatbed scanners. *Lab on a Chip* **14**, 3248–3257 (2014).

265. Hussain, I., Ahamad, K. U. & Nath, P. Low-Cost, Robust, and Field Portable Smartphone Platform Photometric Sensor for Fluoride Level Detection in Drinking Water. *Analytical*

Chemistry **89**, 767–775 (2017).

266. Hussain, I., Bora, A. J., Sarma, D., Ahamad, K. U. & Nath, P. Design of a Smartphone Platform Compact Optical System Operational Both in Visible and Near Infrared Spectral Regime. *IEEE Sensors Journal* **18**, 4933–4939 (2018).

267. Küme, T., Sağlam, B., Ergon, C. & Sisman, A. R. Evaluation and comparison of Abbott Jaffe and enzymatic creatinine methods: Could the old method meet the new requirements? *Journal of Clinical Laboratory Analysis* **32**, 1–8 (2018).

268. Grayson, K., Gregory, E., Khan, G. & Guinn, B.-A. Urine Biomarkers for the Early Detection of Ovarian Cancer – Are We There Yet? *Biomarkers in Cancer* **11**, 1179299X1983097 (2019).

269. Woo, S. Y. & Kim, S. Determination of cutoff values for biomarkers in clinical studies. *Precision and Future Medicine* **4**, 2–8 (2020).

270. Shastri, A. & Shastri, S. S. Cancer screening and prevention in low-resource settings. *Nature Reviews Cancer* **14**, 822–829 (2014).

271. WHO. WHO recommendations on self-care interventions. *Human Reproduction Programme* (2020).

272. Kamath Mulki, A. & Withers, M. Human Papilloma Virus self-sampling performance in low- and middle-income countries. *BMC Women's Health* **21**, 1–11 (2021).

273. Jemal, A. *et al.* Cancer Statistics , 2009, Ca-a Cancer Journal for Clinicians,. **59**, 225–249 (2009).

274. Berchuck, A., Havrilesky, L. J. & Kauff, N. D. Is there a role for ovarian cancer screening in high-risk women? *Journal of Clinical Oncology* **35**, 1384–1386 (2017).

275. Andersen, M. R. *et al.* Use of a Symptom Index, CA125, and HE4 to predict ovarian cancer. *Gynecologic Oncology* **116**, 378–383 (2010).

276. Kight, E. *et al.* Direct Capture and Early Detection of Lyme Disease Spirochete in Skin with a Microneedle Patch. *Biosensors* **12**, 1–18 (2022).

277. Rochlin, I. & Toledo, A. Emerging tick-borne pathogens of public health importance: a mini-review. *Journal of medical microbiology* **69**, 781 (2020).

278. Kugeler, K. J., Schwartz, A. M., Delorey, M. J., Mead, P. S. & Hinckley, A. F. Estimating the frequency of Lyme disease diagnoses, United States, 2010–2018. *Emerging Infectious Diseases* **27**, 616 (2021).

279. Dumic, I. & Severnini, E. "Ticking bomb": the impact of climate change on the incidence of Lyme disease. *Canadian Journal of Infectious Diseases and Medical Microbiology* **2018**, (2018).

280. Prevention, C. for D. C. and. Signs and symptoms of untreated Lyme disease. (2015).

281. Moore, A., Nelson, C., Molins, C., Mead, P. & Schriefer, M. Current guidelines, common clinical pitfalls, and future directions for laboratory diagnosis of Lyme disease, United States. *Emerging infectious diseases* **22**, 1169 (2016).

282. US Dept of Health & Human Services. Tick-Borne Disease Working Group. (2018).

283. Pearlman, S. I. *et al.* Low-Resource Nucleic Acid Extraction Method Enabled by High-Gradient Magnetic Separation. *ACS Applied Materials and Interfaces* **12**, 12457–12467 (2020).

284. Waddell, L. A. *et al.* The accuracy of diagnostic tests for Lyme disease in humans, a systematic

review and meta-analysis of North American research. *PloS one* **11**, e0168613 (2016).

285. Schutzer, S. E. *et al.* Direct diagnostic tests for Lyme disease. *Clinical Infectious Diseases* **68**, 1052–1057 (2019).

286. Priem, S., Rittig, M. G., Kamradt, T., Burmester, G. R. & Krause, A. An optimized PCR leads to rapid and highly sensitive detection of Borrelia burgdorferi in patients with Lyme borreliosis. *Journal of Clinical Microbiology* **35**, 685–690 (1997).

287. Mosel, M. R. *et al.* Molecular microbiological and immune characterization of a cohort of patients diagnosed with early Lyme disease. *Journal of clinical microbiology* **59**, e00615-20 (2020).

288. Dunaj, J., Moniuszko, A., Zajkowska, J. & Pancewicz, S. The role of PCR in diagnostics of Lyme borreliosis. *Przegląd epidemiologiczny* **67**, 35–39 (2013).

289. Straubinger, R. K., Summers, B. A., Chang, Y.-F. & Appel, M. J. Persistence of Borrelia burgdorferi in experimentally infected dogs after antibiotic treatment. *Journal of clinical microbiology* **35**, 111–116 (1997).

290. Zhang, X., Chen, G., Bian, F., Cai, L. & Zhao, Y. Encoded microneedle arrays for detection of skin interstitial fluid biomarkers. *Advanced Materials* **31**, 1902825 (2019).

291. Al Sulaiman, D. *et al.* Hydrogel-coated microneedle arrays for minimally invasive sampling and sensing of specific circulating nucleic acids from skin interstitial fluid. *ACS nano* **13**, 9620–9628 (2019).

292. Liu, G.-S. *et al.* Microneedles for transdermal diagnostics: Recent advances and new horizons. *Biomaterials* **232**, 119740 (2020).

293. Jiang, X. & Lillehoj, P. B. Microneedle-based skin patch for blood-free rapid diagnostic testing. *Microsystems and Nanoengineering* **6**, 1–11 (2020).

294. Yi, K. *et al.* Aptamer-decorated porous microneedles arrays for extraction and detection of skin interstitial fluid biomarkers. *Biosensors and Bioelectronics* **190**, 113404 (2021).

295. Dixon, R. V *et al.* Microneedle-based devices for point-of-care infectious disease diagnostics. *Acta Pharmaceutica Sinica B* **11**, 2344–2361 (2021).

296. Park, S. *et al.* Rapid Extraction and Detection of Biomolecules via a Microneedle Array of Wet-Crosslinked Methacrylated Hyaluronic Acid. *Advanced Materials Technologies* **7**, 2100874 (2022).

297. Samant, P. P. & Prausnitz, M. R. Mechanisms of sampling interstitial fluid from skin using a microneedle patch. *Proceedings of the National Academy of Sciences of the United States of America* **115**, 4583–4588 (2018).

298. Zhang, N. *et al.* Dissolving Polymer Microneedles for Transdermal Delivery of Insulin. *Frontiers in Pharmacology* **12**, (2021).

299. Paul, R. *et al.* Extraction of plant DNA by microneedle patch for rapid detection of plant diseases. *ACS nano* **13**, 6540–6549 (2019).

300. Li, H. *et al.* Instant and Multiple DNA Extraction Method by Microneedle Patch for Rapid and on-Site Detection of Food Allergen-Encoding Genes. *Journal of Agricultural and Food Chemistry* **69**, 6879–6887 (2021).

301. Hassan, C. M. & Peppas, N. A. Structure and morphology of freeze/thawed PVA hydrogels.

Macromolecules **33**, 2472–2479 (2000).

302. Xu, N. *et al.* Swellable PVA/PVP hydrogel microneedle patches for the extraction of interstitial skin fluid toward minimally invasive monitoring of blood glucose level. *Analyst* **147**, 1478–1491 (2022).

303. Oster, J., Parker, J. & à Brassard, L. Polyvinyl-alcohol-based magnetic beads for rapid and efficient separation of specific or unspecific nucleic acid sequences. *Journal of Magnetism and Magnetic Materials* **225**, 145–150 (2001).

304. Schyma, C., Huckenbeck, W. & Bonte, W. DNA-PCR analysis of bloodstains sampled by the polyvinyl-alcohol method. *Journal of Forensic Science* **44**, 95–99 (1999).

305. Otsuka, E. & Suzuki, A. A simple method to obtain a swollen PVA gel crosslinked by hydrogen bonds. *Journal of applied polymer science* **114**, 10–16 (2009).

306. Patterson, J. W., Duncan, A. M., McIntyre, K. C. & Lloyd, V. K. Evidence for genetic hybridization between Ixodes scapularis and Ixodes cookei. *Canadian Journal of Zoology* **95**, 527–537 (2017).

307. Bugmyrin, S. V, Belova, O. A., Bespyatova, L. A., Ieshko, E. P. & Karganova, G. G. Morphological features of Ixodes persulcatus and I. ricinus hybrids: nymphs and adults. *Experimental and Applied Acarology* **69**, 359–369 (2016).

308. BLACKLEGGED TICK ANATOMY AND IDENTIFICATION. Available at: https://www.tickipedia.org/blacklegged-tick-anatomy-and-identification/. (Accessed: 20th May 2022)

309. Sharma, A. *et al.* Cas9-mediated gene editing in the black-legged tick, Ixodes scapularis, by embryo injection and ReMOT Control. *Iscience* **25**, 103781 (2022).

310. Bockenstedt, L. K. *et al.* What ticks do under your skin: two-photon intravital imaging of Ixodes scapularis feeding in the presence of the Lyme disease spirochete. *The Yale journal of biology and medicine* **87**, 3 (2014).

311. Kochhar, J. S. *et al.* Effect of microneedle geometry and supporting substrate on microneedle array penetration into skin. *Journal of Pharmaceutical Sciences* **102**, 4100–4108 (2013).

312. Makvandi, P. *et al.* Engineering microneedle patches for improved penetration: analysis, skin models and factors affecting needle insertion. *Nano-Micro Letters* **13**, 1–41 (2021).

313. Larrañeta, E. *et al.* A proposed model membrane and test method for microneedle insertion studies. *International journal of pharmaceutics* **472**, 65–73 (2014).

314. Arora, A. *et al.* Needle-free delivery of macromolecules across the skin by nanoliter-volume pulsed microjets. *Proceedings of the National Academy of Sciences* **104**, 4255–4260 (2007).

315. Zhang, D., Das, D. B. & Rielly, C. D. Microneedle assisted micro-particle delivery from gene guns: experiments using skin-mimicking agarose gel. *Journal of Pharmaceutical Sciences* **103**, 613–627 (2014).

316. Permana, A. D., Mir, M., Utomo, E. & Donnelly, R. F. Bacterially sensitive nanoparticle-based dissolving microneedles of doxycycline for enhanced treatment of bacterial biofilm skin infection: A proof of concept study. *International journal of pharmaceutics: X* **2**, 100047 (2020).

317. Bonfante, G. *et al.* Comparison of polymers to enhance mechanical properties of microneedles for bio-medical applications. *Micro and Nano Systems Letters* **8**, 1–13 (2020).

318. Enfield, J. G. *et al.* In-vivo dynamic characterization of microneedle skin penetration using optical coherence tomography. *Journal of biomedical optics* **15**, 46001 (2010).

319. Shu, B. *et al.* Design and performance of the CDC real-time reverse transcriptase PCR swine flu panel for detection of 2009 A (H1N1) pandemic influenza virus. *Journal of clinical microbiology* **49**, 2614–2619 (2011).

320. Emery, S. L. *et al.* Real-time reverse transcription–polymerase chain reaction assay for SARS-associated coronavirus. *Emerging infectious diseases* **10**, 311 (2004).

321. Barbour, A. G., Hayes, S. F., Heiland, R. A., Schrumpf, M. E. & Tessier, S. L. A Borrelia-specific monoclonal antibody binds to a flagellar epitope. *Infection and Immunity* **52**, 549–554 (1986).

322. de Leeuw, B. H. *et al.* Evaluation of Borrelia real time PCR DNA targeting OspA, FlaB and 5S–23S IGS and Borrelia 16S rRNA RT-qPCR. *Journal of microbiological methods* **107**, 41–46 (2014).

323. Wills, M. K. B., Kirby, A. M. & Lloyd, V. K. Detecting the lyme disease spirochete, Borrelia burgdorferi, in ticks using nested PCR. *JoVE (Journal of Visualized Experiments)* e56471 (2018).

324. Johnson, A. R. & Procopio, A. T. Low cost additive manufacturing of microneedle masters. *3D Printing in Medicine* **5**, (2019).

325. Johnson, A. R. *et al.* Single-step fabrication of computationally designed microneedles by continuous liquid interface production. *PloS one* **11**, e0162518 (2016).

326. Oh, N. G., Hwang, S. Y. & Na, Y. H. Fabrication of a PVA-Based Hydrogel Microneedle Patch. *ACS omega* **7**, 25179–25185 (2022).

327. Paul, R. *et al.* Integrated microneedle-smartphone nucleic acid amplification platform for in-field diagnosis of plant diseases. *Biosensors and Bioelectronics* **187**, 113312 (2021).

328. Flaten, G. E. *et al.* In vitro skin models as a tool in optimization of drug formulation. *European journal of pharmaceutical sciences* **75**, 10–24 (2015).

329. Kim, M., Jung, B. & Park, J.-H. Hydrogel swelling as a trigger to release biodegradable polymer microneedles in skin. *Biomaterials* **33**, 668–678 (2012).

330. Dick, I. P. & Scott, R. C. Pig ear skin as an in-vitro model for human skin permeability. *Journal of Pharmacy and Pharmacology* **44**, 640–645 (1992).

331. Moniz, T., Costa Lima, S. A. & Reis, S. Human skin models: From healthy to disease-mimetic systems; characteristics and applications. *British Journal of Pharmacology* **177**, 4314–4329 (2020).

332. Jacobi, U. *et al.* Porcine ear skin: an in vitro model for human skin. *Skin Research and Technology* **13**, 19–24 (2007).

333. Cutler, S. J. *et al.* Tick-borne diseases and co-infection: Current considerations. *Ticks and tick-borne diseases* **12**, 101607 (2021).

334. Nieto, N. C. *et al.* Using citizen science to describe the prevalence and distribution of tick bite and exposure to tick-borne diseases in the United States. *PLoS One* **13**, e0199644 (2018).

335. Marques, A. *et al.* Xenodiagnosis to detect Borrelia burgdorferi infection: a first-in-human study. *Clinical infectious diseases* **58**, 937–945 (2014).

336. Jacobs, M. B., Grasperge, B. J., Embers, M. E., National, T. & Rouge, B. Borrelia burgdorferi Migration Assays for Evaluation of Chemoattractants in Tick Saliva. 1–13 (2022).

337. Van Gundy, T. J., Ullmann, A. J., Brandt, K. S. & Gilmore, R. D. A transwell assay method to evaluate Borrelia burgdorferi sensu stricto migratory chemoattraction toward tick saliva proteins. *Ticks and Tick-borne Diseases* **12**, 101782 (2021).

338. Nuttall, P. A. Tick saliva and its role in pathogen transmission. *Wiener Klinische Wochenschrift* (2019). doi:10.1007/s00508-019-1500-y

339. Das, S., Hammond-McKibben, D., Guralski, D., Lobo, S. & Fiedler, P. N. Development of a sensitive molecular diagnostic assay for detecting Borrelia burgdorferi DNA from the blood of Lyme disease patients by digital PCR. *PloS one* **15**, e0235372 (2020).

340. Wesseling, C. *et al.* Chronic kidney disease of non-traditional origin in Mesoamerica: a disease primarily driven by occupational heat stress. *Revista Panamericana de Salud Pública* **44**, (2020).

341. Wang, J. *et al.* Interaction of HE4 and ANXA2 exists in various malignant cells—HE4–ANXA2–MMP2 protein complex promotes cell migration. *Cancer Cell International* **19**, 1–12 (2019).

342. Yu, J. *et al.* Targeting and neutralizing human epididymis protein 4 by novel nanobodies to suppress ovarian cancer cells and attenuate cisplatin resistance. *International Journal of Biological Macromolecules* **199**, 298–306 (2022).

343. Maddison, M. D. *et al.* Development and Validation of a Colorimetric Reverse Transcriptase Loop-Mediated Isothermal Amplification Assay for Detection of Eastern Equine Encephalitis Virus in Mosquitoes. *Journal of the American Mosquito Control Association* **38**, 7–18 (2022).

344. Bourgeois, B. *et al.* Clobetasol increases the abundance of Borrelia burgdorferi in the skin 70 times more in male mice compared to female mice. *Ticks and Tick-borne Diseases* **13**, 102058 (2022).

345. Khan, G., Kangro, H. O., Coates, P. J. & Heath, R. B. Inhibitory effects of urine on the polymerase chain reaction for cytomegalovirus DNA. *Journal of Clinical Pathology* **44**, 360–365 (1991).

346. Roux, A., Thévenot, E. A., Seguin, F., Olivier, M. F. & Junot, C. Impact of collection conditions on the metabolite content of human urine samples as analyzed by liquid chromatography coupled to mass spectrometry and nuclear magnetic resonance spectroscopy. *Metabolomics* **11**, 1095–1105 (2015).

347. Gika, H. G., Theodoridis, G. A. & Wilson, I. D. Liquid chromatography and ultra-performance liquid chromatography–mass spectrometry fingerprinting of human urine: Sample stability under different handling and storage conditions for metabonomics studies. *Journal of Chromatography A* **1189**, 314–322 (2008).

348. Barra, G. B. *et al.* EDTA-mediated inhibition of DNases protects circulating cell-free DNA from ex vivo degradation in blood samples. *Clinical biochemistry* **48**, 976–981 (2015).

349. Bordelon, H. *et al.* Design and use of mouse control DNA for DNA biomarker extraction and PCR detection from urine: Application for transrenal Mycobacterium tuberculosis DNA detection. *Journal of microbiological methods* **136**, 65–70 (2017).

350. Pokress, S. C. & Veiga, J. J. D. MIT App Inventor: Enabling Personal Mobile Computing. 0–2 (2013).

351. Shariq, M. *et al.* COVID-19 and tuberculosis: the double whammy of respiratory pathogens.

European Respiratory Review **31**, (2022).

352. Chakaya, J. *et al.* The WHO Global Tuberculosis 2021 Report–not so good news and turning the tide back to End TB. *International Journal of Infectious Diseases* **124**, S26–S29 (2022).

353. Kant, S., Gupta, H. & Ahluwalia, S. Significance of nutrition in pulmonary tuberculosis. *Critical reviews in food science and nutrition* **55**, 955–963 (2015).

354. Kant, S., Maurya, A. K., Kushwaha, R. A. S., Nag, V. L. & Prasad, R. Multi-drug resistant tuberculosis: an iatrogenic problem. *Bioscience trends* **4**, (2010).

355. Kant, S. & Tyagi, R. The impact of COVID-19 on tuberculosis: challenges and opportunities. *Therapeutic Advances in Infectious Disease* **8**, 20499361211016972 (2021).

356. Shekhtman, E. M. *et al.* Optimization of transrenal DNA analysis: detection of fetal DNA in maternal urine. *Clinical chemistry* **55**, 723–729 (2009).

357. Brosch, R. Genomics, biology, and evolution of the Mycobacterium tuberculosis complex. *Molecular Genetics of Mycobacteria* 19–36 (2000).

358. Coros, A., DeConno, E. & Derbyshire, K. M. IS 6110, a Mycobacterium tuberculosis complex-specific insertion sequence, is also present in the genome of Mycobacterium smegmatis, suggestive of lateral gene transfer among mycobacterial species. *Journal of bacteriology* **190**, 3408–3410 (2008).

359. Antonello, M. *et al.* Rapid detection and quantification of Mycobacterium tuberculosis DNA in paraffinized samples by droplet digital PCR: a preliminary study. *Frontiers in Microbiology* **12**, 727774 (2021).

360. Schormann, N., Ricciardi, R. & Chattopadhyay, D. Uracil-DNA glycosylases - Structural and functional perspectives on an essential family of DNA repair enzymes. *Protein Science* **23**, 1667–1685 (2014).

361. Wardle, J. *et al.* Uracil recognition by replicative DNA polymerases is limited to the archaea, not occurring with bacteria and eukarya. *Nucleic Acids Research* **36**, 705–711 (2008).

362. Greagg, M. A. *et al.* A read-ahead function in archaeal DNA polymerases detects promutagenic template-strand uracil. *Proceedings of the National Academy of Sciences* **96**, 9045–9050 (1999).

363. Fogg, M. J., Pearl, L. H. & Connolly, B. A. Structural basis for uracil recognition by archaeal family B DNA polymerases. *Nature structural biology* **9**, 922–927 (2002).

364. Belkin, S. & Jannasch, H. W. A new extremely thermophilic, sulfur-reducing heterotrophic, marine bacterium. *Archives of microbiology* **141**, 181–186 (1985).

365. Perler, F. B. *et al.* Intervening sequences in an Archaea DNA polymerase gene. *Proceedings of the National Academy of Sciences* **89**, 5577–5581 (1992).

366. Chander, Y. *et al.* A novel thermostable polymerase for RNA and DNA loop-mediated isothermal amplification (LAMP). *Frontiers in Microbiology* **5**, 395 (2014).

367. Coffin, J. M., Hughes, S. H. & Varmus, H. E. Retroviruses. (1997).

368. Malboeuf, C. M., Isaacs, S. J., Tran, N. H. & Kim, B. Thermal effects on reverse transcription: improvement of accuracy and processivity in cDNA synthesis. *Biotechniques* **30**, 1074–1084 (2001).